# Development of CFD Thermal Hydraulics and Neutron Kinetics Coupling Methodologies for the Prediction of Local Safety Parameters for Light Water Reactors

Zur Erlangung des akademischen Grades

Doktor der Ingenieurwissenschaften

der Fakultät für Maschinenbau
Karlsruher Institut für Technologie (KIT)

genehmigte

Dissertation

von

Ing. Jorge Pérez Mañes

Tag der mündlichen Prüfung: 26/2/2013

Hauptreferent: Prof. Dr.-Ing. Robert Stieglitz
Karlsruher Institut für Technologie (KIT)

Korreferent: Ing. Sergio Chiva Vicent, Ph.D.
Universitat Jaume I (UJI)

| | |
|---|---|
| Hauptreferent: | Prof. Dr.-Ing. Robert Stieglitz<br>Karlsruher Institut für Technologie (KIT) |
| Korreferent: | Ing. Sergio Chiva Vicent, Ph.D.<br>Universitat Jaume I (UJI) |
| Betreuung: | Dr.-Ing. Victor Hugo Sánchez Espinoza<br>Karlsruher Institut für Technologie (KIT) |

A mis padres Jorge y Carmen.
A mi hermana Patricia.

# Preface

This thesis was carried out during my activities as a Ph.D. candidate at the Institute for Neutron Physics and Reactor Technology (INR) at Karlsruhe Institute of Technology (KIT) under the auspices of the Nuclear Reactor Integrated Simulation Project (NURSIP). It summarizes the activities performed during three years.

This thesis wouldn't have been possible without the support of the following people and institutions to which I want to thank.

Thanks to Prof. Robert Stieglitz for accepting me as a student in the INR and to Dr. Victor Sanchez for his advices and for giving me the opportunity to study in Germany.

Thanks to Dr. Michael Böttcher for his technical support and for introducing me the art of climbing. I would like to show my gratitude to Prof. Thomas Schulenberg, Prof. Andreas Class and Dr. Abdala Batta for their fruitful lectures.

I particularly appreciate the help of Dr. Sergio Chiva, thanks for his support, not only during my activities as a Ph.D. candidate but also during my stay in the Mechanical Engineering and Construction Department of the Jaume I University.

I am glad to name my KIT/INR friends: Dr. Armando Gómez, Manuel Calleja, Christoph Hartmann, Dr. Javier Jimenez, Coral Herranz, Dr. Wadim Jäger, Miriam Däubler, Markus Schlenker, Cristian Garrido, Rodrigo Gómez, Ana Berkhan, Dr. Sara Pérez and Aleksandar Ivanov. Thanks to all them for the good memories they have brought me during these years, especially for the moments we had in the L.M. group.

And last but not least, I would like to thank the Fundacion Balaguer Gonel Hermanos and its president Don Ernesto Tarragón Albella for the support during my final studies stage in the University Jaume I in Castellón.

# Abstract

This dissertation contributes to the development of high-fidelity coupled neutron kinetic and thermal hydraulic simulation tools with high resolution of the spatial discretization of the involved domains for the analysis of Light Water Reactors transient scenarios.

For safety assessment of reactor systems, the prediction of local safety parameters is mandatory. This prediction is the objective of many computational codes, for instance the system codes devoted to the description of whole systems and components of the nuclear power plant, or the subchannel codes, that work in a smaller and more detailed scale. Since the spatial resolution of systems and subchannel codes is limited to the macro- and meso-scale of thermal hydraulic phenomena, the computational fluid dynamic codes can provide a local description of safety related thermal hydraulic parameters (departure from nucleate boiling, cladding temperatures, etc...).

The coupling of a computational fluid dynamic code with heat conduction solver and a 3D transport based kinetic code will allow the high fidelity prediction of heat generation and transfer process inside fuel pins of reactor cores covering both single and two-phase flow fluid conditions. By coupling thermal hydraulic and neutron kinetic codes at fine spatial discretization it is possible to improve the current methodologies for the prediction of local safety-relevant parameters and hence to reduce the conservatism of actual codes. The main goal of this doctoral thesis is both, to contribute to the validation of the two-phase flow models of NEPTUNE_CFD using Boiling Water Reactor and Pressurized Water Reactor data obtained in experimental facilities and to develop an advanced coupling scheme between NEPTUNE_CFD and the transport based DYN3D_SP3 reactor dynamic code for high fidelity simulations of pin clusters, fuel bundles and in the long term, bundle clusters.

NEPTUNE_CFD is a relatively new code. The two-phase flow models implemented require special review and validation. This validation aims to understand the behaviour of the code in transient scenarios for Light Water Reactors focusing on the flow within fuel assemblies. Based on it, valuable information regarding the deviation of the code predictions from experimental data can be obtained and the main areas for model improvements can be identified. Before starting the coupling work it is important to be aware of the current limitations of the two-phase flow modeling capabilities of the computational fluid dynamics codes.

The main goal of the thesis work is the development of the methodology for a novel coupled solution, which involves the next codes:

- The NEPTUNE_CFD for the fluid domain.
- The simplified multi-group neutron transport solver DYN3D_SP3 for the neutron physical phenomena within the core.

- The coupled solution NEPTUNE_CFD/DYN3D_SP3 needs a heat conduction solver to describe the temperatures in solid domains e.g. fuel rods. This task is performed by the SYRTHES code.

These codes were coupled explicitly in the frame of this doctoral thesis allowing an information exchange of the three domains during time advancement. To solve the mismatch between neutron kinetic and thermal hydraulic meshes the information is exchanged based on a radial and axial mapping scheme. The coupling approach was developed within a parallel environment where the communication between the involved programs is realized using a Message Passing Interface code standard and taking advantage of the parallelization capabilities of NEPTUNE_CFD. All these processes are controlled by the main program, developed specifically for this purpose.

The prediction capability of the new coupled system NEPTUNE_CFD/ SYRTHES/ DYN3D_SP3 (NHESDYN) is evaluated by code-to-code comparison using the DYNSUB code for a set of selected transient cases. The results obtained with the NHESDYN code are encouraging and they contribute to lay the foundations in the utilizations of refined discretization tools for safety parameters predictions. An extensive discussion of the validation work is provided. The main conclusions and possible areas for further developments are listed, too.

# Kurzfassung

Die vorliegende Arbeit trägt wesentlich zu der Entwicklung präziser gekoppelter Neutronik und Thermohydraulik Simulationsprogramme bei. Dabei können die zu untersuchenden Bereiche eines Leichtwasserreaktors relativ hoch räumlich aufgelöst werden.

Die Bestimmung lokaler Sicherheitsparameter ist Voraussetzung zur Bewertung der Sicherheit eines Reaktors. Durch die Beschränkung der räumlichen Auflösung von System- und Unterkanalprogrammen (Makro und Meso-Skalen) kommen für die Bestimmung von sicherheitsrelevanten Parametern (z.B. DNB, Brennstoff- und Hüllrohrtemperaturen) zunehmend CFD Programme zum Einsatz.

Die Kopplung von CFD Programmen mit 3D Neutronikprogrammen erlaubt die genaue Bestimmung der Wärmeproduktion und deren Auswirkungen auf das Kühlmittel sowohl im einphasigen als auch im zweiphasigen Zustand. Durch die höhere räumliche Auflösung in mehreren Dimensionen kann die Ermittlung sicherheitsrelevanter Parameter verbessert werden und dadurch der Konservatismus verringert werden. Die Hauptaufgabe dieser Arbeit richtet sich zum einen auf die Validierung der Zweiphasenmodelle von NEPTUNE_CFD und zum anderen auf der Entwicklung eines modernen Kopplungskonzepts zwischen NEPTUNE_CFD und dem Neutronentransportprogramm DYN3D_SP3. Zur Validierung werden Experimente herangezogen, die sich auf Druck- und Siedewasserreaktoren beziehen. Mit dem gekoppelten System sollen sehr detailliert Brennstäbe und –Brennstabclusters sowie Brennelemente und langfristig ganze Reaktorkerne simuliert werden.

NEPTUNE_CFD ist ein relativ neues Programm und seine Zweiphasenmodelle wie die anderer CFD-codes benötigen eine umfassende Validierung unter Einbeziehung experimenteller Daten.. Im Rahmen dieser Arbeit konzentriert sich die Validierung auf stationäre und transiente Randbedingungen innerhalb eines Leichtwasserreaktor-Brennelements. Dadurch können wertvolle Information hinsichtlich der Leistungsfähigkeit und Genauigkeit der betroffenen Modelle erhalten werden. Diese können, wiederum benutzt werden, um die Modelle zu verbessern bzw. zu ersetzen. Darüber hinaus ist die Identifizierung der Modelldefizite von sicherheitsrelevanten Phänomenen ein wichtiger Beitrag der Codevalidierung und ein notwendiger Schritt bevor die Simulationstools in Rahmen einer Kopplung eingesetzt werden.

Eines der Hauptziele der Promotion ist die Entwicklung einer neuartigen Kopplungsmethode, bei der die folgenden Programme zum Einsatz kommen:

- NEPTUNE_CFD zur Beschreibung der Thermohydraulik innerhalb der Kühlkanäle (Fluiddomäne),
- DYN3D_SP3 zur Beschreibung der neutronenphysikalischen Vorgänge im Brennstab bzw. Kern, und

- SYRTHES zur Beschreibung der Wärmetransport in festen Strukturen, z.B. Brennstoff. Es bildet das Bindeglied zwischen NEPTUNE_CFD und DYN3D_SP3.

Diese drei Programme wurden explizit in Rahmen dieser Doktorarbeit miteinander gekoppelt, wozu der Datenaustausch zwischen dem Neutronikgitter und dem Thermohydraulikgitter in radialer und axialer Richtung vorab definiert werden muss. Die Kommunikation zwischen den Programmen wird mittels Message Passing Interface realisiert, welche die Ausnutzung der Fähigkeit zur parallelen Ausführung von NEPTUNE_CFD ermöglicht. Um den Datenaustausch zwischen den Programmen zu realisieren, wurde ein Steuerprogramm eigens dafür entwickelt.

Um die Vorhersagefähigkeit des neu entwickelten Programmsystems NEPTUNE_CFD/SYRTHES/ DYN3D_SP3 (NHESDYN) wurde durch einen Code-zu-Code-Vergleich mit DYNSUB validiert. Hierfür wurden repräsentative Transienten definiert und sie mit NHESDYN und DYNSUB simuliert. Der Vergleich der mit NHESDYN berechneten Ergebnisse zu den DYNSUB-Ergebnissen ist für die meisten Parameter sehr gut und es zeigt die Leistungsfähigkeit und das Potential des neu entwickelten gekoppelten Programms NHESDYN. Die Entwicklungs- und Validierungsarbeiten in Rahmen dieser Dissertation sind detailliert beschrieben. Mögliche Bereiche zukünftiger Arbeit werden im Zusammenhang explizit aufgelistet und erläutert.

Conference papers:

**“Validation of NEPTUNE_CFD two phase flow models using PSBT experiments”** J. Pérez, M. Böttcher, V. Sánchez. Jahrestagung Kerntechnik (KTG). Berlin, Germany, 2011.

**“Validation of the NEPTUNE_CFD two phase flow models using the OECD/NRC BFBT benchmark database”** J. Pérez, M. Böttcher, V. Sánchez. The 14th International Topical Meeting on Nuclear Reactor Thermalhydraulics (NURETH-14). Toronto, Canada, 2011.

**“NEPTUNE_CFD Two Phase Flow Modeling and Validation for BWR Safety Analyses in Transient Conditions”** J. Pérez, R. Stieglitz, S. Chiva V. Sanchez, M. Böttcher. The 9th International Topical Meeting on Nuclear Thermal-Hydraulics, Operation and Safety (NUTHOS-9). Kaohsiung, Taiwan. 2012.

Journal papers:

**“Comparison of Two-Phase Flow Modeling Capabilities of CFD, Sub-Channel and System Codes by means of Post-Test Calculations of BFBT Transients”** W. Jaeger, J. Pérez, U. Imke, J. Jiménez, V. Sánchez. Nuclear Engineering and Design. (under review).

**“Contribution to NEPTUNE_CFD Two-Phase Flow Models Validation Using Experimental Data”** J. Pérez, R. Stieglitz, S. Chiva V. Sánchez, M. Böttcher. (Submitted for publication).

**“CFD/Neutron Kinetics Coupled Solution for High Fidelity Analyses of LWR”** J. Pérez, R. Stieglitz, S. Chiva V. Sanchez, M. Böttcher. (Submitted for publication).

NURISP project deliverables:

**“Progress Report on Two Phase Flow Simulartions in a Subchannel with NEPTUNE_CFD 1.0.7”** J. Pérez, M. Böttcher. NURISP delivelable D2.3.3.19a (Nuclear Reactor Simulation Integrated Project) SP2 Group, Thermal hydraulics 2010.

**“Contribution to the Validation of NEPTUNE_CFD 1.0.8 Two Phase Flow Models for BWR Applications”** J. Pérez, M. Böttcher. NURISP delivelable D2.3.3.19b. (Nuclear Reactor Simulation Integrated Project) SP2 Group, Thermal hydraulics. 2010.

# Table of Content

PREFACE ........ I

ABSTRACT ........ III

TABLE OF CONTENT ........ IX

LIST OF FIGURES ........ XIII

LIST OF TABLES ........ XIX

LIST OF ACRONYMS ........ XXI

1 INTRODUCTION ........ 1

- 1.1 MOTIVATION ........ 1
- 1.2 OBJECTIVE ........ 1
- 1.3 ORGANIZATION OF THE THESIS ........ 2
- 1.4 WORKING METHODOLOGY ........ 3
- 1.5 STATE OF THE ART OF NUMERICAL SIMULATION TOOLS ........ 3
  - 1.5.1 THERMAL HYDRAULIC SYSTEM CODES. ........ 4
  - 1.5.2 THERMAL HYDRAULIC SUBCHANNEL CODES. ........ 6
  - 1.5.3 COMPUTATIONAL FLUID DYNAMICS CODES ........ 6
  - 1.5.4 THE MULTI-PHYSICS SIMULATION CODES ........ 15

2 THE NK-TH CODES SELECTED FOR THE COUPLED SOLUTION ........ 19

- 2.1 DYN3D_SP3 ........ 19
- 2.2 SUBCHANFLOW ........ 20
  - 2.2.1 FLUID DYNAMIC MODELS ........ 21
  - 2.2.2 HEAT CONDUCTION MODEL ........ 22
- 2.3 DYNSUB ........ 24
- 2.4 SYRTHES ........ 25

3 THE NEPTUNE_CFD CODE ........ 28

- 3.1 BRIEF INTRODUCTION TO THE KINEMATICS OF FLUID MOTION ........ 28
  - 3.1.1 RELATION BETWEEN EULERIAN AND LAGRANGIAN CONSIDERATIONS: ........ 29
- 3.2 GOVERNING EQUATIONS ........ 30
  - 3.2.1 MASS BALANCE EQUATIONS: ........ 30
  - 3.2.2 MOMENTUM BALANCE EQUATIONS: ........ 30
  - 3.2.3 TOTAL ENTHALPY BALANCE EQUATIONS: ........ 31
- 3.3 INTERFACIAL TRANSFER TERMS ........ 31
- 3.4 INTERFACIAL AREA MODELLING ........ 35
- 3.5 TURBULENT TRANSFER TERMS ........ 36
  - 3.5.1 EDDY VISCOSITY MODEL - STANDARD K-ε APPROACH ........ 36
- 3.6 WALL BOILING MODEL ........ 37
  - 3.6.1 BOILING MODEL EXTENSION FOR DNB MODELING ........ 40
- 3.7 WALL FUNCTION MODEL FOR BOILING FLOW ........ 41

4 CONTRIBUTION TO THE NEPTUNE_CFD VALIDATION ........ 43

- 4.1 OECD/NRC BENCHMARK BASED ON NUPEC PWR SUBCHANNEL AND BUNDLE TEST PSBT43
  - 4.1.1 SCOPE AND DESCRIPTION OF THE BENCHMARK ........ 43
  - 4.1.2 APPLIED MODELS ........ 45
  - 4.1.3 SPACE DISCRETIZATION OF THE STUDIED DOMAIN ........ 45
  - 4.1.4 MESH SENSITIVITY ANALYSIS. ........ 46
  - 4.1.5 BUBBLE SIZE SENSITIVITY ANALYSIS ........ 50

4.1.6 Selected results ... 52
4.1.7 Summary and conclusions of the PSBT simulations ... 54
4.2 The NUPEC BWR full size fine mesh bundle test (BFBT) Benchmark ... 56
4.2.1 Scope and description of the benchmark ... 56
4.2.2 Applied models ... 58
4.2.3 Modeling of the rod bundle ... 59
4.2.4 Selected results for the turbine trip without bypass experiment ... 61
4.2.5 Selected results for the recirculation pump trip experiment ... 65
4.2.6 Summary and conclusions on the BFBT simulations ... 67

**5 COUPLING METHODOLOGY ... 70**

5.1 Introduction ... 70
5.2 General coupling scheme ... 71
5.3 Coupled solution execution ... 73
5.4 Time advancement description ... 74
5.5 Steady state coupling scheme ... 75
5.5.1 TH convergence loop ... 77
5.6 Transient coupling scheme ... 77
5.7 Spatial mapping ... 77
5.7.1 NEPTUNE_CFD to interface ... 79
5.7.2 SYRTHES to interface ... 81
5.7.3 Interface to DYN3D_SP3 ... 81
5.7.4 DYN3D_SP3 to interface ... 81
5.7.5 Interface to SYRTHES ... 82

**6 VALIDATION OF THE COUPLED TH/NK SOLUTION ... 85**

6.1 Introduction ... 85
6.2 Initial conditions and problem definition ... 85
6.3 Space discretization ... 88
6.4 Steady state analysis ... 89
6.5 Transient cases ... 94
6.5.1 Transient case: temperature step ... 95
6.5.2 Transient case: Mass flow variation ... 101
6.5.3 Transient case: Depressurization ... 105
6.6 Summary and conclusions of the tested cases ... 109

**7 GENERAL CONCLUSIONS ... 111**

**8 OUTLOOK ... 114**

**9 BIBLIOGRAPHY ... 115**

**10 ANNEX A. THE NEPTUNE_CFD/SYRTHES VALIDATION ... 129**

10.1 BFBT turbine trip without bypass ... 129

**11 ANNEX B. THE MPI COMMANDS ... 131**

11.1 The Message Passing Interface (MPI) ... 131
11.1.1 MPI initialization and finalization ... 131
11.1.2 Communication establishment ... 132
11.1.3 Main MPI commands applied. ... 136

**12 ANNEX C. THE NHESDYN COMMUNICATION. ... 139**

**13 ANNEX D. MODIFIED ROUTINES IN EACH CODE ... 141**

13.1 NHESDYN ... 141
13.2 NEPTUNE_CFD ... 141

13.3 SYRTHES ..... 141
13.4 DYN3D_SP3 ..... 142
13.5 DYNSUB ..... 142
13.6 SUBCHANFLOW ..... 142

**14 ANNEX E. THE NHESDYN VALIDATION. ..... 143**

14.1 $K_{EFF}$ DEVIATION DURING A TRANSIENT ..... 143
14.2 DYN3D_SP3/SYRTHES POWER TRANSFER ERROR ..... 144
14.3 GAP MODELING APPROACH IN DYNSUB ..... 144

## List of figures

Fig. 2-1. SCF space discretization for a 9 pin rod bundle. 20

Fig. 2-2. SYRTHES tetra element. Main nodes (red) and middle nodes (blue) 26

Fig. 2-3. SYRTHES mesh (a) and NEPTUNE_CFD structured mesh (b) 26

Fig. 4-1. (a) Experimental set up of the PSBT benchmark with a cross sectional cut (b) illustrating where is the heat source. (c) Numerical model in NEPTUNE_CFD, calculated velocity field for case 1.2211. 44

Fig. 4-2. Cross section of the four proposed space discretization for the domain (M1, M2, M3 and M4) 45

Fig. 4-3. Axial VF profile in the near heated wall region for case 1.6222. 46

Fig. 4-4. Axial water temperature profile in the near heated wall region and in the subchannel center for Case 1.6222. 46

Fig. 4-5. Water velocity in the near wall region at 1.4 m elevation. Four different meshes comparison, for 0.1 mm bubble diameter. 47

Fig. 4-6. Steam velocity in the near wall region at 1.4 m elevation. Four different meshes comparison, for 0.1 mm of bubble diameter. 47

Fig. 4-7. Water temperature in the near wall region at 1.4 m elevation. Four different meshes comparison, for 0.1 mm bubble diameter. 48

Fig. 4-8. Local VF at 1.4 m elevation. Four different meshes comparison, for 0.1 mm of bubble diameter. 48

Fig. 4-9. Water temperature at the near wall region and at the center of the subchannel of the case 1.2211. Comparison between 4 different meshes. 49

Fig. 4-10. Local VF distribution predicted by NEPTUNE_CFD at the measurement location (Z=1.4 m) for the four purposed meshes. Results for case 1.2211 49

Fig. 4-11. Water temperature in the near heated wall region at 1.4 m elevation. Comparison for different bubble diameters. Case 1.2211. 51

Fig. 4-12. Bubble size distribution in case of using the IAE. Case 1.2211. 51

Fig. 4-13. VF in the near heated wall region at 1.4 m elevation. Comparison for different bubble diameters. Case 1.2211. 51

Fig. 4-14. Steam velocity in the near heated wall region at 1.4 m elevation. Comparison for different bubbles diameters. Case 1.2211 51

Fig. 4-15. Axial VF profile at the center of the subchannel. Comparison for 3 different bubbles diameters. Case 1.2211. 52

Fig. 4-16. Pressure drop calculated for the 3 different bubble diameters. Case 1.2211 52

Fig. 4-17. Axial VF evolution for each case compared against experimental data. 53

Fig. 4-18. Deviation of the NEPTUNE_CFD simulations from experimental VF data. 54

Fig. 4-19. (a) Test bench with the location of the X-ray densitometers and the heated section. (b) Cross section of the tested rod bundle and the selected portion to be modeled. (c) Numerical model of the simulated domain. (d) Local water velocities of the domain calculated by NEPTUNE_CFD and location of the symmetry planes of the model. ........ 57

Fig. 4-20. Test bench outlet pressure measured evolution for turbine trip and recirculation pump trip experiment. ........ 58

Fig. 4-21. Test bench mass flow rate measured evolution for turbine trip and recirculation pump trip experiment. ........ 58

Fig. 4-22. Test bench measured power evolution for turbine trip and recirculation pump trip experiment. ........ 58

Fig. 4-23. Normalized radial FA power coefficients for turbine trip and recirculation pump trip experiment in the context of the BFBT experiment. ........ 58

Fig. 4-24. (a) NEPTUNE_CFD model. (b) NEPTUNE_CFD+SYRTHES model, green ring represent the insulator and the clad according to the real benchmark geometries. .. 60

Fig. 4-25. (a) Location of the measured axial levels. Local VF distribution calculated by NEPTUNE_CFD at different times for the turbine trip without bypass simulation: (b) second 7, (c) second 11.5, (d) second 20, (e) second 30, (f) second 50. ........ 62

Fig. 4-26. Comparison of the BFBT VF data and its measurement error (±2%) with the VF evolution predicted by NEPTUNE/SYRTHES at three axial levels during the turbine trip experiment. ........ 62

Fig. 4-27. Normalized values of power, mass flow and pressure evolution provided by the turbine trip experimental data together with relative error between VF predicted by NEPTUNE_CFD/SYRTHES and experimental VF data at axial level Z=0.67m. ........ 63

Fig. 4-28. Saturation, steam, clad and liquid temperature calculated by NEPTUNE_CFD/SYRTHES. Comparison against the Steam temperature calculated with NEPTUNE_CFD stand alone. ........ 64

Fig. 4-29. Comparison of the BFBT VF data and its measurement error (±2%) with the VF predicted by NEPTUNE/SYRTHES at three axial levels during the recirculation pump trip experiment. ........ 65

Fig. 4-30. Local water temperature at 3 different axial levels, (a) 0.67m, (c) 1.72 m and (c) 2.7m. Calculated by NEPTUNE_CFD/SYRTHES for the recirculation pump trip (second 30). ........ 66

Fig. 4-31. Local void distribution at 3 different axial levels, (a) 0.67m, (c) 1.72 m and (c) 2.7m. Calculated by NEPTUNE_CFD/SYRTHES for the recirculation pump trip (second 30). ........ 66

Fig. 4-32. Local steam temperatures evolution at the bulk and near the heated wall calculated by NEPTUNE_CFD/SYRTHES during the recirculation pump trip. Comparison of two different time scales returning to saturation for the steam. ........ 67

Fig. 5-1. Simplified communication scheme for the coupled solution NEPTUNE_CFD/ SYRTHES/DYN3D_SP3. 70

Fig. 5-2. General distribution of the three MPI groups and the codes included within them. 71

Fig. 5-3. Simplified flow chart for the coupled solution NEPTUNE_CFD/SYRTHES/DYN3D_SP3. 73

Fig. 5-4. Coupled solution execution. Main steps. 74

Fig. 5-5. Time advancement description for the codes. 75

Fig. 5-6. Simulations time comparison during the coupled steady state for SYRTHES using a large time step (10E4) and SYRTHES using the same time step as the other codes. 76

Fig. 5-7: Mapping example for a single pin. (a) NEPTUNE_CFD/SYRTHES model. (b) Averaged values at each axial level of TH parameters. (c) Polynomial approximation of TH parameters. (d) DYN3D_SP3 model. (e)Computed power values. (f) Polynomial approximation of the axial power. 79

Fig. 5-8. Nodalization radial distribution for one pin in NEPTUNE_CFD. 80

Fig. 5-9. Radial nodalization of one pin for SYRTHES. 81

Fig. 5-10. Power transformation through the interface between DYN3D and SYRTHES. 83

Fig. 5-11. (a) Fuel, gap and clad pin discretization by SYRTHES. (b) detail of the fuel discretization 83

Fig. 6-1. a) Plant view of a 17X17 PWR FA. b) Plant view of a single pin with the geometric characteristics. c) 3D view of the numerical domain simulated with the TH tools of NHESDYN. Location of the 3 heights were the measurements take place. 87

Fig. 6-2. a) NHESDYN TH model of one pin. b) NK model of one pin. c) DYNSUB TH model of one pin. 88

Fig. 6-3. 1 pin structure and fluid domain nodalizations. (a) and (b) correspond to a coarse mesh, (b) and (d) to a refined mesh. 88

Fig. 6-4. Comparison of the axial fuel center line (CL) temperature distribution calculated by DYNSUB and by NHESDYN using three different resolutions (R1, R2 and R3). 89

Fig. 6-5. Comparison of the axial fuel outer surface (OS) temperature distribution calculated by DYNSUB and by NHESDYN using three different resolutions (R1, R2 and R3). 90

Fig. 6-6. Comparison of the axial Doppler temperature distribution calculated by DYNSUB and by NHESDYN using three different resolutions (R1, R2 and R3). 90

Fig. 6-7. Comparison of the axial evolution of the fuel-cladding temperatures differences for DYNSUB and different NHESDYN resolutions (R1, R2 and R3). 91

Fig. 6-8. Comparison of the axial evolution of the cladding temperatures for DYNSUB and different NHESDYN resolutions (R1, R2 and R3). .................................................... 91

Fig. 6-9. Comparison of the axial moderator temperature evolution predicted by DYNSUB and by NHESDYN using three resolutions (R1, R2 and R3).......................... 92

Fig. 6-10. Comparison of the axial moderator density evolution predicted by DYNSUB and by NHESDYN using three resolutions (R1, R2 and R3). ........................................... 92

Fig. 6-11. Radial temperature distribution in the fuel, gap and clad in a fuel pin cross section at 1.8 m elevation. Comparison of DYNSUB and different NHESDYN resolutions (R1, R2 and R3)........................................................................................ 93

Fig. 6-12. Comparison of the calculated temperature distribution in °C in a cross section of a fuel pin at 1.8 m elevation (Z direction) for different NHESDYN resolutions (R1, R2 and R3). ......................................................................................................... 93

Fig. 6-13. Comparison of $k_{eff}$ during the iteration of the steady state calculation predicted by both DYNSUB and by NHESDYN with three different resolutions (R1, R2 and R3). ......................................................................................................... 94

Fig. 6-14. Water temperature evolution imposed at the inlet purposed for the transient case analysis.................................................................................................................. 95

Fig. 6-15. Comparison of the pin averaged Doppler temperature computed with DYNSUB and with NHESDYN using three different resolutions (R1, R2 and R3)....... 96

Fig. 6-16. Comparison of the volume averaged moderator temperature predicted by DYNSUB and by NHESDYN using three different resolutions (R1, R2 and R3). ......... 96

Fig. 6-17. Comparison of the local evolution Doppler temperature at axial location 2 (Z=2 m) predicted by NHESDYN R1 and DYNSUB.. ..................................................... 97

Fig. 6-18. Comparison of the local evolution Doppler temperature at axial locations 1 (Z=0.07 m) and 3 (Z=3.63 m) predicted by NHESDYN R1, R2 and R3 and by DYNSUB. ........................................................................................................................ 97

Fig. 6-19. Comparison of the local moderator density evolution for three heights in the Z direction (0.07, 2 and 3.63 m) calculated by DYNSUB and NHESDYN with three resolutions (R1, R2 and R3)........................................................................................ 98

Fig. 6-20. Time evolution of the power flux produced in the fuel and total flux at the interface solid-liquid for NHESDYN R1............................................................................ 100

Fig. 6-21. Comparison of the reactivity evolution predicted by DYNSUB and NHESDYN using the three different resolutions (R1, R2 and R3)................................. 100

Fig. 6-22. Comparison of the total power evolution predicted by DYNSUB and NHESDYN using different resolutions (R1, R2 and R3).................................................. 100

Fig. 6-23. Anticipated Mass flow rate evolution purposed for the transient case analysis. ......................................................................................................................... 101

Fig. 6-24. Calculated power evolution. Comparison for DYNSUB and different NHESDYN resolutions (R1, R2 and R3). ........ 102

Fig. 6-25. Time evolution of the heat flux produced in the fuel and total flux at the interface solid-liquid for NHESDYN R1........ 102

Fig. 6-26. Time evolution of the system reactivity. Comparison for DYNSUB and different resolutions of NHESDYN (R1, R2 and R3). ........ 102

Fig. 6-27. Mass flow rate evolution purposed for the transient case analysis. ........ 103

Fig. 6-28. Comparison of the moderator temperature evolution for two heights in the Z direction (2 and 3.63 m) predicted by DYNSUB and NHESDYN with two different resolutions (R1, R2). ........ 104

Fig. 6-29. Comparison of the local Doppler temperature evolution during the transient at the axial eight 2 (2m) predicted by DYNSUB and NHESDYN using two different resolutions (R1 and R2)........ 104

Fig. 6-30. Comparison of the power evolution calculated by DYNSUB and NHESDYN using two resolutions (R1 and R2). ........ 105

Fig. 6-31. Outlet pressure imposed by NHESDYN during the transient. ........ 106

Fig. 6-32. Local VF predicted by two NHESDYN resolutions (R1 and R2) at the outlet during the transient. ........ 107

Fig. 6-33. Comparison of the local moderator density evolution for two axial heights in the Z direction (2 and 3.63 m) predicted by DYNSUB and NHESDYN using two resolutions (R1 and R2)........ 107

Fig. 6-34. Comparison of the power evolution for the depressurization transient scenario calculated with DYNSUB and NHESDYN using two resolutions (R1 and R2). ........ 108

Fig. 6-35. Comparison of the total averaged Doppler temperature evolution predicted by DYNSUB and NHESDYN using two resolutions (R1 and R2). ........ 108

Fig. 6-36. Comparison of the total averaged moderator temperature evolution predicted by DYNSUB and NHESDYN using two different resolutions (R1 and R2)........ 108

Fig. 8-1. NEPTUNE_CFD/SYRTHES model for a pin cluster model 3x3 pins ........ 114

Fig. 10-1. Comparison of the BFBT computed VF evolution by NEPTUNE_CFD with the experimental VF data and its measurement error (±2%) at three axial levels during the turbine trip experiment. ........ 129

Fig. 11-1. MPI instructions applied in the coupled solution in order of execution for the different codes. ........ 138

Fig. 12-1. Detailed flow chart for the codes involved in the coupling scheme. ........ 140

Fig. 14-1. Water temperature evolution imposed at the inlet purposed for the transient case analysis. ........ 143

Fig. 14-2. Deviation of the $K_{eff}$ during the temperature step transient. comparison for different NHESDYN resolutions (R1, R2 and R3). ........ 143

Fig. 14-3. Power transfer error from DYN3D to SYRTHES during the temperature step transient. Comparison for different resolutions of NHESDYN: (R1, R2 and R3). ....... 144

Fig. 14-4. Axial distribution for: center line, outer fuel, and Doppler temperatures. Comparison for DYNSUB working with two HTC ($10^4$ and 11710 $W/m^2K$) and two NHESDYN resolutions (R1 and R2). .................................................................................... 145

Fig. 14-5. Total averaged Doppler temperatures: Comparison for DYNSUB working with two gap HTC ($10^4$ and 11710 $W/m^2K$) and two NHESDYN resolutions (R1 and R2). ........................................................................................................................ 146

Fig. 14-6. Total averaged moderator temperatures: Comparison for DYNSUB working with two gap HTC ($10^4$ and 11710 $W/m^2K$) and two NHESDYN resolutions (R1 and R2). ........................................................................................................................ 146

# List of Tables

Tab. 4-1. Test conditions for steady state void measurements test series 1 ........................ 44

Tab. 4-2. Discretization details of the four meshes applied in the study of the PSBT benchmark........................................................................................................................ 46

Tab. 4-3. Results for the local and averaged VF for the different meshes applied for the simulation of case 1.2211. ......................................................................................... 50

Tab. 4-4. Computed of the VF measured and calculated by NEPTUNE_CFD .............. 53

Tab. 4-5. Performed simulations for the BFBT benchmark ............................................... 60

Tab. 4-6. Performed simulation for the pump trip experiment .......................................... 65

Tab. 6-1. Nominal conditions for the simulations according to the OECD/NEA and US NRC PWR MOX/UO2 core transient benchmark adapted for a single pin geometry... 86

Tab. 6-2. Rod geometry considered for the validation based on the the OECD/NEA and US NRC PWR MOX/UO2 core transient benchmark. ....................................................... 87

Tab. 6-3. Specifications of the test matrix for the sensitivity study of the influence of a mesh refinement on the prediction of fuel and cladding temperatures. ............................. 89

Tab. 6-4. Transient simulations performed and the mesh refinement applied in each case. ........................................................................................................................................ 94

Tab. 10-1. Performed simulations for the BFBT benchmark ........................................... 129

# List of Acronyms

| | |
|---|---|
| **ASU** | Arizona State University |
| **BE** | Best Estimate |
| **BFBT** | NUPEC BWR Full-size Fine-mesh Bundle Test |
| **BWR** | Boiling Water Reactor |
| **CEA** | Commissariat al'Energie Aatomique |
| **CFD** | Computational Fluid Dynamics |
| **CFL** | Courant-Friederich-Lewi number |
| **CHF** | Critical Heat Flux |
| **DBA** | Design Basis Accidents |
| **DBC** | Design Base Conditions |
| **DNB** | Departure from Nucleate Boiling |
| **DNS** | Direct Numerical Simulation |
| **DYN3D** | DYNamical 3 Dimension code for thermal reactor cores |
| **ECC** | Emergency Core Cooling |
| **EDF** | Electricite de France |
| **EVM** | Eddy Viscosity Model |
| **FA** | Fuel Assembly |
| **FDB** | Fully developed boiling |
| **HTC** | Heat Transfer Coefficient |
| **HZDR** | Helmholtz Zentrum Dresden Rossendorf |
| **IAC** | Interfacial Area Concentration |
| **IAE** | Interfacial Area Equation |
| **INR** | Institute for Neutron physics and Reactor technology |
| **IRSN** | Institute de Radioprotection et de Surete Nucleaire |
| **KAERI** | Korean Atomic Energy Institute |
| **KIT** | Karlsruhe Institute of Technology |
| **KTG** | Jahrestagung Kerntechnik |
| **LES** | Large Eddy Simulations |
| **LOCA** | Loss of Coolant Accident |
| **LWL** | Large Water loop |
| **LWR** | Light Water Reactor |
| **MSLB** | Main Steam Line Break |
| **MPI** | Message Passing Interface |
| **MUSIG** | Multi Size Groups |
| **NHESDYN** | NEPTUNE_CFD/SYRTHES/DYN3D_SP3 |
| **NK** | Neutron Kinetic |
| **NPP** | Nuclear Power Plant |
| **NUPEC** | Nuclear Power Engineering Corporation |
| **NURESIM** | Nuclear Reactor Simulation |
| **NURISP** | Nuclear Reactor Simulation Integrated Project |
| **PSBT** | OECD/NRC PWR Subchannel and Bundle Tests |
| **PTS** | Pressurized Thermal Shock |

| | |
|---|---|
| **PVM** | Parallel Virtual Machine |
| **PWR** | Pressurized Water Reactor |
| **RANS** | Reynols Averaged Navier-Stokes |
| **SMD** | Sauter Mean Diameter |
| **RSTM** | Reynolds Stress Turbulence Model |
| **SCF** | SUBCHANFLOW |
| **TH** | Thermal Hydraulic |
| **VF** | Void Fraction |
| **VLES** | Very Large Eddy Simulations |
| **VOF** | Volume Of Fluid |

# 1 Introduction

## 1.1 Motivation

The design optimisation and the safety assessment of fuel rods, fuel assemblies (FA) and nuclear reactor cores requires the use of numerical simulation tools that are able to describe accurately the fundamental thermal hydraulic (TH), neutronic and mechanical behaviour under normal, off normal and accidental conditions. Recent advances in computer and engineering sciences have led to a gradual improvement in the modeling and simulation of key safety-relevant phenomena taking place in the reactor cores, leading to an enhanced performance and operational flexibility of modern nuclear reactor systems. Currently both conservative and best-estimate (BE) safety analysis methodologies are being applied with increasing importance of the BE computer codes, which are requested by the regulatory organs for licensing the nuclear power plants (NPP).

Due to the increasing complexity of FA and material compositions, there is a general trend to move to multi-scale based simulations of TH and neutron kinetic (NK) physical phenomena, trying to obtain high fidelity simulations. This new trend permits a better assessment of the safety margins and contributes to reduce the conservatism in the applied methodologies for the analysis of FA's and core design.

The use of numerical simulation codes for the evaluation of safety aspects of reactor cores requires a previous validation based on appropriate experimental data performed for representative range of parameters e.g. for BWR or PWR and geometrical configurations.

These investigations are focused on the validation of the prediction capability of a computational fluid dynamic (CFD) code regarding boiling water reactor (BWR) and pressurized water reactor (PWR)-relevant two-phase flow processes and the extension of its simulation capabilities for light water reactors (LWR) by incorporating into it a (NK) solver. The validation of NEPTUNE_CFD (1) has a vital importance since the two-phase flow models of CFD codes are still in a development state.

The availability of high performance computers allow an increase of the spatial resolution of the TH and neutron physical phenomena at very detailed scales paving the way for the possibility to directly predict local safety parameters by developing sophisticated coupling schemes working in serial or parallel environments.

## 1.2 Objective

The main objective in this context is to develop a novel coupling methodology involving TH and NK tools for high fidelity LWR applications. Once the methodology is ready the goal is to ensure its correct operation in a parallel environment and to evaluate the capabilities of the coupled solution. The NK code selected is the transport $SP_3$ approximation DYN3D_SP3 (2), which is being developed by the *Helmholtz Zentrum Dresden Rossendorf* (HZDR). The TH codes are: the NEPTUNE_CFD code developed by *Electricite de France* (EDF) and *commissariat a l'energie atomique* (CEA), and the heat conduction solver SYRTHES developed by EDF. To reach this goal, some previous steps are needed.

Due to the fact that the two-phase flow models of the CFD codes in general are not yet mature an assessment of the NEPTUNE_CFD prediction capabilities of the nominal operational condition of LWR is mandatory. In this context, the validation of the mentioned CFD code will be focused on the following areas:

- Review of the state of the art concerning the NEPTUNE_CFD validation.
- Identification of suitable experiments.
- Perform post-test analysis of the selected experiments or benchmarks to assess both the capabilities and limitations of NEPTUNE_CDF and the heat conduction solver SYRTHES (3).

## 1.3 Organization of the thesis

The first chapter is devoted to introductory remarks including the motivation and the working methodology as well as the state of the art regarding coupled codes and status of the validation of the NEPTUNE_CFD code. In addition, the programs which are used during the studies are introduced (Chapter 2). In Chapter 3, a detailed description of the CFD code is provided.

Chapter 4 presents the validation activities of the TH codes, the selection of data base and the performed simulations followed by a conclusion and lessons learned.

Chapter 5 describes the developed coupling methodology. The time synchronization and advancement as well as the axial and radial mapping schemes for the information exchange between the involved domains via message passing interface (MPI) are explained.

Chapter 6 describes the validation of the coupled solution. This work is performed by comparing the behavior of the new coupled code NEPTUNE_CFD/ SYRTHES/DYN3D_SP3 (NHESDYN) against the DYNSUB code in a code-to-code comparison for selected LWR transient cases. The validation is followed by the conclusion.

Chapter 7 summarizes the work described in the thesis and outlines the achievements and contributions of the author. Furthermore, in Chapter 8, an outlook of the tool applicability together with the necessities for further improvements is given.

## 1.4 Working methodology

This section will provide the methodology used to accomplish the goals mentioned in the above sections. The approach of the process is mainly applied for the validation of the CFD code. At first, the test section of interest will be modeled within the NEPTUNE_CFD code by performing a space discretization. According to the best practice guidelines of the use of CFD in nuclear reactor safety applications (4) more than one nodalization is designed to perform mesh sensitivity analyses. The main phenomena affecting the flow are identified and the models are selected based on these criteria. After an optimized model for a specific problem is available the necessary boundary conditions are defined to perform a simulation. The quality of the simulation will be evaluated by comparing the predicted parameters against the experimental data. Base on this, the most suitable nodalization and model parameters for the analyzed problem are selected. Furthermore, the major weaknesses of the relevant CFD models are identified. This working scheme has been applied to all validation problems studied during this thesis.

The development of the coupling scheme as well as its verification and validation follows another approach. First of all, the information flow between the involved codes must be checked to make sure that the right feedback parameters are being transferred from one domain to the other. It requires constant debugging of the code routines at every time step extending the verification process considerably in time. This includes the checking of how the mesh sensitivity and the mapping scheme of the different domains are affecting the feedback parameters. Secondly, the prediction accuracy of the coupled system (NHESDYN) has to be evaluated by code-to-code validation against DYNSUB.

## 1.5 State of the art of numerical simulation tools

The application of numerical simulation tools in the nuclear power industry is a wide extended technique for both design optimization and safety assessment. The capabilities of the codes allow the user to estimate the consequences that can take place either during operational transients affecting the power plant behavior, design basis accidents (DBA) or even beyond design basis accidents (BDBA). The understanding of the physical phenomena taking place in a NPP under such conditions permits the elaboration of procedures and counter-measures to prevent the development of abnormal occurrences to accidents or BDBA with the goal to bring the plant back to safe conditions.

The design of the NPP of generation II were made following a conservative approach and by this way assuring sufficient safety margins. In the meantime the safety analysis codes have experienced a continuous improvement of the physical and mathematical models to reflect the state of the art in nuclear engineering. The result of this improvement are the BE safety analysis codes characterized by a more realistic description of the physical processes taking place in the core, the primary and secondary systems, etc.

The BE TH system codes can reproduce whole power plants and the interaction between their systems and subsystems. Hence, they are capable of analyzing what is important when a perturbation occurs and propagates through the whole facility. An important aspect for the acceptance of numerical simulation tools in a licensing process (e.g. safety assessment of NPP) is the degree of validation. A code has to be validated to be recognized as a reliable tool for licensing purposes. For this reason, different kinds of experiments (separate effect test, bundle test, integral tests, etc.) were performed in the frame of international cooperation with the leadership of the International Atomic Energy Agency (IAEA), the Nuclear Energy Agency (NEA) within the Organization for Economic Co-operation and Development (OECD/NEA) and the US Nuclear Regulatory Commission (NRC) to provide an extensive data base for code validation purposes. Based on the experimental findings related to e.g. heat transfer mechanisms that are relevant for LWR correlations and models were derived and implemented in the numerical simulation tools such as subchannel codes and system codes. By this way the simulation capability and accuracy of safety analysis codes are continuously improved whenever a new phenomenon was understood by means of experimental investigations.

The increasing complexity of the core internal designs of modern LWR (lower grid plate, spacer grids, FA feet and head, etc.) reveals the necessity to increase the spatial resolution of the TH simulation tools. This permits the description of the physical phenomena in different spatial scales e.g. macro-, meso- and micro-scale, where they are taking place. An example of the accuracy level required is the study of the turbulent enhancement by the inclusions of different kind of spacer grids. Nowadays this can only be simulated by the detailed space discretization provided by the CFD codes.

There are different spatial scales and each one is specialized in solving one kind of problem, depending on the level of detail required, from describing the bubble diameter (some mm) to describe the whole core and the hot legs (several meters). At the component scale whole plant analyses can be performed but for more accurate predictions a channel code can be applied for the FA description. Instead of dealing with averaged assemblies, as usually done by the system codes, the information can be obtained for single pins or cooling channels by making a local zoom.

The multi-scale approach aims to couple codes describing the physics at different scales assuring the accurate transfer of information from one scale to the other. There are many advantages to explore by this approach e.g. the most realistic description of the phenomena within a reactor core or within a FA. TH codes used in nuclear engineering can be classified in system codes, subchannel codes and CFD codes. A short description of these codes will be given in the next subchapters.

### 1.5.1 Thermal hydraulic system codes.

System codes have been widely validated and its application in the industry is quite extended. These codes are able to model entire NPP systems, their working range is the macro scale: steam generators, primary and secondary loop, pumps, etc. They solve the mass, momentum and energy equation mainly for one or two dimensional cells. Those units are interconnected by means of junctions to build entire systems. Actual system codes can deal with single phase flow and two-phase flow transients. Some improvements are needed concerning pressure prediction, where some of them often struggle. Especially when the pressure wave propagation need to be described properly or at some transients where the 3D flow has an important interaction with the system like recirculation phenomenon. They are used to represent whole plants or NPP components but also experimental facilities. Prominent system codes are: RELAP5 (5), CATHARE (6), ATHLET (7), MARS (8) and TRACE (9). They can also model the interaction between systems, like the primary and secondary circuit which has a strong influence on the system response. This is an important capability for the analysis of the plant/system behavior during transients and scenarios belonging to design based conditions (DBC).

The closure relations in the current TH system codes needed to solve the field equations are based on empirical models derived from experiments. Due to the complexity of certain experimental investigations the derived correlations are valid only for a narrow range of parameters. Examples are the flow regime maps in the system codes. For each flow regime (depending on void fraction (VF) and mass flux) a set of correlations are needed.

In system codes the size of the control volume is rather big, ranging from a single centimeter to meters. Hence some small scale physical phenomena like the turbulence or certain boiling effects cannot be taken into account because of the averaging of the system parameters. To describe these phenomena models based on first principles are required. Instead of empirical correlations the trend is to describe the phenomena by mechanistic models.

These codes provide conservative conditions for safety analyses, however, according to (10), they do not deliver data of sufficient resolution, accuracy and scale to better understand the causes of failure in the systems. They play a fundamental role in the operation of the reactor; nevertheless the codes are basically one dimensional and strongly based on experimental correlation than on first principles. They therefore have limited applicability in predicting any deviation from optimal design conditions. They are very accurate only when they are operating in their regime, but it is not possible extrapolate outside of that range. According to (11) in cases where a strong thermal non-equilibrium occurs (e.g. subcooled liquid and superheated steam) the homogenous flow model employed by these codes is inadequate to represent the complicated flow fields developed during some transients, such as a loss of coolant accident (LOCA).

One of the common studied phenomena is the single-phase mixing processes taking place in large volumes of the primary reactor system as a consequence of non-symmetrical injection of fluid at different temperatures. The available system codes cannot model the mixing processes because they don't employ the full 3D fluid equations. This process related with some transients scenarios with injection of cold water, e.g. main steam line break (MSLB), where the temperature distribution in the downcomer, the lower plenum and the core entry is of relevance for structural integrity assessment and proper determination of the reactivity feedback in the core. Another relevant case with single-phase mixing is the boron dilution transient. In this case the amount of mixing is crucial for determining the positive reactivity insertion in the core. Therefore, more sophisticated 3D TH codes have to be employed to predict such distributions.

### 1.5.2 Thermal hydraulic subchannel codes.

With a more refined discretization than the system codes these tools can provide a better modeling of the TH for safety analyses. The distribution of the pressure drop and VF inside a reactor FA depends on local TH conditions, such as mass fluxes in the fuel channels, pressure gradients between flow channels or the arrangement of the rods. The heat removal, the predictions of the pressure drop and the VF are more accurate on this scale.

The reduction of the scale enables the introduction of the cross flow which allow accounting for the exchange of mass in the transversal direction across the interface that separates the subchannels in the FA. The cross flow term in two-phase flow conditions (for BWR of PWR´s transients) is modeled with three different components by (12):

- Diversion cross flow: induced by transversal pressure gradients.
- Void drift: due to the migration of bubble to locations with higher flow velocities.
- Turbulent mixing flow: mixing of the flow caused by the turbulence.

By applying these codes is possible to simulate a single FA or even the whole core regarding its flexibility. They offer the possibility to model the flow as a mixture (liquid/gas) with one set of equations or a multi-phase group where the equations are solved separately for each phase. One approximation to this scale is to deal with 2D problems assuming the predominant axial flow and a transversal direction for the second direction. The component scale, where the FA or core arrangements belong, is suitable to be modeled with this subchannel codes. They are used mainly for safety related design studies, the most well-known subchannel codes are: COBRA-TF (13), MATRA (14), FLICA (15) and SUBCHANFLOW (SCF) (16).

### 1.5.3 Computational Fluid Dynamics codes

To improve the actual knowledge about the fundamental behavior of specific fuel designs and therefore increase the capability of developing new and better solutions, many research institutes have been investigating the feasibility of high fidelity approaches. The CFD codes are tightly involved in this new trend because they can reproduce the flow phenomenology on a detailed scale. It was previously mentioned in point 1.5.1 that the thermal non-equilibrium condition requires the introduction of two enthalpies for each phase. In its complete implementation, 6 equations need to be solved in the so-called two-fluid model: one mass balance, one momentum balance and one enthalpy (energy) balance for each phase. This model supplemented with the required closure laws allows for covering almost the full range of transient states expected during scenarios relevant to LWR reactors.

Trying to obtain an accurate solution to the main governing equations of the fluid is a challenging issue in the engineering field. The conservation equation for mass, momentum and energy are based on partial derivatives and they are not linear. Hence some closure laws, which themselves contain several assumptions, are necessary to complete the system. Some techniques can provide valuable information for the volume averaged values, as the turbulence. The CFD tools are based on the application of the Navier-Stokes equation to predict the behavior of the flow. These codes suggest an approximation of the partial derivatives by algebraic expressions then the system can be solved numerically.

A set of boundary conditions and restrictions to the flow in addition to a fine spatial discretization are applied allowing the CFD codes in principle to reproduce any kind of domain. The numerical schemes applied are experiencing constant improvements. With the computers becoming more powerful respective computer programs like the CFD codes have been developed with increasingly more powerful features. Furthermore, the massive parallelization of the codes provides an exponential growth of the CFD applicability.

This methodology is widely used in the aerodynamics industry to analyze the flow aiming the improvement in the design of planes and cars. Despite that CFD is widely present in some branches of the industry the utilization of these codes remains a little bit restrictive for the nuclear industry. This is mainly due to the high complexity of the flow, where the two-phase flow with boiling is the dominant phenomenon conditioning the design of the LWR. The development of reliable models especially for two-phase flow are under style and even providing reasonable good results they need more studies before being fully accepted for industrial applications, partially due to the fact that by choosing the computational mesh and the turbulence models, the user can have a strong effect on the computational results.

Nuclear engineering has a big interest in CFD analysis. Single phase flow applications have already been established in the nuclear context (4). Therefore, the applicability is growing rapidly. An example of this is the capability of the CFD codes to predict the mixing flow. It is well known that mixing cannot be treated properly with the system codes described previously.

The most extended technique for CFD is the Reynolds averaged Navier-Stokes simulations (RANS). Here all the turbulent scales are modeled, and the discretization needs a set of closure laws in order to complete the number on necessary equations and solve a linear system. The number of approaches needed to complete the required number of equation decrease if the technique applied is a large eddy simulation (LES) (17), or a very large eddy simulations (VLES), where a filtered version of the Navier-Stokes equations along with another equation to represent the turbulent small scales are applied. These methodologies need more refine meshes.

The next step towards a more detailed description of the flow is the direct numerical simulation (DNS). It is a numerical methodology where the Navier-Stokes equations are solved with no model for the turbulence. At these scales the Reynolds number of the eddies is small enough that viscous effects become dominant and the energy is dissipated. An example of DNS application is the study of the bubble departure as a function of the gravity for departure from nucleate boiling (DNB) studies (18). At this scale it is mandatory to impose extremely refined spatial discretization at the Kolgomorov scale, see (19) and (20). For that reason this scale is restrictive to small domains and very simple cases, as discussed in (21). This technique aims to provide detailed information about phenomena not accessible by experiments. DNS or LES or any fine scale simulation may be very beneficial for investigating micro-scale flow processes which are not well known. In the context of the nuclear reactor simulation (NURESIM) project, several LES simulations (22) have been performed to study the development of air-water bubbly flow as well as boiling flow. However, according to (23), the LES technique has a limited applicability and many numerical issues remained open.

The CFD codes can solve the micro- and meso-scale problems and prominent code representatives are: ANSYS_CFX (24), STAR_CD (25), OPEN_FOAM (26), FLUENT (27), TRIO_U (28) and NEPTUNE_CFD. For safety related design studies they are nowadays widely applied. At the moment they are used for supporting analysis of local or small scale effects due to the missing link to connected systems like the secondary or auxiliary systems. Nevertheless those codes have an enormous potential. The main limitation arises from the computational time required. The results of CFD investigations (e.g. mixing behavior in a plenum or inside the core) can be used as additional input data for system code analysis. For TH system analyses, the 3D CFD approaches can be used in the frame of BE system codes.

#### 1.5.3.1 NEPTUNE_CFD state of the art concerning two phase flow simulations

The main tool applied to predict the flow behaviour in this work is the CFD code NEPTUNE. It is developed by EDF and CEA and since it is not a commercial tool it has a restricted access. Regarding its promotion in the NURISP project the code is accessible to the group members of the SP2 TH and user group. This code is devoted to nuclear applications focusing on two-phase flow modelling for LWR. It includes the BE and most advanced models available with some innovations. It can be considered an experimental platform for new advances in the flow modelling. For LWR applications the code is nowadays in a continuous validation process where the biggest contribution comes from the SP2 TH group of the NURISP. The main area to explore in the validation is the application of two-phase flow models with heat and mass transfer. The main models implemented are explained in chapter 3. The work performed in the code concerning its applications and validation is shown next.

In this chapter a review of the most suitable experiments database used as a comparison reference for this code is presented together with the actual state of the art of NEPTUNE_CFD validation focused mainly on two phase flow modeling. Special attention has to be paid to the kind of conditions the coupled solution works with: flow within rod bundles. To test the generality of the two-fluid boiling model, the review first focuses on the channel boiling flow experiments. In this case the Arizona State University (ASU), DEBORA and the Korean Atomic Energy Institute (KAERI) experiments offer a good match in the geometrical aspect. Those experiments differ in working fluid and operating conditions. In ASU experimental facility the refrigerant R-113 is used, the DEBORA facility uses R-12 while water at low pressure (up to 2 bar) is used in the KAERI test section. Density ratios and other scaling numbers are therefore different. The effect of swirls (caused by mixing vanes) on the boiling activity and the code prediction to this perturbation was tested in the frame of the DEBORA mixing experiment. The boiling experiments at ASU and KAERI were both performed in annular vertical channels, the DEBORA experiments were carried out in a pipe test section of CEA Grenoble. Furthermore, a review of the work done with this code in the prediction of the DNB is exposed together with other simulation involving boiling modeling in rod bundles.

Simple simulations with the NEPTUNE_CFD code were compared with the code FLUENT. The studies were performed in a simplified subchannel for adiabatic conditions according to (29). Here the disperse phase velocity prediction is compared between codes. Here, the description of boiling phenomena focuses more on the boiling model validation, like the experiments discussed below.

The ASU experiment is described in (30) and (31). In this experiment measurements over a two-phase boiling flow were performed. The test section consists of a vertical annular channel with a heated inner wall and an almost thermally insulated outer wall. The rod diameter is 38.1mm and it is resistively heated. For a sufficiently high inner wall heating heterogeneous nucleation appears on the wall surface. As the inlet R-113 is subcooled, the bubbles condense into the colder liquid when they are far from the inner wall layer. This is a known phenomenon widely tested in CFD codes (32). According to (31) two layers are observed: a boiling bubbly layer adjacent to the heated wall and an outer liquid region. A dual-sensor optical fiber probe and a micro-thermocouple were installed in the measurement section. The variables measured characterize the dispersed phase: (VF, bubble axial velocity and bubble chord length). The bubble chord length distribution allows the computation of the bubble diameter distribution, and from this the local interfacial area concentration (IAC) by means of some assumptions. The results of the simulation performed with NEPTUNE_CFD are exposed by (33), where the capabilities of the Reynolds stress turbulence model (RSTM), implemented in the code demonstrated. There are some discrepancies on the liquid mean axial velocity near the heated wall. This is normal since the classical single phase logarithmic velocity profile is used to express the boundary condition for the liquid velocity (wall friction law). Nevertheless the liquid temperature profiles are in good agreement with the experimental data for both turbulence models implemented, K-ε and RSTM. Particularly near the wall, there is rather good agreement between the calculations with the RSTM model and the experimental data concerning the VF prediction. Other variables like the liquid turbulent kinetic energy are slightly more correctly predicted near the wall with the RSTM model but calculations using the K-ε model give slightly more satisfactory results in the core of the flow.

Another remarkable experiment simulated with NEPTUNE_CFD is the KAERI experiment (34). It is an annular test channel with an electrically heated inner tube. Local measurements of VF, phase velocities and bubble size over the channel cross-section were performed at an axial location. The temperature and absolute pressure were measured at the inlet. The system pressure was maintained between 1 and 2 bar. Local measurements of void fraction and vapor velocity were carried out using electrical conductivity probes. The VF predictions with two-phase and single phase wall function are presented and compared to experimental data by (35). There is a soft over-prediction of the VF and the turbulent dispersion force seems to be too low. Therefore, there is a weak diffusion of bubbles towards the center of the channel. They accumulate in the near wall region. In general, the calculation with the two-phase wall function model improved the agreement with the measured velocities near the wall.

NEPTUNE_CFD was also applied to simulate the DEBORA experiment, which provides axial vapor velocity, VF and liquid temperature data. Taking as a reference this database the single and two-phase wall friction models implemented in the code are tested and the prediction of the VF with the RSTM model is simulated according to (36). In case of constant bubble size model the bubble diameter is set to constant value of 0.3 mm according to experimental observations. A difference in the liquid temperature is observed, but its magnitude is small. It was observed that calculations with and without the lift force yield similar results. In this case the small bubble diameter (0.3 mm) makes the relative liquid gas phase velocity weak and as a consequence, the lift force is small. Some considerations about the lift force and its interaction with secondary structure flows in channels are addressed in (37). A brief resume of the results obtained reveal that by using any of the turbulent models K-ε or RSTM there is a quite good agreement with the experimental data even if they slightly overestimate the VF near the wall. Furthermore, a comparison between the different ways of implementing a variable bubble diameter is presented. The single size model developed by (38) and the multi-size models (method of statistical moments) developed by (39) and by (40) are applied for the simulations. A better agreement was found with Ruyer's model (40) and the RSTM model.

The addition of mixing vanes provides a new data base from the test bench now called the DEBORA mixing experiment. To investigate the effect of flow mixing an experimental device representing three mixing blades was introduced in a heated tube of 19.2 mm diameter and used for two different programs. The first is the AGATE-mixing experiment (41) with a single-phase liquid water tests measuring the water velocities. The second is the DEBORA-mixing experiment (42) with boiling in R12 refrigerant. The main physical phenomena to reproduce are: wall boiling, entrainment of bubbles in the wakes and condensation, see (23) and (43). According to (43) the main physical phenomena are successfully reproduced by NEPTUNE_CFD. The computations agree favorably with the experimental results, in particular the global effect of the mixing blades can be reproduced. In fact, the steam is produced at the wall but as the flow passes through the mixing device most of the vapor bubbles migrate from the wall towards the center of the blade wakes due to pressure difference. Once they are entrained in a subcooled domain, the steam bubbles collapse. This is how the mixing vans re used to shift the operational threshold by suppressing the local appearance of the critical heat flux (CHF).

In the MTLOOP facility (44) the evolution of a two-phase bubbly flow is observed in a vertical tube having an inner diameter of 51.2 mm and a length of 3.5 m. An air water mixture at a temperature of 30 °C is supplied at the bottom of the tube. The use of a wire-mesh sensor allows to measure radial profiles of VF for a given range of bubble sizes as well as bubble size distribution functions. The results are published by (45), where simulations with different break-up models were performed. For the experimental conditions the best estimated is the Wu et al. correlation (46).

How to model the bubble size is challenging. It is directly related to the IAC. Currently four methods are used. Three of these methods handle the simultaneous existence of multiple bubble sizes. Two of them are momentum approaches, the third is a multi-field approach. The fourth method is the classical single-size approach where all the bubbles are characterized by a single, but variable diameter. The single-size approach is using one IAC balance equation (47). For the simulations based on the MLOPP facility it was used to obtain a reference calculation according to (45). In these simulations the calculation was performed using Wu's break-up model. With this model the cross-sectional averaged IAC and the Sauter mean diameter (SMD) axial evolutions are quite well reproduced, especially in the first half of the tube. The axial evolution of the VF radial profile is also well reproduced showing the formation of a void coring in the second half of the tube for this experiment. Other models for the break-up phenomenon were tested like the ones from (48), (49) and also (38). But none of these models provide results as good as the ones obtained with Wu's model.

Some of the simulations performed with NEPTUNE_CFD were focused on the prediction of the DNB type of CHF in a simple tube. The DNB is an important issue to be model for CFD codes. Especially when the CHF is exceeded a rapid increase of the fuel cladding temperature can lead to the core damage. The CHF is strongly dependent on the flow parameters which itself are impacted by the FA design.

According to(50) standard CHF tables produced by the Russian Academy of Sciences were used as a validation data set. The CHF values for the water flow in a tube are given as a function of local equilibrium quality, mass flux and pressure. The CHF predictions at varied local equilibrium quality are presented to demonstrate the capability of implemented models. For each data point numerical simulations were performed in a way to determine the interval of the wall heat fluxes at which the boiling crisis occurs. An extended wall heat flux partitioning model with CHF criterion based on the VF at the wall was used for numerical prediction of boiling crisis. This publication demonstrates that the simple criterion based on the near-wall VF is capable to predict CHF relatively well. The NEPTUNE_CFD method works fine for the cases with high mass fluxes and high pressures, but further work is needed to predict CHF at low mass fluxes (below 1000 kg/($m^2$s)) and low pressures (below 10 MPa).

The capabilities of the code have been tested not only for single annular domains but also for describing the flow within rod bundles. Simulations of boiling flow in a rod bundle with DNB at the end of the middle rod were performed with NEPTUNE_CFD. For this case "Large Water Loop" (LWL) CHF experiments were used as a data set. The LWL was built at the Nuclear Machinery Plant, Skoda, Plzen Ltd., Czech Republic, see (51).

The CHF experimental facility (part of the LWL) has been designed to investigate the DNB phenomenon in the water flow through a bundle of electrically heated vertical rods (nineteen rods with a diameter of 9.1 mm and pitch distance of 12.75 mm). The heated length is 3.5 m. The critical conditions were determined at a constant pressure, inlet water temperature and mass flux and for quasi steady-state conditions by gradually increasing the heat flux.

Nuclear rods are modeled by direct electrical heating of inner walls of the hollow tubes. The axial distribution of the wall heat flux is uniform while the radial distribution decreases from the central rod with a power coefficient of 1 towards the outer rods with the coefficient 0.7. The computational domain represents a 30° symmetric section of the actual bundle.

Two spatial discretizations with different resolution were used to simulate all selected data points. The grid spacers are not included in the numerical model. The actual heated section of the channel contains 7 grid spacers-plates aligned with the flow. The calculated VF distribution in the domain is rather similar for both grids. The maximum VF is slightly higher on the fine grid. Simulated CHF occurs between the 90% and 100% of the experimental CHF value on both meshes.

According to the report (52) the simulations were successful for cases with low exit equilibrium quality. They fail to predict CHF for high exit equilibrium quality cases ($X_{eq} > 0.2$). These cases are most probably a dry-out type of CHF while the numerical models have been developed for a DNB type of CHF.

Other application case of the code to rod bundles flow is the simulation of a simplified 2x2 rod bundle with mixing vane. A similar geometry to a real FA is considered following the specifications of (53). It consists of a rectangular test section in which a 2x2 rod bundle equipped with a simple spacer grid with mixing vanes is placed. The performed calculations with NEPTUNE_CFD enable estimation of capabilities of numerical models to simulate turbulent boiling flows in the geometry close to the actual FA. This time the TH conditions represent the PWR core configuration close to nominal conditions. The simulations based on this test bench are performed by (36), following the recommendations of (54) and the conclusions of the DEBORA test. The implemented interfacial forces acting on the bubbles are the drag and the added-mass forces. The turbulent dispersion is taken into account by the Tchen's theory (55).

The time step for the calculation with the RSTM model has to be small enough to ensure a Courant-Friedrichs-Lewy (CFL) condition equal to 1. The mixing of the flow predicted by the k-ε model is smaller than for the RSTM model. The k-ε model overpredicts the turbulent heat diffusion and underestimates the turbulent mixing. These two deficiencies have opposite effects and sometimes neutralize each other. The liquid temperature calculated with the k-ε model is more homogeneous over the calculation domain; therefore the gradient of temperature is lower. The VF field downstream of the mixing blades has slightly lower values when calculated by the k-ε model compared with the case of the RSTM model.

Exploratory simulations of NUPEC BWR Full-size Fine-mesh Bundle Test (BFBT) benchmark test (56) were performed with the NEPTUNE_CFD code aiming to evaluate the code's capability to simulate boiling flow in real reactor geometries. Some works were focused on single phase flow calculations, like the one presented by (57). According to (58) the microscopic grade benchmark on steady state void distribution (Phase I – Exercise 2) with the smallest power and exit quality was simulated. Preliminary investigations were performed on a single subchannel test case. For this single subchannel predicted VF values did not change significantly with finer grid resolution but put in evidence some numerical oscillations in the near wall regions (59).

Simplified geometry of 45 degrees with no spacer grids was recreated. With a constant mean bubble diameter of 0.1 mm. Standard models for interface drag, heat transfer and the wall boiling together with steam turbulence modeling were included. They also took into account non-drag forces contribution (lift, added mass and turbulent dispersion force). Steady state conditions were reached within 3 seconds.

The averaged void production was sufficiently well predicted but with significant qualitative differences in the local steam distribution. In the NEPTUNE_CFD simulation the highest vapor concentration was found near the heated rods while in the experiment the maximum VF was observed in the central part of subchannels. Moreover, the predicted steam concentration did not reach the maximum experimental values (> 60%) although the section averaged VF is slightly overestimated (~ 30% with respect to the measured 25%). This indicates a high dispersed VF in the calculation, which can be partly explained by the absence of spacer grids in the numerical model.

A strong sensitivity to the imposed (constant) value of mean bubble diameter was observed in the subchannel studies. New simulations implementing a balance equation for the IAC were performed. The model for the IAE is exhaustively described by(47). The predicted void distribution did not change significantly, even if vapor seems to be less uniformly spread among the sub-channels, cross section averaged VF was reduced to 26%. The model parameter modifications mostly affect the VF distribution and do not change the cross-section averaged values significantly.

Other experiments like the OECD/NRC PWR Subchannel and Bundle Tests (PSBT) international benchmark (60) provide good database suitable for the NEPTUNE_CFD validation. A centred, isolated subchannel geometry based simulations were compared to experimental data. According to (61) where six cases of the database were tested in a steady state simulation in nominal conditions, the discrepancy between calculated and experimental mean void-fraction at the measurement section is on average of the order of ±0.05 VF units.

Another two-phase flow configuration reproduced with the NEPTUNE_CFD found in the literature is the emergency core cooling (ECC). One test bench devoted to the study of core coolant methodologies is the COSI experiment (62). Detail temperature profile comparison against experimental data and NEPTUNE_CFD simulations for the COSI experiment are performed by(63). The COSI experiment studies the cold water ECC injection during a LOCA. This is a relevant safety issue in the context of PWR life extension. It studies the possibility of a cold shock, the so called pressurized thermal shock (PTS), when cold water flows from ECC through the cold leg towards the vessel. The TH problem is to evaluate the heat up of water between ECC injection and the vessel. Different meshes were applied in a sensitivity analyses. By those simulations the capabilities of the code to reproduce free surface flow are demonstrated. The models for interface friction and heat transfer on liquid side are derived from (64). Other three PTS relevant experiments were used to evaluate the code capabilities in this field, see (65). More studies about the two-phase flow configuration with stratified air/water flow in relevant PTS scenario when an ECC occurs are presented in (66). In this study NEPTUNE_CFD results are compared to ANSYS_CFX and FLUENT. The validation of the large interface method of NEPTUNE_CFD 1.0.8 for PTS is demonstrated in (67) by using the database of the LAOKOON experiment (68).

The state-of-the art on the field of two-fluid modeling of boiling flow has been presented for the NEPTUNE_CFD. The use of CFD proved its potential to predict small-scale phenomena in boiling flows and hence contribute to a better understanding of complex flow processes. The “local predictive approach” where CHF empirical correlations are based on local parameters provided by CFD is not available yet in literature. There is no model dedicated to accurately calculate the CHF. Presently, a simple DNB criterion based on the local near-wall VF is used. A simple CHF criterion is used for pipe flow and fuel bundle experiments. The simulated cases of boiling in fuel rod bundles show that CFD methods are the state of the art in FA and spacer grid design.

Steady state analyses were found in the literature for rod bundle flow for the BFBT benchmark. This is a suitable experiment to be simulated with NEPTUNE_CFD. New contributions to the validation can be made by simulating characteristic transient scenarios for LWR not yet addressed by the literature. An exercise of the BFBT database describing transient scenarios (a turbine trip and a recirculation pump trip for BWR) together with the PSBT database are selected to perform simulations with NEPTUNE_CFD (chapter 4). This way the familiarization with the code is achieved and there is a new contribution to its validation.

### 1.5.4 The Multi-physics simulation codes

At the moment only the TH part of the NPP design was mentioned, but the core behavior is model by reactor dynamic codes in charge of solving the neutron physical phenomena.

In LWR the power source is produced due to the fission of uranium-235 by a thermal neutron. NK codes describe the interactions of the neutron with the construction materials of a reactor core either solving the time dependent neutron transport equation using an exact solution or an approximation e.g. diffusion. By the choice of the material composition and geometry of a LWR core, the inherent safety features are determined such as the Doppler and moderator temperature reactivity coefficients. These feedback mechanisms between the neutron physical and the TH processes affect the behavior of the reactor core under accidental conditions. The use of water as a moderator is an important safety feature, as any increase in temperature causes the water to expand and become less dense, thereby reducing the extent to which neutrons are slowed down and hence reducing the reactivity in the reactor.  The Doppler broadening effect of U-238 implies that the neutron absorption increases as the fuel temperature increases representing an essential negative feedback mechanism for reactor control. Therefore, NK are conditioned by TH feedback parameters (Doppler and moderator temperatures, densities, boron concentration, etc.). The simulation of phenomenology of different fields, e.g. system TH, NK and thermo-mechanics has become a very important area of development. The safety assessment of NPP requires integration of several disciplines into the analysis. The analysis of the core behavior requires a tight coupling of reactor physics and TH.

For NK codes the scale issue can also be considered. For the NK, the point kinetics approximation describes the evolution of the reactor power and reactivity in terms of global changes. This method is widely used in safety analysis. This is a rough description of the core behavior and local perturbations of important core parameters are not considered. The neutron diffusion equation can be solved in 3D for homogenized FA providing more detailed information but still in the range of the macro-scale. As the reactor cores become more complex (higher enrichments and burn-up, advanced FA designs, also more heterogeneous loading patterns) higher requirements on the predictive accuracy of the core simulation tools are required. Modern FA designs demand a geometrically more discrete representation of the fuel lattices in the lattice physics codes. By applying refined scales multidimensional effects can be taken into account during anticipated transients or asymmetric power distributions within the core. The pin power distribution can also be predicted in three-dimensional diffusion core simulations via pin-power reconstruction methods in order to identify pins with maximum heat generation rates in the core. These enhancements increase the operational flexibility while still respecting safety thresholds.

The feedback from the TH (fuel temperature and moderator properties) to the neutronic processes is a key aspect for the proper prediction of the core criticality. A coupling with a reliable prediction of the temperature fields in the moderator and in the fuel pins becomes crucial for the NK codes. The accuracy requirements for the prediction of the fuel and moderator temperature are very high since they determine for reactor design and safety evaluations. Both, the axial moderator density and fuel temperature distribution have a strong impact on the power distribution. A good prediction of the coolant temperature in the case of PWR's and of the axial void distribution in the case of BWRs is essential. This emphasizes the importance of the development of high fidelity coupling of NK and TH codes for safety assessments.

Improvements to the TH codes were realized parallel to the advancements of the NK codes. The local treatment of the coolant conditions surrounding the individual fuel pins is necessary for a good prediction of the feedback parameters. Therefore, refined space discretization codes like subchannel or CFD codes are the only methods that permit the direct prediction of local safety parameters and hence efforts are underway to develop high fidelity tools involving the integration of NK and TH modules. Furthermore, detailed multi-physic studies with CFD codes are capable to predict the conjugated heat transfer between the solid and the coolant that enables an accurate prediction of the structural response.

To describe the complete phenomenology within reactor cores, the codes in charge of both phenomena (TH and NK) work together in a multi-physic approach. A combination of multi-physics and multi-scale approach allows the prediction of local safety parameters considering TH and NK feedbacks. Some of the system codes have internal point kinetic routines to provide information about this feedback. For some applications the point kinetic approach is sufficient but a more detailed modeling with respect to neutron physics provides more accurate results. Thus, some schemes have been developed to couple BE system codes with 3D NK codes like: RELAP/PANBOX (69), TRACE/PARCS (70) or RELAP/PARCS (71).

Within the European Nuclear Reactor Simulation (NURESIM) (72) and the recently finished Nuclear Reactor Simulation Integrated Project (NURISP) (73) the multi-physics/multi-scale approach is aimed by means of an open-source integration platform for numerical simulation called SALOME (74). Different European code systems related to nuclear applications are integrated in this platform. Some of those TH codes are: CATHARE3 (75), FLICA, NEPTUNE (76), etc. Neutron physics codes are implemented in the SALOME platform e.g. DYN3D, COBAYA (77), CRONOS (78), etc. Due to the open and flexible architecture, these codes can be coupled in an novel way based on the mesh superposition and the automatic interpolation of the involved domains.

For the long term, it is foreseen that the existing codes will be replaced by codes based on advanced physical, numerical and computational methods. The trend to describe detailed phenomena in a micro-scale is increasing. The development of the codes working in this scale together with the growing computational power that allows processing a huge amount of information are fostering such developments. Thus, the refined TH codes like the CFD´s tools are expected to provide reliable information in a relatively short period of time as soon as the models implemented reach maturity. Investigations to develop coupling schemes between CFD and NK codes are being followed in different places using different approaches such as in ANSYS/PARCS (79), MCNP/STAR_CD (80), or DYN3D/ANSYS CFX.

The mentioned multi-physic solution can be classified according to its coupling methodology. The main trends in that sense are: internal, external and combined coupling.

- External coupling: There is exchange of information at each time step. A code calculation is based on the feedback provided by the other (NK or TH). This is an iterative process. During transient scenarios this methodology is required to be executed with a careful selection of the time step to ensure stability.

- Internal coupling: By this methodology one code is fully integrated in the other like a set of routines. Implementing this way is usually complex and strong programming skills are required.

- Combined coupling: codes can be coupled between each other at the same time maintaining the independence. It means that the codes are able to run stand-alone but for specific calculation they may interact. This requires an interface management and flexible access to common fields and arrays.

Because the effort to validate codes used for safety analysis is very large, a preservation of the established codes is of strong importance. Therefore, coupling between existing codes representing different physics fields such as TH and NK is very attractive compared to the option to develop a complete new code. This approach is followed by the route of a combined coupling and it works well for the TH/NK systems where well validated codes exist.

The methodology applied in the frame of this dissertation is the explicit coupling of a TH and a NK code. Hence, the TH tool is always on step ahead of the NK calculation. The time discretization has to be small enough to avoid possible stability problems. The numerical experimentation reveals that the explicit method of updating the data is free of oscillations only if the time step is small enough. For large time steps some variables develops unphysical oscillations of numerical nature that are unrelated with the physics of the problem under consideration. The explicit method is conditionally stable. Normally the time step is selected by the TH tool attending to the flow characteristics like the Courant number. In case of the simulation of a transient scenario with externally coupled codes, both codes share the same time step. The time scale of the coupled solutions is always conditioned by the most restrictive time step. TH tools use a smaller time step compared to the NK code. Therefore, NK code has always a sufficient time step in the coupled solution.

# 2 The NK-TH codes selected for the coupled solution

The codes involved in this work are presented in this chapter. A description of the models implemented and its capabilities are explained. The coupled solution is composed of one NK solver, a TH tool and a heat conduction solver. In addition the validated code DYNSUB is presented as the reference for the new code to be verified with. The reference and the coupled solution are composed of the same NK solver (DYN3D_SP3). The SCF (16) is the TH module of DYNSUB. NEPTUNE_CFD is the TH solver and SYRTHES is the heat conduction and transfer solver of the new coupled code NHESDYN.

## 2.1 DYN3D_SP3

The DYN3D_SP3 code is a module of the DYN3D diffusion solver. It provides a time dependent solution of the neutron transport equation based on the SP3 approximation for square geometries.

The main motivation for the development of this module was to create a version able to deal with nodal methods in many energy groups (multi-groups), by including a simplified transport approximation SP3, (2), (81) and (82). By implementing this module the code has in addition to the nodal solver the capability to perform pin by pin calculations based on a transport approximation. The main version of the DYN3D code, has been widely validated by Grundmann and Kliem: (83), (84), (85) and (86).

When a reactor has been designed in terms of geometry composition and cross sections the purpose of a neutron transport calculation is to determine the reaction rates and therefore the neutron density or the angle dependent neutron flux $\Psi$(r,Ω,E,t).

The objective of the reactor dynamic code is the solution of the time dependent Boltzmann transport equation, which is based on the balance of the neutrons in a specific volume of a nuclear reactor as a function of the position r, angular direction Ω, energy E and time t. Hence, according to (82), the multi-group transport equation is:

$$\frac{1}{V(E)}\cdot\frac{\partial}{\partial t}\psi(\vec{r},\Omega,E,t)=Q(\vec{r},\Omega,E,t)-\Omega\nabla\Psi(\vec{r},\Omega,E,t)-\sum\nolimits_t(\vec{r},E,t)\Psi(\vec{r},\Omega,E,t), \qquad (2\text{-}1)$$

where for a specific volume dV the variation in time of the angular flux at the left side of the equation divided by the main neutron velocity V(E) is equal to the production of neutrons Q(r,Ω,E,t) minus the leakage of neutrons, minus the missing neutrons due to absorptions and scatterings in the given volume. ∑(r,E,t) is the total macroscopic cross section. The production of neutrons can have three contributions: the neutron source due to fissions taking part in the reactor $Q_f$(r,Ω,E,t), the scattered neutrons in the volume coming from other energy levels and the other angular directions $Q_s$(r,Ω,E,t) and finally, external neutron source $Q_{ext}(r,\Omega,E,t)$. For critical reactors the external source is usually set to zero assuming that all the neutrons originate from fission and scattering.

Several assumptions are usually made in order to obtain a practical solution. The goal is to reformulate the Boltzmann equation by means of numerical discretization of the variables and integral operations in space angular direction, energy and time.

To solve the discretized form of the Boltzmann equation the method of spherical harmonics (PN-method) is applied in the DYN3D_SP3. In the PN-method the angular dependence of the neutron flux is expanded in spherical harmonics functions up to order N. The exact transport solution is recovered as N tends to infinity. In three dimensional geometries, the number of PN equations grows like $(N+1)^2$. For one dimensional planar geometry the number of PN equations is (N+1).

The PN equations in one dimensional planar geometry are relatively simple and can be formulated in second order as (N+1)/2 equations. In multidimensional geometries the case is too complicated. This increase in complexity led to the proposal of the simplified PN approximation. In the SPN method, the second order derivatives in one dimensional planar geometry of the PN equations are replaced or generalized by means of the three dimensional Laplacian operator leading to a multidimensional generalization of the planar geometry PN equations that avoids the complexities of the full spherical harmonics approximation.

## 2.2 SUBCHANFLOW

SCF is being developed at the INR/KIT. The main objective of SCF (16) is to provide a tool fast running, stable and flexible for the description of the single and two-phase flow within subchannels of fuel bundles or of a reactor core. It can be used to model systems cooled/operated with water, air, helium, lead, lead-bismuth and sodium in quadratic and hexagonal lattices using subchannel or subassembly discretization of the reactor core, see Fig. 2-1.

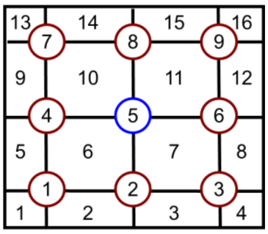

**Fig. 2-1. SCF space discretization for a 9 pin rod bundle.**

Steady state and transient simulations are solved by using a fully implicit iterative solver. For the heat conduction inside the fuel rods a finite difference approach is applied. The user can specify the empirical model to use used for e.g. heat transfer or friction.

To solve a domain where there are two phases (liquid and vapor) SCF models it as a three equation mixture, like a single phase. SCF is based on a 4-equation model for the conservation of mass, energy and momentum. The momentum equation is solved for the axial and lateral directions. It considers the water and the vapor like a homogeneous mixture. This mixture shares a common pressure field and a common velocity profile. The conservation equations are shown next.

### 2.2.1 Fluid dynamic models

For the description of the balance equations is assumed that the velocities and the pressure field is the same for both phases and that they are in thermodynamic equilibrium. The mass conservation equation Eq.(2-2) defines the density according the Eq.(2-3). The energy conservation and momentum equation are given by Eq.(2-4) and Eq.(2-5) respectively.

$$\frac{\partial \rho}{\partial t} + \nabla\left(\rho \cdot \vec{V}\right) = 0, \tag{2-2}$$

$$\rho = \alpha \cdot \rho_v + (1-\alpha)\rho_l \, , \tag{2-3}$$

$$\frac{\partial}{\partial t}\rho(h) + \nabla\left(\rho \cdot h \cdot \vec{V}\right) = -\nabla\left(q^{''} + q^{''T}\right) + \frac{\partial p}{\partial t} + q^{'''}\left(q_{wv}^{'''} + q_{wl}^{'''}\right) \, , \tag{2-4}$$

$$\frac{\partial}{\partial t}\rho\vec{V} + \nabla\left(\rho\vec{V}\vec{V}\right) = -\nabla p + \rho g + \nabla\left(\underline{\underline{\tau}} + \underline{\underline{R}}\right) + \underline{\underline{\tau}}^{'''} \, . \tag{2-5}$$

These equations represent a general formulation of the mass, energy and momentum equations. On this formulation SCF makes some assumptions. For instance, there is no a real modeling of the turbulent stress tensor (R), the effect of the turbulence is included by the closure laws applied in the code. The meaning of the variables of these equations are given below:

$h$ : Enthalpy of the mixture in axial direction $\left(h = xh_v + (1-x)h_l\right)$,

$q''$ : Molecular heat flux,

$q''^{T}$ : Turbulent heat flux,

$q'''$ : Energy generated in the fluid,

$\rho$ : Mixing density Eq.(2-3),

$\underline{\underline{\tau}}$ : Molecular stress tensor,

$\underline{\underline{R}}$ : Turbulent stress tensor,

$\underline{\underline{\tau}}'''$ : Interfacial wall drag tensor,

### 2.2.2 Heat conduction model

Regarding the fuel elements, SCF calculates the heat conduction in a fully implicit finite difference form. After some simplifications of the heat transfer equation SCF solves the following Eq.(2-6):

$$\rho(r,T)\cdot C_p(r,T)\frac{\partial}{\partial t}T(\bar{r},t) = \nabla\cdot k(r,T)\nabla T(r,t) + q'''(r,t), \qquad (2\text{-}6)$$

where:

| | |
|---|---|
| $\rho(\bar{r},T)$ | : Density as a function or radius (position vector - space) and temperature, |
| $C_p(\bar{r},T)$ | : Heat capacity as a function of space and temperature, |
| $T(\bar{r},t)$ | : Temperature as a function of space and time, |
| $k(\bar{r},T)$ | : Heat conductivity as a function of space and temperature, |
| $q'''(\bar{r},t)$ | : Volumetric heat flux as a function of space and time. |

One of the most important assumptions made in Eq.(2-6) is that the heat is transferred mainly in radial direction (axial heat transfer neglected). This can generate sharp temperature gradients between axial levels. By solving the 3D heat conduction with a CFD code smooth gradients are calculated because it takes into account the axial temperature interactions. The equation (2-6) can be rewritten in cylindrical coordinates in the following form:

$$\rho(r,T)\cdot C_p(r,T)\frac{\partial}{\partial t}T(r,t) = \frac{1}{r}\cdot\frac{\partial}{\partial r}\cdot rk(r,T)\frac{\partial}{\partial r}T(r,t) + q'''(r,t) \qquad (2\text{-}7)$$

Different empirical constitutive models were developed to close the system of equations are available in the input of SCF. The next lines are devoted to the description of the most important models (mainly heat transfer models) applied during the simulations performed with the code.

The Blasius model is selected for the single-phase friction factor ($f_{\text{single phase}}$) and a two-phase flow correction factor (Φ), based on the work of Armand (87).

$$f_{\text{single phase}} = \text{MAX}(f_{\text{laminar}}, f_{\text{turbulent}}), \tag{2-8}$$

$$f_{\text{laminar}} = 64 \cdot \text{Re}^{-1.0}\ , \tag{2-9}$$

$$f_{\text{turbulent}} = 0.316 \cdot \text{Re}^{-0.25}, \tag{2-10}$$

$$\Phi = \begin{cases} \frac{(1-x)^2}{(1-\alpha)^{1.42}} & \text{if} \quad 0.0 < \alpha \le 0.6 \\ \frac{0.478 \cdot (1-x)^2}{(1-\alpha)^{2.2}} & \text{if} \quad 0.6 < \alpha \le 0.9\ . \\ \frac{1.73 \cdot (1-x)^2}{(1-\alpha)^{1.64}} & \text{if} \quad 0.9 < \alpha \le 1.0 \end{cases} \tag{2-11}$$

Depending on the void fraction the heat transfer regime is selected. In SCF the boiling curve is divided into four sections following the COBRA approach (88). Each section is described by a different heat transfer correlation. For single phase liquid and for single phase vapor the Dittus-Boelter correlation (89) is used ($h_{\text{single phase}}$).

$$h_{\text{single phase}} = \left(\frac{k}{d_{\text{hydraulic}}}\right) \cdot 0.023 \cdot \text{Re}^{0.8} \cdot \text{Pr}^{0.4}. \tag{2-12}$$

If ($0.0 < \alpha \le 0.8$) SCF employs the model of Thom, $h_{\text{Thom}}$, (90) and section 3 ($0.8 < \alpha \le 0.9$) is an interpolation between the Thom model and the Schrock-Grossman model (91), $h_{\text{SG}}$, given in equation (2-15).

$$h = (\alpha - 0.8) \cdot h_{\text{Thom}} + (0.9 - \alpha) \cdot h_{\text{SG}}\ , \tag{2-13}$$

$$h_{\text{Thom}} = \frac{q''}{t_{\text{sat}} - t_{\text{coolant}} + 22.5 \cdot 10^{-3} \cdot \exp\left(\frac{-p}{8.7 \cdot 10^{7}}\right) \cdot \sqrt{q''}}\ , \tag{2-14}$$

$$h_{\text{SG}} = \left(\frac{k}{d_{\text{hydraulic}}}\right) \cdot 2.5 \cdot 0.023 \cdot [\text{Re} \cdot (1-x)]^{0.8} \cdot \text{Pr}^{0.4} \cdot \left(\frac{1}{x_{tt}}\right)^{0.75}\ , \tag{2-15}$$

where $1/x_{tt}$ is the Lockhard-Martinelli parameter (92).

$$\frac{1}{x_{tt}} = \left(\frac{\rho_{\text{liquid}}}{\rho_{\text{vapor}}}\right)^{0.5} \cdot \left(\frac{x}{1-x}\right)^{0.9} \cdot \left(\frac{\eta_{\text{vapor}}}{\eta_{\text{liquid}}}\right)^{0.1} . \tag{2-16}$$

Exceeding the critical heat flux additional heat transfer models are used which will not be recited here since critical heat flux is not an issue for the present investigation. Subcooled boiling is not considered in the present analysis.

For the calculation of the VF the Chexal-Lellouch model following the drift-flux formulation is activated. This model is based on the liquid and vapor volumetric fluxes ($j_{\text{liquid}}$ and $j_{\text{vapor}}$), a distribution or pipe orientation parameter ($C_0$) and the drift velocity ($V_{gj}$). Depending on the flow direction the values for the orientation parameter and the drift velocity can be calculated following the models provided in the original paper of Chexal et al. (93)

$$\alpha = \frac{j_{\text{vapor}}}{C_0 \cdot (j_{\text{liquid}} + j_{\text{vapor}}) + V_{vj}} . \tag{2-17}$$

## 2.3 DYNSUB

The DYNSUB code is the coupled solution of DYN3D_SP3 and SCF, it is being developed at the INR/KIT, see (94) and (95).

Several neutronic codes are able to solve the diffusion equation on multi-groups considering feedback parameters coming from the TH core model. Those codes contain usually two-phase flow models able to exchange assembly averaged parameters. The TH can be 1D, 2 phase models focused in parallel channels to each FA like FLOCAL in the DYN3D. For more detailed analyses the TH can be solved with a channel code. Those code capabilities describe more detailed phenomenon of the flow e.g. the cross flow phenomena between FA. At this level is possible to find coupled solutions like COBRA-TF/QUABOX-CUBBOX (96), ANDES/COBRA (97) or /COBRA-TF NEM (98)

The efforts are orientated to refine the coupled scale from a FA to the subchannel pin level in order to extend the capabilities of the codes and its physical prediction. With solvers based on the numerical solution of the transport equation (Boltzmann equation), direct predictions of the local power at pin level can be done avoiding the approximation of pin power reconstruction, as for instance the simplified multi-group SP3 transport equation used in the codes DYN3D_SP3 and PARCS (99). In DYN3D_SP3 the coupling with FLOCAL leads to the loss of important local information due to nodal level the TH works (nodal based). To make both codes work at the same spatial resolution the

DYN3D_SP3 has been coupled with the channel code SCF which uses a more refined spatial discretization (pin level) than FLOCAL.

## 2.4 SYRTHES

Proper modeling capabilities for fuel performance and fuel behavior during accidents is a key element for the safety evaluation of LWRs taking into account that many of our current acceptance safety limits are related to the first barrier (cladding).

The prediction of fuel and cladding temperatures or fuel gap conductance are relevant phenomena to assess the fuel performance. Initially, relatively simple fuel modeling approaches were adopted: The fuel pin was represented in three cylindrical regions. The heat conduction was numerically solved only in radial direction. Some fast-running fuel performance codes used for fuel and core design are built from a stack of 1D element with only limited representation of the axial effects. Subchannel code normally neglect the axial direction solving the heat conduction in radial direction. The SYRTHES implements a finite element method to solve the 3D heat conduction in the fuel gap and clad domains. This is a heat conduction solver that works at the same space discretization level as NEPTUNE_CFD.

The heat conduction code must to be able to solve the differential equation for the temperature in solids. This is a requirement due to the ambit of applicability of the code that has to deal with the heat conduction in the fuel clad and gap. As explained previously subchapter the SCF solves the heat condition equation implicitly. The CFD tool applied here doesn't have this capability. Hence EDF has developed a coupled solution with the SYRTHES code to enable NEPTUNE_CFD to solve the temperature in solid domains.

The interaction between these two codes is a semi-implicit coupling allowing to solve the conjugate heat transfer at the solid-liquid interface and the heat conduction in the structures.

The solution at the solid-liquid interface is based on a few local parameters exchanged between the codes. The heat exchange coefficient and liquid temperature are calculated by the CFD and the wall temperature is calculated by SYRTHES. With these variables, the flux at the interface can be solved.

The space discretization performed by SYRTHES is based in a tetra volume approach, formed by 4 main nodes and 6 middle nodes, see Fig. 2-2. The nodalization has to be created as unstructured tetra elements. Unstructured mesh generation will lead to a mismatch at the solid-liquid interface with the CFD mesh (which is hexa based), see Fig. 2-3. To exchange the information between mismatching nodes an interpolation operation is mandatory with the consequence of a loss of accuracy. To avoid this situation the solid mesh is generated like a hexa mesh together with the CFD mesh ensuring the correspondence between nodes. Then the solid hexa discretization is transformed into tetra elements (4 tetra elements fits in one hexa element).

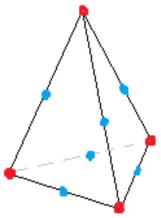

**Fig. 2-2. SYRTHES tetra element. Main nodes (red) and middle nodes (blue)**

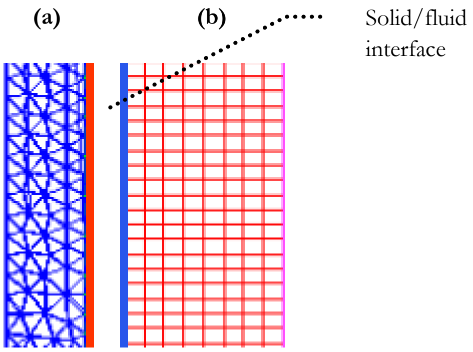

**Fig. 2-3. SYRTHES mesh (a) and NEPTUNE_CFD structured mesh (b)**

This operation has a handicap. In order to obtain a high accuracy the solid nodalization needs to be extremely refined. The computational time is penalized because the SYRTHES code is not parallelized. In most of the cases this refinement is beyond the numerical necessities to develop a proper temperature gradient as will be demonstrated in the last chapter. Hence, the domain that the coupled solution NEPTUNE_CFD/SYRTHES is able to solve within reasonable time frames is limited.

The resolution algorithm implemented in SYRTHES according to (3) is presented by Eq.(2-18)

$$\sum_{l=1}^{N_n}\left[\int_Q \left(\frac{\rho C_p}{\partial t}\right)_l \vartheta_l \vartheta_i \vartheta_j d\Omega + \int_Q (k_s)_l \vartheta_l \nabla \vartheta_i \nabla \vartheta_j d\Omega\right]\cdot T_i^{n+1} =$$

$$\int_Q \left(\sum_l^{N_n}\left(\frac{\rho C_p}{\partial t}\right)_l \vartheta_l T_i^n + \phi_i^n\right)\cdot \vartheta_i d\Omega + \int_\Gamma q_i \vartheta_i d\Gamma, \tag{2-18}$$

where the variables have the following meaning:

$C_p$ : Heat capacity,
$\Gamma$ : Limits for source terms,
$Q$ : Heat,
$T$ : Temperature,
$\phi$ : Volumetric flux,
$\vartheta$ : Base function,
$N$ : Number of nodes per element,
$k$ : Thermal conductivity,
$\rho$ : Density,
$q$ : Heat flux,
$\Omega$ : Volume.

# 3 The NEPTUNE_CFD code

EDF and CEA sponsored by the *Institute de radioprotection et de surete nucleaire* (IRSN) and AREVA are developing the new CFD code NEPTUNE for nuclear reactor applications. In the frame of the SP2 group of the NURISP (Nuclear Reactor Integrated Simulation Project) this code is being enhanced and the simulation capabilities are validated using different types of experiments. The NURISP is a Large scale Collaborative Integrating Project of the Seventh Framework Programme EURATOM.

One of the main objectives of the NURISP is to use the two-phase computational fluid dynamics programs to reach a better understanding of the boiling flow processes in nuclear light water reactors. Those studies would contribute to improve the safety and optimize different areas of the NPP design.

In this chapter a brief description of the CFD basis is provided. Furthermore, the models and closure laws used by NEPTUNE_CFD are outlined.

## 3.1 Brief introduction to the kinematics of fluid motion

For the flow field it is important to describe the velocities, the densities, the pressure and the temperature at each point and at each time.

$$\bar{v} = (u, v, w), \rho, p, T \qquad \bar{x} = (x, z, y) . \tag{3-1}$$

Crucial contributions came from Joseph Louis de Lagrange and Leonhard Euler. The Lagrangian method consists in keeping track of identifiable element of mass, like in particle mechanics. Starting from a fix point in the space and an initial time (x,t). After an increment of time we have a different position, then the velocity can be calculated.

$$x_0 = (x_0, y_0, z_0) \quad , t = 0 \; , \tag{3-2}$$

$$\frac{d\bar{x}}{dt} = \bar{v}(\bar{x}, t) \quad , \quad t = t + dt \; . \tag{3-3}$$

For the determination of the flow field in Lagrangian coordinates the measurement instruments have to track a moving particle. On the other hand the Eulerian method is based in the stationary observation. This method focuses attention on the properties of the flow at a given point. The flow field is described as a function of space coordinates and time.

### 3.1.1 Relation between Eulerian and Lagrangian considerations:

The measurement of the different variables is made from a fix position on the space. The temporal change of a particle property is described as:

$$f(\vec{x},t)=f(\vec{x}(\vec{x}_0,t),t) \quad , \quad \frac{df}{dt}=\frac{d}{dt}f[x(t),y(t),z(t);t] \ , \tag{3-4}$$

$$\frac{df}{dt}=\frac{\partial f}{\partial t}+\frac{\partial f}{\partial x}\frac{dx}{dt}+\frac{\partial f}{\partial y}\frac{dy}{dt}+\frac{\partial f}{\partial z}\frac{dz}{dt}, \tag{3-5}$$

$$\frac{df}{dt}=\frac{\partial f}{\partial t}+u\frac{\partial}{\partial x}f+v\frac{\partial}{\partial y}f+w\frac{\partial}{\partial z}f. \tag{3-6}$$

In Eq.(3-6) the first term on the left side is the substantial (fixed mass) derivation from Lagrange. The first term on the right side is the local time dependent change by Euler. And the last three components are the convective changes, (transport with velocity). The last equation can be written in the vector form with the definition of the gradient vector as:

$$\frac{df}{dt}=\frac{\partial f}{\partial t}+(\vec{v}\cdot\nabla)f \quad , \quad \nabla=\left(\frac{\partial}{\partial x},\frac{\partial}{\partial y},\frac{\partial}{\partial z}\right). \tag{3-7}$$

According to Eq.(3-7) the flow is stationary if the velocities, densities, pressures and temperatures don’t change in time. This doesn’t mean that the particles are at rest.

The different simulations performed during this work are based on the RANS approach. The modeling of the water/steam two-phase flows in three-dimensional space is based on the classical two-fluid one pressure approach for mass, momentum and energy balances in each phase.

The two-fluid models of the NEPTUNE_CFD numerical program are designed specifically for the simulation of two-phase transients in nuclear power plants according to (1), (23) and (43). This code is widely used within the frame of NURISP. The next subchapter will provide a detailed description.

The NEPTUNE_CFD solver is based on a pressure correction approach. It is able to simulate multi-component multiphase flows by solving a set of three balance equations for each field (fluid component and/or phase). These fields can represent many kinds of multiphase flows among them also bubbly boiling flow. The solver is based on a finite volume discretization together with a collocated arrangement for all variables.

## 3.2 Governing equations

The description of boiling two-phase flow in CFD codes is commonly based on the two-fluid approach by Ishii (100) and Delhaye (101). In this approach a set of local balance equations for mass, momentum and energy is written for each phase. These balance equations are obtained by ensemble averaging of the local instantaneous balance equations formulated for the two phases. When the averaging operation is performed, the major part of the information about the interfacial configuration and the microphysics governing the different types of exchanges is lost. As a consequence a number of closure relations (also called constitutive relations) must be supplied for the total number of equations (the balance equations and the closure relations) to be equal to the number of unknown fields. We can distinguish three different types of closure relations: those which express the inter-phase exchanges (interfacial transfer terms), those which express the intra-phase exchanges (molecular and turbulent transfer terms) and those which express the interactions between each phase and the walls (wall transfer terms). The balance equations of the two-fluid model we use for two-phase boiling flows and their closure relations are described in the following subsections. The two-fluid model we use for our two-phase boiling flow calculations consists of the following balance equations.

### 3.2.1 Mass balance equations:

$$\frac{\partial \alpha_k \cdot \rho_k}{\partial t} + \nabla \cdot \left( \alpha_k \cdot \rho_k \cdot \underline{V}_k \right) = \Gamma_k \quad , \quad k = l, v, \tag{3-8}$$

where t is the time, $\alpha_k$, $\varrho_k$ and $\underline{V}_k$ denote the volume fraction of phase *k*, its averaged density and velocity. The phase index *k* takes the values *l* for the liquid phase and *v* for vapour.

### 3.2.2 Momentum balance equations:

$$\begin{aligned} &\frac{\partial \alpha_k \cdot \rho_k \cdot \underline{V}_k}{\partial t} + \nabla \cdot \left( \alpha_k \cdot \rho_k \cdot \underline{V}_k \cdot \underline{V}_k \right) = -\alpha_k \cdot \underline{\nabla} p + \underline{M}_k + \Gamma_k \cdot \underline{V}_k \\ &+ \alpha_k \cdot \rho_k \cdot \underline{g} + \nabla \cdot \left[ \alpha_k \cdot \left( \underline{\Sigma}_k + \underline{R}_k \right) \right] \quad k = l, v, \end{aligned} \tag{3-9}$$

where p is the pressure, g is the gravity acceleration, $\underline{M}_k$ is the interfacial momentum transfer per unit volume and unit time, and $\sum_k$ and $R_k$ denote the molecular and turbulent stress tensors. The latter is also called the Reynolds stress tensor. The wall friction terms for the two phases do not appear in the momentum balance equations because solid walls are only present at the boundaries of the flow domain and the wall friction is expressed through the wall boundary conditions.

### 3.2.3 Total enthalpy balance equations:

$$\frac{\partial}{\partial t}\left[\alpha_k \cdot \rho_k\left(H_k+\frac{V_k^{\,2}}{2}\right)\right]+\nabla\cdot\left(\alpha_k\cdot\rho_k\cdot\left(H_k+\frac{V_k^{\,2}}{2}\right)\cdot\underline{V}_k\right)=$$

$$\alpha_k\cdot\frac{\partial p}{\partial t}+\alpha_k\cdot\rho_k\cdot\underline{g}\cdot\underline{V}_k+\left(\sum_k\Gamma_k^C+\Gamma_k^N\right)\cdot\left(H_{ki}+\frac{V_k^{\,2}}{2}\right)+\Pi_k^{'}\cdot A_i+q_{wk}'''-\tag{3-10}$$

$$-\nabla\cdot\left[\alpha_k\cdot\left(q_k+q_k^T\right)\right]\quad,\quad k=l,v,$$

where $H_k$ is the phase-averaged enthalpy for phase k and $H_{ki}$ is the interfacial-averaged enthalpy. We have assumed that the two phases are governed by the same averaged pressure field p and we make no distinction between the pressures in the two phases or between the bulk pressure and the interface pressure for simplicity. The three terms $\Gamma$, $M_k$ and $\prod_k A_i$ denote the interfacial transfer terms of mass, momentum and heat. The quantity $A_i$ denotes the interfacial area concentration. The terms $q_{wk}$ denote the wall-to-fluid heat transfer per unit volume and unit time for each phase. The two terms $q_k$ and $q_k^T$ represents the molecular and turbulent heat fluxes inside phase *k*. The interfacial mass transfer $\Gamma$ includes the mass transfer between the vapour and liquid that takes place inside the flow $\Gamma_k^C$ and the mass transfer contribution due to the nucleate wall boiling $\Gamma_k^N$.

## 3.3 Interfacial transfer terms

One of the most important issues regarding two phase flow with boiling is the modeling of heat transfer terms. A complete review of those models by an exhaustive literature review is compiled in (102) and (103). The description of two phase flow is complex and it is necessary to define many phenomena like the heat flux partitioning from the heated wall, the bubble nucleation, bubble growth time and detachment frequency, heat transfer between the steam and water interface, interfacial area concentration, bubble size and shape, interfacial momentum transfer between phases, etc. The information concerning which models are used in the NEPTUNE_CFD code can be found in the theory and user manual (55) and (104).

First, how the code deals with the heat and mass transfer is explained. If the mechanical terms are neglected in comparison to the thermal terms in the averaged form of the energy jump condition, this condition reduces to:

$$\sum_k\left(\Gamma_k^C\cdot H_{ki}+q_{ki}''\cdot A_i\right)\approx 0.\tag{3-11}$$

This important relation (together with the mass jump condition: $\Gamma_l^C = \Gamma_v^C$) allows to compute the mass transfer terms as functions of the interfacial heat transfer terms $q_{ki}''A_i$ and the interfacial-averaged enthalpies $H_{ki}$ :

$$\Gamma_l^C = -\Gamma_v^C = \frac{q_{li}^{"} + q_{vi}^{"}}{H_{vi} - H_{li}} \cdot A_i . \tag{3-12}$$

We have no information about the dependence of the interfacial- averaged enthalpies $H_{ki}$. Therefore, two basic assumptions can be made: Either the interfacial-averaged enthalpies $H_{ki}$ are identified to the phase-averaged ones $H_k$ or the interfacial-averaged enthalpies $H_{ki}$ are given by the saturation enthalpies. In the code the first assumption is made. Each interfacial heat transfer term is the product of the interfacial area concentration by the interfacial heat flux density ($q_{ki}^{"} A_i$).

$$q_{ki}^{"} = C_{ki} \cdot (T_{sat}(p) - T_k), \quad C_{ki} = \frac{Nu_l k_l}{d}. \tag{3-13}$$

The interfacial heat flux density can be defined as Eq.(3-13), where $C_{ki}$, $T_k$ and $T_{sat}(p)$ denote a heat transfer coefficient, the average temperature of phase *k* and the saturation temperature. The interfacial area concentration is expressed as $A_i = 6\alpha/d$, where $\alpha$ is the void fraction and d is the Sauter mean bubble diameter, $k_l$ is the thermal conductivity of the liquid. Depending on the Jakob number given by Eq.(3-14) there are two possible scenarios, condensation ($Ja \leq 0$) or evaporation ($Ja \geq 0$).

$$Ja = \frac{\rho_l \cdot C_{pl} \cdot (T_l - T_{sat})}{\rho_g \cdot L}. \tag{3-14}$$

The thermal capacity of the liquid is $C_{pl}$, and L is the latent heat of vaporization. In case of condensation, the Nusselt number is:

$$Nu = 2 + 0.6 \cdot \mathrm{Re}^{1/2}\,\mathrm{Pr}^{1/3}, \quad \mathrm{Re} = \frac{d_s \cdot |V_g - V_l|}{\mu_l}, \quad \mathrm{Pr} = \frac{\mu_1}{\omega_l}, \tag{3-15}$$

where $\mathrm{Re}_b$ is the bubble Reynolds number and $\mathrm{Pr}_r$ is the liquid Prandtl number, $\mu_l$ being the liquid kinematic viscosity and $\omega_l$ is the thermal liquid diffusivity. In case of evaporation the Nusselt number is defined as follows:

$$Nu = \max(Nu_1, Nu_2, Nu_3),$$

$$Nu_1 = \sqrt{\frac{4 \cdot Pe}{\pi}}, \quad Nu_2 = \frac{12}{\pi} \cdot Ja, \quad Nu_3 = 2, \tag{3-16}$$

where Pe is the Péclet number and it is defined as follows:

$$Pe = \mathrm{Re} \cdot \mathrm{Pr} = \frac{d_s \left| V_g - V_l \right|}{\omega_l} \quad . \tag{3-17}$$

The heat transfer coefficient between the vapour and the interface for the case of bubbles is written as:

$$q_{vi}^{''} = \alpha_v \frac{\rho_v \cdot C_{pv}}{\tau} \left( T_{sat} - T_v \right) \ , \tag{3-18}$$

where $C_{pv}$ is the gas heat capacity at constant pressure and $\tau$ is a characteristic time given by the users. This relation simply ensures that the vapour temperature $T_v$ remains very close to the saturation temperature $T_{sat}$, which is the expected result for bubbly flows with sufficiently small bubbles (flow in a PWR core in conditions close to nominal).

The interfacial transfer of momentum $\underline{M}_k$ appearing in the right hand side of Eq. (3-9) is assumed to be the sum of five forces:

$$\underline{M}_k = \underline{M}_k^D + \underline{M}_k^{AM} + \underline{M}_k^L + \underline{M}_k^{TD} + \underline{M}_k^{WL} \quad . \tag{3-19}$$

The five terms are the averaged drag, added mass, lift and turbulent dispersion forces and wall lubrication force per unit volume. Now we will give the expressions we use for these forces and for their coefficients.

Drag force:

$$\underline{M}_v^D = -\underline{M}_l^D = -\frac{1}{8} A_i \rho_l C_D \left| \underline{V}_v - \underline{V}_l \right| \left( \underline{V}_v - \underline{V}_l \right) \ . \tag{3-20}$$

Where $C_D$ is the drag coefficient for bubbles and can be determined experimentally. In the case of bubbly flow the Ishii and Zuber relation(105) is used, where the calculation of drag coefficient is based on the local flow regime.

Added-mass force:

$$\underline{M}_v^{AM} = -\underline{M}_l^{AM} =$$

$$-C_A^{lv} \cdot \frac{1+2\alpha_v}{1-\alpha_v} \cdot \alpha_v \cdot \rho_l \cdot \left[ \left( \frac{\partial \underline{V}_v}{\partial t} + \underline{V}_v \cdot \underline{\underline{\nabla}} \underline{V}_v \right) - \left( \frac{\partial \underline{V}_l}{\partial t} + \underline{V}_l \cdot \underline{\underline{\nabla}} \underline{V}_l \right) \right], \tag{3-21}$$

where $C_A^{lv}$ is the added mass coefficient which is equal to 0.5 for a spherical bubble and the factor $(1+2\alpha_v)/(1-\alpha_v)$ takes into account the effect of the bubbles concentration according to Zuber(106) and Ishii (107).

Lift force:

$$\underline{M}_v^L = -\underline{M}_l^L = -C_L \cdot \alpha_v \cdot \rho_l \cdot \left(\underline{V}_v - \underline{V}_l\right) \wedge \left(\underline{\nabla} \wedge \underline{V}_l\right), \tag{3-22}$$

where $C_L$ is the lift coefficient. This coefficient is equal to 0.5 in the particular case of a weakly rotational flow around a spherical bubble in the limit of infinite Reynolds number according to Auton (108). It has been empirically modelled by Tomiyama et al. (109). This coefficient depends on the modified Eotvös number Eq.(3-26).

If $Eo_H<4$ :

$$C_L = \min\begin{bmatrix} 0.288 \cdot \tanh(0.121\mathrm{Re}) \\ 0.00105 \cdot Eo_H^3 - 0.0159 \cdot Eo_H^2 - 0.0204 \cdot Eo_H + 0.474 \end{bmatrix}. \tag{3-23}$$

If $4 \leq Eo_H \leq 10$:

$$C_L = 0.00105 \cdot Eo_H^3 - 0.0159 \cdot Eo_H^2 - 0.0204 \cdot Eo_H + 0.474. \tag{3-24}$$

If $Eo_H > 10$:

$$C_L = -0.27, \tag{3-25}$$

with the modified Eotvös number defined by:

$$Eo_H = \frac{g \cdot (\rho_l - \rho_v) \cdot d_H^2}{\sigma}, \tag{3-26}$$

Where $\sigma$ is the surface tension and $d_H$ is the maximum horizontal dimension of the deformed bubble, which is calculated using an empirical correlation given by:

$$d_H = d \cdot \sqrt[3]{1 + 0.163 Eo^{0.757}}, \tag{3-27}$$

where d is the spherical equivalent bubble diameter and Eo has a similar expression as $Eo_H$ with d instead of $d_H$.

Turbulent dispersion force:

$$\underline{M}_v^{TD} = -\underline{M}_l^{TD} = -C_{TD} \cdot \rho_l \cdot K_l \cdot \underline{\nabla}\alpha_v \quad , \tag{3-28}$$

Here $K_l$ is the liquid turbulent kinetic energy and $C_{TD}$ is a numerical constant of order 1. This expression was proposed by Lance and Bertodano(110).

## 3.4 Interfacial area modelling

The IAC transport equation for the special case of bubbly flows with spherical bubbles was originally developed by Wu et al. (46), in the following form:

$$\frac{\partial A_i}{\partial t} + \nabla \cdot \left(A_i \underline{V}_v\right) = \frac{2}{3} \cdot \frac{A_i}{\alpha} \cdot \left[\frac{\partial \alpha}{\partial t} + \nabla \cdot \left(\alpha \cdot \underline{V}_v\right)\right] + 12\pi \left(\frac{\alpha}{A_i}\right)^2 \left[\frac{\partial n}{\partial t} + \nabla \cdot \left(n \cdot \underline{V}_v\right)\right] \quad , \tag{3-29}$$

where α is related to the dispersed phase (VF), and n is the bubble number density. Eq. (3-29) can be transformed by using the mass balance equation for the gas phase on one hand:

$$\frac{\partial \alpha \rho_V}{\partial t} + \nabla \cdot \left(\alpha \cdot \rho_v \cdot \underline{V}_v\right) = \Gamma_v = \Gamma_v^C + \Gamma_v^N , \tag{3-30}$$

and the bubble number density balance equation on the other hand:

$$\frac{\partial n}{\partial t} + \nabla \cdot \left(n \cdot \underline{V}_v\right) = \phi_n^{nuc} + \phi_n^{coa} + \phi_n^{brk} . \tag{3-31}$$

In Eq.(3-30) the vapour interfacial mass transfer $\Gamma_v$ is assumed to be split into a nucleation part $\Gamma^N$ (which will be given by a model of wall nucleation) and another part $\Gamma^C$ representing the effect of phase change (vaporization and condensation) at the surfaces of the existing bubbles. The bubble number density transport Eq.(3-31) contains three source terms: ($ø^{nuc}$, $ø^{coa}$, $ø^{brk}$). Those terms corresponds to the bubble nucleation, coalescence and break-up phenomena respectively. Substituting Eq. (3-30) and Eq. (3-31) into Eq. (3-29) yields the following transport equation:

$$\frac{\partial A_i}{\partial t} + \nabla .\left(A_i \underline{V}_v\right) = \frac{2}{3} \frac{A_i}{\alpha \rho_v} \left[\Gamma_v^C + \Gamma_v^N - \alpha \frac{D_v \rho_v}{Dt}\right] + 12\pi \left(\frac{\alpha}{A_i}\right)^2 \left[\phi_n^{nuc} + \phi_n^{coa} + \phi_n^{brk}\right] \quad . \tag{3-32}$$

Now it is possible to regroup the two terms concerning bubble nucleation. If new bubbles are assumed to be nucleated at the SMD $d_{32} = 6\alpha/A_i$ the surface and the mass of a newly nucleated bubble reads to:

$$S = 36\cdot\pi\cdot\left(\frac{\alpha}{A_i}\right)^2, \qquad m = \rho_v\cdot 36\cdot\pi\cdot\left(\frac{\alpha}{A_i}\right)^3. \tag{3-33}$$

Therefore, it can be seen that the term proportional to $\o^{nuc}$ in Eq. (3-32) contains only one third of the IAC source term due to the bubbles nucleation, the two other thirds being contained in the term proportional to $\Gamma^N$ which can be rewritten as:

$$\Gamma_v^N = \phi_n^{NUC}\cdot m = \phi_n^{NUC}\cdot\rho_v\cdot 36\cdot\pi\cdot\left(\frac{\alpha}{A_i}\right)^3. \tag{3-34}$$

Regrouping these two terms, Eq. (3-32) becomes:

$$\begin{aligned}&\frac{\partial A_i}{\partial t} + \nabla\cdot\left(A_i\cdot\underline{V}_v\right) = \\ &\frac{2}{3}\cdot\frac{A_i}{\alpha\rho_v}\cdot\left[\Gamma_v^C - \alpha\cdot\frac{D_v\cdot\rho_v}{Dt}\right] + 12\cdot\pi\cdot\left(\frac{\alpha}{A_i}\right)^2\cdot\left[\phi_n^{coa}+\phi_N^{brk}\right] + \phi_n^{nuc}\cdot\pi\cdot d^{\,2}\quad .\end{aligned} \tag{3-35}$$

The IAC transport equation was presented like Eq.(3-35) by Yao and Morel (38). The advantage of the Eq.(3-35) is that the nucleation phenomenon clearly appears as a single term given by the product of the bubble number density source term $\o^{nuc}$ by the surface of a nucleated bubble. If for this particular term the SMD (d) is replaced by the bubble detachment diameter $d_d$ (for wall nucleation) the IAC is changed accordingly due to the fact that the newly nucleated bubbles often have a smaller diameter $d_d$ than the SMD (d). Bubble detachment diameter is calculated using Unal's correlation (see Eq.(3-42)). Closure relations must be proposed for the bubble number density source terms $\o^{nuc}$, $\o^{coa}$ and $\o^{brk}$. An example of such models is proposed by Yao and Morel (38).

## 3.5 Turbulent transfer terms

### 3.5.1 Eddy viscosity model - standard k-ε approach

The k-ε model describes energy processes in terms of production and dissipation, as well as transport through the mean flow or by turbulent diffusion. The Kolmogorov spectral equilibrium hypothesis also enables to predict a large eddy length-scale. On the other hand the anisotropy of the stresses is quite crudely modeled. First of all the eddy viscosity model (EVM) model assumes the Reynolds stress tensor is aligned with the strain rate tensor (Boussinesq approximation):

$$\underline{R}_l = \rho_l \cdot \nu_l^T \cdot (\underline{\nabla} \cdot \underline{V}_l + \underline{\nabla}^T \cdot \underline{V}_l) - \frac{2}{3} \cdot \underline{I} \cdot (\rho_l \cdot K_l + \rho \cdot_l \nu_l^T \cdot \nabla \cdot \underline{V}_l), \tag{3-36}$$

where I is the identity tensor, $K_l$ is the liquid turbulent kinetic energy and $V^l$t is the liquid turbulent eddy viscosity. The liquid turbulent eddy viscosity is expressed by the following relation:

$$\nu_l^T = C_\mu \cdot \frac{K_l^{\ 2}}{\varepsilon_l}, \tag{3-37}$$

where $C_\mu$ is a constant equal to 0.09. The turbulent kinetic energy $K_l$ and its dissipation rate $\varepsilon_l$ are calculated by using the two-equations K-ε approach.

## 3.6 Wall boiling model

Nucleate boiling term ($q_{wk}'''$), appears in Eq. (3-38) as a wall-to-fluid heat transfer term per unit volume and time. It is assumed that all applied heat is transferred to the liquid phase, hence the contribution to the vapour ($q_{wv}'''$) is zero. To model wall-to-fluid heat transfer at nucleate boiling a two-step approach is used. The two steps include calculation of the condition for boiling incipience in terms of critical wall superheat, according to the Hsu criterion (111), NEPTUNE_CFD theory manual (104) and calculation of heat flux partitioning. Following the analysis of Kurul and Podowski (112) the wall heat flux is split into three terms:

- A single phase flow convective heat flux $q_c$ at the fraction of the wall area unaffected by the presence of bubbles,
- A quenching heat flux $q_q$ where bubbles departure bring cold water in contact with the wall periodically,
- Evaporation heat flux $q_e$ needed to generate the vapour phase.

Each of these three phenomena is expressed by a heat flux density (per unit surface of the heated wall) which is related to the volumetric heat flux by the following relation:

$$q_{wl}''' = \frac{A_w}{V} \cdot q_{wl}'' = \frac{A_w}{V} \cdot \left(q_c + q_q + q_e\right), \tag{3-38}$$

where $A_w$ is the heated wall surface in contact to the cell having volume $V$, therefore $q_{wl}'''$ is expressed in W/m$^3$ and $q_{wl}''$ as well as $q_c$, $q_q$ and $q_e$ are expressed in W/m$^2$. The quantities $q_c$, $q_q$ and $q_e$ denote the heat flux densities due to liquid convective heat transfer, quenching and evaporation. The liquid convective heat transfer per unit surface of the heated wall is written as:

$$q_c = A_c \cdot h_{\log} \cdot \left(T_w - T_l\right) \ , \tag{3-39}$$

where $T_w$ is the wall temperature and $h_{log}$ is a heat exchange coefficient which is given by:

$$h_{\log} = \rho_l \cdot C_{pl} \cdot \frac{u^*}{T^+}, \tag{3-40}$$

in which $u^*$ is the wall friction velocity and $T^+$ is the non-dimensional liquid temperature. The velocity $u^*$ is calculated from the logarithmic wall law of liquid velocity in the wall boundary layer. The non-dimensional temperature follows a similar logarithmic profile.

The heat flux density due to quenching is written as:

$$q_q = A_b \cdot t_q \cdot f \cdot \frac{2 \cdot \lambda_l \cdot \left(T_w - T_l\right)}{\sqrt{\pi \cdot a_l \cdot t_q}}, \tag{3-41}$$

where $A_b$ is the wall fraction occupied by bubble nucleation, $f$ is the bubble detachment frequency, $t_q$ is the quenching time and $a_l$ is the liquid thermal diffusivity. The two fractions $A_c$ and $A_b$ are given by:

$$A_b = \min\left(1, n \cdot \pi \cdot d_d^{\,2} / 4\right) \ , \ A_c = 1 - A \ . \tag{3-42}$$

Here $n$ is the active nucleation sites density (per unit surface of the heated wall) and $d_d$ is the bubble detachment diameter. The active nucleation sites density is modelled according to Kurul and Podowski (112):

$$n = \left(210 \cdot \left(T_w - T_{sat}\right)\right)^{1.8}, \tag{3-43}$$

as a function of the wall superheating. The bubble detachment diameter is given by the correlation from Unal (113) . The Unal's correlation is valid for subcooled liquid but has been extended to saturated liquid. The bubble detachment diameter is given by:

$$d_d = 2.4210^{-5} \cdot p^{0.709} \cdot \frac{a}{\sqrt{b \cdot \varphi}}, \tag{3-44}$$

where p is the pressure and $a$, $b$ and $\varphi$ are given by the following relations:

$$a=\frac{\left(T_w-T_{sat}\right)\cdot\lambda_s}{2\cdot\rho_v\cdot\ell\cdot\sqrt{\pi\cdot a_s}}. \tag{3-45}$$

Here $\lambda_S$ and $a_S$ denote the wall conductivity and thermal diffusivity, $\varrho_v$ specifies the vapour density and $l$ is the latent heat of vaporization. In the modified correlation $b$ is given by:

$$b=\begin{cases}\dfrac{\left(T_{sat}-T_l\right)}{2\cdot\left(1-\rho_v/\rho_l\right)} & , \; St<0.0065\\ \dfrac{1}{2\cdot\left(1-\rho_v/\rho_l\right)}\cdot\dfrac{q_c+q_q+q_e}{0.0065\cdot\rho_l\cdot C_{pl}\cdot\left\|V_l\right\|} & , \; St>0.0065\end{cases}. \tag{3-46}$$

Where $\left\|V_l\right\|$ is the norm of the liquid velocity and St is the Stanton number which is defined by:

$$St\triangleq\frac{q_c+q_q+q_e}{\rho_l\cdot C_{pl}\cdot\left\|V_l\right\|\cdot\left(T_{sat}-T_l\right)}. \tag{3-47}$$

The quantity $\varphi$ appearing in Eq. (3-44) is given by:

$$\varphi=\max\left(1,\left(\frac{\left\|V_l\right\|}{V_0}\right)^{0.47}\right) \quad , \quad V_0=0.61m/s. \tag{3-48}$$

The quenching time and the bubble detachment frequency are modelled as:

$$t_q=\frac{1}{f} \quad , \quad f=\sqrt{\frac{4}{3}\cdot\frac{\vec{g}\cdot\left|\rho_v-\rho_l\right|}{\rho_l\cdot d_d}}. \tag{3-49}$$

The third heat flux density $q_e$ used for evaporation is given by:

$$q_e=f\cdot\frac{\pi\cdot {d_d}^3}{6}\cdot\rho_v\cdot\ell\cdot n. \tag{3-50}$$

To ensure a grid independent solution the liquid temperature $T_l$ in the wall boiling equations is calculated from the logarithmic temperature profile in a given non-dimensional distance from the wall $y^+ = 250$. This solution is proposed by Egorov and Menter (114). The reason is that at the center of the wall-adjacent cell high temperature and void fraction gradients are expected, which are strongly dependent on the nodalization. Taking into account the self-similarity the non-dimensional temperature profile in the wall boundary layer the temperature $T_l$ at $y^+ = 250$ reads to:

$$T_l(y^+ = 250) = T_w - \frac{T^+(y^+ = 250)}{T^+(y^+ = WC)} \cdot \left(T_w - T_l \cdot (y^+ = WC)\right) , \tag{3-51}$$

where the subscript *WC* denotes the wall-adjacent cell. This approach is valid only if the wall-adjacent cells remain in log region of the wall boundary layer ($30 < y^+ \leq 300$).

### 3.6.1 Boiling model extension for DNB modeling

The basic wall heat flux partitioning model assumes that the amount of water on the wall is sufficient to remove heat from the wall and to be used for evaporation. Superheating of the vapor that occurs at high void fractions is not modeled. Given all this the basic heat flux partitioning model cannot be used of CHF conditions. In order to take into account the phenomenon of temperature excursion at DNB conditions, the heat flux partitioning model can be generalized as follows:

$$q_{wall} = f_{\alpha 1} \cdot \left(q_f + q_q + q_e\right) + \left(1 - f_{\alpha 1}\right) \cdot q_v. \tag{3-52}$$

The fourth part of the wall heat flux, $q_v$, is the diffusive heat flux used to preheat the gas phase:

$$q_v = h_{wf,v} \cdot \left(T_{wall} - T_v\right) , \tag{3-53}$$

Where $h_{wf,v}$ is the wall heat transfer coefficient calculated from the temperature wall function for the vapour phase, $T_v$ is the vapour temperature at the centre of the wall-adjacent cell. $f_{\alpha 1}$ is the phenomenological function, which depends on the liquid volume fraction $\alpha_1$ and takes care for the numerically smooth transition between nucleate boiling regime and CHF regime. The generalized model assumes function $f_{\alpha 1}$ in the following form:

$$\alpha_1 > \alpha_{1,crit} : \quad f_{\alpha 1} = 1 - \frac{1}{2} \cdot e^{-20\left(\alpha_1 - \alpha_{1,crit}\right)}, \tag{3-54}$$

$$\alpha_1 < \alpha_{1,crit} : \quad f_{\alpha 1} = \frac{1}{2} \cdot \left(\frac{\alpha_1}{\alpha_{1,crit}}\right)^{20\alpha_{1,crit}} . \tag{3-55}$$

The extension of the wall-heat-flux-partitioning model was used to take into account the CHF condition. The local void fraction equal to 0.8 can be used as a criterion for the CHF occurrence. This value is close to the Weisman DNB criterion with the void fraction equal to 0.82 (115).

## 3.7 Wall function model for boiling flow

Two-equation eddy viscosity models are unable to predict steep gradients in the wall boundary layer. Hence, CFD codes commonly use classical logarithmic wall function to describe the velocity profile of the turbulent flow close to the wall. Mean velocity parallel to the wall and turbulent quantities outside the viscous sub-layer are expressed in terms of the distance from the wall. Such approach allows using relatively coarse computational grids near the wall. Due to the lack of experimental information and uncertainties associated with the two-phase flow the single-phase log-law is usually adopted also for description of the two-phase boundary layer.

At subcooled flow boiling the liquid velocity profile in the boundary layer is significantly disturbed by the bubble formation and detachment mechanisms on the heated wall. In literature, (116),(54),(34), and (117) an overprediction of liquid and gas velocity distributions in the boiling boundary region has been reported. The use of single-phase wall law may be one of the main reasons for these results.

Nevertheless, modeling of bubbly turbulent flow has been extensively investigated in the past years. Most model approaches have been developed for adiabatic bubbly flows, for example(118) and(119). Since the physics of bubble formation and dynamics is completely different in case of a boiling boundary layer the models developed for adiabatic bubbly flows cannot be straightforwardly applied to convective flow boiling.

In order to take into account the influence of boiling in the near wall area a modified logarithmic law of the wall was suggested by(120) and (121), which is usually used for turbulent flows over rough walls. It reads to:

$$u^{+}=\frac{1}{\kappa}-20\cdot\ln(y^{+})+B-\Delta u^{+}, \tag{3-56}$$

where $u^{+}=u_t/u_w$ , $y^{+}=\rho_l u_w \Delta y/\mu_l$ and $u_w=\sqrt{\tau_w/\rho_l}$ ($\tau_w$ is the wall shear stress). Here $u_t$ is the known velocity tangential to the wall and $\Delta y$ is the wall normal. Coefficients $\kappa$ and $B$ are standard single-phase constants with the values of 0.41 and 5.3. The last term represents the offset of $u^{+}$ due to the wall roughness and is given by:

$$\Delta u^{+}=\begin{cases}0; & k_r^{+}\le 11.3\\ \frac{1}{\kappa}\cdot\ln(1+C_{kr}k_r^{+}); & k_r^{+}>11.3\end{cases}. \tag{3-57}$$

($C_{kr}$=0.5 for sand-grain roughness) and $k_r^{+}$ is the so called roughness Reynolds number. $k_r^{+}$ is defined as:

$$k_r^+ = \frac{\rho_l \cdot k_r \cdot \sqrt{u_w \cdot u^*}}{\mu_l}, \tag{3-58}$$

Where *u** is defined by the means of the turbulent kinetic energy as $u^* = c_\mu^{1/4} k_l^{1/2}$. The roughness scale represented by $k_r$ is proportional to the void fraction and bubble diameter in the wall-adjacent cell:

$$k_r = \alpha \cdot d. \tag{3-59}$$

Near-wall values for turbulent kinetic energy $k_l$ and dissipation rate $\varepsilon_l$ can be specified by taking into account that the turbulent mixing in the boiling boundary layer is a predominant effect. Further, it can be assumed that the production of the liquid turbulent energy is equal to its dissipation ($\partial k_l / \partial y = 0$). Boundary conditions for $k_l$ and $\varepsilon_l$ are then defined in a similar way as for a single-phase flow in the form:

$$\varepsilon_l = \frac{u_w^3}{\kappa} \cdot k \cdot \frac{1}{y}, \qquad k_l = \frac{u_w^2}{c_\mu^{0.5}}. \tag{3-60}$$

# 4 Contribution to the NEPTUNE_CFD validation

During this step the familiarization with the code and its capabilities is achieved. The models explained in chapter 3 are applied to describe the two-phase flow. The most sensitive areas for a robust convergence are identified. The validation is focused on the NEPTUNE_CFD two-phase flow models for subcooled boiling and saturated boiling.

The validation contribution of the NEPTUNE_CFD code is made within the frame work of the NURISP. Previous validation was presented in the ASU, DEBORA and DEBORA-mixing experiments, which are focused on the turbulent and wall model validation of two-phase flow LWR relevant conditions. Some experiments provide local information on the temperatures. For instance the SUBO (122) or the Bartolomei (123) experiments are mainly focused on the subcooled boiling phenomena. Both deliver good data for the heat transfer model validation. Other notorious experiment is the TOPFLOW (124) with its wire mesh sensor is providing detailed data about the local bubble distribution what makes it suitable for multi size groups (MUSIG) model validation. From this group of candidates the PSBT (60) and BFBT (56) experiments are selected because they provide suitable data base, mainly VF measurements which are covering interesting operational conditions.

The test bench geometries of the PSBT and BFBT experiments are a single center isolated subchannel and a BWR full sized 8X8 rod bundle. The experiments are performed especially for PWR and BWR operational conditions. These facts make them the most indicated experiments to check the NEPTUNE_CFD capabilities. Furthermore, one of the BFBT exercises provides database not yet simulated with a CFD code: A turbine trip without bypass and a recirculation pump trip.

## 4.1 OECD/NRC benchmark based on NUPEC PWR subchannel and bundle test PSBT

### 4.1.1 Scope and description of the benchmark

The boiling phenomena inside the rod bundles of the nuclear reactor core are being widely investigated since many decades. Steam generation within the subchannels of the rod bundle is an important process to control e.g. during the operation of a BWR. Understanding the different parts of the boiling phenomena is basic to improve the mathematical-physics description in numerical codes that are used for design and safety evaluations. The first issue is the heat flux partition from the heated wall to the water or steam. It is necessary to define the beginning of the nucleation of the steam bubbles, the heat transfers across the interfacial area, the evaporation and the condensation into subcooled liquid. The momentum terms play an important role with the drag and non-drag forces acting on the bubbles. All the terms mentioned need a careful election. An important issue in this work is the selection of the bubble diameter and bubble departure diameter.

The VF of steam is strongly dependent on those parameters. The test bench of the PSBT experiment is shown in Fig. 4-1. The geometry described is a single isolated subchannel with a pitch of 8 mm between the walls of the rods. The subchannel has 4 electrically heated walls (Fig. 4-1), with a heated axial length of 1.55 m and a uniform axial power distribution. The test bench is electrically heated. Averaged VF data is provided over a cross sectional area located at 1.4 m distance from the bottom of the heated section. The experimental data are collected by a X-ray densitometer.

For the comparison six different experiments have been selected from the steady state void measurements test series 1 for the simulation with Neptune CFD. The main parameters of these tests such as power, inlet temperature, pressure, mass flow and subcooled liquid temperature are specified in Tab. 4-1. The code lacks of a steady state algorithm, thus a null transient is performed for those studies.

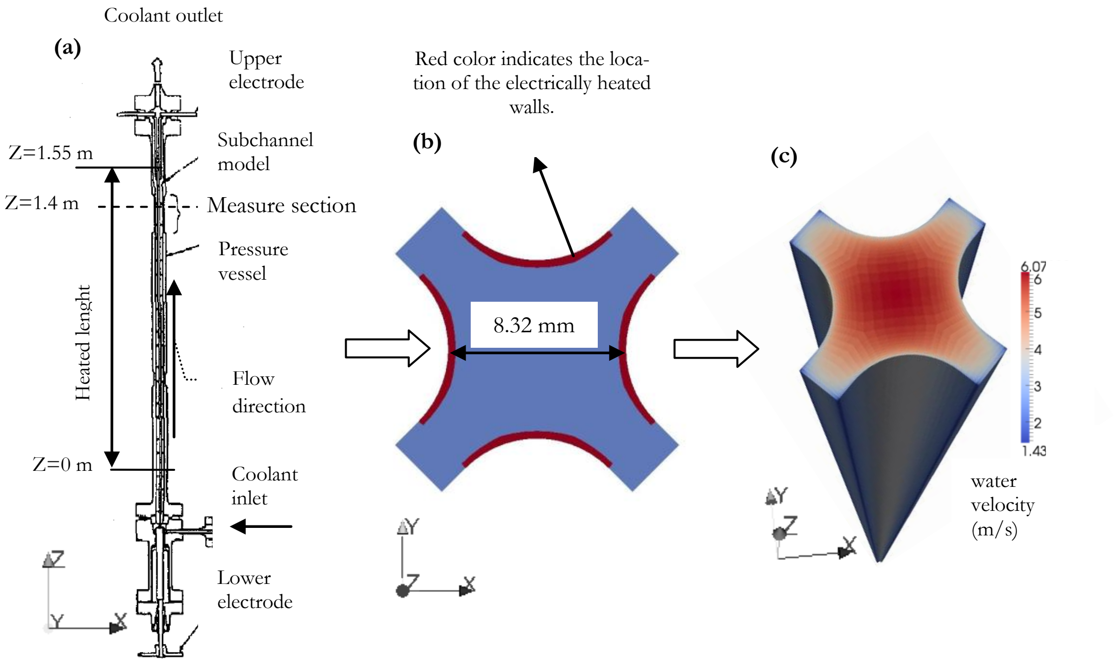
Coolant outlet
(a)
Upper electrode
Z=1.55 m
Subchannel model
Z=1.4 m
Measure section
Pressure vessel
Heated lenght
Flow direction
Z=0 m
Coolant inlet
Lower electrode
Z
Y
X
Red color indicates the location of the electrically heated walls.
(b)
8.32 mm
Y
Z
X
(c)
6.07
6
5
4
3
2
1.43
water velocity (m/s)
Y
Z
X

**Fig. 4-1. (a) Experimental set up of the PSBT benchmark with a cross sectional cut (b) illustrating where is the heat source. (c) Numerical model in NEPTUNE_CFD, calculated velocity field for case 1.2211.**

**Tab. 4-1. Test conditions for steady state void measurements test series 1**

| Run Num. | Heat flux (W/cm$^2$) | T. inlet (K) | Pressure (MPa) | ΔT(K) | Mass flow (kg/s) |
|---|---|---|---|---|---|
| 1.2211 | 194.34 | 568.4 | 15.01 | 46.9 | 0.3248 |
| 1.2223 | 150.72 | 592.6 | 15.01 | 22.6 | 0.3248 |
| 1.2237 | 129.56 | 602.6 | 15.03 | 12.9 | 0.3248 |
| 1.4325 | 129.13 | 526.8 | 10.03 | 57.6 | 0.1487 |
| 1.4326 | 129.77 | 541.8 | 10.01 | 42.4 | 0.1487 |
| 1.6222 | 107.75 | 477.2 | 5.0 | 59.9 | 0.1487 |

### 4.1.2 Applied models

Two-phase flow has been simulated in a subchannel of a rod bundle following the PSBT experiment specifications. The phases are described by the Eulerian approach with liquid as continuous phase and steam as dispersed phase. A single pressure field is shared by all phases. Momentum, energy and mass continuity equations are solved for each phase. The k-ε turbulence model for the liquid phase and local equilibrium turbulence model (55) for the dispersed phase has been applied together with a standard wall function adapted for two-phase flow. Steam/water properties from the system code CATHARE are applied which are based on the IAPWS data (125). The steam is set at saturation temperature by a constant time scale returning to saturation Eq.(3-18). The stream phase has a slip condition at the wall. The drag and non-drag forces explained in chapter 3 are applied to the simulation. The wall lubrication force is not estimated. When a boiling wall is present in the model this force can add an extra artificial quenching flux. Heat flux has been imposed as a boundary condition at the heated walls. The initial condition at the inlet is the water mass flow rate and a constant pressure at the outlet. Different phenomena must be described for the flow within the subchannel the incipient boiling condition, the wall heat partitioning, the heat exchange models and the selection of the bubble diameter.

### 4.1.3 Space discretization of the studied domain

The cross section of the nodalization geometry is illustrated in Fig. 4-2. The cells in the near wall region are thinner in order to describe the velocity and temperature gradients accurately. At those locations where the velocity is not expected to have sharp gradients the grid is coarser, as the center of the subchannel.

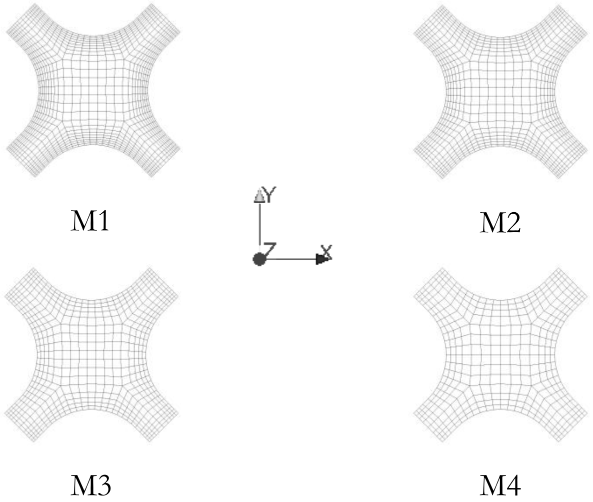

**Fig. 4-2. Cross section of the four proposed space discretization for the domain (M1, M2, M3 and M4).**

The cell size of in the near wall region could be problematic if the wall is heated. The VF there is high and the heat exchange model can overheat the liquid and the steam above saturation. Therefore, different spatial resolutions have been applied. Four different nodalizations are tested, all of them consisting of structured meshes in order to avoid diffusivity problems and to reduce the number of cells, see Fig. 4-2. The nodalizations have the same number of axial levels (176). Geometrical aspects of the spatial discretization are summarized in Tab. 4-2.

**Tab. 4-2. Discretization details of the four meshes applied in the study of the PSBT benchmark.**

| | Subchannel1 (M1) | Subchannel2 (M2) | Subchannel3 (M3) | Subchannel4 (M4) |
|---|---|---|---|---|
| Number of Cells | 182679 | 147429 | 112179 | 77345 |
| 1st cell near the wall (mm) | 0.1 | 0.2 | 0.3 | 0.4 |
| N. Cross Cells (X direction) | 25 | 21 | 17 | 14 |

## 4.1.4 Mesh sensitivity analysis.

The mesh sensitivity is quite high as seen in Fig. 4-3 and Fig. 4-4. Here the case 1.6222 has been simulated and a comparison between two different nodalizations has been made: (M1) and (M4). In Fig. 4-3 the axial VF profile in the near wall region is illustrated for both meshes. Fig. 4-4 describes for these two meshes the axial temperature profile of the water for two locations: in the near wall region and in the center of the subchannel. The biggest difference can be observed for the void generation near the wall. Where the refined mesh (M4) can easily fulfill with vapor the first cell in the near wall region, this phenomenon occurs for the coarse mesh (M1) too but for a higher location. In this case the difference can reach 0.5 meters. A finer mesh leads to an easy increase of the VF near the wall fluid interface while for coarse meshes this rise is shifted to higher axial elevations.

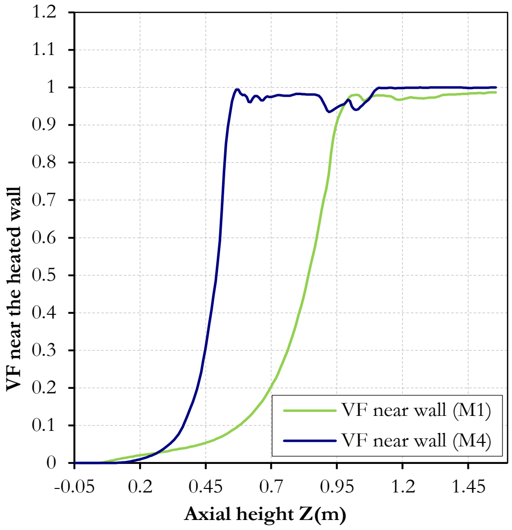

**Fig. 4-3. Axial VF profile in the near heated wall region for case 1.6222.**

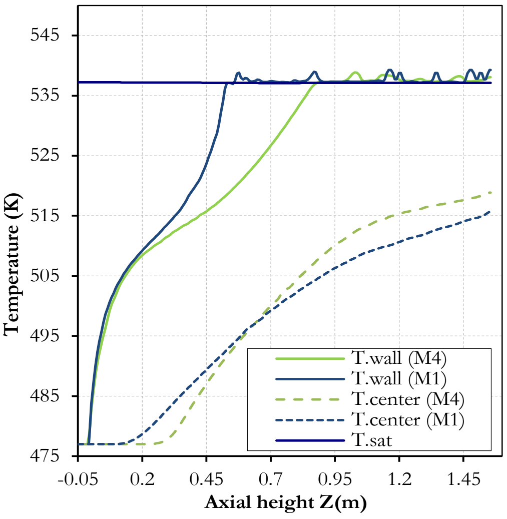

**Fig. 4-4. Axial water temperature profile in the near heated wall region and in the subchannel center for Case 1.6222.**

The heat flux partitioning at the wall is commonly divided in 3 fluxes according to Kurul and Podowsky (112). This model releases the heat flux from the heated wall into the water phase, then it is divided in evaporation, quenching and convective flux. Hence, the water phase receives all the heat flux. In the refined mesh (M4) this is problematic for the water, which cannot dissipate the heat fast enough; hence some small peaks appear in the water temperature once the cell has been filled with vapor (Fig. 4-4). This phenomenon is reproduced also in the coarse mesh but is not that severe. To solve it the wall heat flux is solved according to the 4 fluxes model described in chapter 3. Where the heat flux is redirected to the steam following a CHF criterion based on the void concentration on the near wall region. This measure can relax the water temperature but if the heat flux is high enough the problem is reproduced with the steam temperature.

The conditions of the run number 1.2211 have been selected to test the influence of the four purposed meshes on the CFD predictions. A constant bubble diameter of 0.1 mm has been set in the mesh analysis.

The location selected to visualize the local values of velocities and VF is illustrated in Fig. 4-1 (b), this is a 8.32 mm distance between heated walls at Z=1.4 m. In run 1.2211 the water/steam velocities for the different meshes are rather similar. For the refine mesh lower velocities are registered at the wall region, either for water or steam (Fig. 4-5 and Fig. 4-6), these velocities are calculated as an averaged value a node corresponding to a cell closer to the wall, for that reason at the wall the values are not zero. The steam velocity is slightly higher than the water velocities for the bulk (Fig. 4-6).

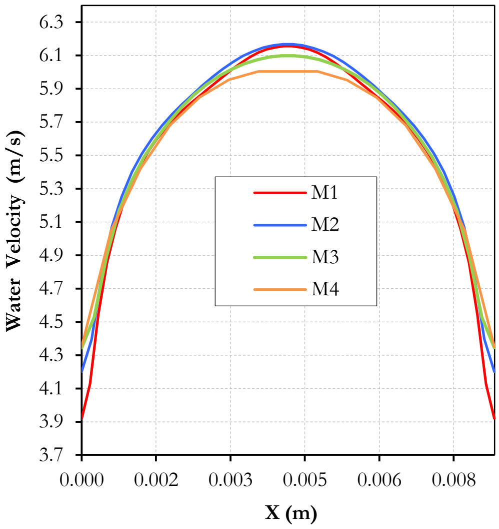

**Fig. 4-5. Water velocity in the near wall region at 1.4 m elevation. Four different meshes comparison, for 0.1 mm bubble diameter.**

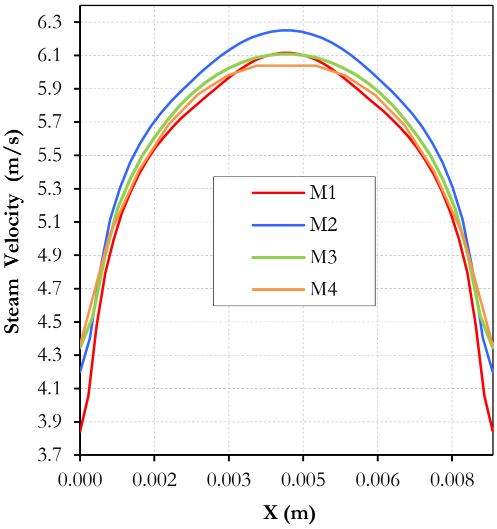

**Fig. 4-6. Steam velocity in the near wall region at 1.4 m elevation. Four different meshes comparison, for 0.1 mm of bubble diameter.**

The temperatures near the wall reach saturation for all cases as illustrated in Fig. 4-7. A coarse nodalization generates flatter profiles than finer meshes, especially regarding the void distribution calculation as shown in Fig. 4-8. Here, the steam production is higher for the smaller cells. The refined meshes (M1) and (M2) produce large gradients of VF in the near wall region. Those differences affects the average VF over the cross sectional area in the measurement position.

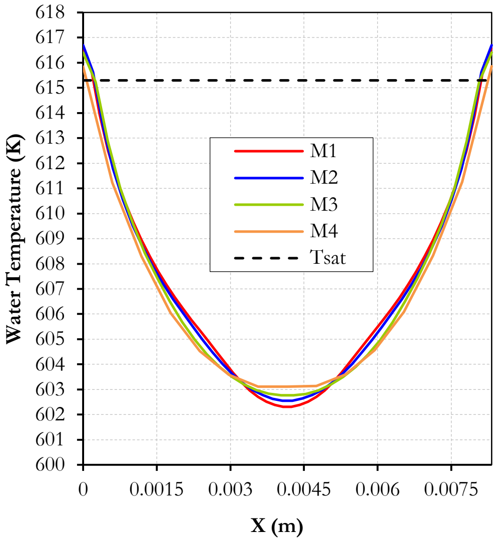

**Fig. 4-7. Water temperature in the near wall region at 1.4 m elevation. Four different meshes comparison, for 0.1 mm bubble diameter.**

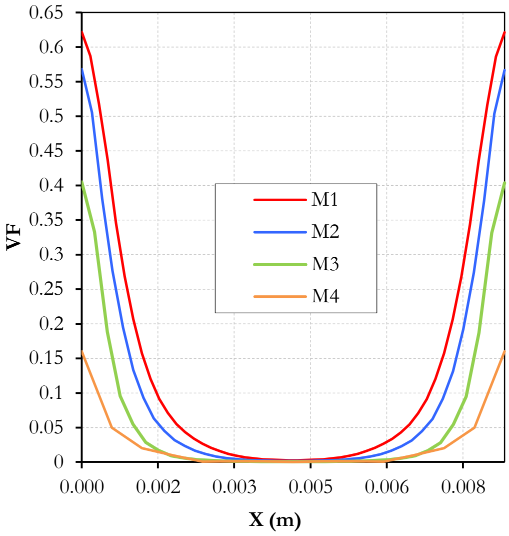

**Fig. 4-8. Local VF at 1.4 m elevation. Four different meshes comparison, for 0.1 mm of bubble diameter.**

The water temperature evolution for the different mesh configurations can be followed axially for two locations in Fig. 4-9. The first location is at center of the subchannel, the second is in near wall heated region (first cell near the wall). These two location are shown graphically in Fig. 4-10. At the center of the subchannel there are no big differences in the temperatures, only close to the outlet there are some deviations. In the near heated wall region locally the difference can reach 6 degrees between refined mesh (M1) and coarse mesh (M4).

The liquid temperature profile is the combination of several phenomena. The liquid phase near the wall is heated by the wall heat flux, which is divided in convective, evaporation and quenching heat flux. Once the bubbles are generated, they migrate and condense within subcooled liquid in the core of the flow and hence heat the liquid. The molecular and turbulent heat fluxes inside the liquid phase also modify the temperature profile.

In addition to the temperature evolution the VF local distribution for the purposed meshes is illustrated in Fig. 4-10.

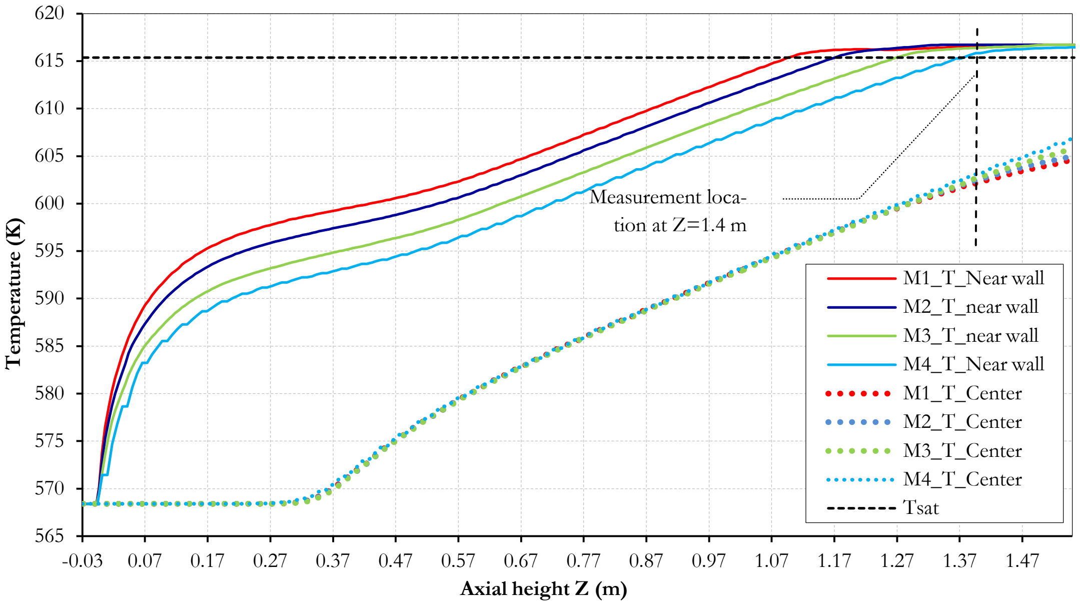

**Fig. 4-9. Water temperature at the near wall region and at the center of the subchannel of the case 1.2211. Comparison between 4 different meshes.**

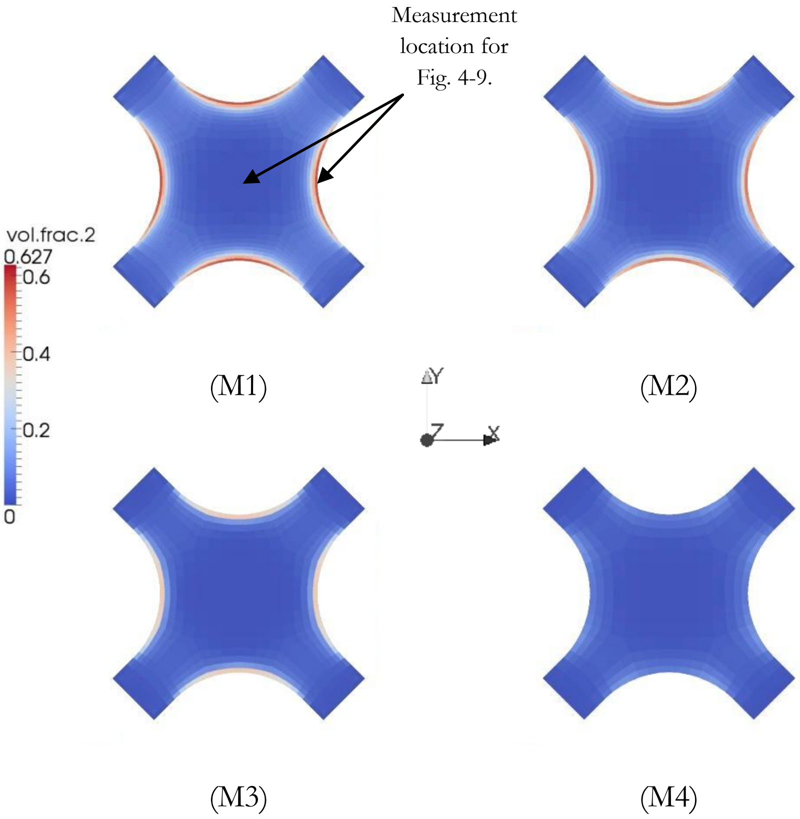
Measurement location for Fig. 4-9.
vol.frac.2
0.627
0.6
0.4
0.2
0
(M1)
(M2)
(M3)
(M4)
Y
Z
X

**Fig. 4-10. Local VF distribution predicted by NEPTUNE_CFD at the measurement location (Z=1.4 m) for the four purposed meshes. Results for case 1.2211.**

The results computed by NEPTUNE_CFD at the measure location (Z=1.4 m) are summarized in Tab. 4-3. The reference value for the case 1.2211 is 3.8 %. The three first nodalizations are over-predicting the average of VF and the last one is slightly under-predicting it. Nevertheless, this experimental value has an error of the 3% in the VF measured and is complicated to say which discretization provides better results.

**Tab. 4-3. Results for the local and averaged VF for the different meshes applied for the simulation of case 1.2211.**

| Mesh | Nearest heated wall cell VF (%) | Average VF (%) at measured cross section (Z=1.4m) |
|---|---|---|
| M1 | 67 | 8.1 |
| M2 | 57 | 6.7 |
| M3 | 40 | 4.6 |
| M4 | 15 | 3.1 |

The computational time for the coarse M4 mesh is around two hours, by applying more refined nodalization this time increases, reaching around seven hours of calculation for the mesh M1. Some of the cases selected to be simulated have rather high VF concentration on the measurement location e.g. case 1.4326 has a 53.1% VF. Case 1.6222 has a 30.6 VF concentration and as was illustrated in Fig. 4-3 the first cell near the heated wall is quickly fulfilled with steam. This amount of gas leads to overheating problems in the water and steam phase. The coarse mesh M4 can shift this negative effect in the water and steam temperatures to higher locations and in some cases avoid them. The election of the coarse mesh to perform the rest of the simulations has been made to preserve the numerical stability while solving the heat transfer problem. In addition, differences in the velocity prediction are rather small, with a relative difference in the velocity provided by M1 and M4 of the 3%. The coarse mesh (M4) is producing maximum $y^+$ values around 300, which makes it still valid for the application of the selected k-ε turbulence model

### 4.1.5 Bubble size sensitivity analysis

In the previous simulations a constant bubble diameter (0.1 mm) has been applied. Incidence of other bubble diameters or the selection of an IAE for the simulation is discussed in this subchapter. For the mesh M4 and the case previously studied 1.2211 three different configurations for the IAC are considered. The first is by applying the previous 0.1 mm constant diameter. In the second configuration the diameter is increased to 0.2 mm. The third applies one IEA, described in (3-32). The selection of the bubble diameter conditions the evolution of the simulation. Therefore, the VF at the measurement location varies depending on this parameter and different results can be obtained. Especially when the code is dealing with simulations where the main phenomena is subcooled boiling and low VF are expected.

For the three configurations purposed the water temperature in the near wall region is illustrated in (Fig. 4-11). Here, no big differences are appreciated. The local bubble size calculated by the IAE is shown by Fig. 4-12. The SMD calculated in this case is much lower, around 0.07 and 0.03 mm, compared with the other cases (0.1 and 0.2 mm). By calculating this small bubble size with an IAE, the IAC is higher compare to the other cases (0.1 or 0.2 mm diameter). As a consequence, the heat and mass transfer is higher and there are two important effects: First, the condensation into subcooled liquid is stronger, decreasing the VF within subcooled regions; Second, the boiling in the superheated near wall region is higher. These effects are illustrated in Fig. 4-13. Here, The VF profile illustrates that steam bubbles are nucleated at the heated wall surface and condense in the subcooled liquid in the core of the flow. Bigger bubbles (0.2 mm) don't condense so easily leading to a higher VF concentration in the bulk flow region. Concerning the impact of the bubble size in the steam velocity (Fig. 4-14) slightly higher velocities are registered for the steam in the case of 0.2 mm bubble diameter in the bulk region. This can be explained as a consequence of a higher VF concentration in this region.

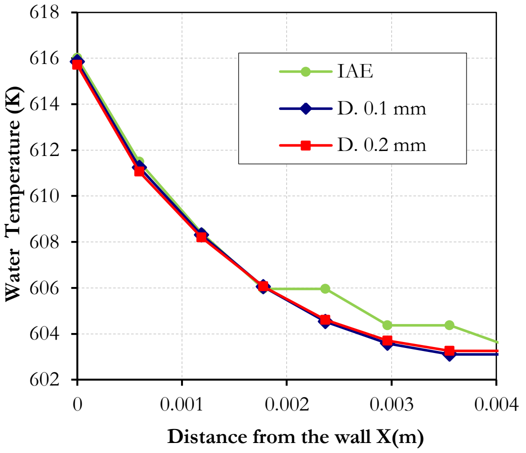

**Fig. 4-11. Water temperature in the near heated wall region at 1.4 m elevation. Comparison for different bubble diameters. Case 1.2211.**

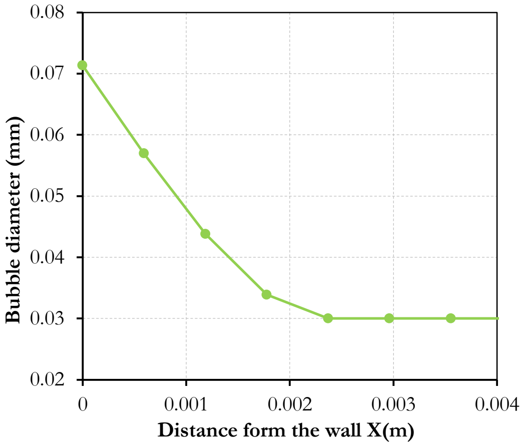

**Fig. 4-12. Bubble size distribution in case of using the IAE. Case 1.2211.**

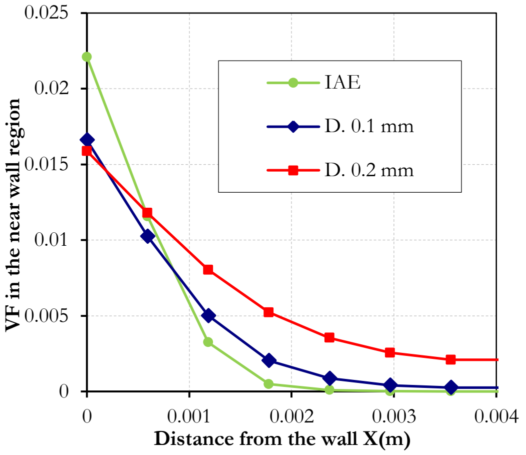

**Fig. 4-13. VF in the near heated wall region at 1.4 m elevation. Comparison for different bubble diameters. Case 1.2211.**

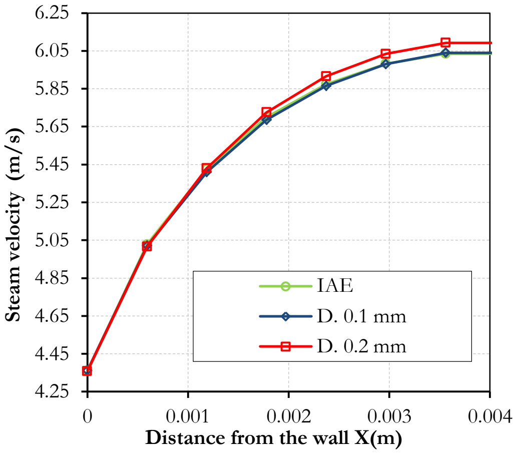

**Fig. 4-14. Steam velocity in the near heated wall region at 1.4 m elevation. Comparison for different bubbles diameters. Case 1.2211.**

In Fig. 4-15 the axial VF evolution in the center of the subchannel is shown. In the center of the subchannel the VF generated by the 0.2 mm bubbles is clearly higher due to the reasons previously explained. The void calculated by the IAE with bubbles of 0.03 mm of diameter is quite low due to the strong condensation into subcooled liquid.

Also the pressure drop in the channel is calculated for the different bubble sizes. The simulated results are presented in Fig. 4-16. Only the case predicted with the IAE exhibits higher values. In this case the concentration of bubbles in the near wall region is bigger leading to an increment of the pressure drop.

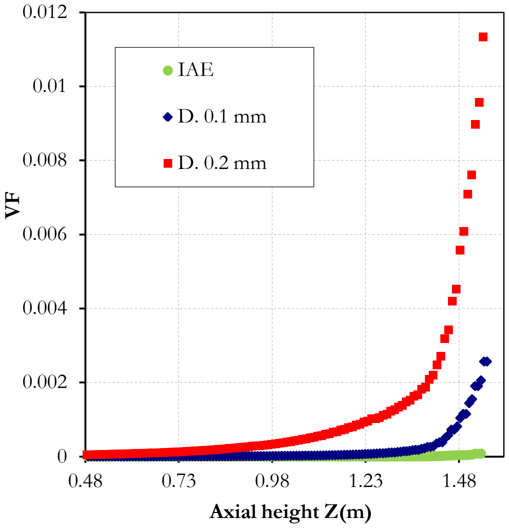

**Fig. 4-15. Axial VF profile at the center of the subchannel. Comparison for 3 different bubbles diameters. Case 1.2211.**

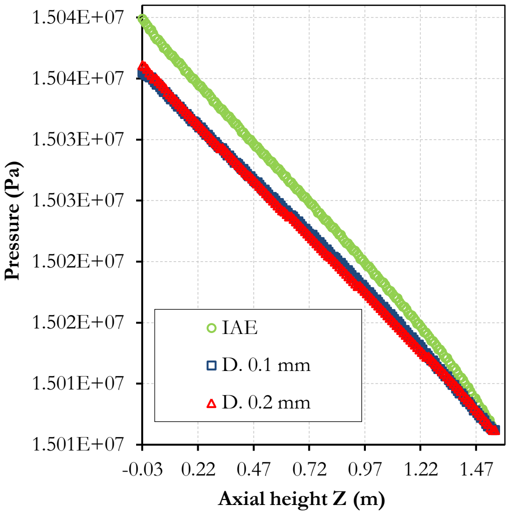

**Fig. 4-16. Pressure drop calculated for the 3 different bubble diameters. Case 1.2211.**

By using an IAE there are some more extra parameters to control. One of the most important measures is to clip the value of the minimum bubble diameter. A very small bubble sizes can lead to numerical instabilities regarding the non-drag forces applied like the added mass force or the turbulent dispersion force. For the simulations a smallest bubble diameter of 0.01 mm is allowed in the computational domain.

### 4.1.6 Selected results

The VF calculated by NEPTUNE_CFD at the measure position (Z=1.4 m) for the six cases selected from the PSBT database are illustrated in Tab. 4-4 together with the experimental measurements. These simulations have been performed with an IAE and the mesh M4.

Three experiments are overpredicted (1.2223, 1.2237, 1.2211) and the other three are underpredicted (1.4326, 1.4325, 1.6222) by NEPTUNE_CFD. In Tab. 4-4 the relative error between the experimental data and the computed results are shown. The simulations performed show a variation of the relative error from -34% to 36% compared with the measured PSBT data.

**Tab. 4-4. Computed of the VF measured and calculated by NEPTUNE_CFD**

| Run number | Experimental VF (%) | Computed VF (%) | Relative Error (%) |
|---|---|---|---|
| 1.2223 | 31.1 | 20.28 | -34.79 |
| 1.2237 | 44 | 31.85 | -27.61 |
| 1.2211 | 3.8 | 3.1 | -18.42 |
| 1.4326 | 53.1 | 58.89 | 10.90 |
| 1.4325 | 33.5 | 40.47 | 20.81 |
| 1.6222 | 30.6 | 41.62 | 36.01 |

The axial VF profile for each case is illustrated in Fig. 4-17, the experimental measure and its measurement error (3%) are also included. Computed results can also be analyzed in Fig. 4-18.

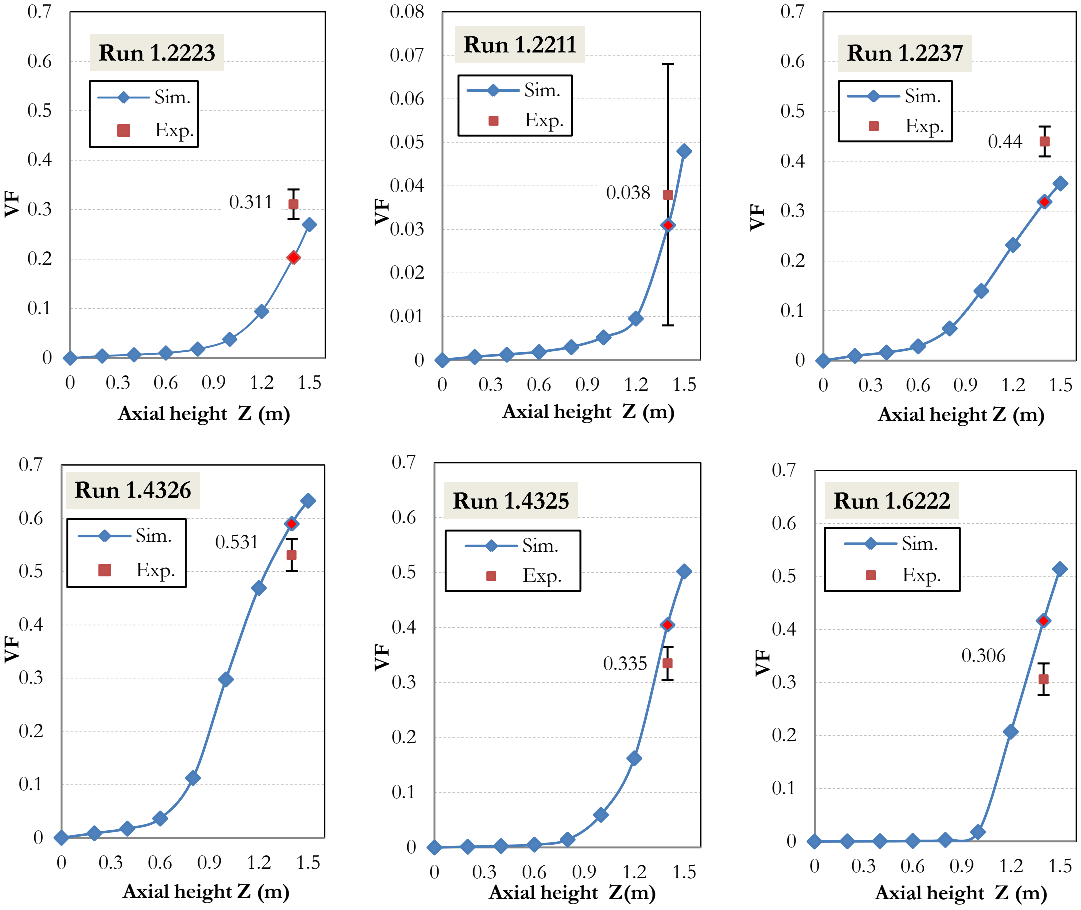

**Fig. 4-17. Axial VF evolution for each case compared against experimental data.**

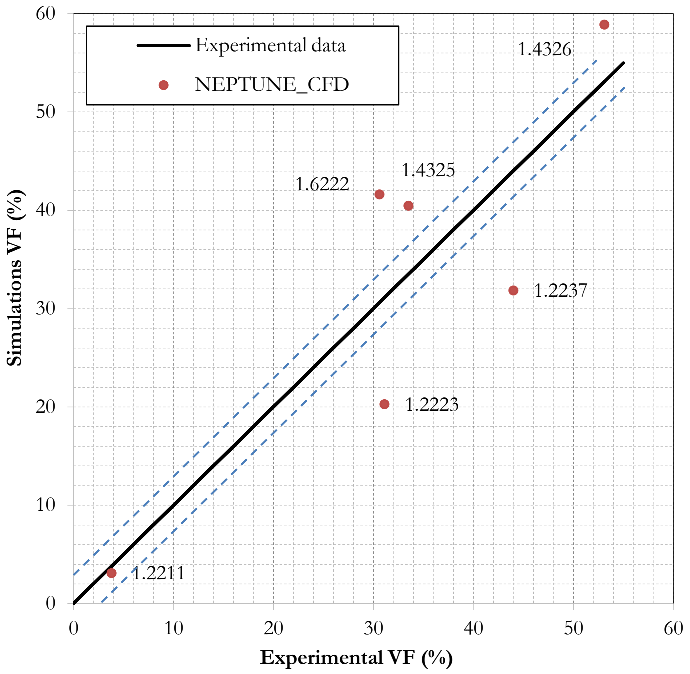

**Fig. 4-18. Deviation of the NEPTUNE_CFD simulations from experimental VF data.**

### 4.1.7 Summary and conclusions of the PSBT simulations

Six cases of the PSBT database are selected to be simulated with NEPTUNE_CFD. These experiments belong to the exercise 1 (steady-state single subchannel benchmark) from the Phase 1 (void distribution Benchmark). The test bench describes a single centered isolated subchannel. The information provided is averaged VF measurements at elevation Z=1.4 m.

The selected results computed show a deviation in the prediction of the experimental averaged VF data and a strong influence of the nodalization on the predictions. With the described physical models a relative good agreement with the experimental data is obtained for subcooled boiling conditions. The deviation from the experimental data grows as the conditions move from subcooled boiling to nucleate saturated boiling.

Since the refinement of the mesh plays an important role in the nucleated boiling, four nodalizations were tested with the reference case 1.2211. From the nodalization study it can be concluded that the finest nodalizations tend to overpredict the VF by generating sharp void gradients in the near wall region. The coarse space discretization generates less void in subcooled conditions, therefore underestimates slightly the experimental data. It was found that very refined meshes for boiling phenomena are problematic because of large steam gradients near the wall.

After a sensitivity study of the different nodalizations with the reference case 1.2211, the mesh (M4) has been selected to perform the rest of the simulations.

A study of the sensitivity to the bubble size has been performed applying two constant bubble sizes (0.1 and 0.2 mm) and a variable size with an IAE. This bubble size selection aims to investigate the behavior of the steam generation depending on these variables. where the main phenomenon is subcooled boiling. The heat exchange model is strongly influenced by the IAC. Bubbles may rise close to the heated wall and eventually depart from it and migrate into subcooled liquid were they condense. Smaller diameters produce more IAC and more condensation. Hence, for smaller selected bubble sizes, less void will appear in the domain. The smaller bubble size generated by the IAE produce more interface and thus the condensation is stronger and the void predicted is less compared with the other two bigger bubble sizes selected (0.1 and 0.2 mm).

The assumption of a single bubble size per cell has influence on the bubble mean size. If all bubbles have locally the same size they will condense at the same speed and their diameter will decrease. If a multi-size model is applied, the small bubbles will decrease and collapse rapidly leaving the bigger ones, which increase the mean bubble size. Therefore, the assumption of a single bubble size can lead to an underestimation of this bubble mean size in this case, affecting the void generation.

Local temperatures for the liquid in the near wall region can be overestimated, calculating values many degrees above the saturation temperature. The selection of the classical wall heat exchange model that decomposes the flux in three different terms releases all the heat flux into the liquid increasing its temperature. By applying the 4 flux model this situation can be mitigated only partially, since the steam temperature can suffer the same problems when the void concentration near the wall increases. The liquid temperature prediction problem can be fixed by increasing the near wall cell size more than 0.3 mm. By this way the $y^+$ values increases, it is important to maintain those values in a range according to the turbulence model selected. The turbulence model selected in this case is the two equation based k-ε. The wall-adjacent cells must belong to the log region of the wall boundary layer ($30 < y^+ \leq 300$) for this model to work properly. Other more sophisticate turbulent models have been tested, for instance a 7 equation model, but no convergence has been obtained, mainly because they require a near wall region discretization to reach $y^+$ values below 10.

## 4.2 The NUPEC BWR full size fine mesh bundle test (BFBT) Benchmark

### 4.2.1 Scope and description of the benchmark

The BFBT void distribution benchmark (56) was made available by the Nuclear Power Engineering Corporation (NUPEC). It this is one of the most valuable databases identified for TH modeling. The NUPEC database includes subchannel VF and critical power measurements in a representative (full-scale) BWR FA. The high resolution and high quality of subchannel VF data encourage advancement in understanding and modeling of complex two-phase flow in real bundles and make BFBT experiments valuable for the NEPTUNE_CFD multiphase models validation.

The benchmark consists of two parts: void distribution benchmark (Phase I) and critical power benchmark (Phase II). Each part has different exercises including simulations of steady-state and transient tests as well as uncertainty analysis. An exercise from phase I has been selected for the validation of NEPTUNE-CFD. The transient tests performed in the frame of this benchmark represent the TH conditions that may be encountered during a postulated BWR turbine trip transient without bypass and a recirculation pump trip. From this postulated transient scenarios important TH parameters are derived for the test such as the evolution of the pressure, total bundle power, mass flow, radial and axial power profile, etc. which serves as initial and boundary conditions for the CFD simulations. Many parameters measured during the tests are used as a reference for the code predictions.

In case of a turbine trip a pressure wave propagates from the steam line to the core due to the fast closure of the turbine stop valves and because the bypass valves remain closed. As a consequence the void in the core collapses improving the moderation of neutrons and hence leading to a sudden power increase. Due to the power increase the fuel temperature increases. Due to the increased absorption of neutrons in U-238 (Doppler effect) the power increase is stopped. Depending of the conditions of the main recirculation pumps the total power will be reduced and will stabilize at a lower power level. As long the recirculation flow is low in the core the power remains low and it will increase if the mass flow rate increases due to the improved moderation.

In case of a recirculation pump trip the physics is the same. If the mass flow decreases it leads to a decrease of the power due to a reduced moderation. After some seconds when the mass flow returns to nominal conditions the power recovers. As long as the recirculation flow is low the power remains low and it will increase if the mass flow rate increases due to the improved moderation.

The test section of the experiment is a full sized 8x8 BWR FA (Fig. 4-19), with sixty electrically heated rods (12.3 mm diameter, 16.2 mm rod pitch) and one water channel (34 mm diameter). The electrically heated section is 3708 mm high, the heaters are surrounded by an insulator (boron nitride) and by the cladding (Inconel 600). An X-ray densitometer is used to measure the averaged VF at three different axial levels from the bottom from the heated section (Z=0.67m, Z=1.72m, Z=2.7m). What the BFBT experimental data provides is the evolution in time of the averaged VF at the three axial levels mentioned.

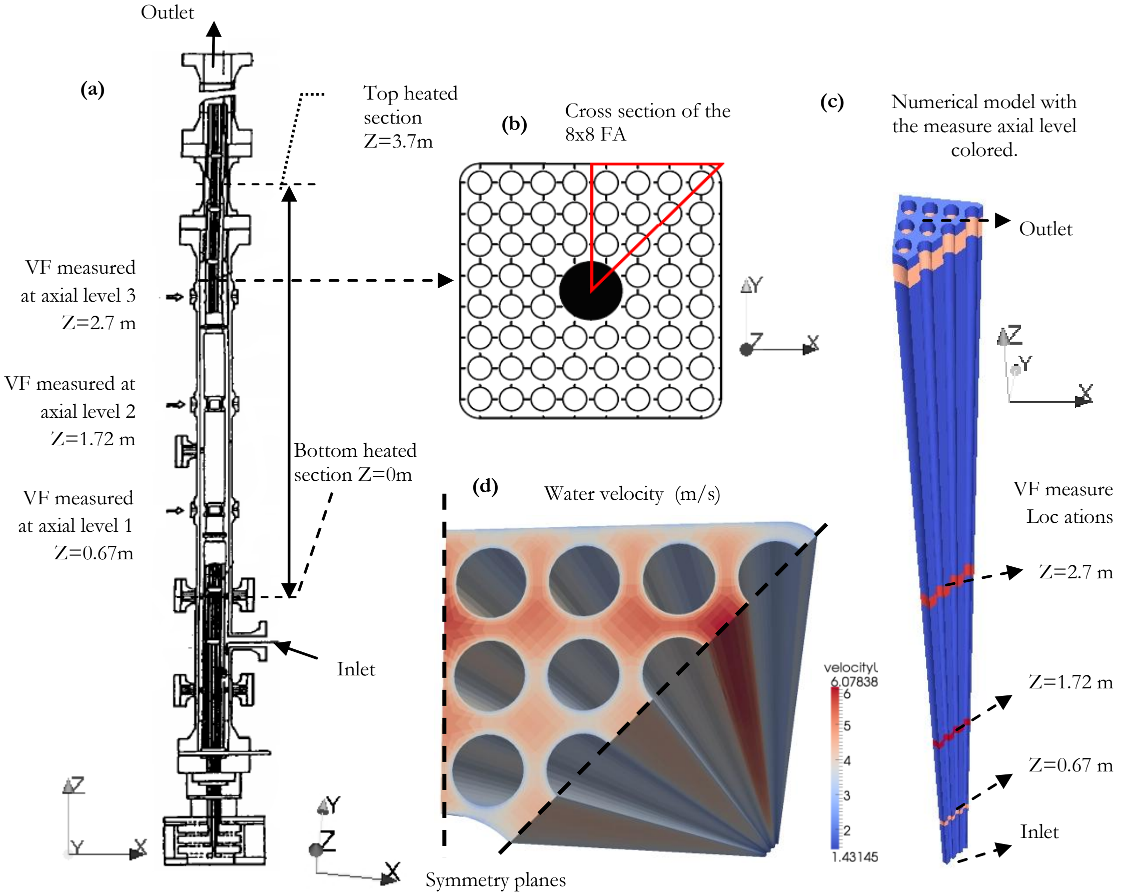
Outlet
(a)
Top heated section Z=3.7m
VF measured at axial level 3 Z=2.7 m
VF measured at axial level 2 Z=1.72 m
VF measured at axial level 1 Z=0.67m
Bottom heated section Z=0m
Inlet
Z
Y
X
Y
Z
X
(b)
Cross section of the 8x8 FA
Y
Z
X
(c)
Numerical model with the measure axial level colored.
Outlet
Z
Y
X
VF measure Loc ations
Z=2.7 m
Z=1.72 m
Z=0.67 m
Inlet
(d)
Water velocity (m/s)
velocityL
6.07838
6
5
4
3
2
1.43145
Symmetry planes

**Fig. 4-19. (a) Test bench with the location of the X-ray densitometers and the heated section. (b) Cross section of the tested rod bundle and the selected portion to be modeled. (c) Numerical model of the simulated domain. (d) Local water velocities of the domain calculated by NEPTUNE_CFD and location of the symmetry planes of the model.**

To reproduce in the test bench the turbine trip without bypass and the recirculation pump trip the BFBT database provides the evolution of the water mass flow rate the system pressure and the power. This data is used as boundary condition for the NEPTUNE_CFD. In Fig. 4-20, Fig. 4-21 and Fig. 4-22 the evolution of the outlet pressure, the mass flow rate and the power during the 60 seconds transient is given for both scenarios. The experiment was performed with a uniform axial power shape. The radial power shape is described by Fig. 4-23. The water inlet temperature remains constant at 552° K during the experiment.

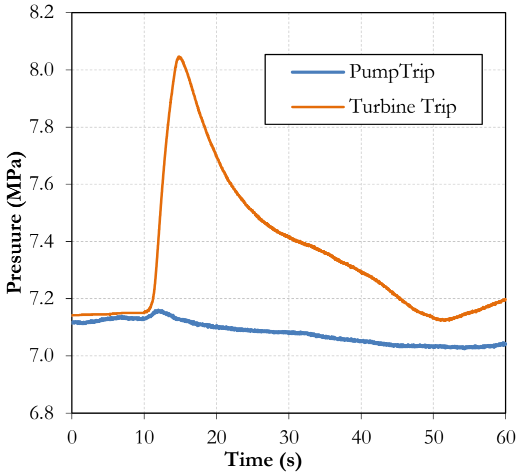

Fig. 4-20. Test bench outlet pressure measured evolution for turbine trip and recirculation pump trip experiment.

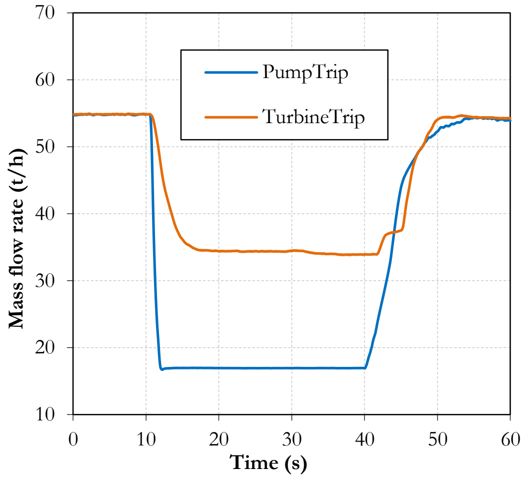

Fig. 4-21. Test bench mass flow rate measured evolution for turbine trip and recirculation pump trip experiment.

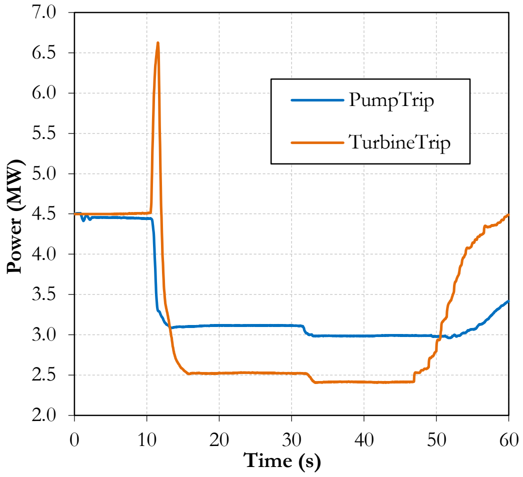

Fig. 4-22. Test bench measured power evolution for turbine trip and recirculation pump trip experiment.

| | | | | | | | |
|---|---|---|---|---|---|---|---|
| 1.15 | 1.30 | 1.15 | 1.30 | 1.30 | 1.15 | 1.30 | 1.15 |
| 1.30 | 0.45 | 0.89 | 0.89 | 0.89 | 0.45 | 1.15 | 1.30 |
| 1.15 | 0.89 | 0.89 | 0.89 | 0.89 | 0.89 | 0.45 | 1.15 |
| 1.30 | 0.89 | 0.89 | | | 0.89 | 0.89 | 1.15 |
| 1.30 | 0.89 | 0.89 | | | 0.89 | 0.89 | 1.15 |
| 1.15 | 0.45 | 0.89 | 0.89 | 0.89 | 0.89 | 0.45 | 1.15 |
| 1.30 | 1.15 | 0.45 | 0.89 | 0.89 | 0.45 | 1.15 | 1.30 |
| 1.15 | 1.30 | 1.15 | 1.15 | 1.15 | 1.15 | 1.30 | 1.15 |

Fig. 4-23. Normalized radial FA power coefficients for turbine trip and recirculation pump trip experiment in the context of the BFBT experiment.

### 4.2.2 Applied models

The numerical simulation is performed with the models explained in chapter 3. The two phase flow water/steam mixture is described by an Eulerian approach with liquid as continuous and steam as dispersed phase. A single pressure field is shared by all phases. Momentum, energy and continuity conservation equations are solved for each phase. A (k-ε) turbulence model for the liquid phase is used with the two phase modified wall function. Local equilibrium turbulence model (55) is considered for the dispersed phase. The libraries for the liquid properties are provided by the IAPWS data (125), furthermore steam close to saturation condition is assumed. For heat transfer through the gas/liquid interface a thermal phase change model is applied. The heaters are modelled in terms of a heat flux boundary condition. At the inlet, a mass flow rate is set and the pressure is imposed at the outlet. The temporal evolution of mass power and pressure are taken from the experimental conditions (Fig. 4-20, Fig. 4-21 and Fig. 4-22) The phenomena which will be described in the frame of this investigation are: the incipient boiling condition, the wall heat partitioning, the heat exchange between phases and the bubble diameter.

For the liquid to steam heat transfer two models are used, for the steam to liquid a time scale returning to saturation is applied Eq.(3-18). The two different heat transfers coefficients from the liquid to the steam are: the Astrid model described by (126) and the Ranz-Marshall model Eq.(3-15). The time step is adaptive depending on the Courant number. The time step width ranges form from 1 to 3 ms. The convergence criteria applied is $10^{-5}$.

The drag and non-drag forces: lift, added mass and turbulent dispersion force are computed for the simulation. Since the IAE requires a minimum bubble size two different values are chosen: 0.15 and 1 mm. To clip the minimum bubble size is important to avoid numerical problems in the calculation of the added mass or turbulent dispersion, these values can increase a lot if the bubbles are very small. Here, no dominant subcooled boiling phenomena is expected, for that reason two relative big minimum bubble diameters have been chosen.

### 4.2.3 Modeling of the rod bundle

Previous simulations performed for the PSBT experiment provided information about the proper nodalization geometry for this exercise. The nearest wall heated region cell has a constant width of 0.3 mm. The mesh is composed by 135 axial levels and 12 cross cells in each subchannel. Globally the NEPTUNE_CFD nodalization has 211928 cells. The maximum $y^+$ values are located close to the outlet. They oscillate between 300 and 400 depending on the transient conditions. These high values correspond to the high velocities locally achieved by the steam.

Taking into account the radial symmetry of the FA only 1/8 of the fluid domain is modeled with two symmetry planes (Fig. 4-19). This decision is taken although being aware that the radial power distribution has no axial symmetry according to Fig. 4-23 but bigger models penalize the computational time. For the initialization of the simulations the power is increased gradually from 0 to nominal values which are reached after 6 seconds. The simulations are conditioned by the large amount of void present in the domain. Numerical simulations find convergence problems in very refined meshes with boiling flow, especially with respect to the water and steam temperature close to the heated wall region. If the void concentration at the wall region is high the heat flux tends to overheat the steam. This can be mitigated by increasing the cell size.

To set the heat flux defined by the experimental measurements (Fig. 4-22) two different configurations are investigated. The first option is to locate the flux at the rod wall of the fluid domain using the NEPTUNE_CFD standalone, Fig. 4-24 (a). The second option is to model the clad and insulator of the test bench and place the heat flux at the inner diameter insulator surface, Fig. 4-24 (b). In both cases the power is set like a superficial heat flux (W/m$^2$). NEPTUNE_CFD is not able to solve the thermal problem for the solid domain by itself. It has to be coupled with the heat conduction tool SYRTHES (3).

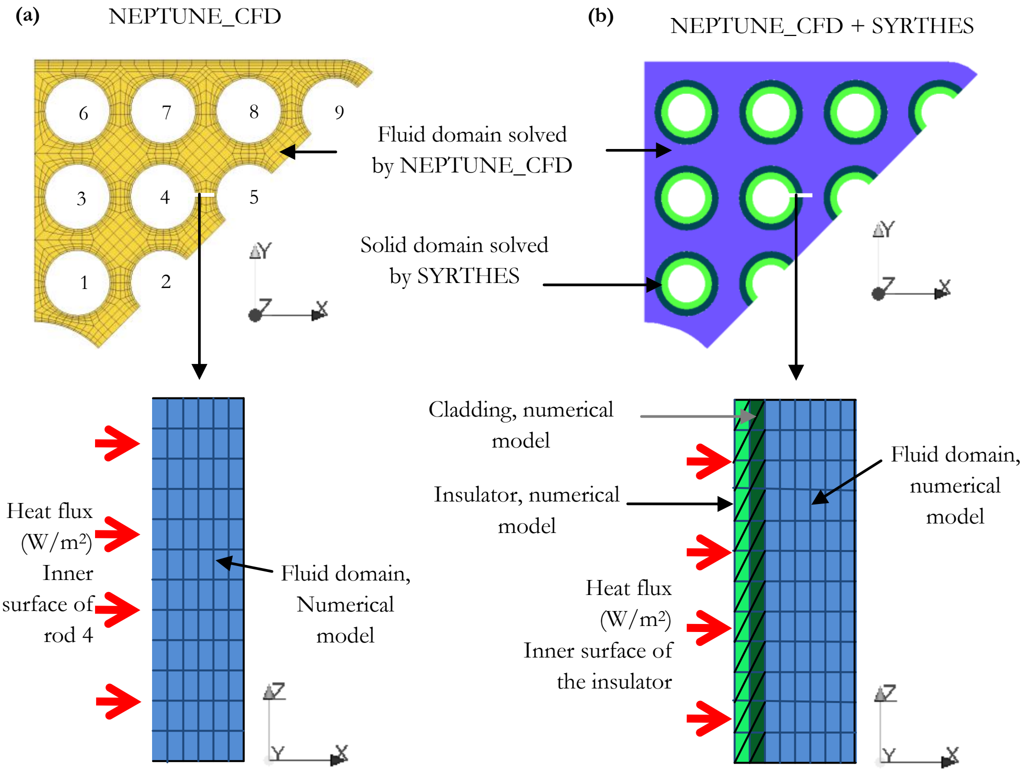
(a)
NEPTUNE_CFD
(b)
NEPTUNE_CFD + SYRTHES
6
7
8
9
3
4
5
1
2
Fluid domain solved by NEPTUNE_CFD
Solid domain solved by SYRTHES
Y
Z
X
Heat flux (W/m²) Inner surface of rod 4
Fluid domain, Numerical model
Cladding, numerical model
Insulator, numerical model
Heat flux (W/m²) Inner surface of the insulator
Fluid domain, numerical model

**Fig. 4-24. (a) NEPTUNE_CFD model. (b) NEPTUNE_CFD+SYRTHES model, green ring represent the insulator and the clad according to the real benchmark geometries.**

Tab. 4-5 summarizes the simulations performed, with the heat transfer coefficient (HTC) model selected for the liquid/steam interface and the minimum bubble diameter for the IAE. Furthermore, Tab. 4-5 points to the utilization or not of the SYRTHES code for the simulations. All these simulation have been performed taken as a boundary condition for the CFD code the experimental measurements (pressure, mass flow and power) provided by the BFBT database.

**Tab. 4-5. Performed simulations for the BFBT benchmark**

| Run Number | Min Bubble ø (mm) | HTC Model water/steam | SYRTHES |
|---|---|---|---|
| R1 | 0.15 | "Ranz-Marshall"/sat. | No |
| R2 | 0.15 | "Ranz-Marshall"/sat. | Yes |
| R3 | 1 | "Ranz-Marshall"/sat. | No |
| R4 | 0.15 | "Astrid"/sat. | No |

The averaged VF for the cross sectional area of the FA is calculated each 0.02 seconds at the three axial levels, (Z=0.67 m, Z=1.72 m and Z=2.7 m) from the bottom of the heated section. Fig. 4-19 shows the location of the measured sections.

Due to the complexity of the radial cell size distribution is not possible to conduct an arithmetic average of the VF in the measure section. The void predicted ($\alpha_s$) is weighted with the volume of the cell ($V_i$). This means that the alpha value of each cell ($\alpha_i$) is multiplied by the cell volume. This is done for all the cells (n) in the measured axial level, and finally it is divided by the total volume of the axial level ($V_s$), according to Eq.(4-2).

The original experimental measurements were consider not enough accurate and a correction factor has been proposed to be applied, see (127). $D_0$ is the original experimental data in percentage of void, and $D_1$ is the resulting data after the application of the correction factor. The new corrected data is obtained according to Eq.(4-1).

$$D_1 = \frac{D_0}{\left(-0.001 * D_0 + 1.167\right)} \quad , \tag{4-1}$$

$$\alpha_s = \frac{\sum_i^n V_i \cdot \alpha_i}{V_s} \quad . \tag{4-2}$$

### 4.2.4 Selected results for the turbine trip without bypass experiment

From the simulations performed the configuration R2 using NEPTUNE_CFD and SYRTHES and the HTC of Ranz-Marshal for the liquid/steam interface is selected to be analyzed. This problem configuration provides globally better VF predictions and local temperature calculations than the other configurations. The VF predictions of all tested configurations are included in annex A.

Fig. 4-25 illustrates with different figures the local VF distribution calculated by NEPTUNE_CFD and SYRTHES in the domain for different time steps during the transient: at second 7, at second 11.5 (during the maximum void concentration), at second 20, 30 and at second 50, where the combination of power and mass flow decreases the void to the minimum values of the simulation. Furthermore the location of the measured axial levels is shown.

The comparison between the evolution of the calculated mean void averaged calculated by NEPTUNE_CFD and SYRTHES and the experimental data is shown in by Fig. 4-26 for the three different axial levels, The experimental measurement error of the mean averaged VF (±2%) is also included.

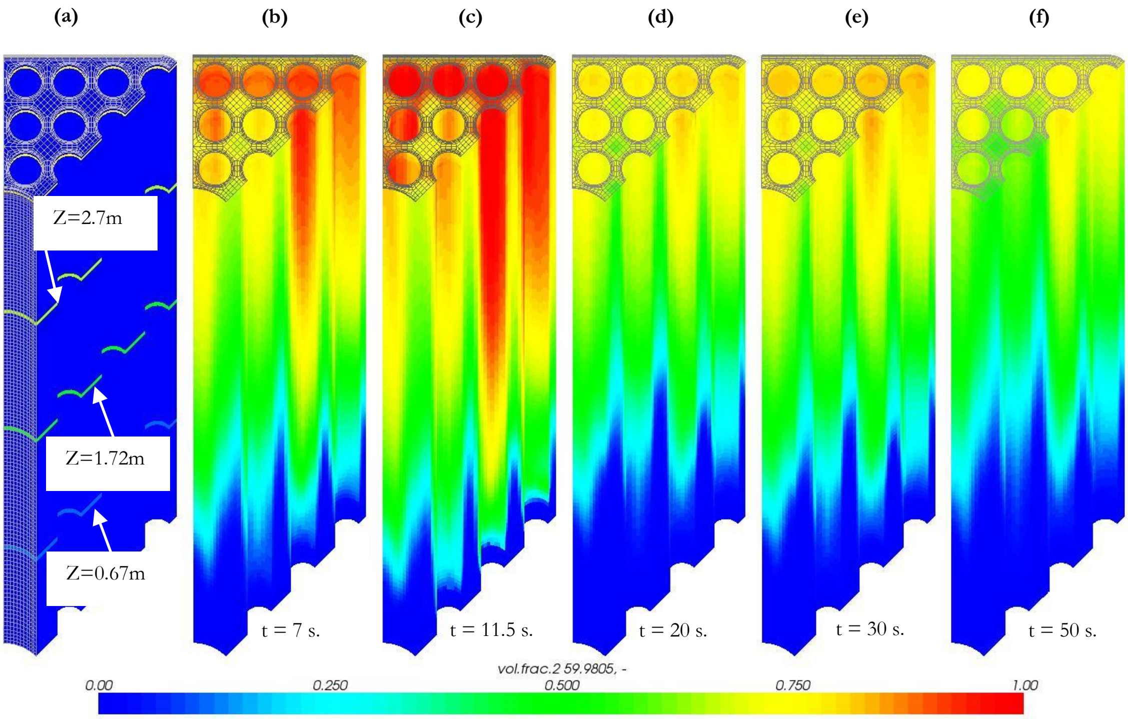
(a)
(b)
(c)
(d)
(e)
(f)
Z=2.7m
Z=1.72m
Z=0.67m
t = 7 s.
t = 11.5 s.
t = 20 s.
t = 30 s.
t = 50 s.
vol.frac.2 59.9805, -
0.00
0.250
0.500
0.750
1.00

**Fig. 4-25. (a) Location of the measured axial levels. Local VF distribution calculated by NEPTUNE_CFD at different times for the turbine trip without bypass simulation: (b) second 7, (c) second 11.5, (d) second 20, (e) second 30, (f) second 50.**

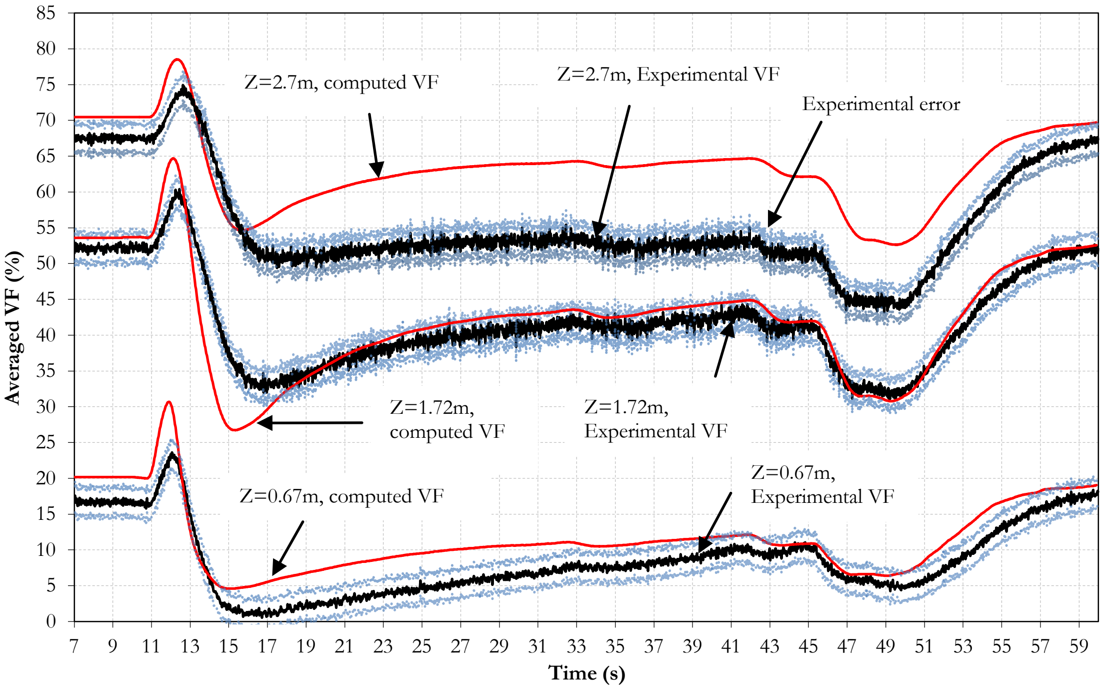

**Fig. 4-26. Comparison of the BFBT VF data and its measurement error (±2%) with the VF evolution predicted by NEPTUNE/SYRTHES at three axial levels during the turbine trip experiment.**

At this point is important to remark that the models implemented regarding interfacial interactions like mass, heat transfer and momentum are designed for bubbly flow only. The water is set as continuous phase and the vapor is set as the disperse phase, this condition is valid for bubbly flow. When the amount of void in the fluid exceeds 60%, the regime is no longer bubbly flow. Therefore, the results of the second and third elevation cannot be considered reliable and more developments in the modeling are necessary to properly describe the flow at those elevations. This is not an easy issue since the description of different flow regimes in the same domain requires the definition of a change of continuous and dispersed phase at each location. This is a challenging modeling but not the objective of this work. Nevertheless the code is able to trace the tendency of the void generation in line with the experimental data even in those flow regimes.

Fig. 4-27 illustrates the relative error of the computed VF against the measurements for the first axial level (Z=0.67m) together with the normalized values of the pressure mass flow rate and power of the transient. By this figure is possible to observe how the code struggles especially when the mass flow rate decreases. The code has a constant relative error around -10% during the rest of the transient.

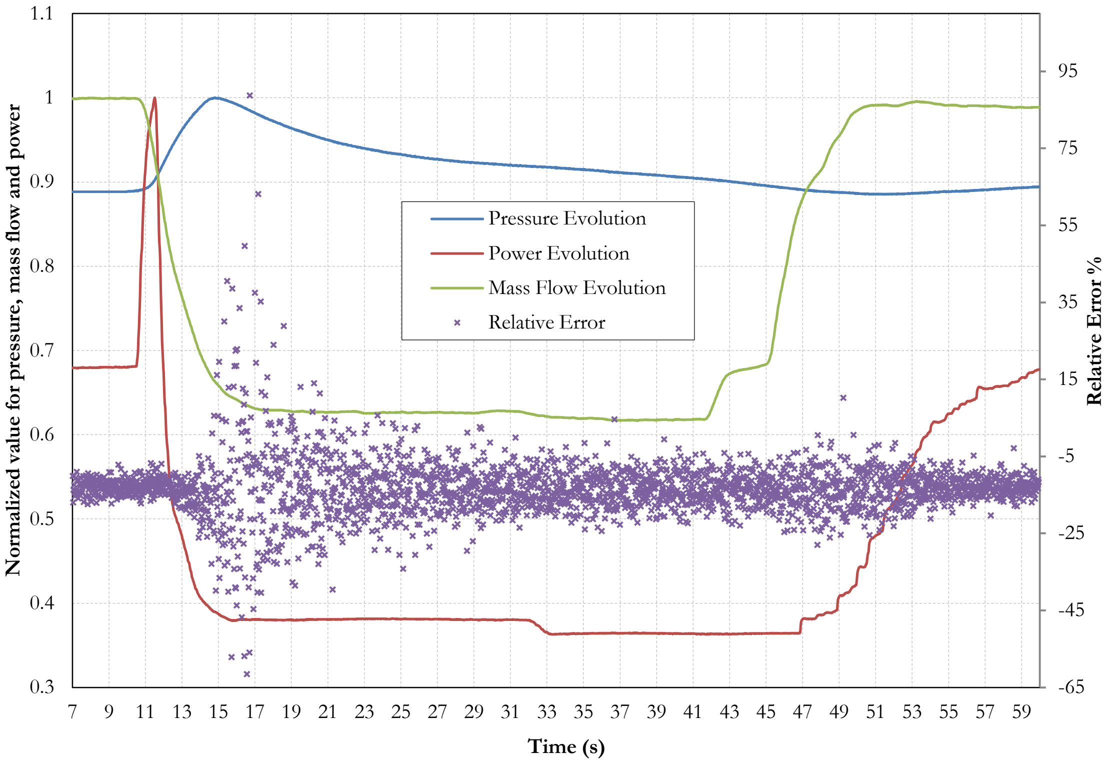

**Fig. 4-27. Normalized values of power, mass flow and pressure evolution provided by the turbine trip experimental data together with relative error between VF predicted by NEPTUNE_CFD/SYRTHES and experimental VF data at axial level Z=0.67m.**

The coupling of NEPTUNE_CFD with SYRTHES leads to a significant improvement due to the accurate steam temperature calculation. In Fig. 4-28 illustrates the evolution during the turbine trip simulation of the local temperatures of the water and steam together with the saturation and clad temperature. Those temperatures are taken from one point near the wall region of the rod 4 at the end of the heated section of the simulation R3, where the temperatures are expected to be the highest in the domain.

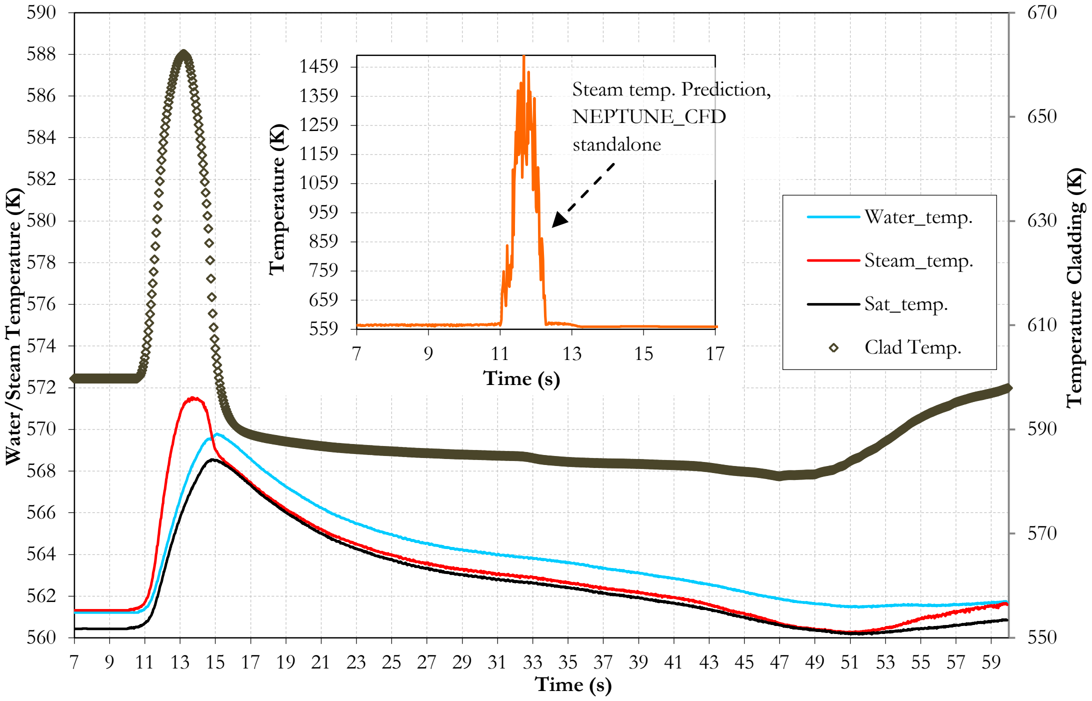

**Fig. 4-28. Saturation, steam, clad and liquid temperature calculated by NEPTUNE_CFD/SYRTHES. Comparison against the Steam temperature calculated with NEPTUNE_CFD stand alone.**

In simulation R3 by applying NEPTUNE_CFD and SYRTHES during the power peak the steam temperature remains as maximum at 3 degrees over saturation (red data), while in other simulations without solving the thermal wall problem (NEPTUNE_CFD standalone) this temperature can reach locally hundreds of degrees over saturation (orange data in Fig. 4-28), which is physically not correct. This originates from the heat flux is directly transferred into the fluid domain. On the other hand if the heat flux is defined at the insulator, the water and steam temperatures are calculated in a better way since SYRTHES is providing the wall temperature. Thus, the heat flux at the solid-fluid interface is calculated according to Eq.(4-3) with the wall and fluid temperature ($T_w$,$T_f$) and a heat transfer coefficient.

$$\varphi_w = \frac{\rho \cdot c_p \cdot u^*}{T^+} \cdot \left(T_w - T_f\right) . \qquad (4\text{-}3)$$

Where $u^*$ is the wall friction velocity, and $T^+$ is the non-dimensional liquid temperature. Hence the heat flux from the wall to the steam phase is regulated avoiding excessive overheating. The wall temperature increases at those locations with high VF. In Fig. 4-28, the local temperature jump between the wall and the liquid oscillate from 20 to 30 degrees during the transient and when the power peak occurs this difference rises up to 90 degrees.

### 4.2.5 Selected results for the recirculation pump trip experiment

In case of the recirculation pump trip the main models for the simulation are shown in Tab. 4-6. Using the experience acquired from the turbine trip simulations, the different parameters selected are: small minimum bubble diameter (0.15 mm), the Ranz-Marshal heat transfer coefficient for the liquid to the interface and the implementation of the SYRTHES code for the conjugated heat transfer. The boundary condition applied for the transient are taken from the experimental measurements of power mass flow and pressure (Fig. 4-20, Fig. 4-21 and Fig. 4-22)

**Tab. 4-6. Performed simulation for the pump trip experiment**

| Run Number | Min Bubble Size (mm) | H.T. Model water/steam | SYRTHES |
|---|---|---|---|
| R1 | 0.15 | "Ranz-Marshall"/sat. | Yes |

The comparison between the experimental data provided by the BFBT database and the computed VF of NEPTUNE_CFD/SYRTHES is illustrated in (Fig. 4-29).

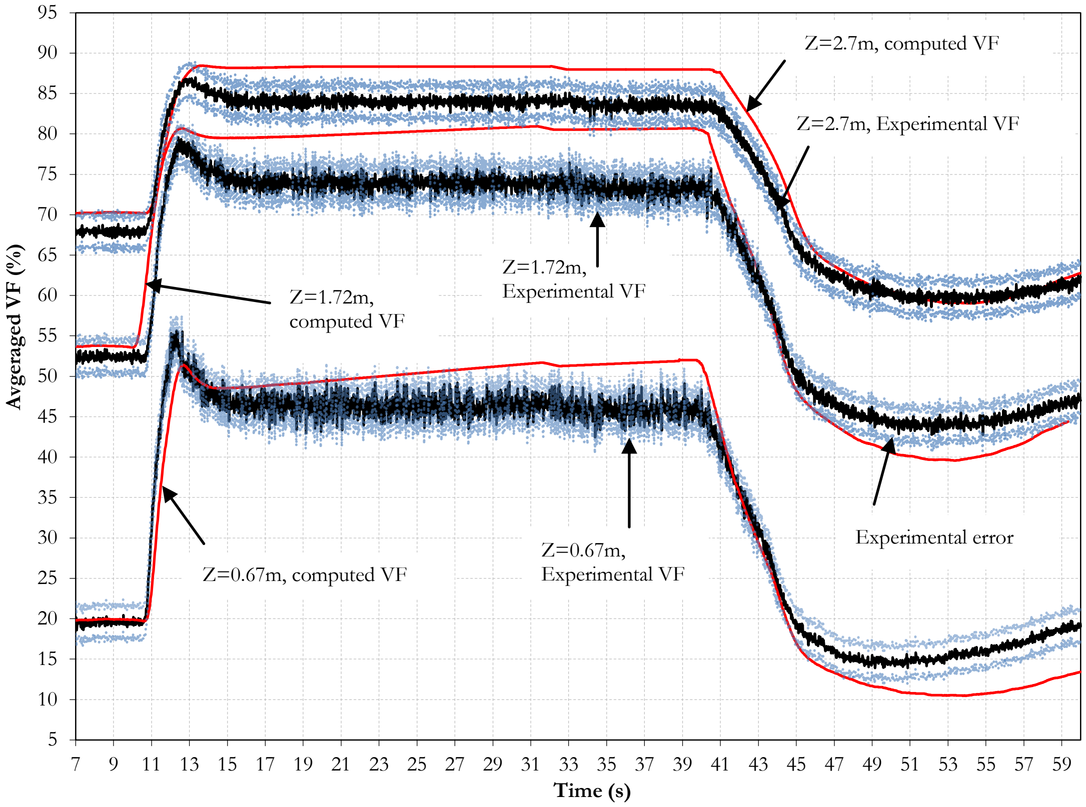

**Fig. 4-29. Comparison of the BFBT VF data and its measurement error (±2%) with the VF predicted by NEPTUNE/SYRTHES at three axial levels during the recirculation pump trip experiment.**

For this case the prediction fits well with the experimental data during the void increase between seconds 11 and 13. This time there is no power peak and the void rises due to the decrease of mass flow. At this point the simulation is underestimating the experimental data only at the first axial level. For the lapse of time between seconds 15 and 42 an over prediction occurs for all axial levels. At the last third of the transient when the mass flow increases up to nominal conditions the void predicted is slightly underestimated for axial levels 1 (Z=0.67m) and 2 (Z=1.72m), while for axial level 3 (Z=2.7m) a good agreement is achieved.

Fig. 4-30 shows the local liquid temperature distribution for the 3 axial levels of the measurements at second 30 of the recirculation pump trip simulation. For the first axial level the temperature is 3 degrees overheated in the near wall region and subcooled in the center of the subchannels. In upper locations the steam concentration in the near wall region is above 80 % (Fig. 4-31) and all the heat flux is transferred into the steam decreasing the liquid temperature.

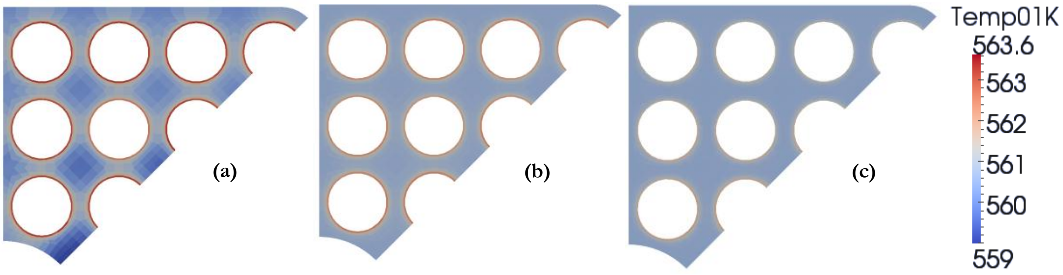

**Fig. 4-30. Local water temperature at 3 different axial levels, (a) 0.67m, (c) 1.72 m and (c) 2.7m. Calculated by NEPTUNE_CFD/SYRTHES for the recirculation pump trip (second 30).**

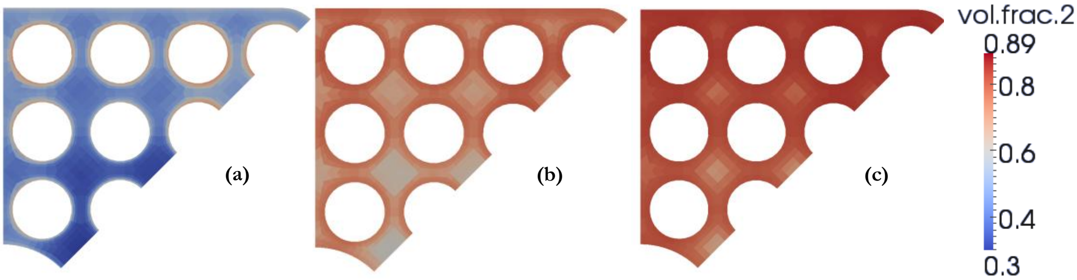

**Fig. 4-31. Local void distribution at 3 different axial levels, (a) 0.67m, (c) 1.72 m and (c) 2.7m. Calculated by NEPTUNE_CFD/SYRTHES for the recirculation pump trip (second 30).**

In Fig. 4-32 the local temperature evolution is shown for two locations: the near wall region and the bulk of the fluid in the center of one subchannel. Both locations are Z= 3.69 m high from the beginning of the heated section. The biggest deviation from saturation takes place for the steam temperature in the near wall region. It can reach locally 17 degrees more than saturation. This steam temperature has different values by decreasing the time scale returning to saturation, Eq.(3-18). This time scale should be lower than the time step to work properly. In the figure the red data represent a time scale of 0.05 seconds, while the blue data is a time scale of 1 ms. The temperature difference between those two settings is about 10 degrees. The lower time scale helps to maintain the steam temperature close to saturation in the near wall region. The temperature of the liquid in the near wall region is slightly over saturation and it is not affected by the different time scales of the steam heat transfer coefficient. This parameter is not affecting significantly the steam generation or the temperature of the steam and the liquid at the bulk region which remains at saturation.

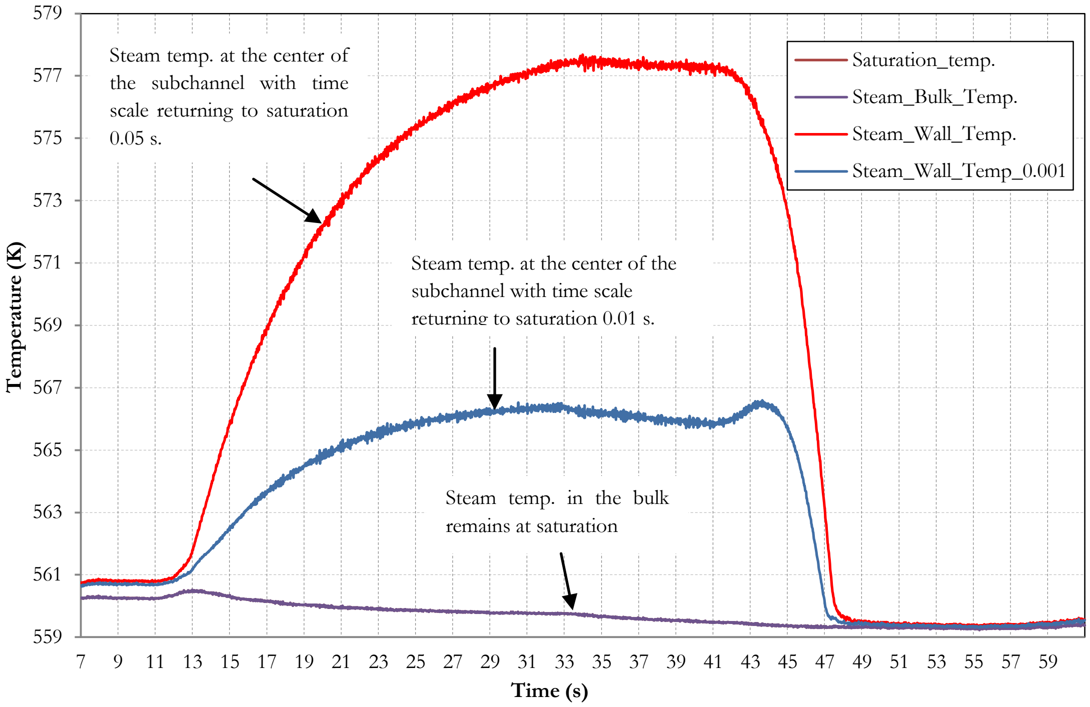

**Fig. 4-32. Local steam temperatures evolution at the bulk and near the heated wall calculated by NEPTUNE_CFD/SYRTHES during the recirculation pump trip. Comparison of two different time scales returning to saturation for the steam.**

### 4.2.6 Summary and conclusions on the BFBT simulations.

This work is a contribution to validate the two phase flow models of NEPTUNE_CFD for the conditions that may occur during a turbine trip without bypass and a recirculation pump trip transients. A wide range of averaged VF is calculated, from single phase flow to values up to 83 %. By adding to the momentum equation the source terms of the mass added, lift, wall lubrication, turbulent dispersion and drag force, the bubbly flow regime is assumed. The drag coefficient is calculated assuming spherical shape of the bubbles. The water is defined as continuous phase and the steam is assigned as dispersed phase. The description of different flow regimes such slug or annular flow or the transition between them is still an open issue for the CFD codes. The assumption of only one kind of flow regime might be one of the reasons for the deviation from the experimental data, therefore only the results of the first axial level (Z=0.67m) were bubbly flow happens are taken into account.

The improvement area is located mainly at the evaporation modeling. The increase of power generates more VF than expected and quite rapidly (see Fig. 4-26). The steam must be set as compressible. The high steam generation makes this condition mandatory, otherwise the pressure field is not solved properly during the power peak of the turbine trip simulation (Fig. 4-20) and the simulation doesn't reach convergence. If one time step is not converged it is repeated and the second order scheme for the velocities and VF change to first order upwind scheme to ensure the convergence. The quick change of the boundary conditions due to the power peak forces the code to repeat a very few time steps.

Reliability and accuracy of the predicted results usually depend on the implemented constitutive relations for interfacial transfer. Different heat transfer models available in NEPTUNE_CFD have been used and compared. A sensitivity analyses was performed by using two different heat transfer models for the liquid to the steam interface This comparison is illustrated in annex A, the results exhibited in this chapter only apply the Ranz-Marshall model.

The coupling NEPTUNE_CFD with SYRTHES has been applied in this work and its capabilities tested. The different location definition of the heat flux as boundary condition by solving or not the thermal inertia of the solid walls has a strong influence on the simulation. Local temperatures and VF predictions have sensitivity to these changes. This exercise provides useful information about the capabilities of SYRTHES and its strengths working together with NEPTUNE_CFD.

A very refine mesh can make the simulation problematic. In addition to the recommendation of the cell size near the wall of the previous PSBT conclusions, it is important to point out the problems of setting a very refined axial nodalization. The code has problems calculating the pressure field if there are an excessive number of axial levels. It is better to enlarge the cells in the axial direction in the locations where large amounts of steam are generated.

The treatment of the flux in the heated wall with boiling phenomenon is complex and after the experience acquired with the PSBT and BFBT simulations the next lessons can be addressed. By using very refine meshes in the near wall region the classical 3 fluxes approach exchange the heat flux into the water for the three contribution fluxes: quenching, convection and evaporation. If boiling occurs in this region and the amount of liquid decreases, the enthalpy rises and the water can be several degrees above saturation temperature. To avoid this problem the four flux model decomposition, see Eq.(3-52), transfers all the heat flux into the steam when the void is above the 80 % in the near wall region (condition frequently present near the wall). With this measure the liquid temperature remains close to saturation but now the steam temperature can be locally many degrees above saturation temperature in the near heated wall region if the flux is quite high.

The mesh refinement plays unfortunately an important role in the results. Local refinement can lead to an overheating of the steam, especially when the wall heat flux is set as a boundary condition. During the power peak of the turbine trip, the superheat of steam is several hundred degrees (Fig. 4-28), this happens because heat transfer model set for the steam (a constant time scale returning to saturation) is not able to keep the steam at saturation temperature. To mitigate this issue the cell volume has to be increased by making a coarse mesh. Furthermore, the calculation of a HTC of the wall-fluid interface helps in the temperature regulation. To calculate this HTC, NEPTUNE_CFD has to be coupled with the heat conduction solver SYRTHES. The interaction between codes allows the calculation of the wall-fluid HTC taken into account local TH parameters. In addition the wall thermal inertia effect of the cladding and insulator is taken into account by SYRTHES. These measures make the steam temperature remain close to saturation even during severe power peaks, leading to a better temperature prediction.

# 5 Coupling methodology

## 5.1 Introduction

In this chapter the coupled solution between the different codes involved is presented. The coupled solution NHESDYN is described in detail with all the internal steps. The communication tool applied is the message passing interface (MPI), all the MPI commands for the communication are described in annex B. The main parts of the chapter are: first, a brief introduction about how the codes work together (general coupling scheme). Second part summarizes how is each program is executed (time advancement) for steady state and transient cases. The last subchapter is devoted to the explanation about the information exchange (mapping scheme).

Fig. 5-1 shows a simplified communication scheme to understand the main information path ways exchanged during time step. This exchange has several stages:

- The SYRTHES code receives the information of the volumetric heat flux from DYN3D_SP3.
- The fuel temperature gradients plus gap and cladding heat conduction are solved.
- The heat flux is transferred from the cladding to the fluid domain, solving the conjugated heat transfer, between TH codes.
- The NEPTUNE_CFD code calculates the temperatures, pressure, IAC and velocities of the fluid.
- DYN3D_SP3 updates the cross sections by taking the information of the Doppler temperature (calculated by SYRTHES) and moderator temperature and density (calculated by NEPTUNE_CFD).

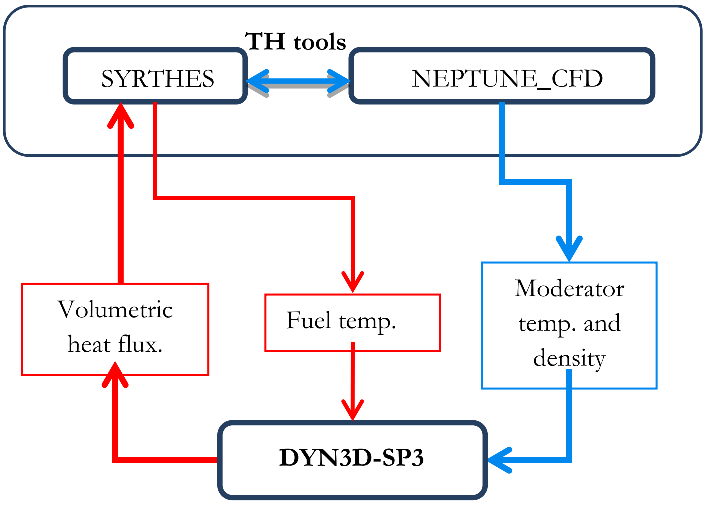

**Fig. 5-1. Simplified communication scheme for the coupled solution NEPTUNE_CFD/ SYRTHES/DYN3D_SP3.**

Finally the power calculated by the NK code is delivered to the SYRTHES code to restart again the process. This methodology is repeated each time step. The codes involved have to wait for the information generated by its predecessor to start the calculation and each code is normally executed one time, respecting the time linearity. This kind of time hierarchy in the coupled solutions is called explicit. The solution can be considered a combination of external and internal coupling. The heat conduction solver SYRTHES is coupled in NEPTUNE_CFD by means of a semi implicit approach. Therefore the TH tools are considered as one. The combination of NEPTUNE_CFD/SYRTHES performs an external coupling with the NK tool.

The coupled solution between the NK code Dyn3D_SP3 and TH codes SYRTHES and NEPTUNE_CFD is an explicit approach. The information is exchanged at each time step, once each program has finished its task.

## 5.2 General coupling scheme

A general overview about when and how the codes exchange the information is elaborated in this subchapter. It is necessary to create MPI groups with the codes for the first step of the communication. A general scheme concerning the group distribution of the different codes is shown by Fig. 5-2. This scheme defines the direct dependencies between the two TH codes involved and the NK code with the main program. The amount of information to deal with is high and to work with three different outputs is tedious. To unify the information provided by the codes an extra program is used. It is called NHESDYN. It is FORTRAN programmed and it was developed to control the timing for the coupled solution and to inform about the ongoing of the simulations.

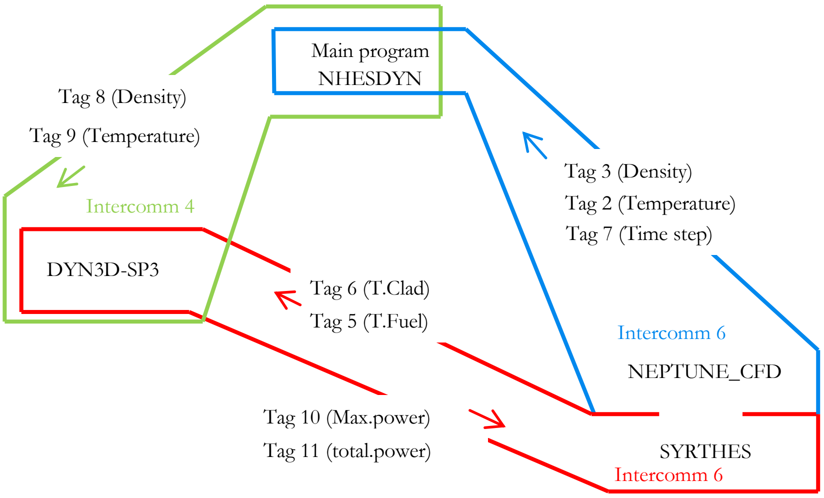

**Fig. 5-2. General distribution of the three MPI groups and the codes included within them.**

NHESDYN is considered the main program in the coupled solution. It generates DYN3D-SP3 as a sub process (spawn operation) and creates a point to point communication with NEPTUNE_CFD. At the same time the NK code creates a point to point communication with SYRTHES. In the MPI point to point communication there is a client and a server, as it is explained in annex B. The NEPTUNE_CFD is a client from the main program and SYRTHES is the client of the NK code. Thus, three inter-communicators or groups are created. In each one two codes are hosted.

Regarding the spawn process the NHESDYN and DYN3D codes share the same command display, in which instruction from the TH codes are also showed due to the different dependencies. In the group description by Fig. 5-2 the TH tools are considered like a single code. These codes were already coupled by their main developers (EDF and CEA) and the communication between them to solve the conjugated heat transfer is done directly with no MPI interaction. Some extra information is showed in Fig. 5-2 concerning the kind of information transferred (densities, temperatures, etc.) a further subchapter is devoted to this topic and deeper information will be provided.

According to the MPI groups arrangement, the information from NEPTUNE_CFD has to pass through the main program to reach DYN3D, the information has to be duplicated because those codes don't share a common inter-communicator. The duplication operation is performed by the main program (e.g. the density tagged with number 3 is duplicated as tag 8 after passing through the main program). The duplicity issue is worth in order to show all the information exchange in real time in the main command line. This option offers control and easy debugging in case of failure, especially when checking the content of the multiple strings exchange every time step.

Fig. 5-3. shows a simplified flow chart to understand the function of each module in the coupled solution. The NK/TH tools follow a specific order in the information flow while the main code controls the times and performs the convergence loops during some stages of the simulation.

Considering that the NK code has solved the previous time step, the information (volumetric heat flux) is sent to the SYRTHES code. Then the TH step is calculated and the conjugated heat transfer through the solid-liquid interface is solved.

The information generated takes two different ways. The information from SYRTHES (Doppler temperature) can be transferred directly to DYN3D_SP3 because both are included in the same MPI group. Detailed description of this process is explained in the paragraph 5.7. The second way is followed by the information from NEPTUNE_CFD (moderator temperatures and densities). It is sent to the main code. Here, if it applies some operations are performed (e.g. convergence loops for a steady state case). Afterwards, the information is resent to the NK code. By this last operation the NK has enough information to refresh the pre-calculated cross sections and solve the transport equation. When the calculation finishes the heat flux is sent again to the TH code which is waiting for the next time step calculation.

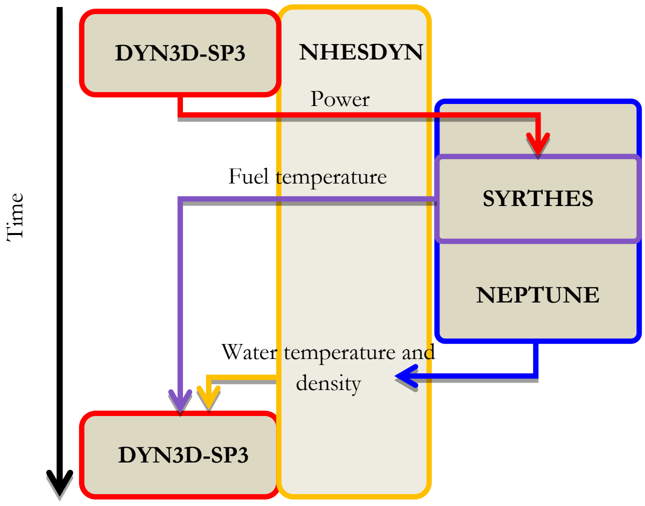

**Fig. 5-3. Simplified flow chart for the coupled solution NEPTUNE_CFD/SYRTHES/DYN3D_SP3.**

## 5.3 Coupled solution execution

To initialize the codes first the user has to execute a script (nhesdyn.sh) calling the main program NHESDYN, after some seconds the program shows by display: **"[MAIN] waiting for NEPTUNE…."** which is the client of NHESDYN. The next instruction is **"[DYN3D] waiting for SYRTHES…"**, this is the DYN3D waiting for SYRTHES to start the communication as a server. Then, in another command window the user has to launch the NEPTUNE_CFD/SYRTHES codes by running the script "runcase.sh". As soon as the TH tools accept the communication new instructions will appear in the command line informing about the ongoing of the simulation. By executing the scripts nhesdyn.sh and runcase.sh, the coupled solution is running.

Fig. 5-4 illustrates the different steps performed while the coupled solution is running, and explanation of each of them comes next. To avoid any kind of numerical instability at the beginning of the coupled solution simulation is it necessary to initialize the coupled run from a previous converged case, where a fully developed variables profile for all the TH variables is calculated. This previous simulation is a standalone NEPTUNE_CFD/SYRTHES calculation. The NEPTUNE_CFD code lacks of a steady state algorithm. To get a converged initial calculation, a simple null transient simulation is performed where the boundary conditions are set as constant.

During the initial TH null transient calculation some variables are checked. The velocities, Doppler temperatures at different points and the heat flux at the clad-liquid interphase are monitored. If those variables remain constant in time the case is considered to be steady and converged. A converged initial TH conditions avoid possible instabilities during the first steps of the coupled solutions an helps is a rapid $K_{eff}$ eigenvalue calculation. This initial simulation is useful to find the ideal time step of the case. For this initial calculation the time step in NEPTUNE_CFD is set as variable dependent on TH parameters like the Courant number. The time step calculated during this stage will be used as a common time step for the rest of the codes once the coupled solution is running.

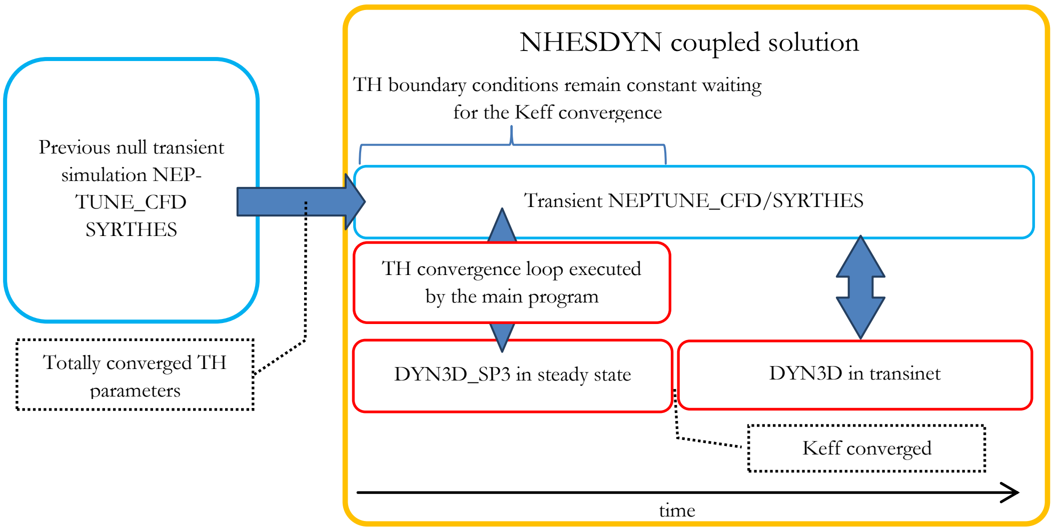
NHESDYN coupled solution
TH boundary conditions remain constant waiting for the Keff convergence
Previous null transient simulation NEP-TUNE_CFD SYRTHES
Transient NEPTUNE_CFD/SYRTHES
TH convergence loop executed by the main program
DYN3D_SP3 in steady state
DYN3D in transinet
Totally converged TH parameters
Keff converged
time

**Fig. 5-4. Coupled solution execution. Main steps.**

When the coupled solution is working the first stage is conditioned by the NK code, which needs to perform a steady state calculation with fixed power to calculate the $K_{eff}$ eigenvalue of the system. At the first iteration the TH variables are provided by the converged initial file. When the NK code performs the steady state iterations develops a power map with power profiles that affects the evolution of the TH forcing the utilization of a convergence loop, this point is explained in paragraph 5.5.

During the NK steady state the TH boundary conditions are set as constant. When the NK steady state is finished the transient starts, all the thermal inertias are taken into account and the convergence loop is no longer necessary, both codes run at the same time and the TH boundary conditions can be modified to perform thermal initiated transients.

## 5.4 Time advancement description

And easy representation of each process of the coupled solution is shown by Fig. 5-5. Here the first operation (step 1) is to transfer the initial TH variables from the previous converged simulation directly to the NK with no convergence loop. Then DYN3D_SP3 refreshes the cross section (step 2) and calculates a power which is delivered to the SYTHES code (step 3). Step 4 is the TH calculation; both TH codes advance one time step. For the next step, the convergence loop applies. In step 5, the information calculated by the TH codes is sent to the main program. The main code receives information from the CFD via the inter-communicator of the group, for the SYRTHES parameter this information has to be duplicated and sent via DYN3D_SP3.

In a steady state case when all the information is collected by the main code the convergence loop is executed. If the convergence criteria are achieved then in the step 6 the TH parameters are sent to the NK code. The next step 7 is analog to the step 2.

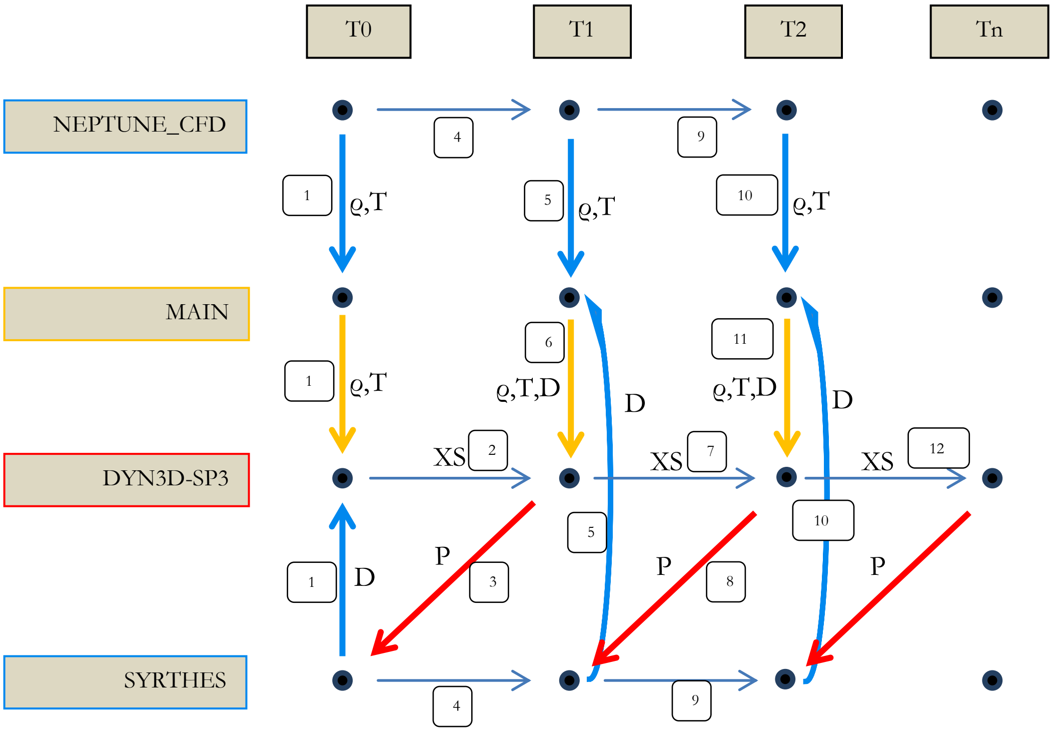

**Fig. 5-5. Time advancement description for the codes.**

When the NK is executed in transient the only difference is that before step 6 there is no convergence loop and the TH parameters are send directly after been collected by the main program.

## 5.5 Steady state coupling scheme

The coupling scheme is different depending on the type of calculation (steady state or transient). During the steady state the main objective is the calculation of the $K_{eff}$ eigenvalue according to the TH parameters. At this stage the power map calculated is adjusted each time step and the power distribution in the fuel rod changes. Before calculating the next NK steady state iteration the TH code must provide converged information by applying a convergence loop. The TH tools are very sensible to those power distribution changes, before reaching a state where there is no more temperature variation it may execute hundreds of iterations slowing the overall coupling process.

There is a method to palliate this slow process. The biggest part of time consumption is made by the thermal inertia in the fuel, which takes many seconds to stabilize after a power map variation. The SYRTHES code works in normal conditions with the same constant time step as the other codes (dependent time step) this time step is chosen according to the TH parameters, normally (1 or 2 ms). During the steady state this condition is not mandatory. Hence, the time step can be modified to decrease the convergence time.

To neglect the thermal inertia from the energy equation of the heat conduction solver, the time step is changed to a high value ($10^4$ seconds). This way the temperature changes in the fuel are rapidly adapted to the new power distribution. The TH converge during the steady state is now only an issue for the CFD. A similar methodology could be applied for NEPTUNE_CFD code to have a fast convergence, but due to code access restrictions this was not possible. However, with the changes applied to the SYRTHES code a considerable time reduction is achieved by means of reducing the number of convergence loops. In Fig. 5-6, the two possibilities regarding the configuration of the time step are shown. The dependent time step takes around 4 seconds to converge, with a constant time step of 2 ms. The code needs around 1300 iterations to converge. By making the time step size independent ($10^4$ seconds) this process can be done in 50 time steps. A reduction in the computational time is achieved by means of reducing the number of converge loops.

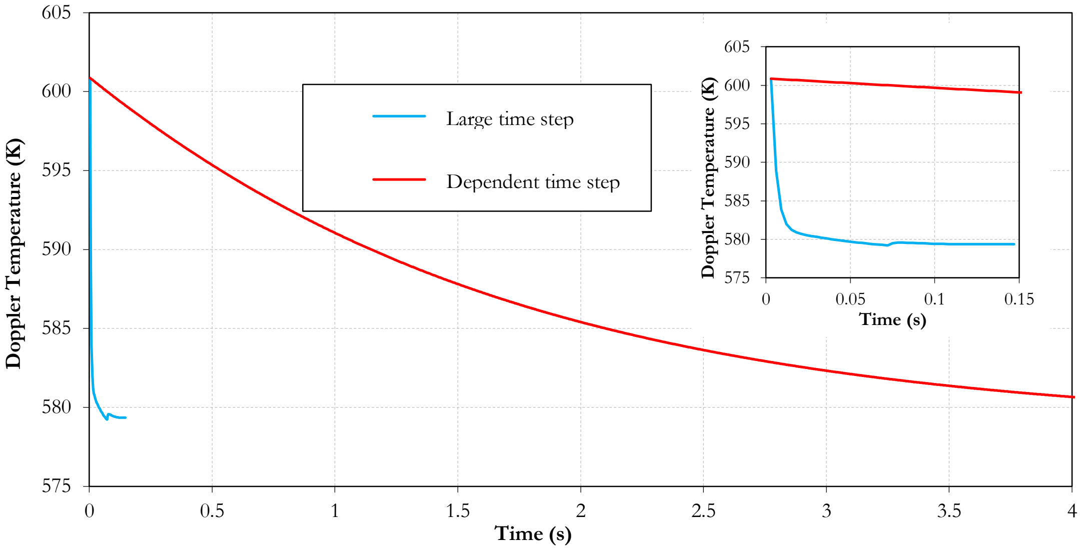

**Fig. 5-6. Simulations time comparison during the coupled steady state for SYRTHES using a large time step (10E4) and SYRTHES using the same time step as the other codes.**

To make this modification to the SYRTHES code the time dependence from NETPUNE_CFD has to be avoided and substituted by the new time value. This is possible by modifying a routine in the SYRTHES source code, which is called every time step. To implement this change successfully SYRTHES must know that the simulation is a steady state mode. For that reason a flag is set in DYN3D_SP3. If the simulation is steady state the NK set the flag to 1, if not then the flag becomes 0. The heat conduction solver checks this flag every time step, applying the proper changes to the time step value. As soon as the NK code changes to a transient simulation the flag is set to 0 and the time step depends on NEPTUNE_CFD, setting the same time step for all the codes.

### 5.5.1 TH convergence loop

During the steady state a convergence loop is executed by the main program to converge all the TH variables. When the power map changes inducing a temperature transient in the TH tools the NK code waits until this transient is stabilized. The variables to control in the TH are: Doppler temperature, moderator temperature and moderator density. Furthermore the heat flux at then interface solid-liquid is considered like a convergence criteria too. The relative error between time steps of these variables is checked every time step. The convergence criterion is reached when the relative error of these variables between time steps is below $10^{-4}$. To have an idea about the evolution of the steady state the main code shows in a command window the convergence for each axial level of the TH discretization. Providing each time step the number of axial levels already converged. When all the axial levels are converged then the information is sent to the NK code to perform another time step calculation. In addition to the variables that control the convergence the total heat flux at the interface solid-liquid is monitored.

## 5.6 Transient coupling scheme

Once the calculation of the $K_{eff}$ eigenvalue is finished the transient simulation starts. From the TH side there is no difference in the execution of the codes. Both are being executed in transient mode. For this new scenario the effects of the thermal inertia are very important to have an accurate description of the temperature field. Therefore the convergence loop is not executed and the time step for SYRTHES is in agreement with the other codes.

Taking as example the time advancing of Fig. 5-5, once the cross-section have been refreshed in the step 7, the power is transferred to the SYRTHES code (Step8). With the new power map the TH tools perform a new time step calculation (Step 9) then the TH feedback parameters are sent to the main code (Step10). Here is when during the steady state case the convergence loop is executed, now in the transient case there convergence loop is not executed and the TH information is sent directly to the NK code (Step11).

The Fig. 5-5 represents a simplification of operations. A complete and detailed flow chart description of the steps involved in the coupled solution can be found in the annex C.

## 5.7 Spatial mapping

Several operations are mandatory for the information exchange between codes. Not only in terms of message passing but also in terms of information preparation before and after the exchange. Those operations are motivated by the different axial and radial discretizations of each code. While the NK code considers a pin like working unit in the radial plane, the TH code can have 20 cells in the radial direction for describing the same pin geometry. In the axial direction the NK works usually with 25 axial levels. In the case of the CFD this number can be increased up to 150 axial levels. Those values are not constant and the user can change the refinement of the mesh in each case depending on to the calculation demands. The coupling methodology has to deal with this problem and solve it.

To avoid mesh dependencies in the communication a virtual interface is created before the information exchange. This means that the important values are extrapolated to continuous functions, creating a set of strings. The functions are described by 4th degree polynomial approximations. Therefore the strings are composed by 5 coefficients. This group of strings is the real information exchanged between codes. The amount of information to pack and send from the MPI code is reduced considerably by the creation of these strings.

In the next paragraphs the mapping operations performed by each code are explained for both directions: from the code to the interface and from the interface to the code. Fig. 5-7 summarizes these mapping operations:

- The representation of the mesh for a single pin is illustrated by (a), where the fuel gap and clad is modeled by SYRTHES and the fluid domain is modeled by NEPTUNE_CFD.

- For each axial level of this mesh the averaged valued of the TH parameters are taken (b), these are: moderator temperature and density and Doppler temperature.

- These TH values are approximate to polynomial functions (c).

- The DYN3D_SP3 code reads the TH values at the required location by interpolation the polynomial functions (d).

- The NK computes the information generating a power map distribution (e).

- The power values are approximated to a polynomial function (f) and finally these values are recognized as an input the next time step of SYRTHES.

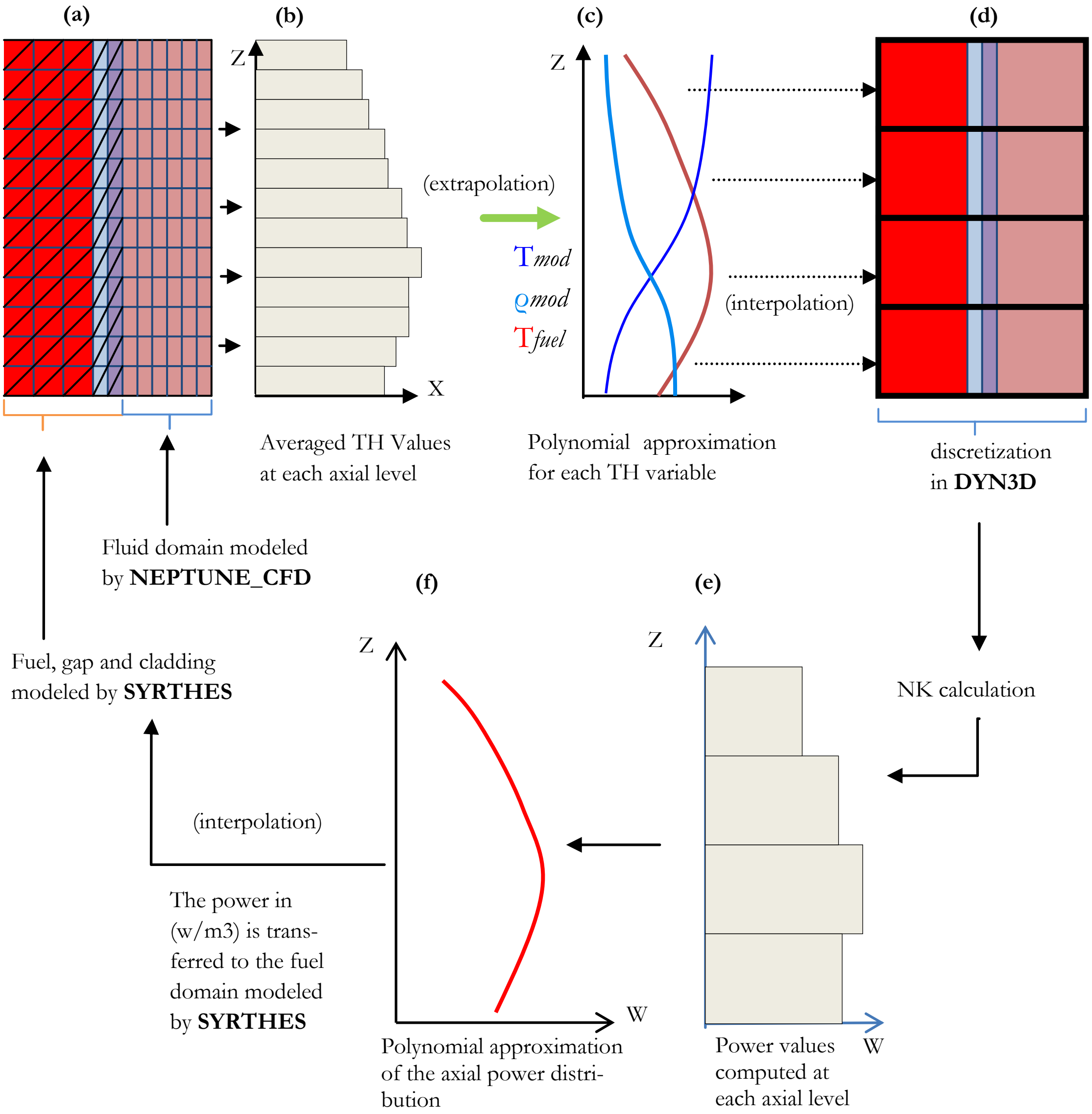
(a)
(b)
(c)
(d)
Z
X
Averaged TH Values at each axial level
(extrapolation)
Z
Tmod
ρmod
Tfuel
(interpolation)
Polynomial approximation for each TH variable
discretization in **DYN3D**
Fluid domain modeled by **NEPTUNE_CFD**
Fuel, gap and cladding modeled by **SYRTHES**
(f)
(e)
Z
Z
NK calculation
(interpolation)
The power in (w/m3) is transferred to the fuel domain modeled by **SYRTHES**
W
Polynomial approximation of the axial power distribution
Power values computed at each axial level
W

**Fig. 5-7: Mapping example for a single pin. (a) NEPTUNE_CFD/SYRTHES model. (b) Averaged values at each axial level of TH parameters. (c) Polynomial approximation of TH parameters. (d) DYN3D_SP3 model. (e)Computed power values. (f) Polynomial approximation of the axial power.**

### 5.7.1 NEPTUNE_CFD to interface

The operations summarized in Fig. 5-7 (b) and (c) represent the mapping from NEPTUNE_CFD to the virtual interface. In Fig. 5-8 the nodalization for 1 pin is presented. This model is composed by 16 cells in the radial direction. Thus, an average value per axial level of the moderator temperature and density has to be calculated before sending the information.

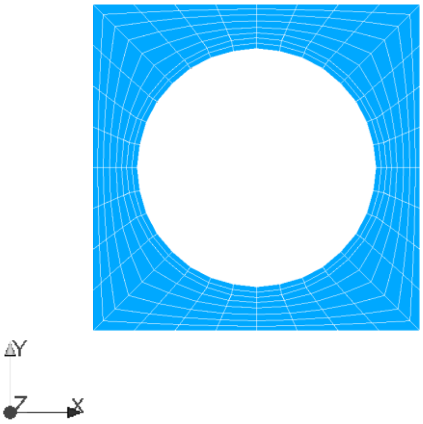

**Fig. 5-8. Nodalization radial distribution for one pin in NEPTUNE_CFD.**

The NEPTUNE_CFD mesh has local refinements (it must be adapted to the proper calculation of TH parameters). The volume of the cell is used as a weighting factor for the average temperature and density calculation. This operation is performed according to Eq.(5-1) for the temperature and density. In Eq.(5-1) $i_0$ and n indicate the first and the last cell of the axial level, while *i* is the counter for the cell number.

If during the simulations void appears in the fluid domain is necessary to take into account the VF for the average temperature and density of the moderator at each axial level Eq. (5-2) and (5-3).

$$T_s = \frac{\sum_{i_o}^{n} V_i \cdot T_i}{V_s} \quad , \qquad \rho_s = \frac{\sum_{i_o}^{n} V_i \cdot \rho_i}{V_s} \quad , \tag{5-1}$$

$$T_s = \left( \sum_{i_o}^{n} V_i \cdot \left[ \alpha_i \cdot T_i + (1-\alpha_i) \cdot T_i \right] \right) \cdot V_s^{-1} \ , \tag{5-2}$$

$$\rho_s = \left( \sum_{i_o}^{n} V_i \cdot \left[ \alpha_i \cdot \rho_i + (1-\alpha_i) \cdot \rho_i \right] \right) \cdot V_s^{-1} \ . \tag{5-3}$$

Once the averaged density and temperature is calculated the code generated is a discrete temperature and density axial distribution, see Fig. 5-7(b). The last operation is performed by approximating the discrete distribution by a $4^{th}$ degree polynomial function, Fig. 5-7(c). The approximation is based on the last squares method. The coefficients of the polynomial are stored in a string which is ready for being packed and sent. This methodology ensures a mesh independence of NEPTUNE_CFD and SYRTHES and the virtual interface, and minimizes the amount of information later on MPI has to deal with.

### 5.7.2 SYRTHES to interface

SYRTHES is in charge of calculating the temperatures in the fuel clad and gap in the pin Fig. 5-9.

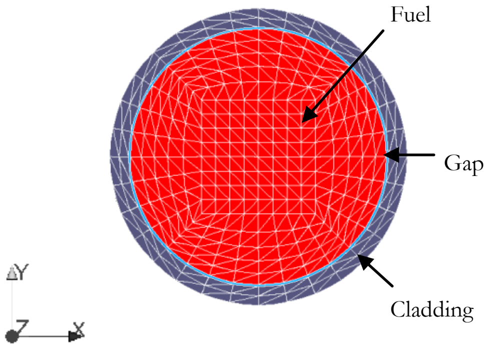

**Fig. 5-9. Radial nodalization of one pin for SYRTHES.**

What the code sends to the interface is the Doppler temperate. The center line temperature and the outer fuel surface temperature of the pin are corrected to calculate the Doppler temperature according to Eq.(5-4). This operation takes place for every axial level, providing a discrete axial temperature profile. Like previously explained for NEPTUNE_CFD, in the last step this discrete axial distribution is approximated to a 4th degree polynomial function.

$$T_D = 0.3 \cdot T_{CL} + 0.7 \cdot T_{OS} \tag{5-4}$$

### 5.7.3 Interface to DYN3D_SP3

When all the information provided by the TH codes is available at the interface the NK code can interpolate the data at any radial or axial location. The different kind of spatial distribution is no longer a problem. The receiver code (DYN3D_SP3) has to unpack this information and place it in the proper array to initialize the calculation.

### 5.7.4 DYN3D_SP3 to interface

After updating the cross section, the information generated by DYN3D_SP3 is available to be transferred back to the TH. The different powers at each axial level generate an axial power shape, which is converted to a polynomial function by applying the methodology previously described. As soon as the information is available it is sent to the SYRTHES code. The information provided to the interface is described below:

- Power (W). This can be arranged and sent like total power of the whole pin cluster or local pin power.

- Power map distribution. This is a power map normalized according to the maximum local power registered. It provides information about the power in every single node of the NK discretization.

- Sum_power_distribution ($m^2$). This is the sum of each element of the power map distribution multiplied by the lateral area of each NK node.

The power is sent to the interface with no changes. The power map distribution needs to be mapped and approximate to a polynomial function. The sum_power_distribution is just one number and enters unchanged the interface.

### 5.7.5 Interface to SYRTHES

SYRTHES requires a setting of the volumetric heat flux ($W/m^3$) within the fuel domain. In SYRTHES the heat flux is set by node. This means that the volume of the element has to be taken into account. What the interface provides is numbered in the previous point. In addition to what is already provided what SYRTHES needs is:

- Averaged heat flux ($W/m^2$). Resulting from division of the total power by the sum_power_distribution.

The calculation of the averaged flux is done inside SYRTHES and is a single value for the whole studied domain.

Now, the power map distribution and the averaged heat flux are multiplied providing ($W/m^2$) for each pin and axial level of the TH model. Then, the last operation is to multiply the value by the lateral area of a fuel level and divide it by the volume of the fuel level domain, obtaining the volumetric power density ($W/m^3$) ready for the SYRTHES input. This last operation has to be done taking into account the geometrical properties of the refined space discretization provided by the TH code and not the discretization of the NK code.

At this point is important to summarize the multiple transformations performed before the information is ready to feed the input of the TH tool. Fig. 5-10 illustrates a scheme of the main calculations.

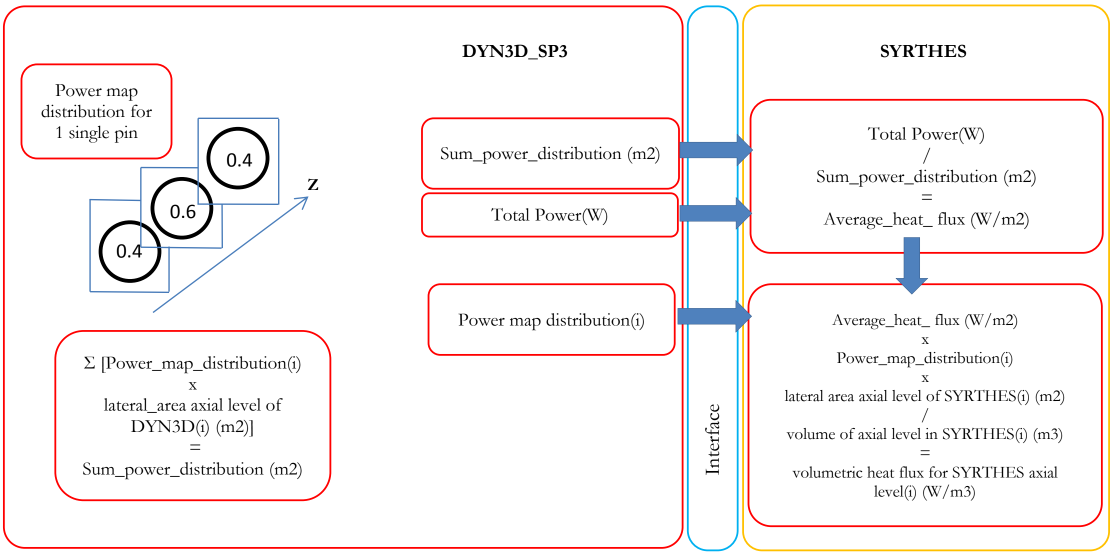
DYN3D_SP3
Power map distribution for 1 single pin
0.4
0.6
0.4
Z
Σ [Power_map_distribution(i) x lateral_area axial level of DYN3D(i) (m2)] = Sum_power_distribution (m2)
Sum_power_distribution (m2)
Total Power(W)
Power map distribution(i)
Interface
SYRTHES
Total Power(W) / Sum_power_distribution (m2) = Average_heat_ flux (W/m2)
Average_heat_ flux (W/m2) x Power_map_distribution(i) x lateral area axial level of SYRTHES(i) (m2) / volume of axial level in SYRTHES(i) (m3) = volumetric heat flux for SYRTHES axial level(i) (W/m3)

**Fig. 5-10. Power transformation through the interface between DYN3D and SYRTHES.**

The discretization of the SYRTHES code is composed of tetra cells of 10 nodes. Four nodes define the shape of the tetra volume, and the other six are located in the middle of each edge. In Fig. 5-11 a detail of the fuel nodalization is presented with the location of the middle nodes at one axial level.

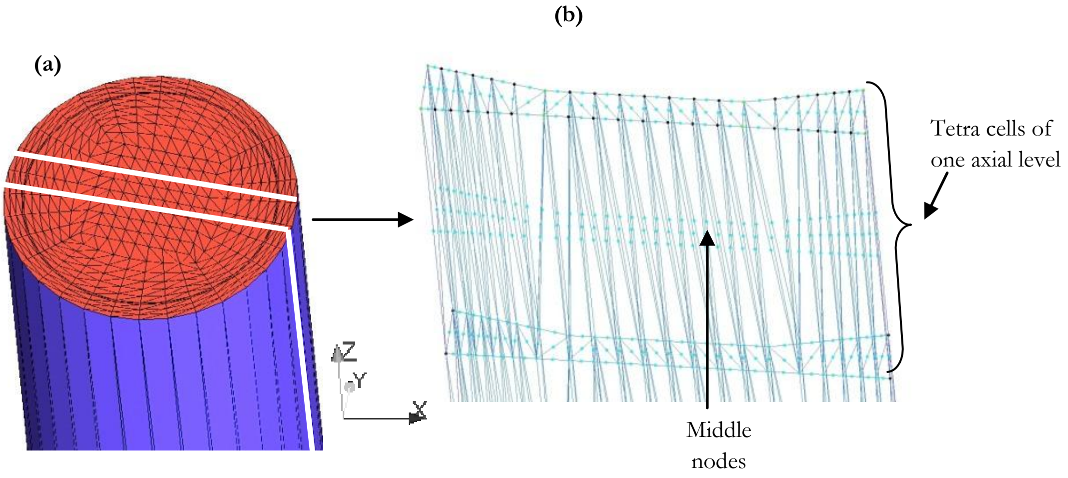
(b)
(a)
Z
Y
X
Tetra cells of one axial level
Middle nodes

**Fig. 5-11. (a) Fuel, gap and clad pin discretization by SYRTHES. (b) detail of the fuel discretization**

The power is set by node, and there are mid nodes every axial level, hence the surface and volume calculated has to be half of the axial level for the fuel domain. If the nodes are located at the top or at the bottom of the fuel domain a quarter of the area and volume of the axial level is taken. The volume and area values for the last operation described are taken directly from the geometry of the mesh. For this case the mesh volume and area is slightly smaller than the real one, because there is an error due to trying to describe a circumferential shape with tetra-shape areas. Then the area considered is smaller than the real one. This is a small error, and it will decrease with refined meshes, but when dealing with volumetric heat flux this difference can be significant. A careful calculation of the fuel volume has to be done to obtain a reasonable accuracy in the definition of the volumetric heat flux. The best way to calculate the total volume and the required areas of the fuel is by using a post processor of the mesh. For this case the post processor from ANSYS_CFX (24) has been applied.

In the tests performed, if the exact geometry is not taken into account, SYRTHES can register a 2.54% of deviation from the nominal power sent by DYN3D_SP3. By means of using the right geometrical parameters this deviation in the power is about 0.03%. This small error is due to the many transformations performed at the interface, but during a transient scenario it can reach 0.7%. This error is analyzed during the simulations in the Annex E.

# 6 Validation of the coupled TH/NK solution

## 6.1 Introduction

Once the coupled methodology is ready it is tested to ensure its correct behaviour. This chapter aims to understand and identify which are the most important parameters that affect the correct development of the coupled simulations, e.g. (nodalization distribution). A comparison to the well validated coupled code DYN3D_SP3/SCF (DYNSUB) is performed. A set of simulations are performed and analyzed for steady state and thermally initiated transients, where guided changes in the moderator state (mass flow, temperature and pressure) are performed.

As mentioned in the previous chapter to ensure a correct information exchange between solid and fluid domains there must be a correspondence between the nodes located in the solid-fluid interface. This way, when the conjugated heat transfer is calculated between NEPTUNE_CFD and SYRTHES, the interpolation between nodes is avoided and a high numerical accuracy is reached in the interface energy balance. The mesh correspondence between the solid and the fluid domain concentrate a high number of nodes in the fuel domain. This node concentration and the fact that the heat conduction code in charge of solving this domain (SYRTHES) is not parallelized make the simulation quite slow when the temperature field is solved in the fuel. During the simulation, the NEPTUNE_CFD has to wait SYRTHES to solve the conjugated heat transfer for the solid-liquid interface and therefore, the DYN3D_SP3 has to wait too. An agreement must be achieved between accuracy and affordable calculation time. For that reason the coupled solution is tested considering a small physical domain, a single pin.

The geometrical characteristics and essay conditions are based on the OECD/NEA and US NRC PWR MOX/UO2 core transient benchmark (128). The material properties encoded in the different TH tools and the pre-generated cross sections are in agreement with this benchmark. The initial TH parameters are summarized at Tab. 6-1.

## 6.2 Initial conditions and problem definition

As explained in the previous chapter the case has to be initialized from converged conditions. Those conditions are summarized in Tab. 6-1. A stand-alone null transient case is performed for the TH codes according to those parameters. When all the TH parameters (Doppler temperature and moderator density and temperature) are converged the coupled solution can be initialized.

When the coupled solution is initialized it is divided mainly in two steps. In the first step the NK code perform a steady state to calculate the $K_{eff}$ eigenvalue. In the second step and when the $K_{eff}$ eigenvalue of the system is calculated, the TH tools perform the thermally initialized transients by a guided modification of the moderator temperature mass flow rate and pressure. These guided modification of the boundary conditions are performed one by one, for instance, first the mass flow is modified and the evolution of the different system variables (power and temperature) is analyzed.

**Tab. 6-1. Nominal conditions for the simulations according to the OECD/NEA and US NRC PWR MOX/UO2 core transient benchmark adapted for a single pin geometry.**

| | Power (kW) | Inlet temp (K) | Pressure (MPa) | Mass flow (kg/s) |
|---|---|---|---|---|
| Test 1 | 21.68 | 560 | 15.5 | 0.28 |

For a reliable code-to-code comparison of both DYNSUB and NHESDYN some parameters need to be commonly configured. First, the material libraries must match. The correspondence between the thermo-physical properties is mandatory to analyse the difference between codes under equal conditions. The specific conductivity, density and the heat capacity libraries for the $UO_2$ and clad are selected according to (128). Here, the conductivity and heat capacity are temperature dependent. The density is decided to be set as constant. The reason is that any of the TH tools applied in this work is a mechanical code, no volume variation is consider in the domains, the discretization doesn't change during the code execution.

The second point to deal with is the gap modeling. The gap is the space between the fuel and the inner face of the cladding having a width of about 0.05 mm . This empty space is filled with Helium under pressure. In the tested cases the integrity of the gap is respected, a constant width is configured. The DYNSUB code models this region just by setting a constant HTC with a value of $10^4$ W/m$^2$K. In the NHESDYN approach the temperature drop produced in the gap is calculated by solving locally the conduction within a solid using the thermo-physical properties of the Helium. Another possible solution was to model the gap as a fluid domain but the complexity and number of interfaces involved in this solution makes it high time consuming in the modeling and calculation. The difference between these two solution approaches generates significant changes in the Doppler temperature prediction. To partially avoid this uncertainty a common HTC has been calculated. According to the NHESDYN steady state results geometrical aspects (superficial area), heat flux and gap temperature drop an interfacial averaged HTC is calculated. This value is 11710 W/m$^2$K, which is sensibly higher than the previous default value. For the DYNSUB simulations this value is used as a constant HTC for modeling the gap. The differences in the DYNSUB temperature predictions by changing this parameter from $10^4$ W/m$^2$K to 11710 W/m$^2$K can be found in annex E.

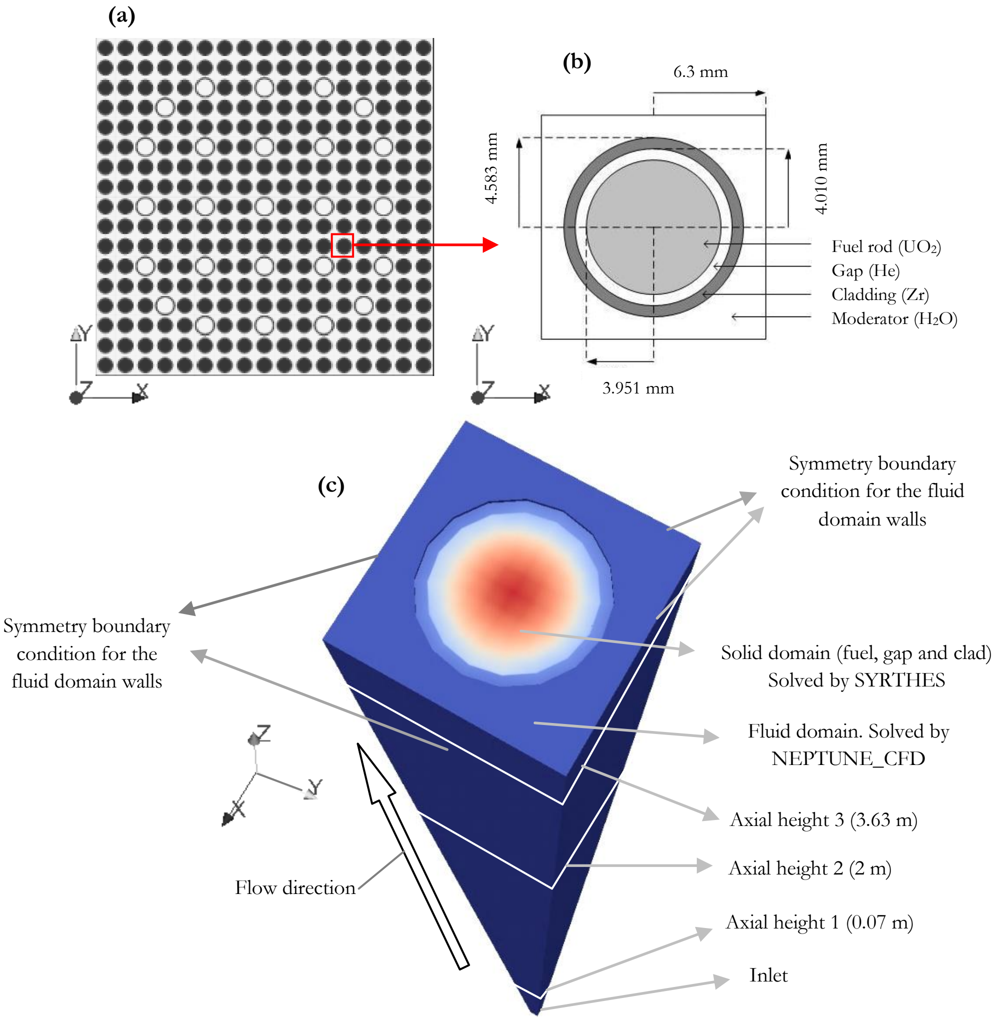
(a)
Y
Z
X
(b)
6.3 mm
4.583 mm
4.010 mm
Fuel rod (UO2)
Gap (He)
Cladding (Zr)
Moderator (H2O)
Y
Z
X
3.951 mm
(c)
Symmetry boundary condition for the fluid domain walls
Symmetry boundary condition for the fluid domain walls
Solid domain (fuel, gap and clad) Solved by SYRTHES
Fluid domain. Solved by NEPTUNE_CFD
Z
Y
X
Axial height 3 (3.63 m)
Axial height 2 (2 m)
Flow direction
Axial height 1 (0.07 m)
Inlet

**Fig. 6-1. a) Plant view of a 17X17 PWR FA. b) Plant view of a single pin with the geometric characteristics. c) 3D view of the numerical domain simulated with the TH tools of NHESDYN. Location of the 3 heights were the measurements take place.**

The configuration for the boundary conditions of the problem is similar to the PSBT and BFBT benchmarks configuration. TH tool defines the channel domain in which the mass flow rate is imposed at the inlet (bottom of the subchannel) and the pressure is set at the outlet (top of the subchannel) as boundary conditions. The fluid domain is 12.6 mm in the X and in the Y direction. The walls of the perimeter are set with a symmetry boundary condition. The domain is 3.7 m long in the Z direction, the fuel and clad diameters are summarized in Tab. 6-2.

**Tab. 6-2. Rod geometry considered for the validation based on the the OECD/NEA and US NRC PWR MOX/UO2 core transient benchmark.**

| Fuel radius (mm) | Clad inner radius (mm) | Rod radius (mm) |
|---|---|---|
| 3.951 | 4.010 | 4.583 |

## 6.3 Space discretization

The different space discretizations provided by the codes are illustrated by Fig. 6-2. Here, figure (a) represents the spatial discretization of NHESDYN for the TH domain, which is composed by the fluid domain discretization by NEPTUNE_CFD and the solid domain discretization (fuel, gap and clad) by SYRTHES. On figure (c) the nodalization for the TH domain of the DYNSUB code is presented. SCF solves the TH domain. To do so, it divides the space in four sub channels which are the calculation nodes around the pin. The fuel temperatures are solved in 10 calculation points in the radial direction, plus two points for the clad. For the CFD (a) the fluid domain is divided in smaller control volumes, the number of nodes inside the solid domain can be higher than SCF (c) but it depends on the mesh set by the user. Figure (b) represents the single pin configuration for the NK code DYN3D_SP3 which has 24 axial levels, for the NK part both coupled codes use the same configuration.

The CFD nodal distribution is tested with two different meshes, a coarse one and a refined one. The distribution is shown by Fig. 6-3, the coarse distribution has 44 axial levels and the refined mesh has 60 axial levels. The solid and fluid domains are placed separately to emphasize that the first is solve by SYRTHES and the second one by NEPTUNE_CFD. The TH tool of the DYNSUB code divides the subchannel in 24 axial levels.

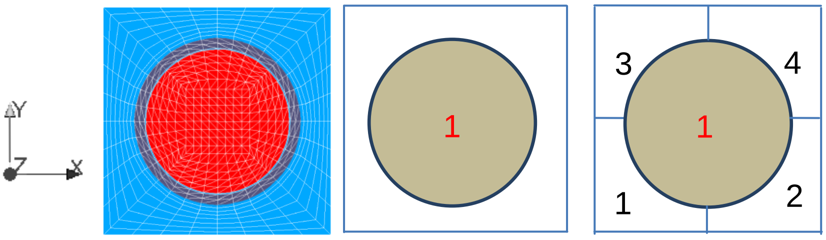

(a) (b) (c)

**Fig. 6-2. a) NHESDYN TH model of one pin. b) NK model of one pin. c) DYNSUB TH model of one pin.**

(a) (b) (c) (d)

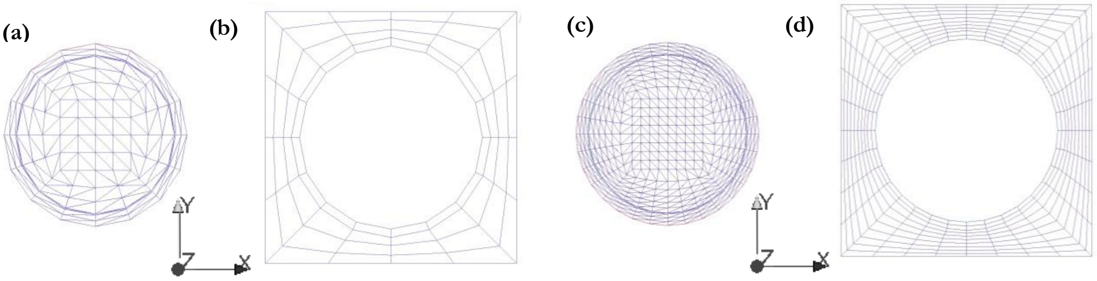

**Fig. 6-3. 1 pin structure and fluid domain nodalizations. (a) and (b) correspond to a coarse mesh, (b) and (d) to a refined mesh.**

During the test performed for the coupled solution it has been found that the gap modeling has a big influence on the temperature prediction in the fuel domain. The temperature drop across the gap changes depending on how many nodes are included in this region. To check how the temperature drop is modified by the nodalization distribution, a simple sensitivity mesh analysis has been performed. For the gap domain defined by SYRTHES two configurations are tested by placing one or two nodes in the radial direction.

To illustrate the different set ups for the cases Tab. 6-3 summarizes the different configuration tested the mesh used, the nodalization in the gap and the test case.

**Tab. 6-3. Specifications of the test matrix for the sensitivity study of the influence of a mesh refinement on the prediction of fuel and cladding temperatures.**

| | Mesh | N° cells in gap |
|---|---|---|
| Run_1 (R1) | Refined | 2 |
| Run_2 (R2) | Coarse | 2 |
| Run_3 (R3) | Coarse | 1 |

## 6.4 Steady state analysis

The coupled solution performs a steady state calculation before starting the transient. At this stage the total power provided from DYN3D_SP3 is fixed. The power map changes during the calculation of the $K_{eff}$ using the pre-tabulated cross sections and TH parameters. When NHESDYN steady sate is finished, the simulation results for runs R1, R2 and R3 are analyzed. For the steady state the variables analyzed are: fuel center line temperature, fuel outer surface temperature and Doppler temperature profiles. The results are shown by Fig. 6-4, Fig. 6-5 and Fig. 6-6 for the axial direction.

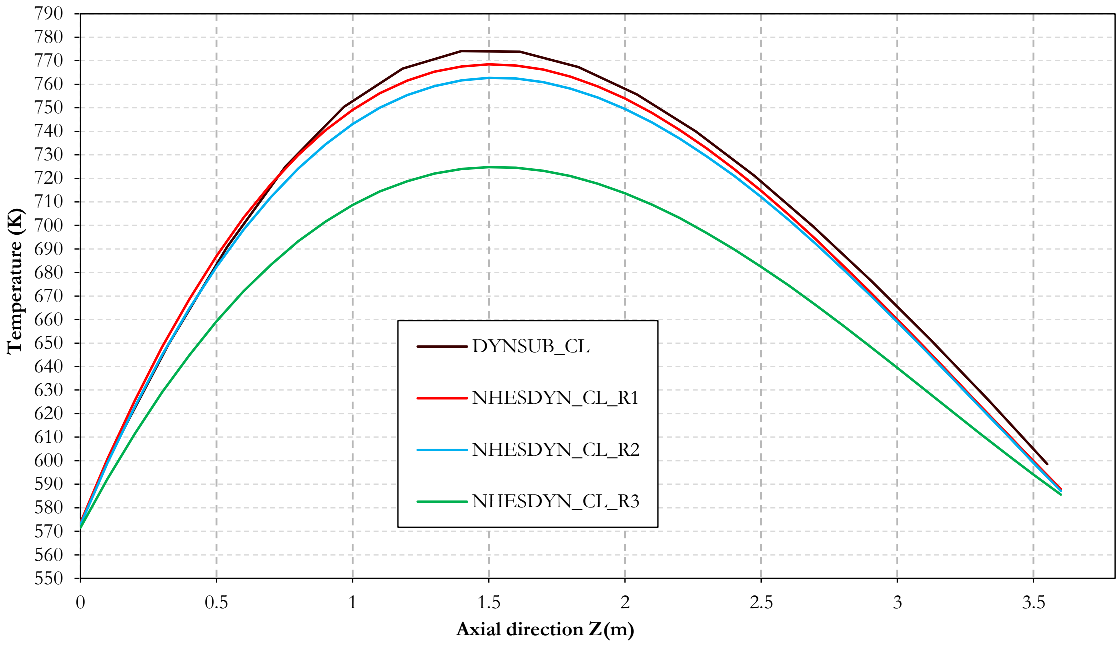

**Fig. 6-4. Comparison of the axial fuel center line (CL) temperature distribution calculated by DYNSUB and by NHESDYN using three different resolutions (R1, R2 and R3).**

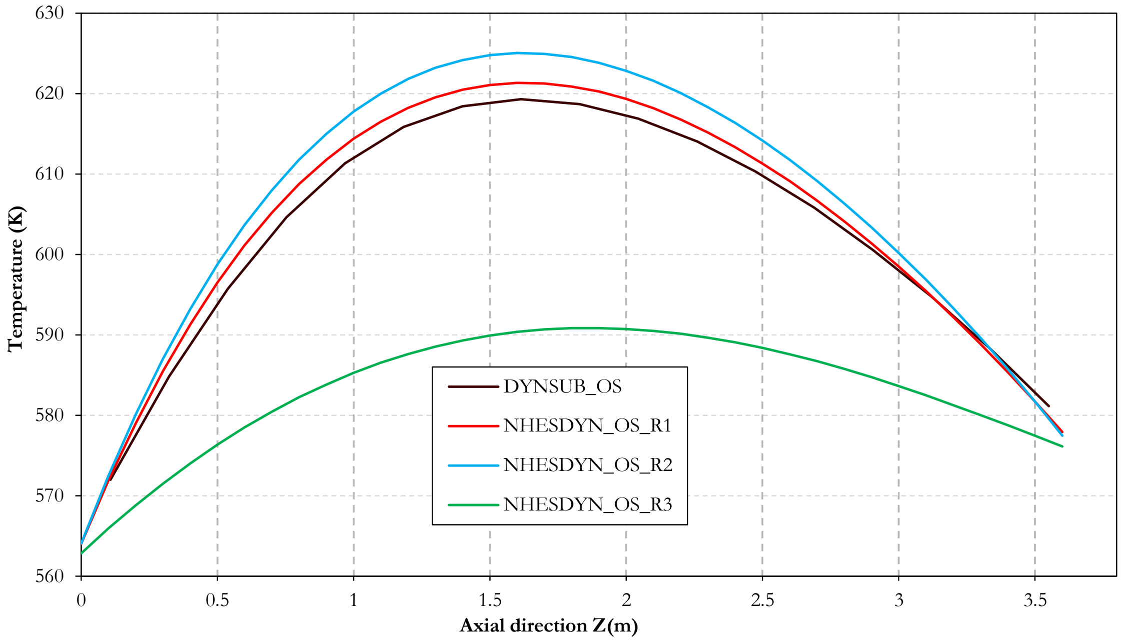

**Fig. 6-5. Comparison of the axial fuel outer surface (OS) temperature distribution calculated by DYNSUB and by NHESDYN using three different resolutions (R1, R2 and R3).**

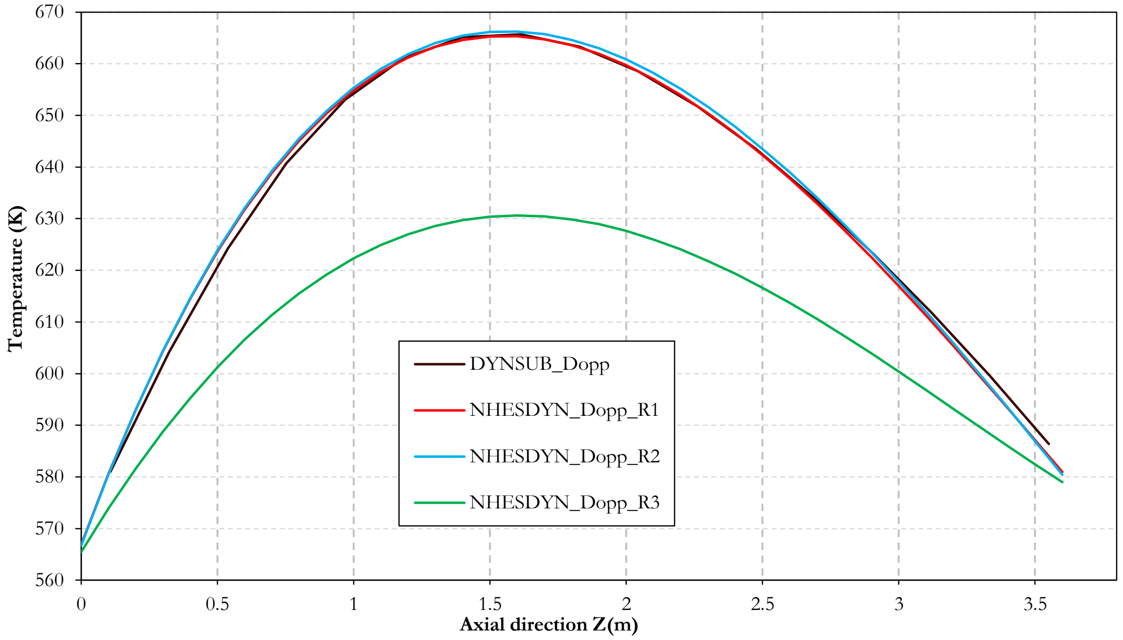

**Fig. 6-6. Comparison of the axial Doppler temperature distribution calculated by DYNSUB and by NHESDYN using three different resolutions (R1, R2 and R3).**

Regarding to the Doppler temperature (Fig. 6-6) the R1 and R2 configuration provides a very good agreement with the reference. The Doppler temperature is calculated according to Eq.(5-4) taking into account the fuel center line and the fuel outer surface. Hence, a good agreement is found for R1 and R2 in these locations too, where the highest deviation (10 degrees) is located in the center line temperature (Fig. 6-4) for R2.

The case with the single gap node configuration (R3) doesn't reproduce well either the center line or the outer fuel temperature with an under prediction of 54 and 30 degrees respectively. Hence, the Doppler temperature is far away from the reference (Fig. 6-6).

The difference between the outer fuel surface and the inner clad surface temperature is shown in Fig. 6-7 which is the temperature drop produced by the gap. The results provided by R3 at the gap are far away from the ones provided by DYNSUB considered as the reference. For this configuration no significant temperature differences are registered. The results are better in the case of using two nodes (R1 and R2). For those two simulations the temperature drop is about 10 to 5 degrees below the DYNSUB calculation in the mid-axial elevation.

Fig. 6-8 shows the averaged cladding temperature as a function of the axial height Z. This data doesn't show significant variation between the different runs. This is due two facts: first, the clad is influenced by the moderator temperature. And secondly, the temperature distortion produced in the gap is affecting mainly the fuel where the heat is generated.

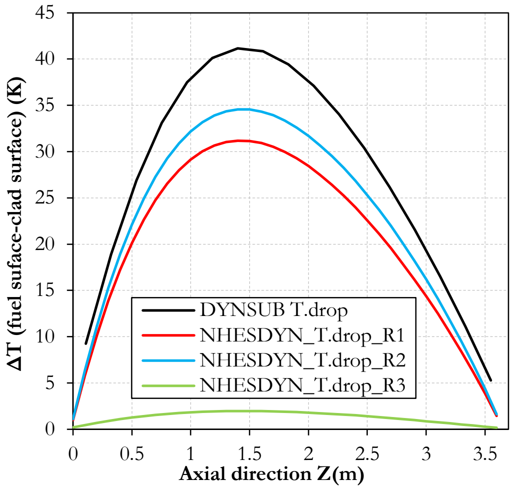

**Fig. 6-7. Comparison of the axial evolution of the fuel-cladding temperatures differences for DYNSUB and different NHESDYN resolutions (R1, R2 and R3).**

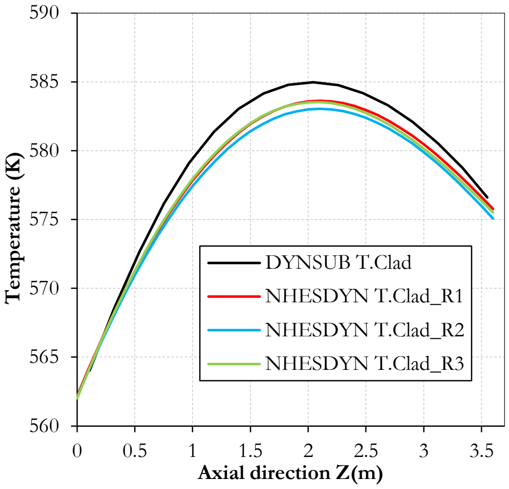

**Fig. 6-8. Comparison of the axial evolution of the cladding temperatures for DYNSUB and different NHESDYN resolutions (R1, R2 and R3).**

The model configuration proposed by R3 cannot be considered reliable enough due to the lack of temperature drop in the fuel-clad gap. It is necessary to include at least 2 nodes in this region to develop a physically sensible temperature profile. This small detail has big consequences with respect to the fuel temperature prediction.

At steady state the liquid temperature and density axial distribution are shown and compared to DYNSUB in Fig. 6-9 and Fig. 6-10. For those parameters the deviations are negligibly small. They increase slightly with the axial height. It seems that a better match is achieved using a refined mesh. But the differences between the calculations are smaller than one degree.

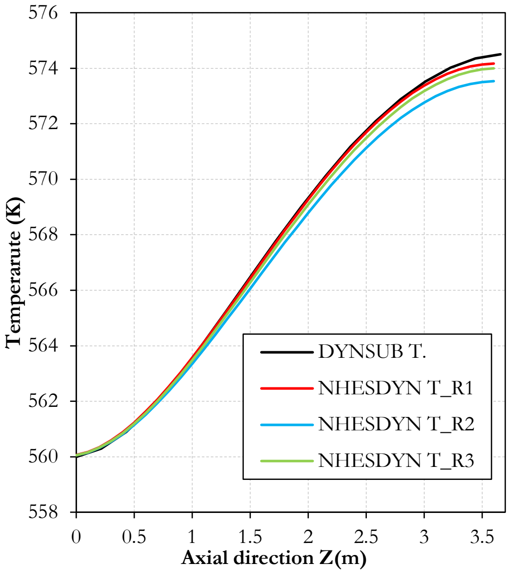

**Fig. 6-9. Comparison of the axial moderator temperature evolution predicted by DYNSUB and by NHESDYN using three resolutions (R1, R2 and R3).**

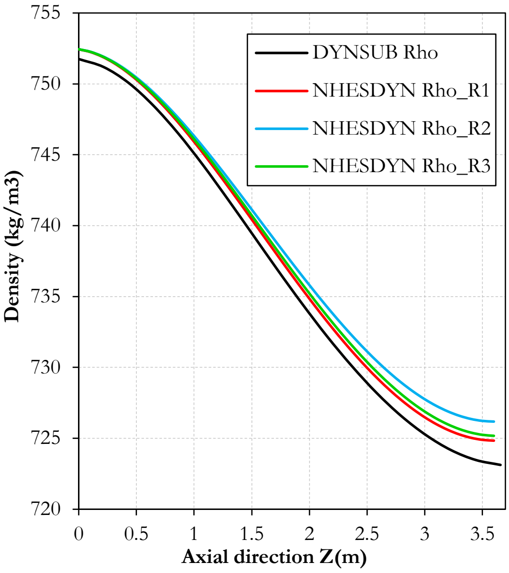

**Fig. 6-10. Comparison of the axial moderator density evolution predicted by DYNSUB and by NHESDYN using three resolutions (R1, R2 and R3).**

The radial temperature profile provided by the different configurations is depicted in Fig. 6-11, where the radial temperature profile in the fuel, gap and clad is compared to the reference. This is a local parameter. The temperature calculated by DYNSUB is slightly higher but a good match is achieved especially for a fine grid resolution (grid R1). The excessive heat conduction in the gap for the grid R3 is illustrated in Fig. 6-11. There, no significant temperature change at the gap is visible. The coarse grip of case R2 and the refined grid of case R1 don't generate significant differences in the temperatures of the fuel or clad, even when the refined mesh has double number of nodes compared to the coarse one.

In Fig. 6-12 the local temperature distribution is shown for a cross section (X-Y plane) of a fuel pin at 1.8m elevation (Z direction). The figure is divided in three parts, a 45 degrees section for the results obtained with the coarse discretizations of cases R2 and R3 and a 180 degrees section for the refined mesh of case R1. Here is possible to appreciate again the importance of the gap modeling. The refinement of this small domain has more impact on the results than the refinement of the fuel or the clad.

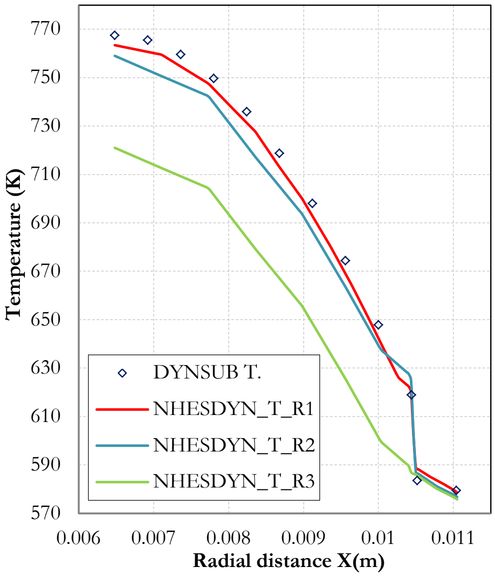

**Fig. 6-11. Radial temperature distribution in the fuel, gap and clad in a fuel pin cross section at 1.8 m elevation. Comparison of DYNSUB and different NHESDYN resolutions (R1, R2 and R3).**

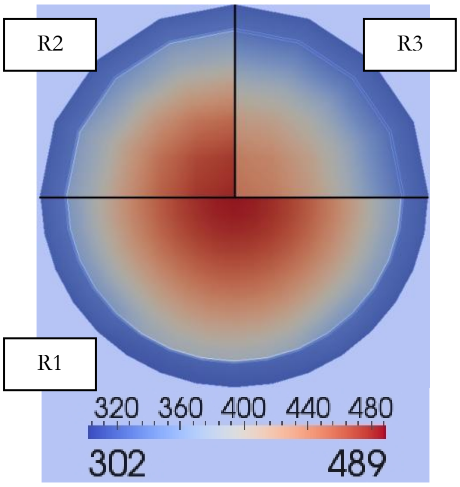

**Fig. 6-12. Comparison of the calculated temperature distribution in °C in a cross section of a fuel pin at 1.8 m elevation (Z direction) for different NHESDYN resolutions (R1, R2 and R3).**

For the radial boundaries of the TH domain a symmetry condition is set, the code considers that there is an equal domain in the normal direction across the walls. For the NK domain a similar condition has to be set. The radial boundaries of the of the single pin model are set to totally reflective, the NK code considers the domain as an infinite FA. This measure leads to the calculation of quite high $k_{eff}$ eigenvalues during the steady state, in the range of 1.28.

Fig. 6-13 illustrates the $k_{eff}$ value evolution as a function of the iteration for a steady state case. In this figure the comparison of the result of DYNSUB and different NHESDYN resolutions (R1, R2 and R3) is shown. Due to the simplicity of the case, the steady state calculation has a rapid convergence after only 4 iterations for the NK code. For the NHESDYN solution, the CFD code is not converging as fast. For each one of the time steps the DYN3D_SP3 changes the power map and the TH has to adapt to the new conditions. In this specific case the TH tools executed around 360 iterations in total to reach convergence. The poor Doppler prediction of configuration R3 yields the highest deviation in the values compared to DYNSUB. Case R1 provides better results in terms of $k_{eff}$ compared with the reference.

For the coupled solution, before starting the transient and to adjust the reactivity for a critical state, the value of the K-effective must be normalized. During the transient scenario iterations the deviation to this value is monitored to ensure that is never higher that the imposed criteria ($k_{eff}$ relative error $< 10^{-5}$). An example of this deviation can be found in annex E.

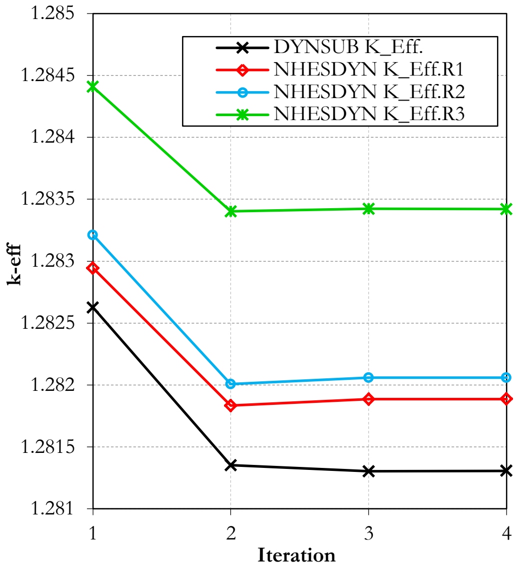

**Fig. 6-13. Comparison of $k_{eff}$ during the iteration of the steady state calculation predicted by both DYNSUB and by NHESDYN with three different resolutions (R1, R2 and R3).**

## 6.5 Transient cases

Some transient scenarios are designed to prove the robustness of the coupled solution. These are thermal initiated transients that modify the TH properties and analyses the NK interactions. The variations of the TH boundary conditions of the flow are controlled by NEPTUNE_CFD and they originate a reaction in the power calculation of the NK code. Those changes in the boundary conditions are performed on: The moderator inlet temperature, with a sudden decrease of 10 degrees; The moderator mass flow rate, with two cases, a sudden increase of the 7% of the nominal values and a progressive decrease to the 50 % of nominal conditions; The system pressure, a depressurization is perfumed to decrease the saturation temperature and produce VF in the domain. The initial conditions for the transient scenarios are shown in Tab. 6-1, taken from the previous converged steady state based on the OECD/NEA and US NRC PWR MOX/UO2 core transient benchmark (128). The simulations performed and what mesh refinement has been applied for each one are summarized in Tab. 6-4.

**Tab. 6-4. Transient simulations performed and the mesh refinement applied in each case.**

| | Mesh | N° cells in gap | Thermally initiated transient cases performed. |
|---|---|---|---|
| Run_1 (R1) | refined | 2 | Temperature, mass flow and pressure |
| Run_2 (R2) | coarse | 2 | Temperature, mass flow and pressure |
| Run_3 (R3) | coarse | 1 | Temperature and mass flow |

### 6.5.1 Transient case: temperature step

A simple transient case is set to probe the physical behaviour of the coupled solution. The inlet temperature is decreased suddenly 10 degrees from the initial 560 °K (Fig. 6-14). This condition remains 6 second then the temperature returns back to nominal conditions. This is not a realistic scenario that can be found in a PWR but it imposes a severe boundary change to investigate the robustness of the code. The cold mass of fluid increases the moderator density and improves the moderation; as a consequence a power rise should occur. This case is tested with the three proposed resolutions of NHESDYN (R1, R2 and R3) and with DYNSUB as a reference.

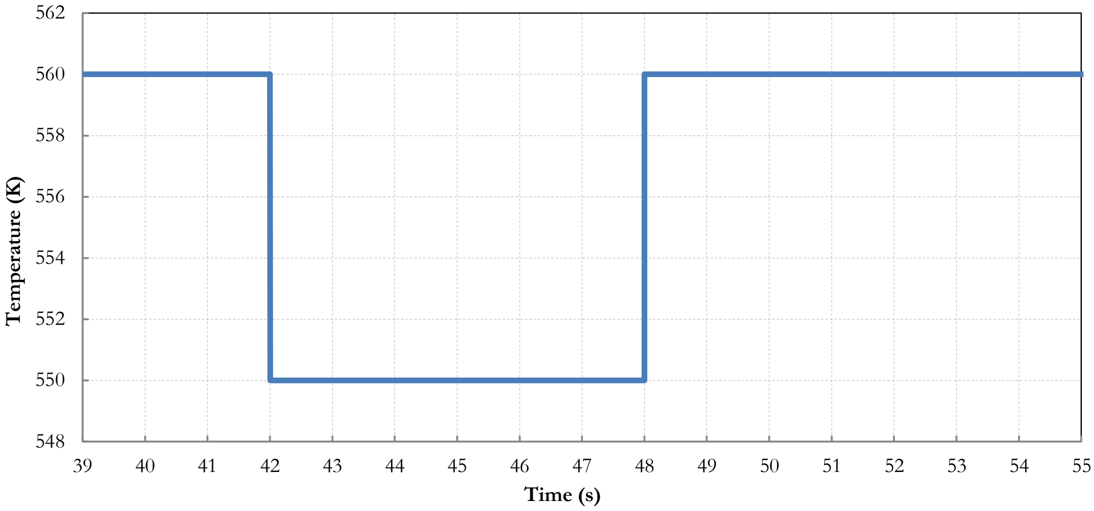

**Fig. 6-14. Water temperature evolution imposed at the inlet purposed for the transient case analysis.**

For this transient scenario the total pin averaged Doppler temperature is shown in Fig. 6-15. To follow the evolution of the moderator, the total averaged moderator temperature is shown in Fig. 6-16.

In Fig. 6-15 The Doppler temperature before the temperature step starts (second 42) has a good match for cases R1 and R2. For the case R3 this difference is quite big, reaching 24 degrees. This big deviation has been already observed in steady state and is connected with the single node for the gap modeling. For cases R1 and R2 the Doppler temperature has a good match with the reference. What happens if the DYNSUB code uses its default HTC instead of the one calculated by NHESDYN is shown in annex E.

The total averaged moderator temperature in Fig. 6-16 doesn't have big difference in any of the cases, with a maximum deviation of 3 degrees in the worst case. The refined discretization provided by case R1 has a better agreement with the reference. The time evolution has a quick reaction in the case the DYNSUB where the temperature changes as soon as the inlet temperature step occurs (seconds 42 and 48). For the NHESDYN code this change is not so fast, and the changes start with a ¼ of second delay.

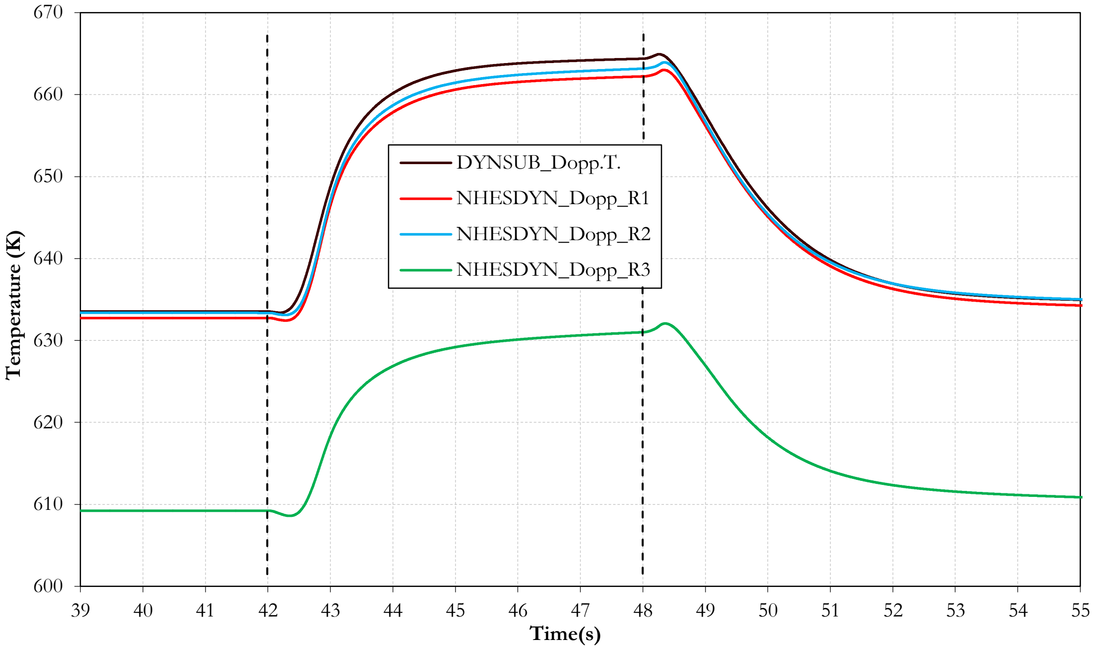

**Fig. 6-15. Comparison of the pin averaged Doppler temperature computed with DYNSUB and with NHESDYN using three different resolutions (R1, R2 and R3).**

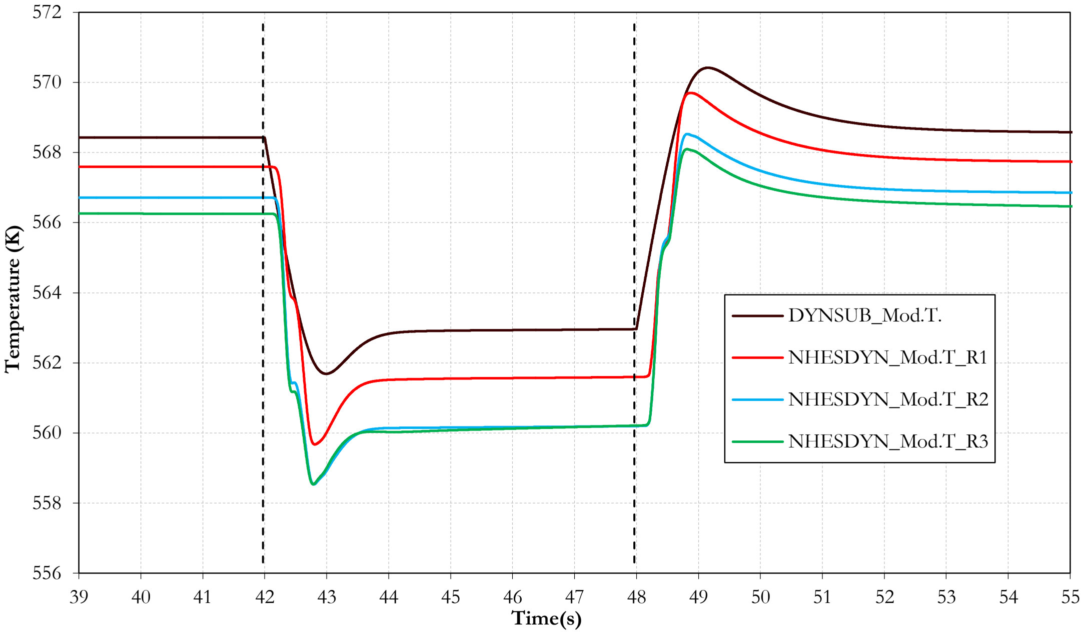

**Fig. 6-16. Comparison of the volume averaged moderator temperature predicted by DYNSUB and by NHESDYN using three different resolutions (R1, R2 and R3).**

To have a better idea of the behaviour of the different calculations the local Doppler temperature is monitored at three axial levels, located at: 0.07, 2 and 3.63 m height from the inlet. The first and the last axial levels can be considered the inlet and outlet of the domain. The results for the axial levels are shown in  Fig. 6-17 and Fig. 6-18. This time only the results provided by the refined discretization (R1) are included. Actually the results calculated by coarse mesh R2 match with the R1 data. The results provided by R3 are neglected due to its previously demonstrated lack of accuracy especially in the prediction of temperatures in pellet. For the first and the last axial level (Fig. 6-18) deviation against the DYNSUB code is about four degrees overpredicted for the first axial level and one degree under predicted for the last axial level. This information can be compared with the steady state data of Fig. 6-4, where the Doppler temperature predicted by NHESDYN agrees with the reference but it is above the DYNSUB data for the firsts axial levels and slightly below for the last ones. For the axial location 2 ( Fig. 6-17), the local Doppler temperature is matching well towards the reference.

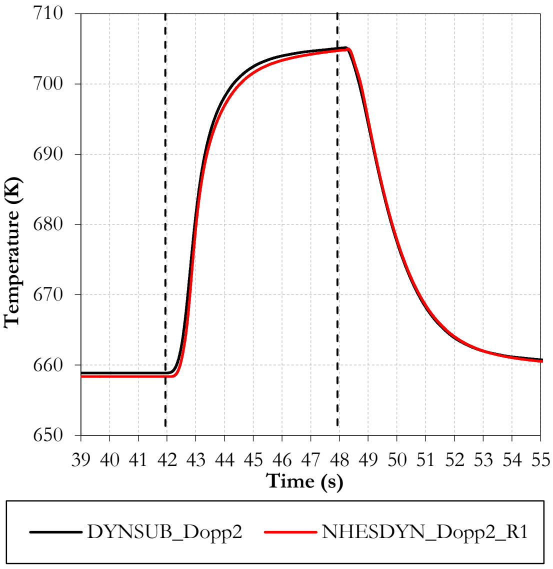

**Fig. 6-17. Comparison of the local evolution Doppler temperature at axial location 2 (Z=2 m) predicted by NHESDYN R1 and DYNSUB..**

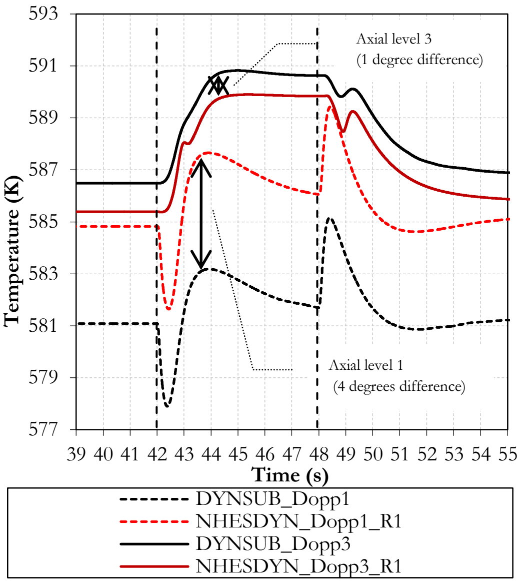

**Fig. 6-18. Comparison of the local evolution Doppler temperature at axial locations 1 (Z=0.07 m) and 3 (Z=3.63 m) predicted by NHESDYN R1, R2 and R3 and by DYNSUB.**

The evolution of the corresponding water density is illustrated as a function of the axial height in Fig. 6-19. For the CFD code that provides the TH information, the temperature and the density are calculated like averaged values for the entire axial level. This calculation is done according to Eq.(5-1). For the refined mesh (R1) there are 60 axial values and for the coarse mesh (R2 and R3) there are 44 axial values. For the SCF code the TH information is calculated in a similar way. The value for the temperature and the density is obtained by averaging the data from the four surrounding nodes of the rod at the discrete axial level. For DYNSUB there are 27 axial values. The information is chosen from the axial level that fits better with the selected three axial heights (0.07, 2 and 3.63m). Hence, the axial levels of the codes don't match exactly because of the different scale of the nodalization. Fig. 6-19 is divided in three graphs, one for each selected axial height.

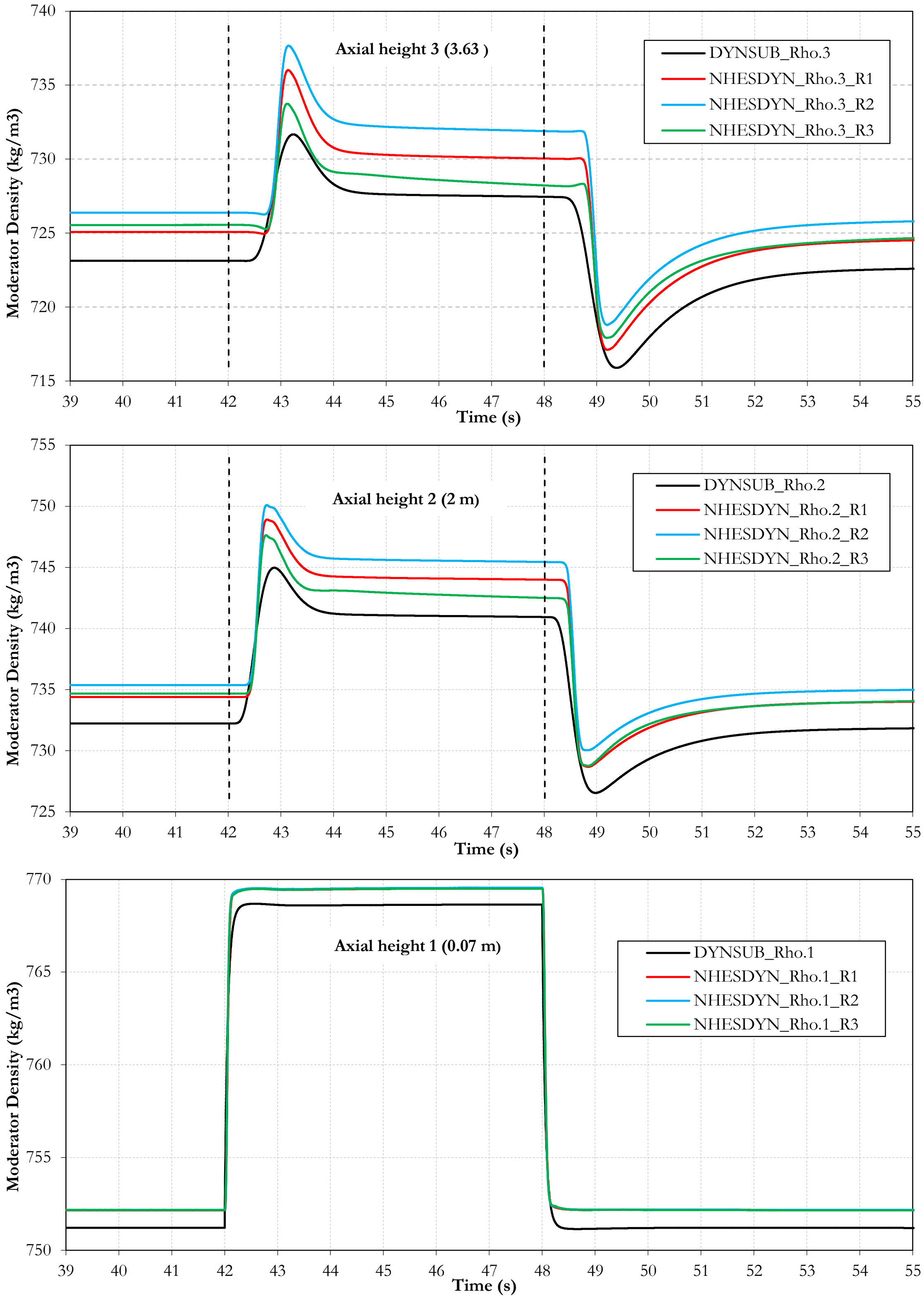

**Fig. 6-19. Comparison of the local moderator density evolution for three heights in the Z direction (0.07, 2 and 3.63 m) calculated by DYNSUB and NHESDYN with three resolutions (R1, R2 and R3).**

The densities exhibit a good agreement between NHESDYN and DYNSUB, especially for the first axial level which is not affected by the power changes due to the feedback. Here a mismatch in the water densities predicted by the two codes exists even having the same temperature. Both codes use the same water/steam tables (125), this difference can be explained due to the different mesh resolutions. Nevertheless the difference is not higher than 1 kg/m$^3$. Both codes simulate the same amplitude for the temperature and density change. As the axial elevation increases deviations are evolving and NHESDY calculates higher values compared with the reference. The results provided by the resolution R3 are closer to the DYNSUB values during the temperature step, the density values are lower because more power is generated as illustrated in Fig. 6-22. But during the null transient conditions (before second 42) R1 shows a constant deviation of one degree, with a better behave than R2 and R3.

Concerning the time the TH changes are apparently started with some delay for the CFD code. The density changes calculated by SCF have smoother shapes and slopes. On other hand the NHESDYN provides more sharp slopes during the transient for the same situation. Again DYNSUB show a faster reaction to the TH changes, NHESDYN has a few tenths delay in comparison.

To check the correctness of the conjugated heat transfer between the TH tools (NEPTUNE_CFD/SYRTHES) of the new coupled solution, the total flux at the interface solid-liquid and the total power received by SYRTHES in the fuel domain is depicted in Fig. 6-20. For simplicity only configuration R1 is shown. This figure demonstrates that in steady conditions the heat flux generated in the fuel domain is conserved through the gap and clad to reach the fluid domain with no important numerical leakages. During the power peak the flux at the interface is damped by thermal inertia and after some seconds both fluxes tend to join again. At the beginning of the temperature step, the flux at the interface increases even before the flux at the fuel. This is because the moderator temperature decreases improving the heat transfer coefficient.

The evolution with the time of the reactivity of the case is shown in Fig. 6-21. The most notorious effect is the small reactivity peak that appears just before the power returns to nominal conditions, this peak in reproduced only by NHESDYN. The Effect is related to the small delay in the TH moderator temperature calculated by NHESDYN.

Fig. 6-22 shows the power provided by DYN3D_SP3 during the transient for the DYNSUB and for the different configurations of NHESDYN. Again, the simulation R1 and R2 match almost perfectly between each other but there some little differences during the power peak. Compared with the DYNSUB results, R2 provides 1.55% less power and R1 1.03% more power at the power peak (second 43). Simulation R3 provides more power after the peak according to a lower Doppler temperature.

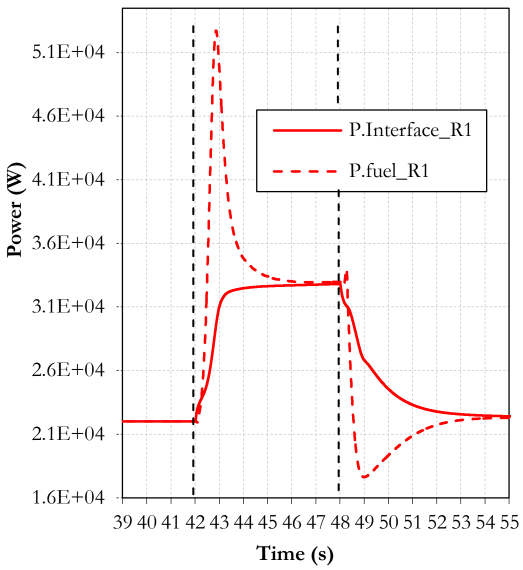

**Fig. 6-20. Time evolution of the power flux produced in the fuel and total flux at the interface solid-liquid for NHESDYN R1.**

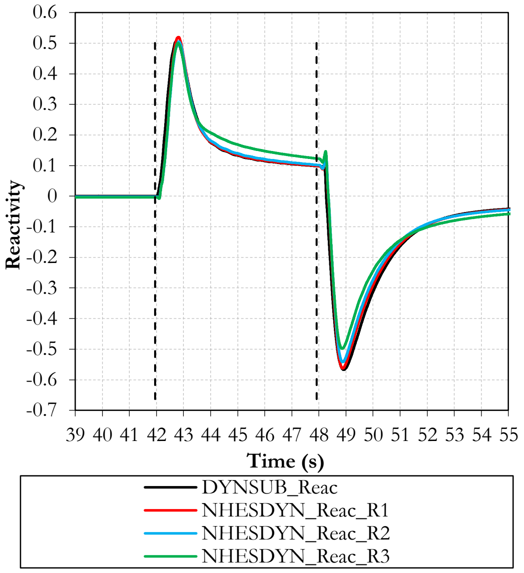

**Fig. 6-21. Comparison of the reactivity evolution predicted by DYNSUB and NHESDYN using the three different resolutions (R1, R2 and R3).**

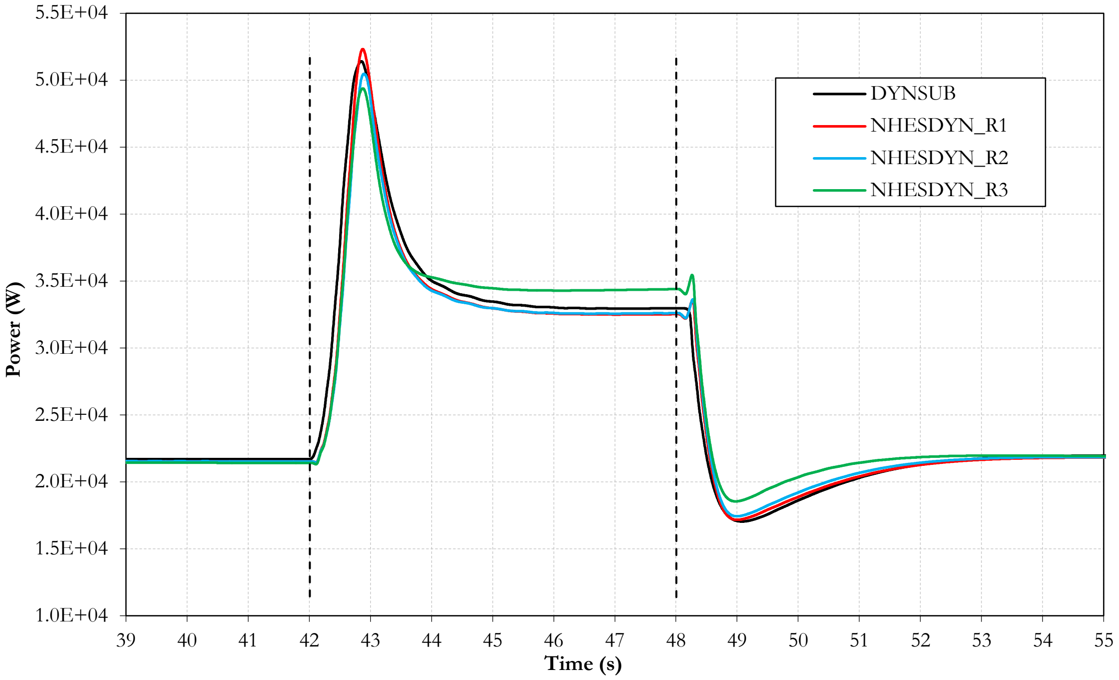

**Fig. 6-22. Comparison of the total power evolution predicted by DYNSUB and NHESDYN using different resolutions (R1, R2 and R3).**

### 6.5.2 Transient case: Mass flow variation

This transient case assumes a variation of the moderator mass flow rate. It is divided in two cases. The first is a temporal mass flow increase with a step shape; this increase is about the 7% of the nominal conditions. The second is a temporal and progressive decrease of the mass flow to the 50% of the nominal conditions.

#### 6.5.2.1 Fast mass flow rate variation

To prove the code robustness a severe step change in the inlet mass flow is tested. The mass flow rate is increased a 7% of the nominal value during 10 seconds (Fig. 6-23), then it returns to nominal conditions.  By increasing the mass flow rate an improvement of the moderator is expected followed by an increase of the reactivity and power. This case is simulated with the three purposed resolutions of NHESDYN (R1,R2 and R3) and with DYNSUB as a reference.

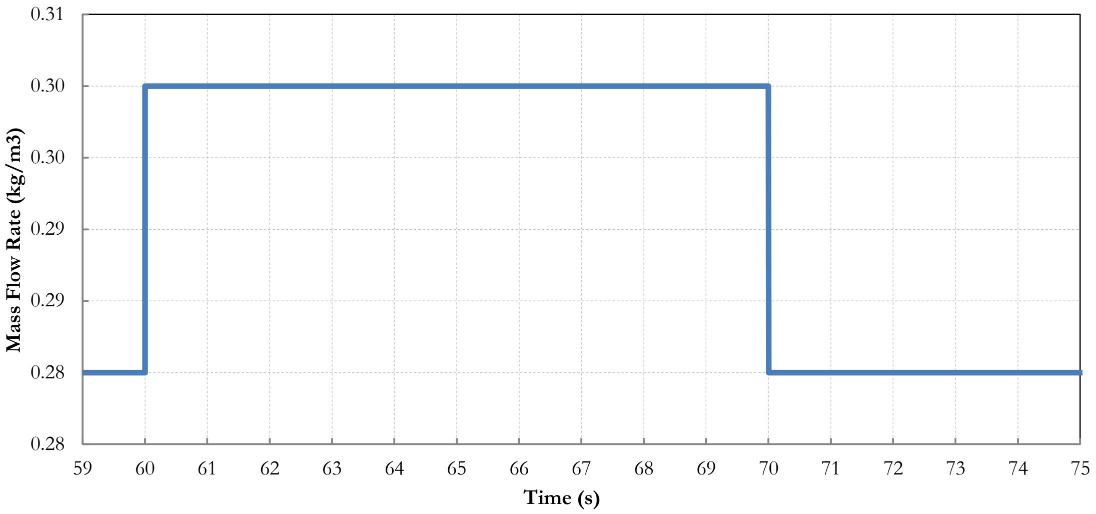

**Fig. 6-23. Anticipated Mass flow rate evolution purposed for the transient case analysis.**

In Fig. 6-24 the comparison of the temporal evolution between the power calculated by DYNSUB and the different resolutions of NHESDYN (R1, R2 and R3) is shown. For this case the power seems to be lower for the NHESDYN code. Here the scale is quite detailed and the relative error is in the range of the 1%.

Fig. 6-25 shows the balance between the heat flux generated in the fuel and the total heat flux registered at the interface clad-moderator. The data in the figure corresponds to the refined resolution of the case NHESDYN R1. As is expected when the mass step takes place a sudden increase of the heat flux happens at the interface because the HTC is suddenly improved. After some seconds the equilibrium between the flux generated and transferred is achieved by the balance of the energy.

In this scenario the codes (specially the CFD) struggle in the mass and momentum balance which provokes some oscillations in the system. Nevertheless, the oscillations are quickly damped.

The reactivity calculated for this case is illustrated in Fig. 6-26. The NHESDYN simulation with the refined resolution (R1) has a better agreement with the reference.

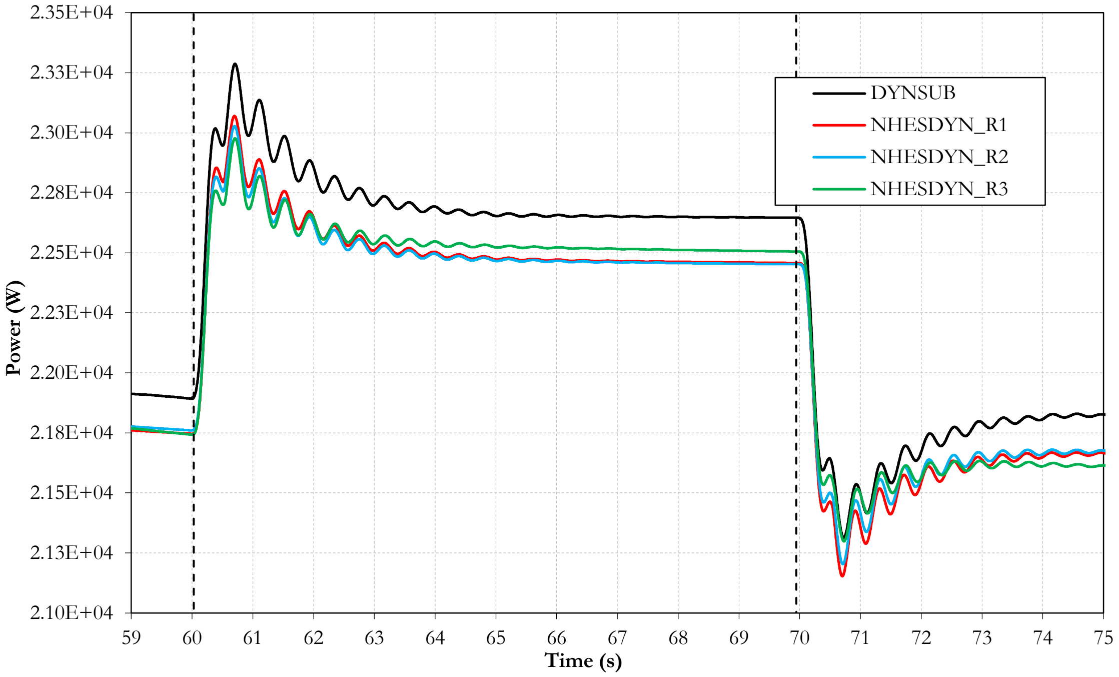

**Fig. 6-24. Calculated power evolution. Comparison for DYNSUB and different NHESDYN resolutions (R1, R2 and R3).**

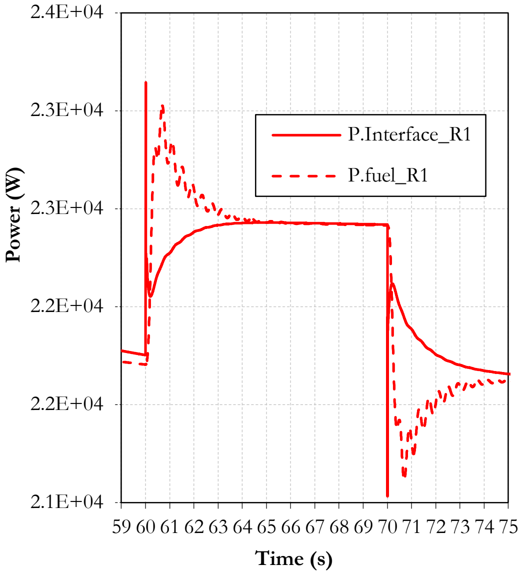

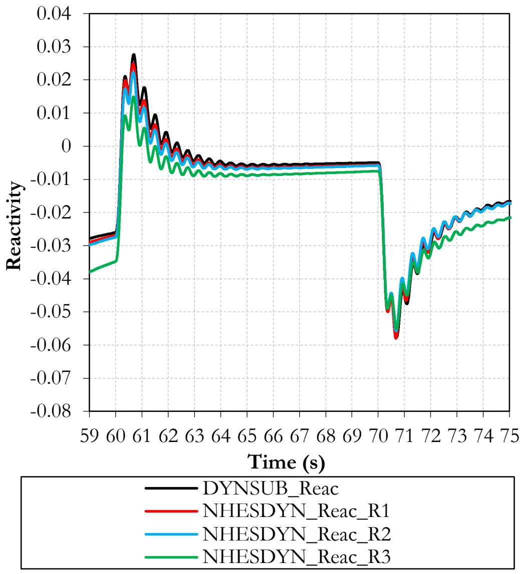

**Fig. 6-25. Time evolution of the heat flux produced in the fuel and total flux at the interface solid-liquid for NHESDYN R1.**

**Fig. 6-26. Time evolution of the system reactivity. Comparison for DYNSUB and different resolutions of NHESDYN (R1, R2 and R3).**

#### 6.5.2.2 Slow mass flow rate variation

Another scenario regarding the mass flow variation at the inlet is tested. This time a 50% gradual decrease of the nominal mass flow rate occurs, from 0.28 kg/s to 0.14 kg/s. After four seconds it returns to nominal conditions (Fig. 6-27).

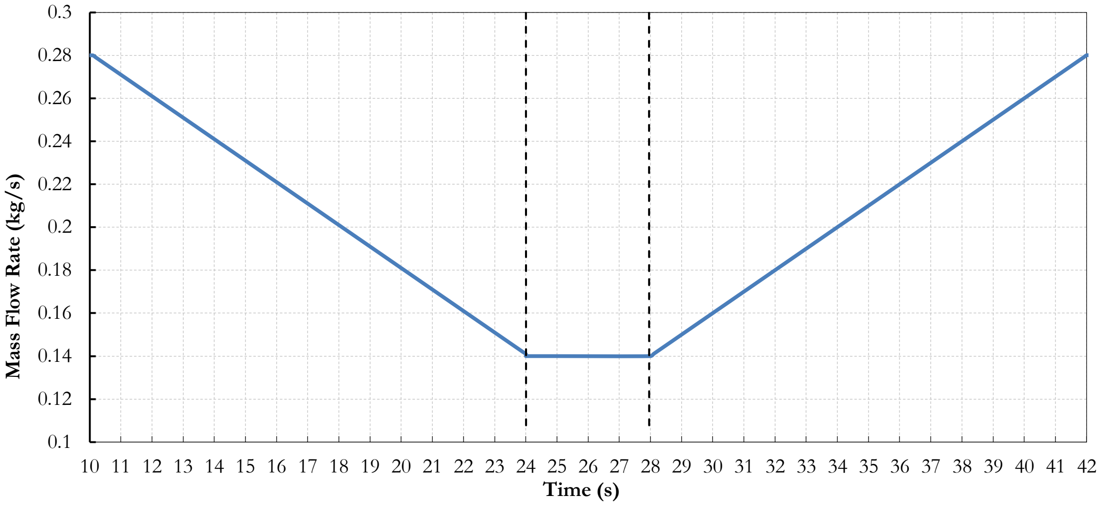

**Fig. 6-27. Mass flow rate evolution purposed for the transient case analysis.**

This transient represent a more realistic scenario than the previous mass flow rate step, (e.g. a recirculation pump trip leads to a gradual mass flow decrease). This case is simulated with two purposed resolutions of NHESDYN (R1 and R2) and with DYNSUB as the reference. This time, the single node for the gap modeling configuration (R3) is refused due to its lack of accuracy. The comparison is focused on the behaviour of the code for the refined and coarse mesh of NHESDYN. It is expected that the decrease of the mass flow decreases the moderator density leading to a power decrease.

The evolution of the prediction in the moderator temperature for two axial eights (2 and 3.63 m) is illustrated in Fig. 6-28. In this figure, the first axial level (0.07 m) is omitted because the data is the constant inlet temperature (560 degrees Kelvin). Compared with DYNSUB a better match is reached by the refined mesh of NHESDYN (R1) where only a deviation of 0.2 degrees is registered. But no big differences are registered with the coarse mesh (R2) either in the axial height 2 (2m) or 3 (3.63m).

Fig. 6-29 illustrates the local Doppler temperature at the axial height of 2 m. The differences in the predictions are quite small. There is a constant two degrees deviation where the NHESDYN code is overestimating the temperatures. For this case there are no visible differences in the results provided from simulations R1 and R2.

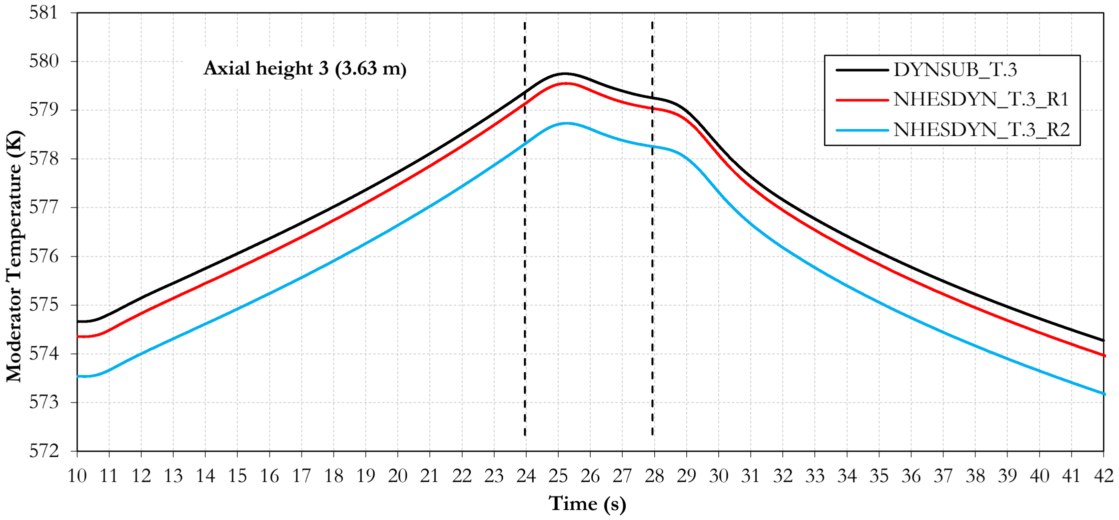

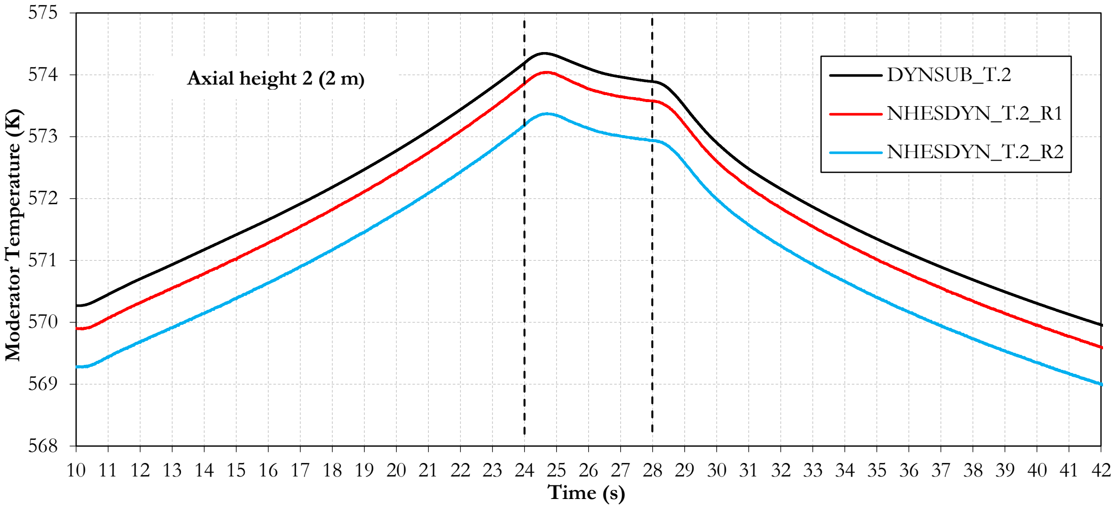

**Fig. 6-28. Comparison of the moderator temperature evolution for two heights in the Z direction (2 and 3.63 m) predicted by DYNSUB and NHESDYN with two different resolutions (R1, R2).**

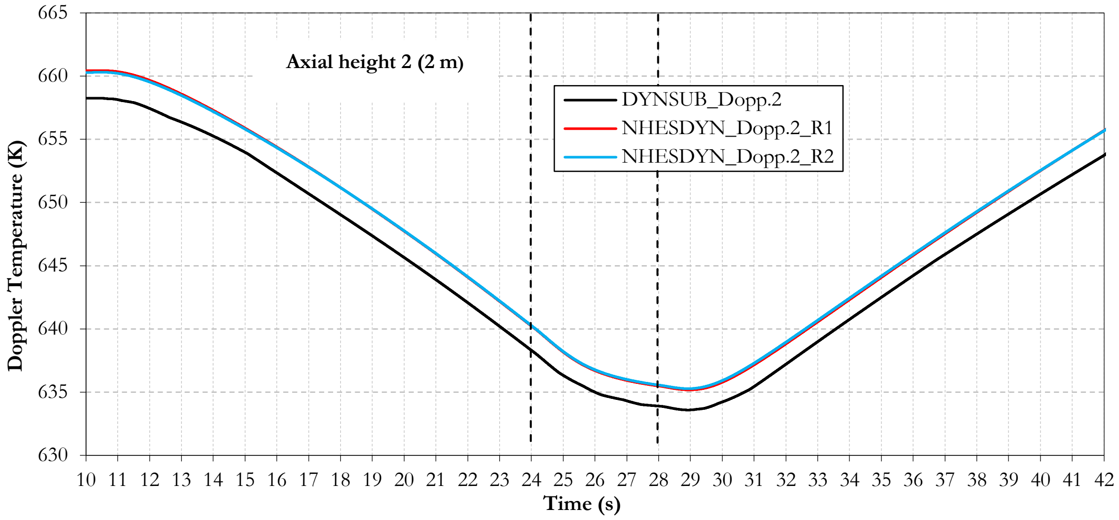

**Fig. 6-29. Comparison of the local Doppler temperature evolution during the transient at the axial eight 2 (2m) predicted by DYNSUB and NHESDYN using two different resolutions (R1 and R2).**

In terms of power, in (Fig. 6-29) the values for the total pin power show a very good agreement for both NHESDYN testes cases (R1 and R2) with the reference DYYNSUB.

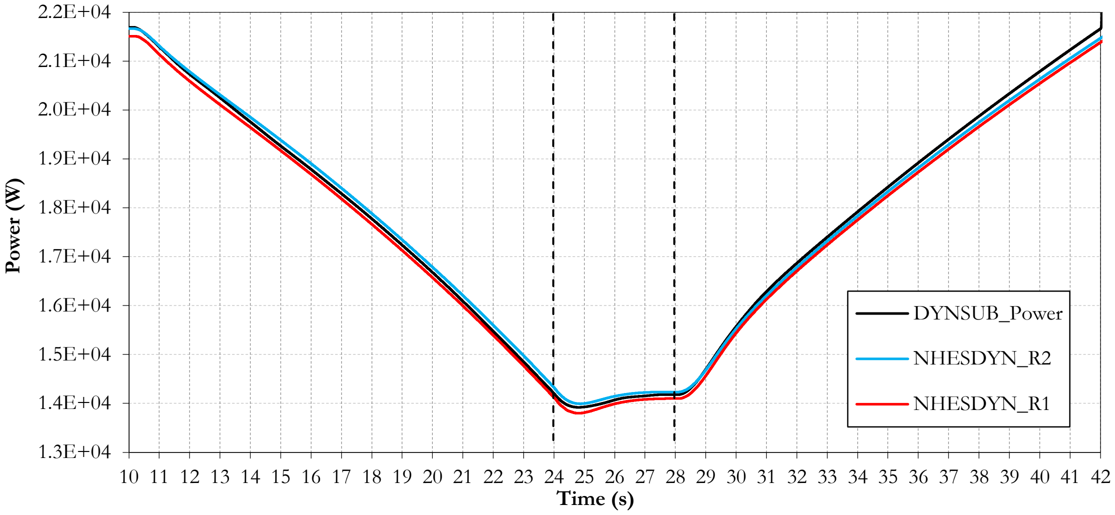

**Fig. 6-30. Comparison of the power evolution calculated by DYNSUB and NHESDYN using two resolutions (R1 and R2).**

### 6.5.3 Transient case: Depressurization

A depressurization scenario is simulated with the coupled solution to investigate the behaviour of the code with the presence of void in the domain. For PWR the depressurization is expected if failure occurs in the pipe system. The pressure drops and when the saturation temperature is reached boiling happens.

A pressure guided transient is performed. With constant inlet temperature and mass flow according to Tab. 6-1, the domain is depressurized to 7.1 MPa from its initial 15.5 MPa. At this pressure the moderator has already reached the saturation temperature and VF appears in the domain. Then a pressure oscillation is reproduced to force the saturation temperature oscillate and consequently the void generation.

Like in the previous case, two configurations of the NHESDYN code are disposed for this test, R1 (refined mesh resolution) and R2 (coarse mesh resolution). Additionally the reference results are provided by DYNSUB.

When the void appears, large density gradients in the moderator are expected. The decrease of the density of the moderation leads to a decrease of the power generated. On the other hand if the moderation is improved an increase in the power is expected.

Fig. 6-31 shows the evolution of the absolute pressure, which is set at the outlet of the studied domain.

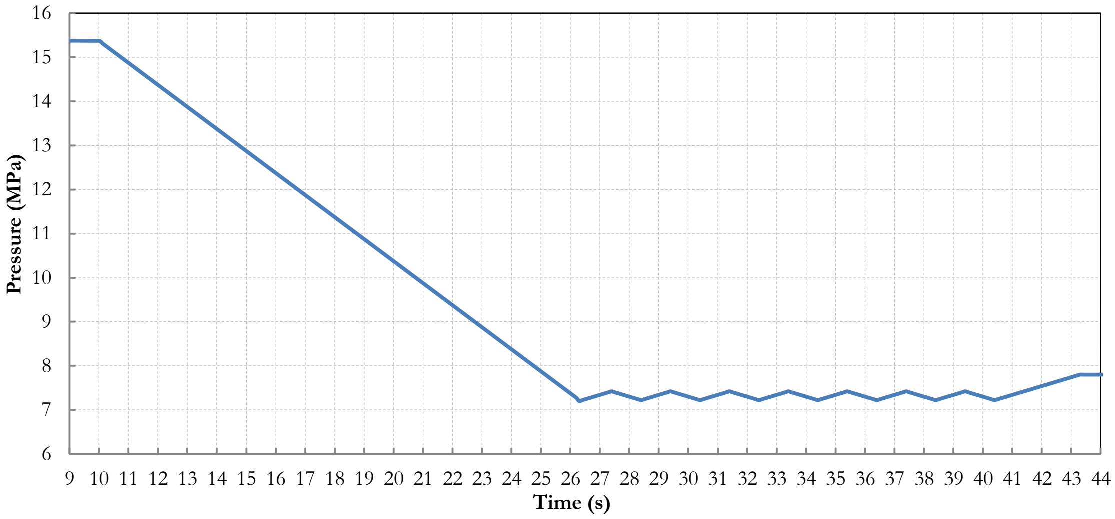

**Fig. 6-31. Outlet pressure imposed by NHESDYN during the transient.**

When the pressure reaches saturation temperature (second 24.5) boiling starts, see Fig. 6-32. This figure illustrates the void generation at the axial eight of 3.63 m, close to the outlet of the domain for two resolutions of the NHESDYN code (R1 and R2). The driven oscillations of the outlet pressure lead to variation in the void generation. As expected the refined mesh provided by case R1 starts boiling before and generates more void than the coarse mesh provided by case R2. Those differences are observed in the moderator density.

The local density evolution for two axial heights of the domain (2 and 3.63 m) is illustrated in Fig. 6-33. Differences in the density evolution between codes are small. Compare to the reference better agreement is reached the coarse resolution of NEHSDYN (R2) for the axial height located close to the outlet (3.63m). For the axial height of 2 m the refined mesh (R1) match better with the reference especially during the first VF peak (second 26.5).

Before the boiling starts (before second 24) the moderator density decreases due to the pressure decrease, this facts provides negative reactivity and the power decreases to (Fig. 6-34). As a consequence the total averaged Doppler temperature and later the total averaged moderator temperature decrease, Fig. 6-35 and Fig. 6-36.

When boiling starts (second 24.5) sudden power decrease occurs due to the negative reactivity provided by the moderator density (Fig. 6-34), followed by the total averaged Doppler and total averaged moderator temperatures, Fig. 6-35 and Fig. 6-36.

During the pressure oscillation the void generated oscillates with its effect on the moderator density and power. The power peaks fit in time with the guided pressure peaks which increase saturation temperature and moderation of the system.

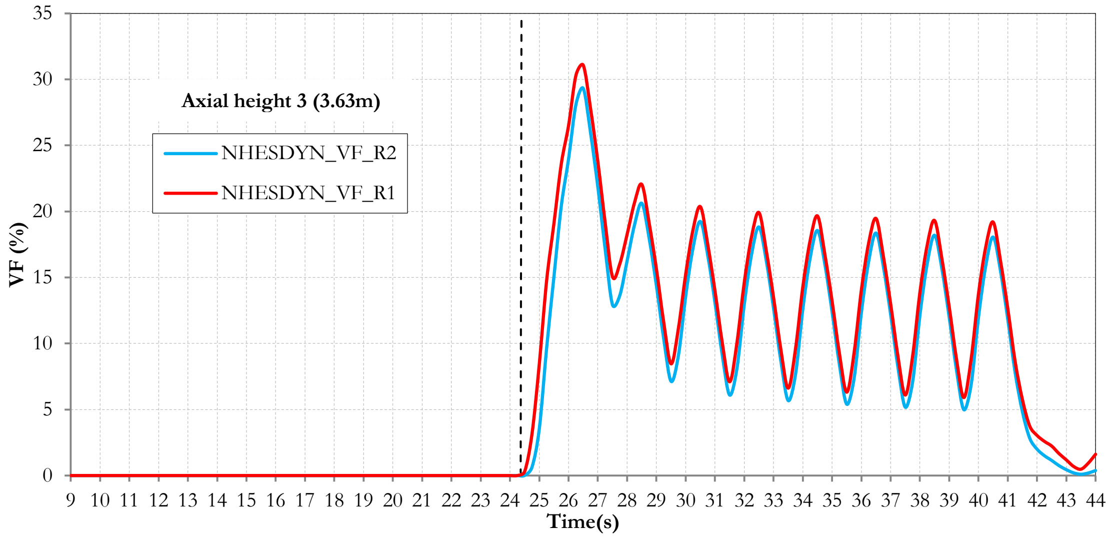

**Fig. 6-32. Local VF predicted by two NHESDYN resolutions (R1 and R2) at the outlet during the transient.**

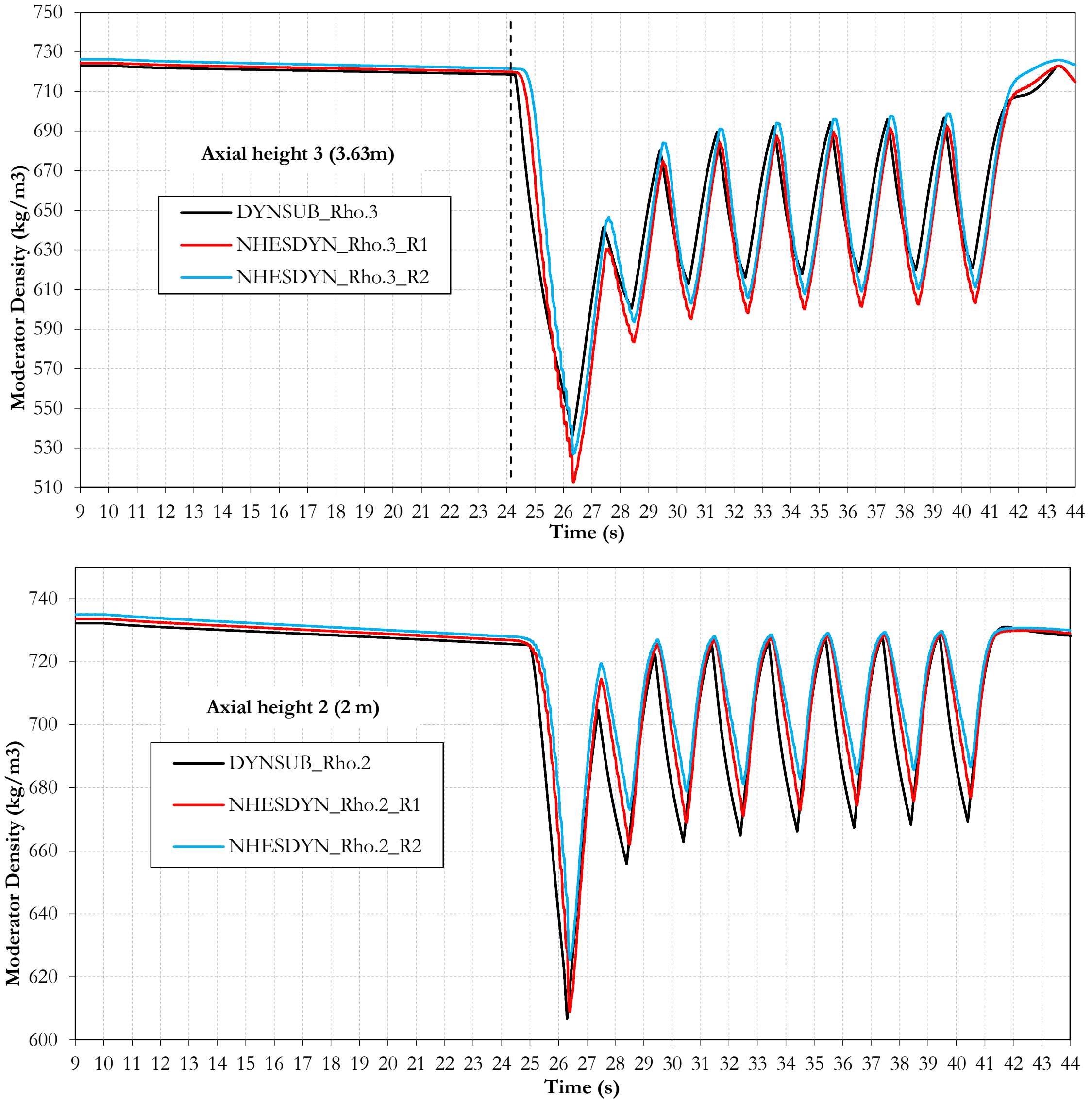

**Fig. 6-33. Comparison of the local moderator density evolution for two axial heights in the Z direction (2 and 3.63 m) predicted by DYNSUB and NHESDYN using two resolutions (R1 and R2).**

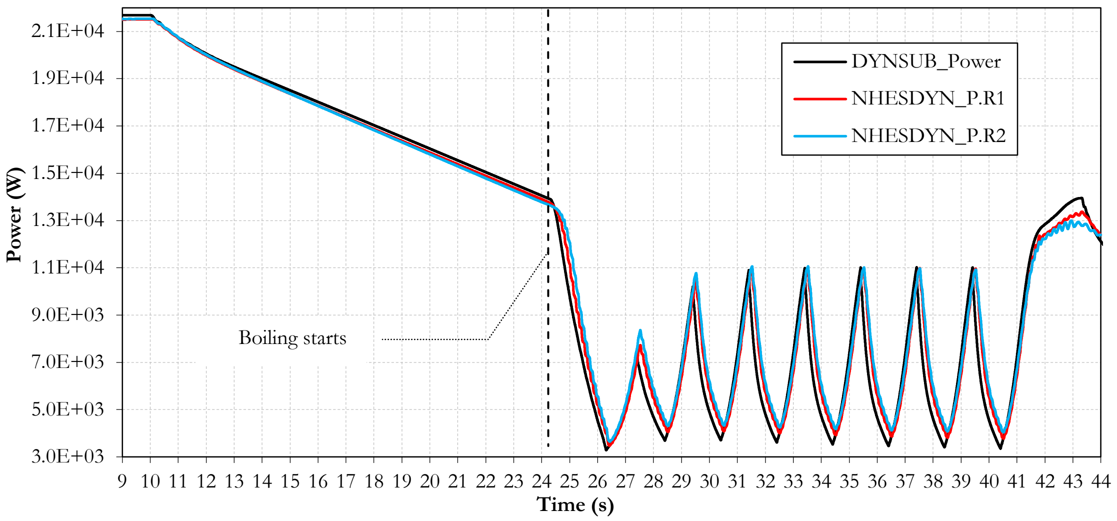

Fig. 6-34. Comparison of the power evolution for the depressurization transient scenario calculated with DYNSUB and NHESDYN using two resolutions (R1 and R2).

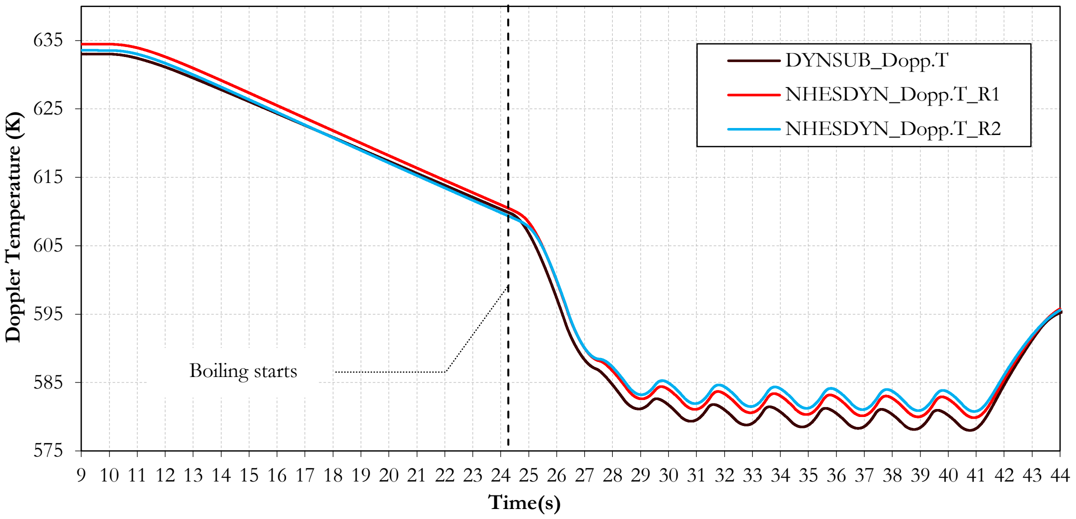

Fig. 6-35. Comparison of the total averaged Doppler temperature evolution predicted by DYNSUB and NHESDYN using two resolutions (R1 and R2).

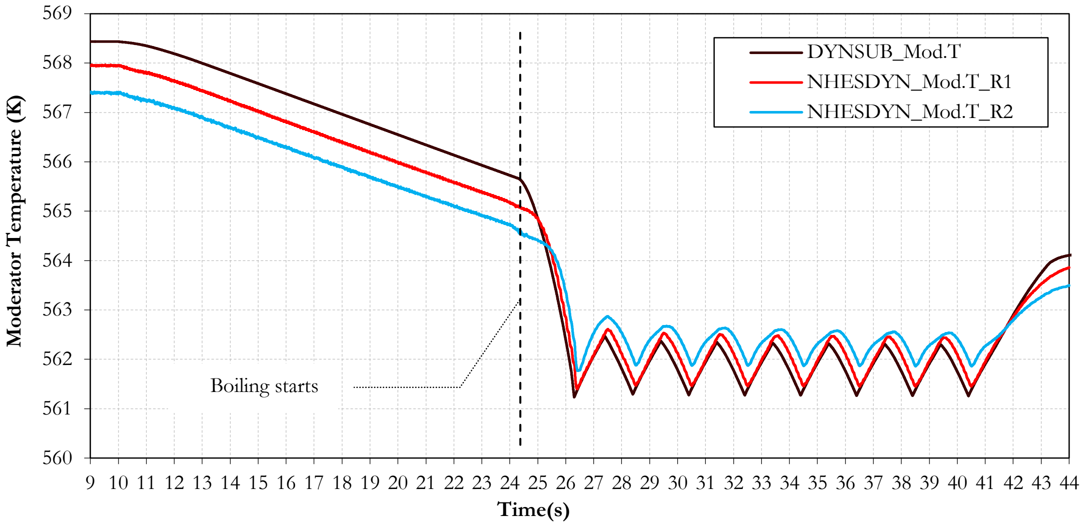

Fig. 6-36. Comparison of the total averaged moderator temperature evolution predicted by DYNSUB and NHESDYN using two different resolutions (R1 and R2).

For the averaged total Doppler temperatures (Fig. 6-35) there is a constant 2-3 degrees overprediction, refined case (R1) is closer to the reference, this NHESDYN resolution predicts also the moderator temperature better than case coarse resolution (R2) during the transient (Fig. 6-36).

## 6.6 Summary and conclusions of the tested cases

The code NHESDYN has been verified for tests with PWR conditions against the well validated coupled solution DYNSUB. For the simulation performed both codes (NHESDYN and DYNSUB) shares the same material properties for the simulations based on the information provided by the OECD/NEA and US NRC PWR MOX/UO2 core transient benchmark (128). The tests selected are a temperature, mass variation in the moderator and a system pressure variation. The code behaviour has been satisfactory for all the considered tested cases. The code capability to solve slow thermal transients can be conceived as demonstrated.

The simulations show a strong sensitivity to the gap modeling. The DYNSUB code uses a constant HTC for solving the gap heat transfer, while the SYRTHES models the gap like a solid with the Helium properties. The nodalization of this domain is conditioning the evolution of the simulation as being demonstrated by comparing the cases R1 and R2 (two nodes at the gap) against case R3 (one node in the gap). A correct code comparison is only achieved by implementing similar gap models for both codes. Originally during the null transient there was 5 degrees difference in the Doppler temperature between DYNSUB and NHESDYN, this difference is explained by the different gap treatment. To demonstrate this, the averaged HTC for NHESDYN is calculated during the null transient. Then the new coefficient is implemented in the DYNSUB code for further simulations. This process improves the comparison between codes but is not expected to totally neglect the differences between them, mainly because DYNSUB uses a global HTC and NHESDYN calculates different values depending on the local parameters of the domain. This change of the coefficient makes the Doppler temperature to be in a good agreement between codes. A comparison for the default HTC used by DYNSUB and the new proposed is illustrated in Annex E.

The heat conduction problem in the fuel or clad doesn't have a big sensitivity to the space discretization. In NHESDYN refined mesh case R1 is providing similar temperatures to the coarse mesh case R2. The discretization provided by R2 is good enough and R1, even having the double number of cells in the radial direction, doesn't improve the results.

The fluid domain show a small sensitivity to the discretization. This is normal since the coupled code works with averaged values over cross sectional areas for each axial level of the pin geometry. The local temperature in the near wall region is strongly dependent on the nodalization, but when the values are averaged, the near wall region is weight together with the fluid temperatures at the bulk (central subchannel region), then the difference between discretizations decrease.

It was mentioned that axially the nodalizations of the code doesn’t match. This can be a deviation source, because the axial average operations done by the DYNSUB code deal with more volume than the NHESDYN code. Furthermore, the

To use the same material libraries is mandatory. A deviation in the results of the code to code comparison happens if this point is not respected. Heat capacity and conductivity depends on the temperature, density has been decided to be set as constant. The DYNSUB code uses constant density. This is due to the non-variation of the volume, the geometry is fixed and the effects of the temperature on the expansion of the material is not taken into account, the temperature is integrated over a constant volume and as a consequence it shouldn’t change significantly by effects of the density. This principle can be applied also to SYRTHES, because this is not a mechanical code and it works with constant nodalizations.

# 7 General conclusions

First of all, the validation basis of NEPTUNE_CFD has been extended by using LWR-relevant transient test data obtained in both a PWR-specific (NUPEC PSBT) and a BWR-specific (NUPEC BFBT) test facility. It is the first time that the two-phase flow models of NEPTUNE_CFD have been validated using transient data obtained for tests representing the LWR plant conditions of postulated transients like a turbine trip or a recirculation pump trip. This validation process has clearly shown the status of the two-phase flow modeling of NEPTUNE_CFD. According to the appreciations made after each simulated experiment in Chapter 4 it is possible to summarize the global conclusions about the NEPTUNE_CFD capabilities, identifying its strengths and weaknesses.

According to the interfacial exchange terms, the main flow regime currently implemented in NEPTUNE_CFD is the bubbly flow which is good enough to describe the flow with a certain void concentration. However, and especially in BWR the amount of void generated is beyond the limits of the bubbly flow and other flow regimes (slug flow or annular flow) must be taken into account for an accurate description of safety-relevant phenomena. How to model the transition between flow regimes describing a whole flow map is an open issue for CFD codes. In addition to the presented approach, other methodologies can be applied in order to achieve a description of the flow, like the volume of fluid method (VOF) that solves the two phase flow like a mixture and reconstructs the interface water/steam.

NEPTUNE_CFD cannot solve heat conduction. For that reason it is coupled with SYRTHES which is in charge of calculating the temperature in the solid domains (fuel and clad). The capabilities of the NEPTUNE_CFD working together with SYRTHES have been demonstrated by the prediction of the thermal inertia at the walls. By applying SYRTHES the simulations of the turbine trip are in better agreement with experimental data compared with the application of NEPTUNE_CFD standalone. In addition, this heat conduction solver helps to a reasonable control of steam and water temperatures in the near wall region by computing a proper HTC at the solid/fluid interface. The use of SYRTHES for the coupled solution is mandatory to solve the conjugated heat transfer between solid and liquid and it has a positive contribution to the NEPTUNE_CFD prediction capabilities. However, it is not parallelized and penalizes the computational time.

Due to the different mesh distribution applied for each code (tetra volumes for SYRTHES and hexa volumes for NEPTUNE_CFD) a carefully mesh design is required to match the nodes at the solid/liquid interface and have a good energy balance regarding the heat flux.

NEPTUNE_CFD includes an extension of the classical three fluxes approach for the boiling wall modeling. In addition to the convective, evaporation and quenching flux which are transferred from the wall to the liquid phase, when the VF exceeds the 80% at the wall, the flux is transferred to the steam phase. This model is under validation. According to the results obtained it contributes to the water temperature regulation avoiding excessive overheating.

The spatial discretization has a big influence in the CFD simulations. The design of the mesh affects the prediction of the VF and mesh sensitivity analyses are mandatory. A very refined mesh density especially near the heated wall is problematic regarding the water and steam temperature prediction. The near wall cells must have the right size to solve the heat transfer problem properly without penalizing excessively the $y^+$ values.

According to the results obtained during the validation process, the subcooled and saturated boiling description can be considered sufficient enough in its range of applicability. NEPTUNE_CFD has demonstrated to be good TH tool which has the state of the art in two phase flow modeling for LWR applications.

Furthermore, the validation of NEPTUNE_CFD previous to the development of the coupling approach between NEPTUNE_CFD and DYN3D_SP3 has been important to investigate the optimal spatial nodalization of fuel rod clusters and the surrounding fluid requested for the accurate prediction of the feedback parameters in the frame of coupled simulations.

Secondly, a novel coupling scheme between the NEPTUNE_CFD/SYRTHES code and the transport code DYN3D_SP3 in the frame of a parallel environment (MPI-based) has been developed, tested and validated. The new coupled code, named NHESDYN, permits in principle to perform high-fidelity multi-physic simulations describing the TH phenomena in a multi-scale sense e.g. at a micro- and meso-scale. By this way the prediction of local safety parameters such as clad temperature, pin power, etc. are feasible using a refined space discretization if demanded. The coupled code NHESDYN has been tested extensively to demonstrate the programmed information exchange between the involved computational domains operating consistence and it is predicting physical sound results. In addition, the stability of the coupled code NHESDYN has been analysed together with the handling of different boundary conditions that allow the simulation of transient cases. NHESDYN shows a stable behaviour and the communication between the different modules is proved to be consistent. The code has enough robustness to deal with rapid boundary changes like sudden inlet or mass flow changes which are challenging transient scenarios especially for a CFD code.

The steady state analyses provide satisfactory result for the moderator and fuel, with a good agreement with the reference code regarding the axial and radial temperature profiles. The convergence loop for the steady state works properly and ensures a converged solution as initial condition for transient simulations. The designed main program drives properly the transition steady state to transient.

During the transients a small time delay in the calculated TH by NHESDYN for the temperatures of the moderator are observed compared with the DYNSUB predictions.

This delay evolves with the axial elevation and its due the different discretization applied for the TH tools (NEPTUNE_CFD and SCF). NHESDYN is able to compute the axial heat conduction in the pin providing smooth axial temperature profiles compared with DYNSUB which leads to differences in the TH predictions.

The overall prediction capability of NHESDYN has been demonstrated by the validation process where both steady state problems and transient test cases have been analyzed.

# 8 Outlook

Despite the reasonable well NHESDYN predictions with respect to the selected validation cases and compared to DYNSUB results, further effort is necessary to fully explore its prediction accuracy and potentials. Further investigations should be performed to tackle the following areas:

- Extension of the coupling scheme for the analysis of boron dilution transients in PWR cores or fuel pin arrangements.
- Simulation of BWR relevant transient cases for fast (e.g. rod drop accidents) and slow transients such as pressure, coolant temperature and coolant mass flow rate perturbations e.g. the BWR Turbine Trip Benchmark (129)
- Extension of the pin model to pin clusters (Fig. 8-1). The radial mapping of the case is mandatory. By this extension more variables can be analysed (cross flow, radial power feedbacks, etc.)

Taking advantage of parallel computing it is feasible to perform high fidelity simulations of fuel rod clusters and large problems in a very detailed spatial resolution. At present, the size of the problems to be analyzed by NHESDYN is limited by the SYRTHES code which requires high computational time even for small problems. since it is well known that commercial CFD codes are numerically robust and more user friendly than research codes like NEPTUNE_CFD, the replacement of NEPTUNE_CFD and SYRTHES e.g. by ANSYS CFX or FLUENT may be very promising for the analysis of larger problems in combination with the used of massive parallel computers.

Finally, the modularity of the developed coupling scheme makes possible to implement of a Monte Carlo transport code instead of DYN3D_SP3 so that the coupled system can be run fully in a parallel mode in the frame of high fidelity simulations for reactor design and safety.

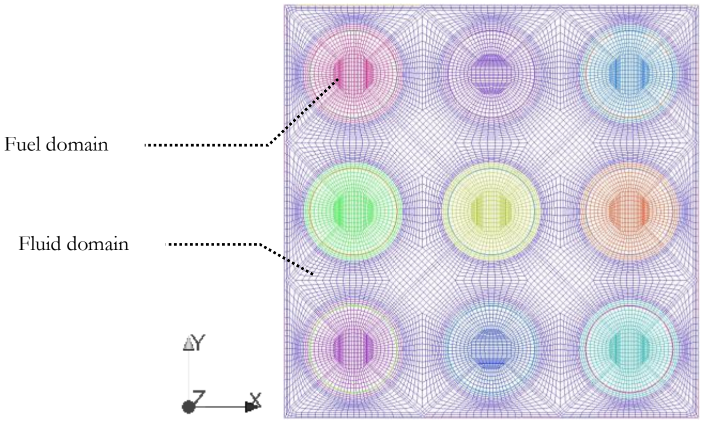

**Fig. 8-1. NEPTUNE_CFD/SYRTHES model for a pin cluster model 3x3 pins**

# 9 Bibliography

1. **A. Guelfi, D. Bestion, M. Boucker, P. Bouldier, P. Fillion, M. Grandotto, J.M. Hérard, E. Hervieu, P. Péturaud.** NEPTUNE: A new software platform for advanced nuclear thermal hydraulic. Nuclear science and engineering, 2007. Vol. 156. 281-324.

2. **U. Grundmann.** DYN3D-MG-V2.0: code for calculation of steady states and transients of reactors by using the multigroup neutron diffusion aproximation for hexagon or quadratic fuel assemblies with multrigroup SP3 approximation. Institute for Safety Research HZDR, 2009.

3. **C. P´eniguel, I. Rupp.** SYRTHES 3.4 - Manuel Théorique. EDF R&D 6 Quai Watier 78401 CHATOU.

4. **Nucelar Energy Agengy (NEA), Commitee on the safety of nuclear installations.** Best Pratice Guidelines fo rthe use of CFD in Nuclear Reactor Safety Applications. 2007.

5. INL RELAP5 Development Team. *RELAP5/MOD3 Users Guide.* Idaho National and Environmental Laboratory, 1996.

6. **F. Bernard, M. Barre.** The CATHARE code strategy and assessment. Nuclear Engineering and Design, 1990. Vol. 124, 3. 257-284.

7. ATHLET Mod 2.0 Cycle A Input Data Description. *Gesellschaft für Anlagenund und Reaktorsicherheit (GRS) mbH.* GRS, 2003.

8. **J. Jeong, K. Ha, B. Chung, W. Lee.** Development of a multi-dimensional thermal-hydraulic system code MARS 1.3.1. Annals of Nuclear Energy, 1999. Vol. 26, 18. 611–1642.

9. TRACE V5.0 User's Manual - Volume 2: Modeling Guidelines. U.S. Nuclear Regulatory Commission, 2008.

10. **E. Baglietto.** New perspectives of nuclear reactor design. International Journal for Nuclear Power, 2012. 1431-5254.

11. **M. A. Zimmermann.** Status of current methods for NPP analysis and need for code coupling. NURISP internal report.

12. **M. Sadatoni, A. Kawahara, Y. Ouhe, A. Yoshifusa.** Flow redistribution due to void drift in two phase flow in a multiple channel consisting of two subchannles. Nuclear Engineering and Design, 1994. Vol. 148. 463-474.

13. **D. Cuervo, M. Avramova, K. Ivanov, R. Miró.** Evaluation and enhancement of cobra-TF efficiency for LWR calculations. Annals of Nuclear Energy, 2006. Vol. 33, 9. 837-847.

14. **W. S. Kim, Y. G. Kim, Y. J. Kim.** A subchannel analysis code MATRA-LMR for wire wrapped LMR subassembly. Annals of Nuclear Engineering, 2002. Vol. 29. 303-321.

15. **P. Plas.** FLICA-3 programme pour l'etude thermohydraulique de réacteurs et de boucles d'essais. Commissariat a l'Energie Atomique. CEA-N-1802.

16. **U. Imke, V. H. Sánchez, A. Gómez.** SUBCHANFLOW: A new empirical knowledge based sub channel code. Berlin, Germany : KTG, 2010.

17. **G. Házi.** Numerical models for direct numerical and large eddy simluations of critical heat flux related phenomena. Deliverable D2.2.18.2. NURESIM Nuclear Reactor Simulation.

18. **G. Márkus, A. Házi.** Direct numerical simulation of nucleate boiling. Deliverable 2.2.3.18b. Nuclear Reactor Integrated Simulation Project NURISP.

19. **A. Kolmogorov.** The local structure of turbulence in incompressible viscous fluid for very large Reynolds numbers. Dokl. Akad. Nauk. SSSR, 1941. Vol. 30. 301-305.

20. **A. Kolmogorov.** Dissipation of energy in locally isotropic turbulence. Dokl. Akad. Nauk. SSSR, 1941. Vol. 32. 16-18.

21. **D. Jamet, O. Lebaigue, C. Morel, B. Arcen.** Towards a Multiscale Approach of the two Phase Flow Modeling in the Context of DNB modeling. Nuclear Engineering and Design, 2010. Vol. 240. 2131 2138.

22. **M. T. Dhotre, B. Niceno, B. L. Smith.** Large eddy simulation of a bubble column using dynamic sub-grid scale model. Chemical Engineering Journal, 2008. Vol. 136. 337 348.

23. **S. Mimouni, M. Boucker, J. Laviéville, A. Guelfi, D. Bestion.** Modelling and computation of cavitation and boiling bubbly flows with the NEPTUNE_CFD code. : Nuclear Engineering and Design, 2008. Vol. 238, 3. 680-692.

24. CFX-11.0 User Manual. *ANSYS.* Canonsburg, USA. ANSYS Inc. 2006.

25. STAR_CD Adapco version 4.0. User manual. New York, USA. CD Adapco.

26. **D. P. Hill.** The computer simulation of dispersed two phase flows. London. Imperial College os Science, technology and medicine, 1998. PhD thesis.

27. **A. Schaffrath, K. Ch. Fischer, T. Hahm, S. Wussow.** Validation of the CFD code fluent by post-test calculation of a density-driven ROCOM experiment. Nuclear Engineering and Design, 2007. 15-17. 1899-1908.

28. **U. Graffard, E. Bieder.** Qualification of the CFD code Trio_U for full scale reactor applications. : Nuclear Engineering and Design, 2008. Vol. 238, 3. 671-679.

29. **I. Farkas, G. Házi.** CFD calculations of bubbly flows in subchannels of fuel assemblies using the NEPTUNE CFD code. D2.2.2.18c Nuclear Reactor Integrated Simulation Project.

30. **A. Hasan, R. P. Roy, S. P. Kalra.** Experiments on subcooled flow boiling heat transfer in a vertical annular channel. Int. J. Heat Mass Transfer, 1990. Vol. 33. 2285-2293.

31. **R. P. Roy, Y. Velidandla, S. P. Kalra, P. Péturaud.** Local measurements in the two-phase boiling region of turbulent subcooled boiling flow. Journal of Heat Transfer, 1994. Vol. 116. 660-669.

32. **F. Pellacani, S. Matturro, S. Chiva, R. Macian.** CFD modeling of subcooled boiling in vertical bubbly flow conditionsusing ANSYS CFX12. Proceedings of the 18th Interbational Conference on Nuclear Engineering ICONE, 2010.

33. **S. Mimouni, F. Archambeau, M. Boucker, J. Laviéville, C. Morel.** A second order turbulence model based on a Reynols stress approach for two phase boiling flow Part I: Application to the ASU annular channel case. Nuclear Engineering and Design, 2010. Vol. 240, 2233-2243.

34. **T. H. Lee, G. C. Park, D. J. Lee.** Local flow characteristics of subcooled boiling flow of water in a vertical concentric annulus. Int. J. Multiphase Flow, 2002. Vol. 28. 1351-1368.

35. **B. Koncar, C. Morel, S. Mimouni, L. Vyskocil, G. Hazi, M. C. Galassi.** CFD modeling of boiling bubbly flow for DNB investigation. : Deliverable NURISP, Nulcear Reactor Simulation Integrated Project, 2011.

36. **S. Mimouni, F. Archambeau, M. Boucker, J. Laviéville, C. Morel.** A second order turbulence model based on a Reynols stress approach for two-phase boiling flow and application to fuel asembly analysys. Nuclear Engineering and Design, 2010. Vol. 240, 2225-2232.

37. **G. Házi, I. Farkas.** Two-Phase Rans Calculations of a Subchannel. Deliverable 2.2.18.1. Integrated Project NURESIM, Nuclear Reactor Simulations, sub-project 2: Thermal Hydraulics. 2005.

38. **W. Yao, C. Morel.** Volumetric interfacial area prediction in upward bubbly two-phase flow. Int. J. Heat Mass Transfer, 2004. Vol. 47, 307-328.

39. **A. M. Kamp, A. K. Chesters, C. Colin, J. Fabre.** Bubble coalescence in turbulent flows : a mechanistic model for turbulence induced coalescence applied to microgravity bubbly pipe flow. Int. J. Multiphase Flow, 2001. Vol. 27. 1363-1396.

40. **P. Ruyer, N. Seiler, M. Beyer, F. P. Weiss.** A bubble size distribution model for the numerical simulation of bubbly flows. Leipzig, Germany. 6th International Conference on Multiphase Flow, ICMF, 2007.

41. **A. Giacommell, F. Falk.** Rapport d'essais AGATE promotour de melange. technical report CEA DTP/SETEX/LTAC/, 2003. Internal Report. 03-191.

42. **F. Falk, R. Hugonnard.** Rapport d'essais DEBORA PROMOTEUR DE MELANGE, essais de BO et de topologie. Technical Report, CEA DTP/SETEX/LTAC, 2002. Internal report. 02-158.

43. **S. Mimouni, F. Archambeau, M. Boucker, J. Lavieville, C. Morel.** A second order turbulence model based on a Reynolds stress approach for two-phase flow - Part I : Adiabatic cases. Science and Technology For Nuclear Installations, 2009. 79.

44. **D. Lucas, E. Krepper, H. M. Prasser.** Development of co-current air-water flow in a vertical pipe. Int. J. Multiphase Flow, 2005. Vol. 31. 1304-1328.

45. **C. Morel, P. Ruyer, N. Seiler, J. Laviéville.** Comparison of several models for multi-size bubbly flows on an adiabatic experiment. International Journal of Multiphase Flow, 2010. Vol. 36. 25-39.

46. **Q. Wu, S. Kim, M. Ishii, S. G. Beus.** One-group interfacial area transport in vertical bubble flow. Int. J. Heat Mass Transfer, 1998. Vol. 41. 1103-1112.

47. **W. Yao, D. Bestion, P. Coste.** A Three-Dimensional Two-Fluid Modelling of Stratified Flow with Condensation for Pressurized Thermal Shock Investigations. Nuclear Technology, 2005. Vol. 152.

48. **T. Hibiki, M. Ishii.** One-group interfacial area transport of bubbly flows in vertical round tubes. Int. J. Heat Mass Transfer, 2000. Vol. 43. 2711-2726.

49. **M. Ishii, S. Kin.** Micro four-sensor probe measurement of interfacial area transport for bubbly flow in round pipes. Nucear Engineering and Design, 2001. Vol. 205. 2711-2726.

50. **L. Vyskocil, J. Macek.** CFD Simulation of Critical Heat Flux in a Tube. Bethesda, MD, USA : CFD4NRS-3: CFD for Nuclear Reactor Safety Applications, OECD/NEA & IAEA, 2010.

51. **D. Bestion, D. Caraghiaur, H. Anglart, P. Péturaud, E. Krepper, H.M. Prasser, D. Lucas, M. Andreani, S. Smith, D. Mazzini, F.Moretti, J. Macek.** Review of the Existing Data Basis for the Validation of Models for CHF. NURESIM-SP2 Deliverable D2.2.1, 2006.

52. **L. Vyskocil, J. Macek.** CFD Simulation of Critical Heat Flux in a Rod Bundle. Bethesda, MD, USA : CFD4NRS-3: CFD for Nuclear Reactor Safety Applications, OECD/NEA & IAEA, 2010.

53. **B. S. Shin, S. H. Chang.** Experimental study on the effect of angles and positions of mixing vanes on CHF in a 2x2 rod bundle with working fluid R-134a. Nuclear Engineering and Design, 2005. Vol. 235. 1749-1759.

54. **B. Koncar, E. Krepper.** CFD simulation of convective flow boiling of refrigerant in a vertical annulus. : Nuclear Engineering and Design, 2008. Vol. 238. 693-706.

55. **J. Lavieville, E. Quemarais, M. Boucker, L. Maas.** Neptune CFD user guide. 2010.

56. **B. Neykov, F. Aydogan, L. Hochreiter, K. Ivanov, E. Sartori, M. Martin.** NUPEC BWR Full-size Fine-mesh Bundle Test (BFBT) Benchmark Volume I: Specifications. Nuclear Science Nuclear Science. NEA/NSC/DOC, 2005. Vol. 92, 64.

57. **I. Farkas, G. Házi.** Single Phase Rod Bundle Calculations with Neptune_CFD. NURESIM Nuclear Reactor Simulations, sub-project 2: Thermal Hydraulics.

58. **M. C. Galassi, F. Moretti, F. D'Auria.** CFD Code Validation and Benchmarking Against BFBT Boiling Flow Experiment. Grenoble : Procedures of Experiments and CFD Code Applications to Nuclear Reactor Safety (XCFD4NRS), 2008.

59. **M. C. Galassi, F. D'Auria.** Simulation of the BFBT experiment with NEPTUNE_CFD Code. Deliverable D2.2.10.2. NURESIM. Nuclear reactor Integrated Simulation Project, 2007.

60. **A. Rubin, A. Schoedel, M. Avramova, H. Utsuno, S. Bajorek, A. V. Lozada.** OECD/NRC Benchmark based on NUPEC PWR subchannel and bundle test (PSBT).

61. **C. Baudry, M. Guingo, A. Douce, J. Laviéville, S. Mimouni, M. Boucker.** OECD/NRC NUPEC PSBT benchmark: Simulaion of the steady state. Toronto, Canada. The 14th International Topical Meeting on Nuclear Reactor Thermal Hydraulics (NURETH-14), 2011.

62. **A. Janicot, D. Bestion.** Condensation Modeling for ECC Injection. Nuclear Engineering and Design, 1993. Vol. 145. 37-45.

63. **P. Coste, J. Pouvreau.** Nuresim_CFD Code Calculations of COSI Tests Without weir. Deliverable D2.1.1.1a. NURESIM Nuclear Reactor Simulations, sub-project 2: Thermal Hydraulics.

64. **P. Coste.** Computational simulation of liquid-vapor thermal shock with condensation. Yokohama. International Conference On Multiphase Flow, 2004.

65. **P. Coste, J. Laviéville, J. Pouvreau, C. Baudry, M. Guingo, A. Douce.** Validation of the Large Interface Method of NEPTUNE_CFD 1.0.8 for Pressurized Thermal Shock (PTS) applications. Nuclear Engineering and Design, 2012. Vol. 253. 296-310.

66. **F. Terzuoli, M. C. Galassi, D. Mazzini, F. D'Auria.** CFD Code Validation and Benchmarking on Air/water Flow in Rectangular Channel. Delivelable D2.1.10.1. NURESIM Nuclear Reactor Simulation.

67. **M. C. Galassi, F. D'Auria, P. Coste.** Neptune_CFD module validation for condensation on stratified steam-water flow. Deliverable D2.1.10.4. NURESIM. Nuclear Reactor Simulations, sub-project 2: Thermal Hydraulics.

68. **D. Hein, H. Ruile, J. Karl.** Kühlmittelerwärmung bei Direktkontaktkondensation an horizontalen Schichten und vertikalen Streifen zur Quantifizierung des druckbelasteten Thermoschocks. Munich : BMBF Forschungsvorhaben 1500906, thermische Kraftanlagen, TUM, 1995.

69. **V.H. Sánchez, W. Hering, A. Knoll, R. Boeer.** Analysis of the OECD/NEA PWR Main Steam Line Break (MSLB) Benchmark Exercise 3 with the Coupled Code System RELAP/PANBOX. Karlsruhe : Forschungszentrum Karlsruhe, 2002. FZKA (KIT) 6518.

70. **W. Jaeger.** Sicherheitstechnische Untersuchung für einen Druckwasserreaktor mit dem gekoppelten Programmystem TRACE/PARCS. 2006. Ph.D. Thesis.

71. **A. B. Salah, G. M. Galassi, F. D'Auria, B. Koncar.** Assessment study of the coupled code RELAP5/PARCS against the Peach Bottom BWR turbine trip test. Nuclear Engineering and Design, 2005. Vol. 235. 1727-1736.

72. **D. G. Cacuci, J. M. Aragonés, D. Bestion, P. Coddington, L. Dada, C. Chauliac.** NURESIM : A european platform for nuclear reactor simulation. Luxembourg. 2006 FISA Conference on the 6th Framework Euratom Research Pogram, European Commission, 2006.

73. **C. Weiss, F. P. Chauliac.** Nurisp overview. *NURISP General Seminar*, 2009.

74. **M. Calleja, R. Stieglitz, V. Sánchez, J. Jiménez, U. Imke.** A coupled neutronic / thermal-hybraulic scheme between COBAYA3 and SUBCHANFLOW within the NURESIM simulation platform. PHYSOR, Advances in Reactor Physics, 2012.

75. **P. Emonot, A. Souyri, J. L. Gandrille, F. Barré.** CATHARE-3: A new system code for thermal-hydraulics in the context of the NEPTUNE project. Nuclear Engineering and Design, 2011. Vol. 241, 11. 4476-4481.

76. **A. Guelfi, M. Boucker, J. M. Hérard, P. Péturaud, D. Bestion, P. Boudier, P. Fillion, M. Grandotto, E. Hervieu.** A new multi-scale platform for advanced nuclear thermal-hydraulics. Status and prospects of the NEPTUNE project. Avignon, France International Topical Meeting on Nuclear Reactor Thermal Hydraulics (NURETH-11), 2005.

77. **J. Jiménez, D. Cuervo, J. M. Aragones.** A domain decomposition methodology for pin by pin coupled neutronic and thermal-hydraulic analyses in COBAYA3. Nuclear Engineering and Design, 2010. Vol. 240, 2. 313–320.

78. **J. J. Lautard, D. Schneider. A. M. Baudron.** Mixed dual methods for neutronic reactor core calculations in the CRONOS system. Madrid : International Conference on Mathematics and Computation, Reactor Physics and Environmental Analysis of Nuclear Systems, 1999. 814-826.

79. **C. Peña, F. Pellacani, S. Chiva, T. Barrachina, R. Miró, R. Macián.** CFD-neutronic coupled calculations of a quarter of a simplified PWR fuel assembly using ansys CFX 12.1 and PARCS. Toronto, Canada. International Topical Meeting on Nuclear Reactor Thermal Hydraulics (NURETH-14), 2011.

80. **V. Seker, J. W. Thomas, T. J. Downar.** Reactor physics simulations with coupled monte carlo calculation and computational fluid dynamics. Istambul : International Conference on Emerging Nuclear Energy Systems. ICENES, 2007.

81. **U. Grundmann, C. Beckert.** Development and verification of a nodal approach for solving the multigroup SP3 equations. Annals of Nuclear Energy, 2008. Vol. 35. 75-86.

82. **C. Beckert, U. Grundmann.** Entwicklung einer Transportnährung für das reaktordynamische Rechenprogramm DYN3D. FZD, 2008. Vol. 497.

83. **U. Grundmann, U. Rohde.** Verification of the code DYN3D/R wth the help of international benchmarks. Forschungsznt rum Rossendorf, 1997. Vol. 195.

84. **U. Grundmann, S. Kliem.** Analyses of the OECD main steam line break benchmarkwith DYN3D and ATHLET codes. Nuclear Technology, 2003. Vol. 142.

85. **U. Grundmann.** Calculations of a steady state of the OECD/NRC PWR MOX/UO2 transient benchmark with DYN3D. Aachen. Proc. Annual meeting on Nuclear Technology, 2006.

86. **S. Kliem.** DYN3D, Overview on code validaion for VVER reactors. Kiev. EU TACIS Project, DYN3D trainig course, 2008.

87. **G. Treshchev, A. Armand.** Investigation of the resitance during the movement of steam-water mixture in heated boiler pipe at high pressure. Atomic Energy Research Establishment, 1959.

88. **C. W. Stewart, C. L. Wheeler, R. J. Cena, C. A. McMonagle, J. M. Cuta, D. S. Trent.** COBRA IV: The model of the method. BNWL-2214, NRC-4, 1977.

89. **F. W. Dittus, L. M. K. Boelter.** Heat transfer in automobile radiators of tubular type. University of California Press, 1930. pp. 443-461.

90. **R. S. Thom.** Boiling in sub-cooled water during flow up heated tubes or annuli. Manchester, England. Symposium on Boiling Heat Transfer in Steam Generating Units and Heat Exchangers, 1965. Vol. 180, 226.

91. **V. E. Schrock, L. M. Grossman.** Forced convective boiling in tubes. Nuclear Science & Engineering, 1962. Vol. 12, 474-481.

92. **R. W. Lockhart, R. C. Martinelli.** Proposed correlation of data for isothermal two-phase two-component flow in pipes. Chemical Eng. Progress, 1949. Vol. 45. 39-45.

93. **B. Chexal, G. Lellouche, J. Horowitz, J. Healzer.** A void fraction correlation for generalized applications. Progress in Nuclear Energy, 1992. Vol. 27, 4, 255-295.

94. **A. Gómez, V. H. Sánchez, K. Ivanov, R. Macián.** DYNSUB: A high fidelity coupled code system for the evaluation of local safety parameters – Part I: Development, implementation and verification. Annals of Nuclear Energy, 2012. Vol. 48. 108-122.

95. **A. Gómez, V. H. Sánchez, K. Ivanov, R. Macián.** DYNSUB: A high fidelity coupled code system for the evaluation of local safety parameters – Part II: Comparison of different temporal schemes. Annals of Nuclear Energy, 2012. Vol. 48. 123-129.

96. **Y. Perin, K. Velkov, A. Pautz.** COBRE-TF/QUABOX-CUBBOX:Code system for coupled core and subchannel analysis. Pittsburg, USA. Procedures PHYSOR conference, 2010.

97. **A. Lozano, J. M. Aragones, N. Garcia.** Transient analysis in the 3Dnodal kinetics and thermal hydraulics ANDES/COBRA coupled system. Kursaal. Internatinal Conference on the Physics of Reactors, 2008.

98. **I. Gouja, M. Avramova, A. Rubin.** Development and optimization of coupling interfaces between reactor core neutronics and Thermal hydraulics. PHYSOR, 2010.

99. **T. J. Downar, Y. Xu, V. Seker.** PARCS v2.7 US NRC Core Ceutronics Simulator, User manual. University of Purdue, 2006.

100. **M. Ishii.** Thermo-fluid dynamic theory of two-phase flow. Paris. Eyrolles, 1975.

101. **J. M. Delhaye, M. Giot, M. L. Riethmuller.** Thermal-hydraulics of two-phase systems for industrial design and nuclear engineering. Hemisphere and McGraw Hill, 1981.

102. **E. R. G. Eckert, R. J. Goldstein, W. E. Ibele, S. V. Patankar, T. W. Simon, P. J. Strykowski, K. K. Tamma, T. H. Kuehn, A. Bar-Cohen, J. V. R. Hberlein, D. L. Hofeldt, J. H. Davidson, J. Bischof, F. Kulacki.** Heat transfer a review of 1994 literature. International Journal of Heat and Mass Transfer, 1997. Vol. 40, 16. 3729-3804.

103. **R. J. Goldstein, E. R. G. Eckert, W. E. Ibele, S. V. Patankar, T. W. Simon, T. H. Kuehn, P. J. Strykowski, K. K. Tamma, A. Bar-Cohen, J. V. R. Heberlein, J. H. Davidson, J. Bischof, F. A. Kulacki, U. Kortshagen, S. Garrick.** Heat transfer, a review of 2000 literature. International Journal of Heat and Mass Transfer, 2002. Vol. 45. 2853–2957.

104. **J. Lavieville, E. Quemarais, M. Boucker, S. Mimouni, N. Mechitoua.** Neptune_CFD V1.0 Theory manual. 2006.

105. **M. Ishii, N. Zuber.** Drag coefficient and relative velocity in bublly, dropet or particulate flows. AIChE journal, 1979. Vol. 25, 5. 843-855.

106. **N. Zuber.** On the dispersed two phase flow in the laminar flow regime. Chem. Engineering. Science. 1964. Vol. 19, 897.

107. **M. Ishii.** Two-fluid model for two-phase flow. Multiphase Science and Technology, 1990. Vol. 5. 1-58.

108. **T. R. Auton.** The lift force on a spherical body in a rotational flow. Journal of Fluid Mechaniics, 1987. Vol. 193. 199-218.

109. **A. Tomiyama, H. Tamai, I. Zun, S. Hosokawa.** Transverse migration of single bubbles in simple shear flows. Chemical Engineering Science, 2002. Vol. 57, 1849-1858.

110. **M. Lance, M. Lopez de Bertodano.** Phase distribution phenomena and wall effects in bubbly two-phase flows. Multiphase Science and Technology, 1994. Vol. 8. 69-123.

111. **Y. Hsu.** On the size range of acting nucleation cavities on a heating surface. : Journal of Heat Transfer , 1962. Vol. 87, 207, 207-216.

112. **N. Kurul, M. Podowski.** Multi dimensional effects in forced convection subcooled boiling. Jerulasem. 9th Heat Transfer Conference, 1990. 21.

113. **H. C. Unal.** Maximun bubble diameter, maximun bubble growth time and bubble growth rate during subcooled nucleate flow boiling of water up to 17.7Mw/m2. Int. J. Heat Mass Transfer, 1976. Vol. 19. 643-649.

114. **A. Burns, Y. Egorov, F. Menter.** Experimental Implementation of the RPI wall boiling model CFX-11. Ansys CFX Germany, 2004.

115. **J. Weisman, P. S. Pei.** Prediction of critical heat flux in flow boiling at low qualities. Int. J. Heat Mass Transfer, 1983. Vol. 26. 1463-1477.

116. **B. Koncar, E. Krepper, Y. Egorov.** CFD Modelling of Subcooled Flow Boiling for Nuclear Engineering Applications. Bled, Slovenia. Int. Conference: Nuclear Energy for New Europe, 2005.

117. **C. Morel, S. Mimouni, J. Laviéville, M. Boucker.** R113 boiling bubbly flow in an annular geometry simulated with the NEPTUNE code. Avignon, France. The 14th International Topical Meeting on Nuclear Reactor Thermal Hydraulics (NURETH 11), 2005. 248.

118. **A. A. Troshko, Y. A. Hassan.** A two-equation turbulence model of turbulent bubbly flows. Int. J. Multiphase Flow, 2001. Vol. 27. 1965-2000.

119. **C. Gabillet, C. Colin, J. Fabre.** Experimental study of bubble injection in a turbulent boundary layer. Int. J. Multiphase Flow, 2002. Vol. 28. 553-578.

120. **B. Ramstorfer, H. Breitschadel, A. Steiner.** Modelling of the near wall liquid velocity field in subcooled boiling flow. San Francisco, USA. Proceedings of the ASME Summer Heat Transfer Conference, 2005.

121. **B. Koncar, I. Tiselj.** Influence of near wall modelling on boiling flow simulation. Nuclear Engineering and Design, 2010. Vol. 240. 275-283.

122. **H. Kyu Cho, H. Y. Yoon, C. Morel.** Assessments of the NEPTUNE_CFD and CUPID Codes for the SUBO Experiment. NURISP. Nuclear Reactor Integrated Simulation Project.

123. **G. G. Bartolomei, V. M. Chanturiya.** Experimental study of true void fraction within boiling subcooled water in vertical tubes. Thermal Engineering, 1967. Vol. 14. 123-128.

124. **Y. Liao, D. Lucas, E. Krepper, M. Schmidtke.** Development of a generalized coalescence and breakup closure for the inhomogeneous MUSIG model. Nuclear Engineering and Design, 2011. Vol. 241, 4. 1024-1033.

125. Release on the IAPWS Industrial Formulation 1997 for the thermodynamic properties of water and steam. Erlangen, Germany. The International Association for the Properties of Water and Steam, 1997.

126. **J. Laviéville, O. Simonin.** Equations et modèles diphasiques du code Astrid 3.4 et du code saturne polyphasique. Technical Report. HE-44/99/041A, EDF R&D, 1999.

127. **M. Glück.** Validation of the sub-channel code F-COBRA-TF Part II. Recalculation of void measurements. Nuclear Engineering and Design, 2008. Vol. 238. 2317 2327.

128. **T. Kozlowski, T. J. Downar.** PWR MOX/UO2 Core Transient Benchmark. OECD NEA, 2007.

129. **J. Solis, K. Ivanov, B. Sarikata.** Boiling Water Reactor Turbine Trip (TT) benchmarck. NEA/OECD, 2001. NEA/NSC/DOC.

# ANNEX

# 10 Annex A. The NEPTUNE_CFD/SYRTHES validation

## 10.1 BFBT turbine trip without bypass

A sensitivity analysis has been performed for the HTC of the liquid phase to the steam phase for the turbine trip scenario of the BFBT database. The different models tested are summarized in Tab. 10-1. The results of the simulation for the three axial locations are illustrated in Fig. 10-1.

**Tab. 10-1. Performed simulations for the BFBT benchmark**

| Run Number | Min Bubble ø (mm) | HTC Model water/steam | SYRTHES |
|---|---|---|---|
| R1 | 0.15 | "Ranz-Marshall"/sat. | No |
| R2 | 0.15 | "Ranz-Marshall"/sat. | Yes |
| R3 | 1 | "Ranz-Marshall"/sat. | No |
| R4 | 0.15 | "Astrid"/sat. | No |

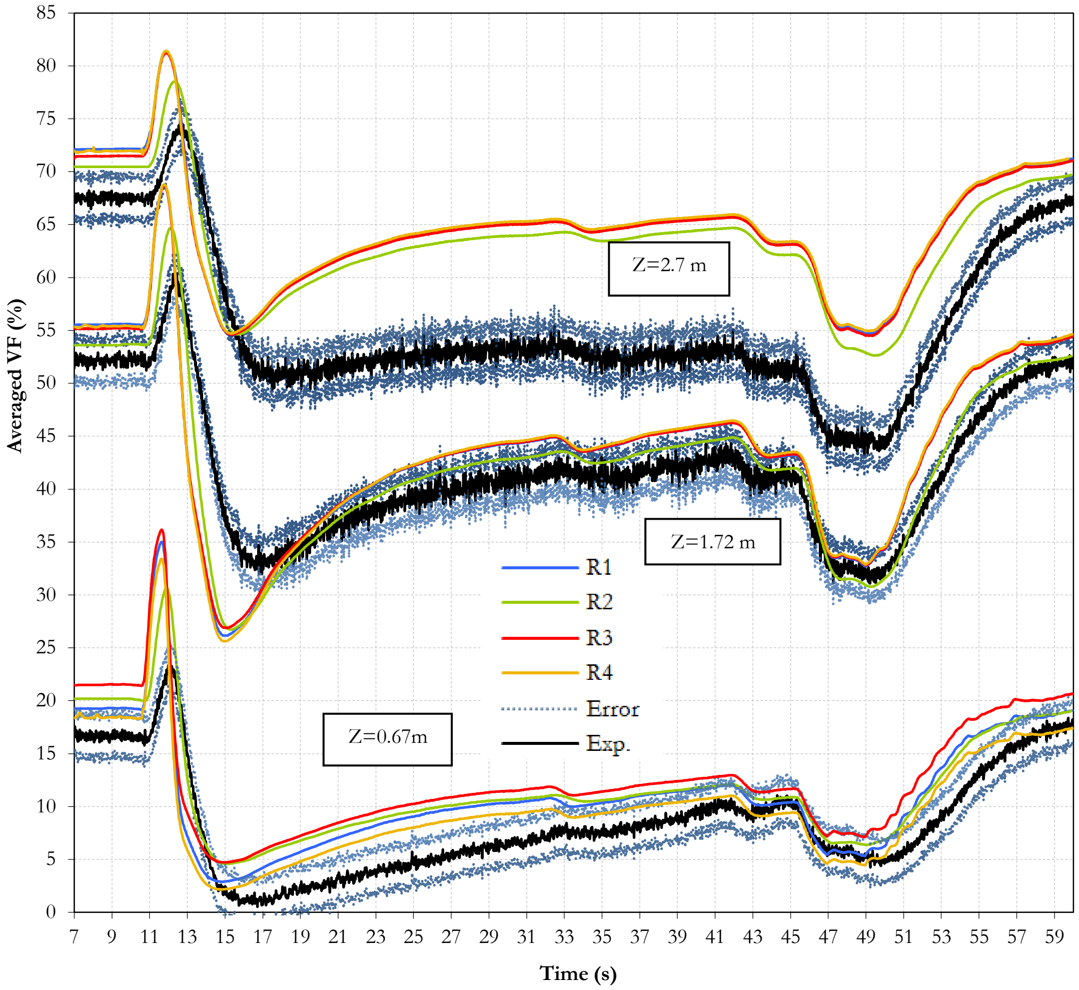

**Fig. 10-1. Comparison of the BFBT computed VF evolution by NEPTUNE_CFD with the experimental VF data and its measurement error (±2%) at three axial levels during the turbine trip experiment.**

According to Fig. 10-1, the first 10 second under steady state conditions shows a good agreement with the experimental data, specially the run R1 at the lower measurement location (Z=0.67m). At second 10.5 there is a power peak plus a flow decrease that produces a large amount of steam in the domain. At that moment all runs are over predicting the void for Z=0.67m.

The computed void evolution during the power peak unveils the "fast" steam generation produced in the domain. While the experimental data has a gradual increase, the calculated void increases as soon as the power peak appears. The maximum VF calculated during the simulations fits in time with the maximum power peak. While the maximum void registered during the experiment has a time delay from 0.5 to 1 second (depending on the location) from the power peak. Only the run R2 is producing a little delay in the steam generation, in this simulation the heat flux is set by SYRTHES and the insulator and cladding effect is taken into account. The different location definition of the heat flux as boundary condition by solving or not the thermal inertia of the solid walls has a strong influence on the simulation. VF has clearly for run R2 has a different evolution compare to the other configurations without SYRTHES especially during the power peak were the computed VF is closer to the experimental data.

From second 17 the power and mass flow are stabilized and the void variation is due to the pressure change. At second 33 there is a small power drop with its correspondent void decrease. From second 42 the mass flow starts recovering up to nominal values, and due to that the void decreases. At second 47, the power starts increasing again to initial conditions.

Only the location Z=0.67m can be considered to have a reliable prediction of the VF concentration, due to its bubbly flow regime. NEPTUNE_CFD provides closure laws for this kind of flow. In the other axial locations the VF concentration suggest that the flow regime is no longer bubbly flow, nevertheless the code can follow the tendency of the data.

In R1 and R3 two minimum bubble sizes are selected to clip the bubble size. This is important to avoid numerical errors in the calculation of the non drag due to excessive small bubbles. The differences between the two minimum bubble diameters are only appreciable at axial level (Z=0.67m) were the regime is bubbly flow and the main phenomena is the subcooled boiling. If the bubble size is smaller generates mode interfacial area and the condensation is stronger, leading to VF concentration in the domain. At higher locations the results are similar for the whole transient and the selection of this diameter is less important.

Direct comparison between different HTC models for the liquid to steam interface "Astrid" (simulation R4) and "Ranz-Marshal" (simulation R1) have similar result, but the second one is numerically more stable.

# 11 Annex B. The MPI commands

## 11.1 The Message Passing Interface (MPI)

The first approach to solve the communication was made with parallel virtual machine (PVM). This option was abandoned because the development of this tool is nowadays over. The philosophy of PVM is similar to MPI, actually the commands of both codes are rather similar. The experience acquired during the PVM work was applied to implement the communication with MPI.

The MPI is an extended tool and a lot of information and feedback can be found about it. It is widely used in the parallelization of codes, what explains its constant development. Many different distributions of this tool can be found since it is free software. The chosen distribution for this work was OpenMPI version 1.5.4 beta, which behaves better during the server-client communication establishment than its predecessor, the stable version 1.4.4.

The NEPTUNE_CFD code uses a distribution called LAM/MPI to parallelize the processes. In order to use the same MPI code and avoid duplicities by working with two different MPI installations, the LAM/MPI 1.7.7 implemented in the CFD code was replaced by the OpenMPI 1.5.4. This version is able to compile the code from the distribution LAM 1.7.7, this means that no further changes has to be done regarding the parallelization in NEPTUNE_CFD processes. The modification in the installation is affecting basically the Makefile and the macros file. The macros file has to point the include folder and the libraries of the new Open MPI 1.5.4. By this way is possible to use the same MPI installation to solve the communication between the different codes and the CFD parallelization.

The MPI works by creating groups which are called MPI_COMM_WORLD. The processes are called tasks. The task included in one MPI_COMM_WORLD share an inter-communicator. One task can join at the same time more than one group, handling with more than one inter-communicator. Once the communication is established, the information is packed and sent to destination classified by inter-communicators and tags. The basic working methodology is to use blocking senders and receivers plus barrier instructions implemented to control the timing between codes.

### 11.1.1 MPI initialization and finalization

Before perform any king of instruction the MPI has to be initialized. The usual way is to modify the source code of the program to be coupled, by including some instructions. Those examples are written in FORTRAN but it possible to do it in C language too.

```
CALL MPI_INIT (error)
if (error.EQ.0) then
  write(*,*)'[NHESDYN] : MPI_initializated'
else
  write(*,*)'[NHESDYN] : MPI_INI ERROR',error
endif
```

```
CALL MPI_FINALIZE (error)
```

All the MPI commands have a flag that provides information in case of a fatal error. In case of failure the user manual contains information about each flag. It is strongly recommended to include some simple instructions to visualize the error like in the example of the CALL MPI_INIT. Once the program is no longer in use the mpi_finalize command is used to switch of the server.

There are some extra operations to do after the initialization. The most common are the mpi_comm_size, which checks the number of processes regards the code which initializes MPI. And the other is the mpi_comm_rank, this command names each process with a number starting from 0. This rank number is very important when dealing with parallelized codes like NEPTUNE_CFD. The reason is that the command will be duplicated in many processors as we chose for the CFD code to run. For the information exchange we only need one process, in this case the process named with rank number 0.

```
CALL MPI_COMM_SIZE ( MPI_COMM_WORLD,nprocs,error )

CALL MPI_COMM_RANK ( MPI_COMM_WORLD,myrank,error )
```

### 11.1.2 Communication establishment

The next step is to establish communication between the codes. Two types of communications are used in this work, the point to point communication (client/server) and the spawn command, which creates a link between a code and its "parent". Both systems can communicate independent codes by establishing a common connection called inter-communicator.

#### 11.1.2.1 Client/Server communication

This can also be called the point to point or dynamic communication. In this method a direct link is created between two tasks. One is working as a server and the other as a client. The server publishes a "name" and a IP port and the client applies to connect to the server task by searching for that "name". Once the server accepts the communication both tasks share and inter-communicator, which is a number. The most common commands for this kind of communications are listed below for the server side:

- The MPI__ERRHANDLER_SET. Before starting this communication is common to use this command which allows getting the error massage in case of failure. If this command is not called is possible that the code fails with no apparently reason and no feedback information.

- The MPI_OPEN_PORT. It copies a system-supplied port name into the variable "port_name". This variable identifies the newly opened port and can be used by a client to contact the server. The maximum size string that may be supplied by the system is MPI_MAX_PORT_NAME. Then, the port name has to be defined as a character string with this maximum length. E.g.: character*(MPI_MAX_PORT_NAME)port_name

- The MPI_PUBLISH_NAME. It publishes the pair (port_name, service_name), so that an application may retrieve a system-supplied port_name using a well-known service_name. The service name is chosen by the user, e.g. service_name="public1"

At this point the server program waits until the client provides an answer. The commands to be implemented for the client side at this stage are:

- The MPI_LOOKUP_NAME. This command looks for the server name published by the server, in this case "public1". When found the port name is provided as an output.

- The MPI_COMM_CONNECT. Whit the recently recognized port name the server accepts the communication.

From the side of the client the work is done. Back to the server the only thing left to do is to accept the communication the client demands:

- The MPI_COMM_ACCEPT. It accepts the communication for the server and produces an inter-communicator.

After this command the communication is establish and the operations for the information exchange can start. After the program is completed the disconnection is performed by the server by calling the next command:

- The MPI_COMM_DISCONECT. This command disconnects the server from the inter-communicator. Both codes are independent again.

- The MPI_UNPUBLISH_NAME. The service name is unpublished.

- The MPI_CLOSE_PORT. The port where the server name was opened is closed.

To have an idea about what are the inputs and outputs for each commands a detailed description of the MPI code regarding the point to point communication is explained: here, first from the side of the server:

CALL **MPI_ERRHANDLER_SET** (MPI_COMM_WORLD, MPI_ERRORS_RETURN, error )

*Comment:* The MPI_COMM_WORLD and MPI_ERRORS_RETURN are generic variables of the MPI and they don't need to be defined.

CALL **MPI_OPEN_PORT** (MPI_INFO_NULL, port_name, error)

*Comment:* The MPI_INFO_NULL is a generic variable of the MPI and it doesn't need to be defined. The port_name is provided by the system and it is defined like a character.

The instructions for the client program are explained bellow. In this coupled solution the client programs are: NEPTUNE_CFD and SYRTHES. They both are program mainly in FORTRAN language, however the routines where the communication is initialized are program in C language, for that reason the next commands are provided in C.

The instructions described below summarize the actions to be performed by the client to establish a successful communication, by applying the mpi_lookup_name and mpi_comm_connect. This code is taken from one of the routine modified in the SYRTHES code.

```
MPI_Lookup_name ("public1",MPI_INFO_NULL,&port);
printf ("\n [syrc1] port received from lookup : %s\n",port);
if (MPI_Comm_connect(port,MPI_INFO_NULL,0,MPI_COMM_WORLD, & intercomm) == MPI_SUCCESS)
{printf("\n [syrc1] Connection to DYN3D stablished!\n");
  printf("\n [syrc1] intercomm: %02d\n",intercomm);
 }else{ printf("\n [syrc1] MPI_Comm_connect Failed\n");}
```

*Comment:* here the code is looking up for the service name "public1". As an output it gets the port name, it is defined as: char port [MPI_MAX_PORT_NAME]. Then, the port is used as an input for the MPI_COMM_CONNECT and the inter-communicator is provided as an output.

From the side of the client the communication is ready. To finally establish the common inter-communicator the acceptance from the server is needed:

CALL **MPI_COMM_ACCEPT** (port_name,0,0,0,newcomm,error)

*Comment:* With the port name as an input, the server program gets the inter-communicator "newcom" as an output. In this case the value 0 replaces the MPI_ INFO_NULL, and the MPI_COMM_WORLD, which is the default value for those variables.

Now the programs share a common link and can work together. When the communication is no longer necessary the server turns of the communication by calling the next commands.

CALL **MPI_COMM_DISCONNECT** (newcomm,error)

*Comment:* Uses the inter-communicator as an input.

CALL **MPI_UNPUBLISH_NAME** (public1,MPI_INFO_NULL,TRIM(port_name), error)

*Comment:* the service_name "public1" of the port_name is removed.

CALL **MPI_CLOSE_PORT**(TRIM(port_name),error)

For this coupled solution the combination of FORTRAN language and C is mandatory. In principle this shouldn't be a problem for the MPI distribution, however some incidents in that sense were found in the Open_MPI_1.4.5, where the **Lookup_name** command was not working properly. The beta version Open_MPI_1.5.5 was tested successfully for all the command applied and this is the version used for solving the communication.

The **Lookup_name** operations is not able to recognize by itself the service_name published by the other code. It needs the help of the called OMPI_SERVER. This function acts as a data server for Open_MPI jobs to exchange contact information in support of MPI-2's **Publish_name** and **Lookup_name** commands.

The OMPI_SERVER sets a URI file where the information for the open port is stored. Normally the program that is acting like a server must call this server before being initialized. In this case this call is made only by the NHESDYN main code, because DYN3D_SP3 is a spawned process and it acquired this capability from its parent program by default. An example about how to set this server is shown below:

```
ompi-server -d --report-uri URIfile &
```

And it must be followed by the execution of the program in the Open_MPI environment pointing to the location of the URI file generated. For executing the main program the command is:

```
mpirun -ompi-server
file:/home/perez/NHESDYN/NHESDYN_MAIN/URIfile -np 1 NHESDYN
```

The client programs have to be executed pointing to this file too, and example of how to do this for the SYRTHES and NEPTUNE code is shown below:

```
mpirun -ompi-server
file:/home/perez/NHESDYN/NHESDYN_MAIN/URIfile -np 1 syrthes
```

```
mpirun -ompi-server
file:/home/perez/NHESDYN/NHESDYN_MAIN/URIfile -np
${NOMBRE_DE_PROCESSEURS} neptune
```

In the case of the SYRTHES code this is not the only modification on the launching script. This code is not parallelized, hence it needs to be executed in a MPI environment. The **mpirun** command must be called before the execution of the code and the number of processors (**-np**) set to 1. A detail description of the routines modified and its location on the different codes can be found in the Annex A.

#### 11.1.2.2 Slave programs.

The other system to link two different processes is applying the spawn command. This way a program can be lunched from the "parent" process, automatically they share a inter-communicator. In this case one task (DYN3D) is spawned by the main one (NHESDYN). The command to spawn a program from the master is The MPI_COMM_SPAWN. This command needs some information to be called. The inputs and outputs are xplained below.

```
CALL MPI_COMM_SPAWN (cmd, array_of_argv, maxpes,info1, myrank,
MPI_COMM_WORLD, dyncomm, errcodes, error)
```

The spawn order is given by the array "cmd" which is calling a script to initialize the DYN3D program. If the spawn process need some input arguments they are stores in the string array_of_argv. For this case it is not necessary because all the information needed by the DYN3D is in its input file.

### 11.1.3 Main MPI commands applied.

When the connection between codes is operative, is possible to control the processes by create dependencies such: wait for code A until code B is finished, or code C doesn't start until A and B had deliver the information, and so on. The most popular system to do this with MPI is by using the sender and the receiver commands, in addition to those two, the barrier instruction is quite extended to.

The sender and receiver commands have mainly two modalities, the blocking or the non-blocking condition. The blocking option stands by the execution of the code until the message has been received. The non-blocking option doesn't stop the code until the message has arrived to destination. E.g.: Code A has to send a variable to code B, when A is supposed to send the information B is not ready to get it. In a blocking sender instruction A enters in a standby mode until B is ready to get the information. In a non-blocking sender command, A sends the info and continues its execution, the info is store in a buffer until is claimed by B. The receiver command has an analog function, but this time from the receiver side. In this coupled solution the main instruction type applied is the blocking one. A more detailed description of those commands is explained bellow.

CALL **MPI_SEND**(TCOEF,5,MPI_REAL8,0,15,4,error)

CALL **MPI_RECV**(CCWOEF,5,MPI_REAL8,0,20,4,status,error)

The barrier instruction is applied over a group, where a number of programs share an inter-communicator. Its finality is to synchronize the execution of the different programs. When MPI_BARRIER is called all the programs that belong to a group have to reach this point to be able to continue. E.g. in a three members group (A, B and C), A and B have just executed the barrier command, they are in standby waiting to C, which at the moment is occupied. When C reached the code line where the Barrier is located, then all the codes in the group can continue its normal execution.

CALL **MPI_BARRIER** (4,error)

All the MPI instructions applied in the coupled solution are summarized in figure Fig. 11-1. The commands appear in order of execution. The first column corresponds to the SYRTHES code, the second to the DYN3D_SP3 NK code, the third corresponds to the MAIN code (NHESDYN) and the fourth to NEPTUNE_CFD.

| SYRTHES | | DYN3D_SP3 | | MAIN_NHESDYN | | NEPTUNE_CFD |
|---|---|---|---|---|---|---|
| **CADTMY.F** | | **NDINPSTA** | | | | |
| MPI_RECV(timelong,1,MPI_INT,0,22,6,status,error) | < | MPI_SEND(timlong,1,MPI_INT,0,22,6,error) | | | | |
| | | | | *flag =1* | | |
| | | | | *10* | | **USCASE.F** |
| | | | | MPI_RECV(TCOEF,5,MPI_REAL8,0,2,newcomm,...) | < | MPI_SEND(TCOEF,5,MPI_REAL8,0,2,6,error) |
| **CPHYSO** | | | | MPI_RECV(DCOEF,5,MPI_REAL8,0,3,newcomm...) | < | MPI_SEND(DCOEF,5,MPI_REAL8,0,3,6,error) |
| MPI_RECV(flag-close,1,MPI_int,0,18,6,status,error) | < | MPI_SEND(flag_close,1,MPI_INT,0,18,6,error) | | MPI_RECV(TEMXL,44,MPI_REAL8,0,4,newcomm,...) | < | MPI_SEND(TEMXL,44,MPI_REAL8,0,4,6,error) |
| *if flag =1 continue / if noit go to 104* | | | | MPI_RECV(DENXL,44,MPI_REAL8,0,5,newcomm...) | < | MPI_SEND(DENXL,44,MPI_REAL8,0,5,6,error) |
| | | **NHES2DYN_INI.F** | | | | |
| MPI_SEND(CLCOEF1,5,MPI_REAL8,0,16,6,error) | > | MPI_RECV(CLCOEF,5,MPI_REAL8,0,16,6,status,error) | | *if flag = 1 time step1* | | |
| MPI_SEND(WTCOEF,5,MPI_REAL8,0,17,6,error) | > | MPI_RECV(WTCOEF,5,MPI_REAL8,0,17,6,status,error) | | *flag=0* | | |
| MPI_SEND(DOPPLER,5,MPI_REAL8,0,18,6,error) | > | MPI_RECV(DOPPLER,5,MPI_REAL8,0,18,6,status,error) | | | | |
| go to end cphyso | | MPI_RECV(TCOEF,5,MPI_REAL8,0,15,4,status,error) | < | MPI_SEND(TCOEF,5,MPI_REAL8,0,15,4,error) | | |
| | | MPI_RECV(DCOEF,5,MPI_REAL8,0,16,4,status,error) | < | MPI_SEND(DCOEF,5,MPI_REAL8,0,16,4,error) | | |
| | | | | flag 0 , never more entering (only first time step | | |
| **CFLUVS.F** | | **NK CALCULATION** | | *go to 10 (new loop)* | | |
| | | **NDSTAT.F** | | | | |
| | | *36* | | | | |
| MPI_BARRIER(6,error) | | MPI_BARRIER(6,error) | | | | |
| MPI_RECV(sum_powdist,1,MPI_REAL8,0,11,6,...) | < | MPI_SEND(sum_powdist,1,MPI_REAL8,0,11,6,...) | | | | |
| MPI_RECV(PCOEF,5,MPI_REAL8,0,3,6,...) | < | MPI_SEND(PCOEF,5,MPI_REAL8,0,3,6,...) | | | | |
| MPI_RECV(POW_WS,1,MPI_REAL8,0,12,6,...) | < | MPI_SEND(POW_ST,1,MPI_REAL8,0,12,6,...) | | | | |
| **BILFLU.F** | | | | | | |
| MPI_SEND(WPOWER,1,MPI_REAL8,0,26,6,error) | > | MPI_RECV(WPOWER,1,MPI_REAL8,0,26,6,status,error) | | | | |
| **TH CALCULATION** | | | | | | **TH CALCULATION** |
| **CADTMY.F** | | | | | | |
| MPI_RECV(timelong,1,MPI_INT,0,22,6,status,error) | < | MPI_SEND(timlong,1,MPI_INT,0,22,6,error) | | | | |
| **CPHYSO** | | *send flag = 0 (no first time step)* | | | | |
| MPI_RECV(flag-close,1,MPI_int,0,18,6,status,error) | < | MPI_SEND(flag_close,1,MPI_INT,0,18,6,error) | | | | |
| *if flag =1 continue / if noit go to 104* | | | | | | |
| *104* | | | | *10* | | **USCASE.F** |
| MPI_SEND(CLCOEF1,5,MPI_REAL8,0,13,6,error) | > | MPI_RECV(CLCOEF,5,MPI_REAL8,0,13,6,status,error) | | MPI_RECV(TCOEF,5,MPI_REAL8,0,2,newcomm,...) | < | MPI_SEND(TCOEF,5,MPI_REAL8,0,2,6,error) |
| MPI_SEND(WTCOEF,5,MPI_REAL8,0,14,6,error) | > | MPI_RECV(WTCOEF,5,MPI_REAL8,0,14,6,status,error) | | MPI_RECV(DCOEF,5,MPI_REAL8,0,3,newcomm...) | < | MPI_SEND(DCOEF,5,MPI_REAL8,0,3,6,error) |
| MPI_SEND(DOPPLERC,5,MPI_REAL8,0,19,6,error) | > | MPI_RECV(DOPPLERC,5,MPI_REAL8,0,19,6,status,error) | | MPI_RECV(TEMXL,44,MPI_REAL8,0,4,newcomm,...) | < | MPI_SEND(TEMXL,44,MPI_REAL8,0,4,6,error) |
| MPI_SEND(DOPPLER,44,MPI_REAL8,0,21,6,error) | > | MPI_RECV(DOPPLER,44,MPI_REAL8,0,21,6,status,error) | | MPI_RECV(DENXL,44,MPI_REAL8,0,5,newcomm...) | < | MPI_SEND(DENXL,44,MPI_REAL8,0,5,6,error) |
| MPI_SEND(COEFD,5,MPI_REAL8,0,23,6,error) | > | MPII_RECV(COEFD,5,MPI_REAL8,0,23,6,status,error) | | *flag = 0 goto 120* | | |
| MPI_SEND(CCOEF,5,MPI_REAL8,0,24,6,error) | > | MPII_RECV(CCOEF,5,MPI_REAL8,0,24,6,status,error) | | | | |
| MPI_SEND(CCWOEF,5,MPI_REAL8,0,25,6,error) | > | MPII_RECV(CCWOEF,5,MPI_REAL8,0,25,6,status,error) | | | | |
| | | MPI_SEND(WPOWER,1,MPI_REAL8,0,21,4,error) | > | MPI_RECV(WPOWER,1,MPI_REAL8,0,21,4,status,error) | | |
| | | MPI_SEND(CLCOEF1,5,MPI_REAL8,0,13,4,error) | > | MPI_RECV(CLCOEF,5,MPI_REAL8,0,13,4,status,error) | | |
| | | MPI_SEND(WTCOEF,5,MPI_REAL8,0,14,4,error) | > | MPI_RECV(WTCOEF,5,MPI_REAL8,0,14,4,status,error) | | |
| | | MPI_SEND(DOPPLERC,5,MPI_REAL8,0,15,4,error) | > | MPI_RECV(DOPPLERC,5,MPI_REAL8,0,15,4,status,error) | | |
| | | MPI_SEND(DOPPLER,44,MPI_REAL8,0,17,4,error) | > | MPI_RECV(DOPPLER,44,MPI_REAL8,0,17,4,status,error) | | |
| | | MPI_SEND(COEFD,5,MPI_REAL8,0,18,4,error) | > | MPII_RECV(COEFD,5,MPI_REAL8,0,18,4,status,error) | | |
| | | MPI_SEND(CCOEF,5,MPI_REAL8,0,19,4,error) | > | MPII_RECV(CCOEF,5,MPI_REAL8,0,19,4,status,error) | | |
| | | MPI_SEND(CCWOEF,5,MPI_REAL8,0,20,4,error) | > | MPII_RECV(CCWOEF,5,MPI_REAL8,0,20,4,status,error) | | |
| | | MPI_SEND(TTS,1,MPI_INT,0,16,4,error) | > | MPI_RECV(TTS,1,MPI_INT,0,16,4,error) | | |
| | | | | *TTS = 0 continue* | | |
| | | | | *130 convergence check* | | |
| | | MPI_RECV(TOTALCONV,1,MPI_INT,0,11,4,error) | < | MPI_SEND(TOTALCONV,1,MPI_INT,0,11,4,error) | | |
| MPI_RECV(TOTALCONV,1,MPI_INT,0,15,6,status,error) | < | MPI_SEND(TOTALCONV,1,MPI_INT,0,15,6,error) | | *if convergence=1 continue, if not goto 10* | | |
| *if flag =1 continue/ if not go to 20* | | *if flag =1 continue/ if not go to 36* | | | | |
| | | **SUB2DYN** | | | | |
| MPI_SEND(CLCOEF1,5,MPI_REAL8,0,5,6,error) | > | MPI_RECV(CLCOEF,5,MPI_REAL8,0,5,6,status,error) | | | | |
| MPI_SEND(WTCOEF,5,MPI_REAL8,0,6,6,error) | > | MPI_RECV(WTCOEF,5,MPI_REAL8,0,6,6,status,error) | | | | |
| MPI_SEND(DOPPLER,5,MPI_REAL8,0,20,6,error) | > | MPI_RECV(DOPPLER,5,MPI_REAL8,0,20,6,status,error) | | *15* | | |
| *20* | | MPI_RECV(TCOEF,5,MPI_REAL8,0,9,4,status,error) | < | MPI_SEND(TCOEF,5,MPI_REAL8,0,9,4,error) | | |
| **CFLUVS.F** | | MPI_RECV(DCOEF,5,MPI_REAL8,0,8,4,status,error) | < | MPI_SEND(DCOEF,5,MPI_REAL8,0,8,4,error) | | |
| | | **NK CALCULATION** | | | | |
| | | *supose end of steady state* | | | | |
| | | **NDTRAN.F** | | | | |
| | | **DYN2SUB** | | | | |
| MPI_BARRIER(6,error) | | MPI_BARRIER(6,error) | | | | |
| MPI_RECV(sum_powdist,1,MPI_REAL8,0,11,6,...) | < | MPI_SEND(sum_powdist,1,MPI_REAL8,0,11,6,...) | | | | |
| MPI_RECV(PCOEF,5,MPI_REAL8,0,3,6,...) | < | MPI_SEND(PCOEF,5,MPI_REAL8,0,3,6,...) | | | | |
| MPI_RECV(POW_WS,1,MPI_REAL8,0,12,6,...) | < | MPI_SEND(POW_ST,1,MPI_REAL8,0,12,6,...) | | | | |
| **BILFLU.F** | | | | | | |
| MPI_SEND(WPOWER,1,MPI_REAL8,0,26,6,error) | > | MPI_RECV(WPOWER,1,MPI_REAL8,0,26,6,status,error) | | | | |
| **TH CALCULATION** | | | | | | **TH CALCULATION** |
| **CADTMY.F** | | | | | | |
| MPI_RECV(timelong,1,MPI_INT,0,22,6,status,error) | < | MPI_SEND(timlong,1,MPI_INT,0,22,6,error) | | | | |
| **CPHYSO** | | *send flag = 0 (no first time step)* | | | | |
| MPI_RECV(flag-close,1,MPI_int,0,18,6,status,error) | < | MPI_SEND(flag_close,1,MPI_INT,0,18,6,error) | | | | |
| *if flag =1 continue / if noit go to 104* | | | | | | |
| *104* | | | | | | |
| MPI_SEND(CLCOEF1,5,MPI_REAL8,0,13,6,error) | > | MPI_RECV(CLCOEF,5,MPI_REAL8,0,13,6,status,error) | | *10* | | **USCASE.F** |
| MPI_SEND(WTCOEF,5,MPI_REAL8,0,14,6,error) | > | MPI_RECV(WTCOEF,5,MPI_REAL8,0,14,6,status,error) | | MPI_RECV(TCOEF,5,MPI_REAL8,0,2,newcomm,...) | < | MPI_SEND(TCOEF,5,MPI_REAL8,0,2,6,error) |
| MPI_SEND(DOPPLER,5,MPI_REAL8,0,19,6,error) | > | MPI_RECV(DOPPLER,5,MPI_REAL8,0,19,6,status,error) | | MPI_RECV(DCOEF,5,MPI_REAL8,0,3,newcomm...) | < | MPI_SEND(DCOEF,5,MPI_REAL8,0,3,6,error) |
| MPI_SEND(DOPPLER,44,MPI_REAL8,0,21,6,error) | > | MPI_RECV(DOPPLER,44,MPI_REAL8,0,21,6,status,error) | | MPI_RECV(TEMXL,44,MPI_REAL8,0,4,newcomm,...) | < | MPI_SEND(TEMXL,44,MPI_REAL8,0,4,6,error) |
| MPI_SEND(COEFD,5,MPI_REAL8,0,23,6,error) | > | MPII_RECV(COEFD,5,MPI_REAL8,0,23,6,status,error) | | MPI_RECV(DENXL,44,MPI_REAL8,0,5,newcomm...) | < | MPI_SEND(DENXL,44,MPI_REAL8,0,5,6,error) |
| MPI_SEND(CCOEF,5,MPI_REAL8,0,24,6,error) | > | MPII_RECV(CCOEF,5,MPI_REAL8,0,24,6,status,error) | | *flag = 0 goto 120* | | |
| MPI_SEND(CCWOEF,5,MPI_REAL8,0,25,6,error) | > | MPII_RECV(CCWOEF,5,MPI_REAL8,0,25,6,status,error) | | | | |
| | | MPI_SEND(WPOWER,1,MPI_REAL8,0,21,4,error) | > | MPI_RECV(WPOWER,1,MPI_REAL8,0,21,4,status,error) | | |
| | | MPI_SEND(CLCOEF1,5,MPI_REAL8,0,13,4,error) | > | MPI_RECV(CLCOEF,5,MPI_REAL8,0,13,4,status,error) | | |
| | | MPI_SEND(WTCOEF,5,MPI_REAL8,0,14,4,error) | > | MPI_RECV(WTCOEF,5,MPI_REAL8,0,14,4,status,error) | | |
| | | MPI_SEND(DOPPLER,5,MPI_REAL8,0,15,4,error) | > | MPI_RECV(DOPPLER,5,MPI_REAL8,0,15,4,status,error) | | |
| | | MPI_SEND(DOPPLER,44,MPI_REAL8,0,17,4,error) | > | MPI_RECV(DOPPLER,44,MPI_REAL8,0,17,4,status,error) | | |
| | | MPI_SEND(COEFD,5,MPI_REAL8,0,18,4,error) | > | MPII_RECV(COEFD,5,MPI_REAL8,0,18,4,status,error) | | |
| | | MPI_SEND(CCOEF,5,MPI_REAL8,0,19,4,error) | > | MPII_RECV(CCOEF,5,MPI_REAL8,0,19,4,status,error) | | |
| | | MPI_SEND(CCWOEF,5,MPI_REAL8,0,20,4,error) | > | MPII_RECV(CCWOEF,5,MPI_REAL8,0,20,4,status,error) | | |
| | | MPI_SEND(TTS,1,MPI_INT,0,16,4,error) | > | MPI_RECV(TTS,1,MPI_INT,0,16,4,error) | | |
| | | | | *TTS=1 then no need to check convercence goto 15* | | |
| | | *totalconv=1* | | | | |
| MPI_RECV(TOTALCONV,1,MPI_INT,0,15,6,status,error) | < | MPI_SEND(TOTALCONV,1,MPI_INT,0,15,6,error) | | | | |
| *if flag =1 continue* | | **SUB2DYN** | | | | |
| MPI_SEND(CLCOEF1,5,MPI_REAL8,0,5,6,error) | > | MPI_RECV(CLCOEF,5,MPI_REAL8,0,5,6,status,error) | | | | |
| MPI_SEND(WTCOEF,5,MPI_REAL8,0,6,6,error) | > | MPI_RECV(WTCOEF,5,MPI_REAL8,0,6,6,status,error) | | | | |
| MPI_SEND(DOPPLER,5,MPI_REAL8,0,20,6,error) | > | MPI_RECV(DOPPLER,5,MPI_REAL8,0,20,6,status,error) | | *15* | | |
| *20* | | MPI_RECV(TCOEF,5,MPI_REAL8,0,9,4,status,error) | < | MPI_SEND(TCOEF,5,MPI_REAL8,0,9,4,error) | | |
| | | MPI_RECV(DCOEF,5,MPI_REAL8,0,8,4,status,error) | < | MPI_SEND(DCOEF,5,MPI_REAL8,0,8,4,error) | | |
| | | | | *goto10* | | |

**Fig. 11-1. MPI instructions applied in the coupled solution in order of execution for the different codes.**

# 12 Annex C. The NHESDYN communication.

A complete description of the MPI instruction used at each moment is showed below. The information flux for both types of calculation: Stead state and transient, can be followed. Fig. 12-1 shows a detail flow chart or the coupling process, flowing the tagged steps the communication is developed as follows:

- The SYRTHES code recognizes the first iteration by the information provided by DYNSTART.F and sets an independent time step form the CFD code.
- The TH parameters from NEPTUNE_CFD are sent via USCASE to the NHESDYN code (step1). The TH info generated by SYRTHES is send via CPHYSO.F to NHES2DYN_INI.F (step2).
- NEP2MAIN_INI.F sends the CFD data to NHES2DYN_INI.F (step 3).
- DYN3D_SP3 performs the first NK time step calculation and enters in the STATIC.F routine.
- In step 4, SYRTHES receives the data (power, power map distribution and sum power distribution) by the routine DYN2NHES.F inside STATIC.F.
- SYRTHES and NEPTUNE_CFD perform the TH time step calculation.
- SYRTHES sends the fuel Doppler temperature to the STATIC.F routine (step 5) who resent it to the main code (step7) in the meanwhile NEPTUNE_CGD has sent the TH info to the main code in step 6.
- NHESDYN recognizes the steady state and with all the information collected exectes the convergence loop for the TH variables.
- If convergence is not reached the previos steps are repeated. With the NK code looping the STATIC.F routing and providing always the same power.
- If convergence is reached, CPHYSO.F sends the Doppler to NHES2DYN.F (step 8), and MAIN2DYN.F send the TH feedback to NHES2DYN.F too (step 9).
- DYN3D_SP3 executes a new time step calculation.
- If the next time step is no longer a NK steady state, the TRANSIT.F routine is called. It sends the power to the CFLUVS.F routine in the SYRTHES code (step10).
- Then the TH tools can calculate again a new time step.
- The SYRTHES TH info is send from CPHYSO.F to the routine NHES2DYN.F (step11), and the CFD code repeats the step 6.
- The Doppler previously sent in step 11 is transferred to the main code in step 12 to visualize all the TH parameters. The convergence loop is no longer executed.
- DYN3D_SP3 collects all the info via step 8 and 9 for the next NK calculation.

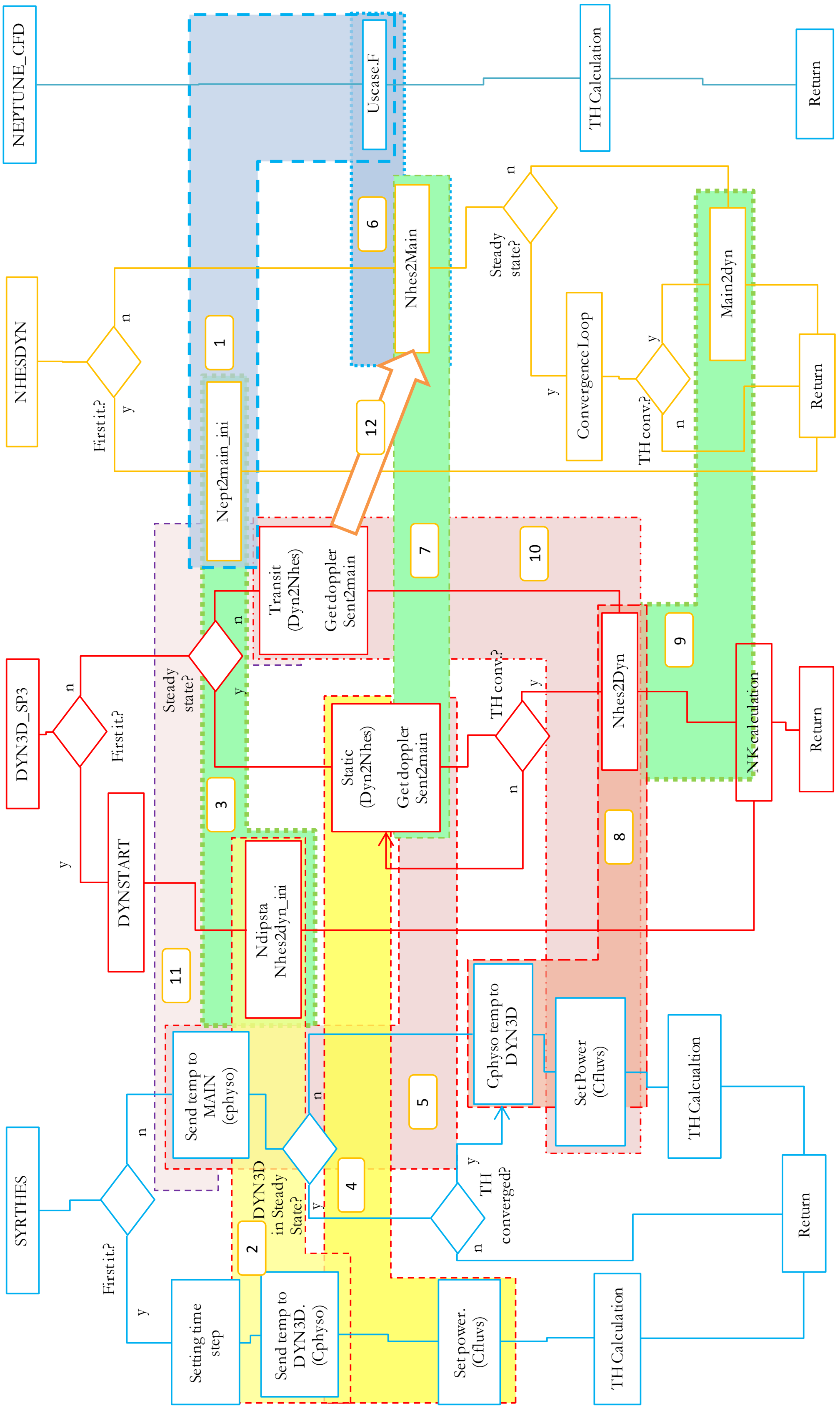
NEPTUNE_CFD
Uscase.F
TH Calculation
Return
NHESDYN
First it.?
y
n
Nept2main_ini
1
6
Nhes2Main
Steady state?
n
y
Convergence Loop
TH conv.?
y
n
Main2dyn
Return
DYN3D_SP3
First it.?
y
n
DYNSTART
Steady state?
n
y
Transit (Dyn2Nhes)
Get doppler Sent2main
12
7
10
3
Static (Dyn2Nhes)
Get doppler Sent2main
TH conv.?
y
n
Nhes2Dyn
9
8
NK calculation
Return
11
Ndipsta Nhes2dyn_ini
SYRTHES
First it.?
y
n
Send temp to MAIN (cphyso)
DYN3D in Steady State?
n
y
2
4
5
Cphyso temp to DYN3D
Set Power (Cfluvs)
TH Calcualtion
TH converged?
y
n
Return
Setting time step
Send temp to DYN3D. (Cphyso)
Set power. (Cfluvs)
TH Calculation

**Fig. 12-1. Detailed flow chart for the codes involved in the coupling scheme.**

# 13 Annex D. Modified routines in each code

## 13.1 NHESDYN

- **NHESDYN.F** : Main code that controls the coupled solution by implementing MPI instructions.
- **USPOLY**.F : last square method for the creation of polynomial functions
- **INTERP**.F : interpolation routine to obtain a value form a polynomial function

## 13.2 NEPTUNE_CFD

- **RUNCASE.SH** : The script that launches the CFD code has to modified to be executed in a new MPI environment. It also determines whether NEPTUNE_CFD runs coupled with SYRTHES or stand alone.
- **CS_BASE.C** : Initializes the MPI process as a client of the main program.
- **USCASE.F** : Averaged values for temperatures, densities, VF, etc. are calculated by this routine. It also sends the information to the main program.
- **USCLIM.F** : Any boundary conditions concerning TH are controlled by calling an external data file via this routine.
- **USKPDC.F** : Local pressure drop can be set by modifying this routine.
- **USINI.F** : Initial values for velocities, VF, turbulent kinetic energy or pressure field.
- **XPLUS.F** : Calculates the $y^+$ values

## 13.3 SYRTHES

- **CFLUVS.F** : Sets the volumetric heat flux in a specific domain (fuel). It receives information from the NK code.
- **XFLUX**.F : Sets the heat flux in a surface used for the TH tools validation.
- **CADTMY.F** : Sets the dependences in the time step, can be NEPTUNE_CFD dependent or independent.
- **CPHYSO.F** : Material properties (densities, heat capacity and conductivity) are defined in this routine. It controls the communication with the NK too.
- **SYRTHES.DATA** : Standard input file for SYRTHES. Determines whether SYRTHES is executed coupled with NEPTUNE_CFD or stand alone.
- **SYRTHES.ENV** : Standard input file which points to the mesh, and files location.
- **SYRT.ERM_C2.C** : Initializes the MPI process as client of DYN3D.
- **SYRT.ERM_C1.C** : Finalizes the MPI process.
- **BILFLU.F** : The heat flux at the interface solid/liquid is registered by this routine.

## 13.4 DYN3D_SP3

- **MPI_INI.F**: initializes the MPI environment as a spawn process of the main progam.
- **MPI_END.F**: finalizes the MPI environment.
- **DYNSTART.F** : Sends the first flat telling SYRTHES the NK code is in steady state.
- **NHES2DYN_INI.F** : Gets the TH parameters of the first iteration.
- **STATIC.F**: Manages the information exchange during the NK steady state calculations.
- **NHES2DYN.F** : Receives information from the TH tools
- **DYN2NHES.F** : Sends information to the TH tools
- **TRANSIT.F** : Manages the information exchange during the NK transient calculations.
- **NDOBOU_MG.F** : Makes the code to recognize single pin geometries.
- **NDINCRS22.F** : Modified to support the new BWR cross sections.

## 13.5 DYNSUB

- **NDDYNT_DYNSUB.F** : Modified to call the rhotem.F routine
- **ROTHEM.F** : This routine finds the arrays for the density, Doppler and moderator temperature for any axial level needed and stores them in a data file.
- **SUBCHANFLOW_TRANSIENT.F90** : Was modified to support guided mass flow transients.
- **A2_VAR_GLOBAL.F90** : A new variable was defined to support the guided mass flow transients.

## 13.6 SUBCHANFLOW

- **A5_FUELPROP.F90** : Set the material properties for the fuel according to SYRTHES.
- **A6_CLADPROP.F90** : Set the material properties for the clad according to SYRTHES.
- **SUBCHANFLOW_TRANSIENT.F90** : Occasionally the routine is modified to show results every time step by calling the routine results.f90.
- **RESULTS.F90** : Shows temperature, heat flux, pressure, mass flow, etc. at each node.

# 14 Annex E. The NHESDYN Validation.

## 14.1 $K_{eff}$ deviation during a transient

When in the coupled solution the transient starts is possible to calculate the error in the calculation of the $K_{eff}$ against the eigenvalue computed during the steady state. The biggest relative errors take place during the power changes due to the initialized thermal transient (Fig. 14-1). The relative error is illustrated for the different NHESDYN simulation in Fig. 14-2 and it is always bellow $10^{-5}$. In an explicit coupling to maintain under control this variable is important the selection of a small enough time step, otherwise the convergence of the system can be compromised.

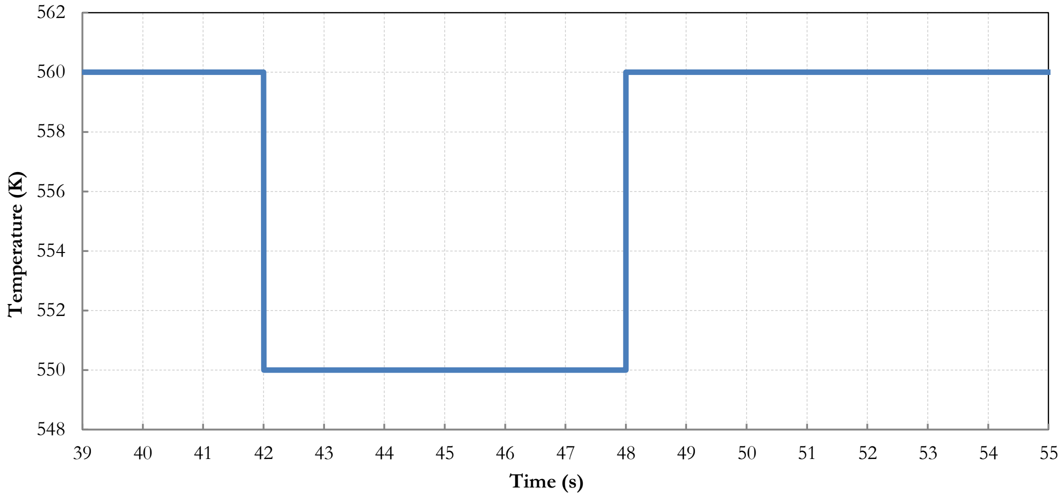

**Fig. 14-1. Water temperature evolution imposed at the inlet purposed for the transient case analysis.**

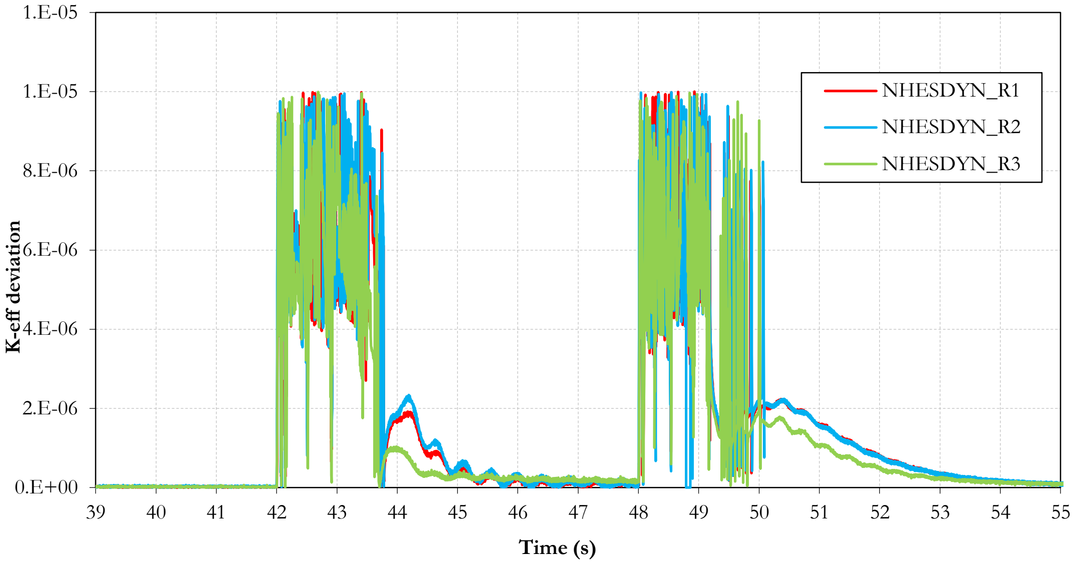

**Fig. 14-2. Deviation of the $K_{eff}$ during the temperature step transient. comparison for different NHESDYN resolutions (R1, R2 and R3).**

## 14.2 DYN3D_SP3/SYRTHES power transfer error

During the mapping operations, the power calculated by DYN3D is transferred to the heat conduction code SYRTHES by executing the instructions explained in paragraph 5.7.5. The amount of operation carries a numerical error in the real power produced by the NK code and the one that SYRTHES finally reads. The relative error between the total power provided by DYN3D and the power registered in SYRTHES is shown for the temperature step transient by Fig. 14-3. Here, for configurations R1 and R2 the error is similar, for the case R3 this value is higher. The error is constant during stable conditions (around 0.04%), and increases during the power peaks of the transient reaching ±0.6%.

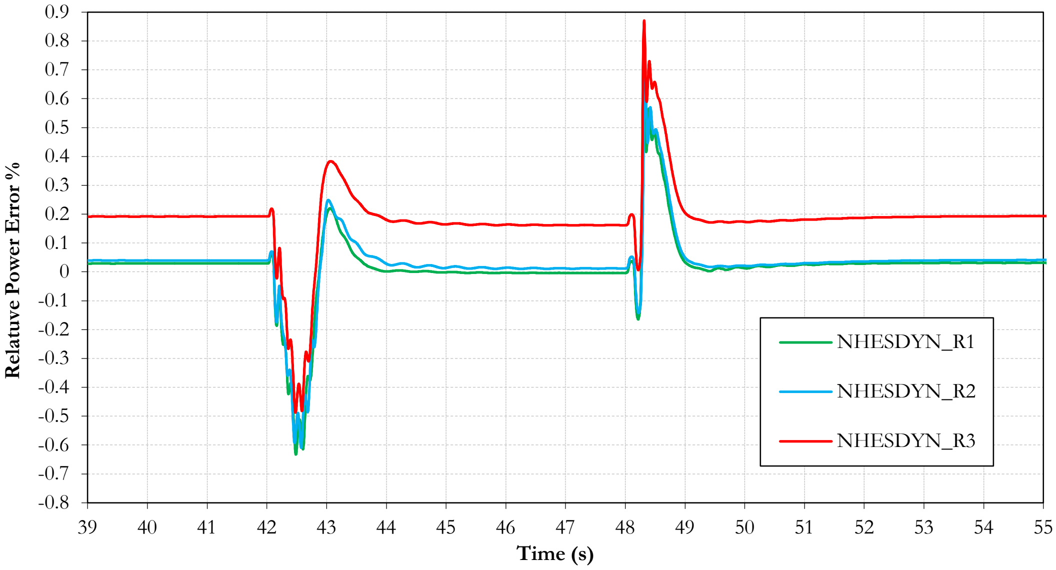

**Fig. 14-3. Power transfer error from DYN3D to SYRTHES during the temperature step transient. Comparison for different resolutions of NHESDYN: (R1, R2 and R3).**

## 14.3 Gap modeling approach in DYNSUB

The narrow region between the fuel and clad of the pin is called gap and it is fulfilled with helium. This domain is modelled in a different way by NHESDYN and DYNSUB. NHESDYN calculates the local convective HTC taking into account the wall temperature of the fuel and clad. DYNSUB sets a constant HTC for the gap domain, this is default value of $10^4$ ($W/m^2K$). The averaged value calculated by NHESDYN during the steady state is slightly higher: 11710 ($W/m^2K$). This value is set in DYNSUB as a default value for the HTC at the gap. Fig. 14-4 illustrates the sensitivity of the DYNSUB simulations to this variable. Here, the axial distribution for the center line, outer surface and Doppler temperature of the fuel are shown together with two NHESDYN simulations (R1 and R2), simulation R3 is neglected due to its lack of accuracy. As expected, the value 11710 ($W/m^2K$) for the gap HTC in DYNSUB computes closer results to NHESDYN.

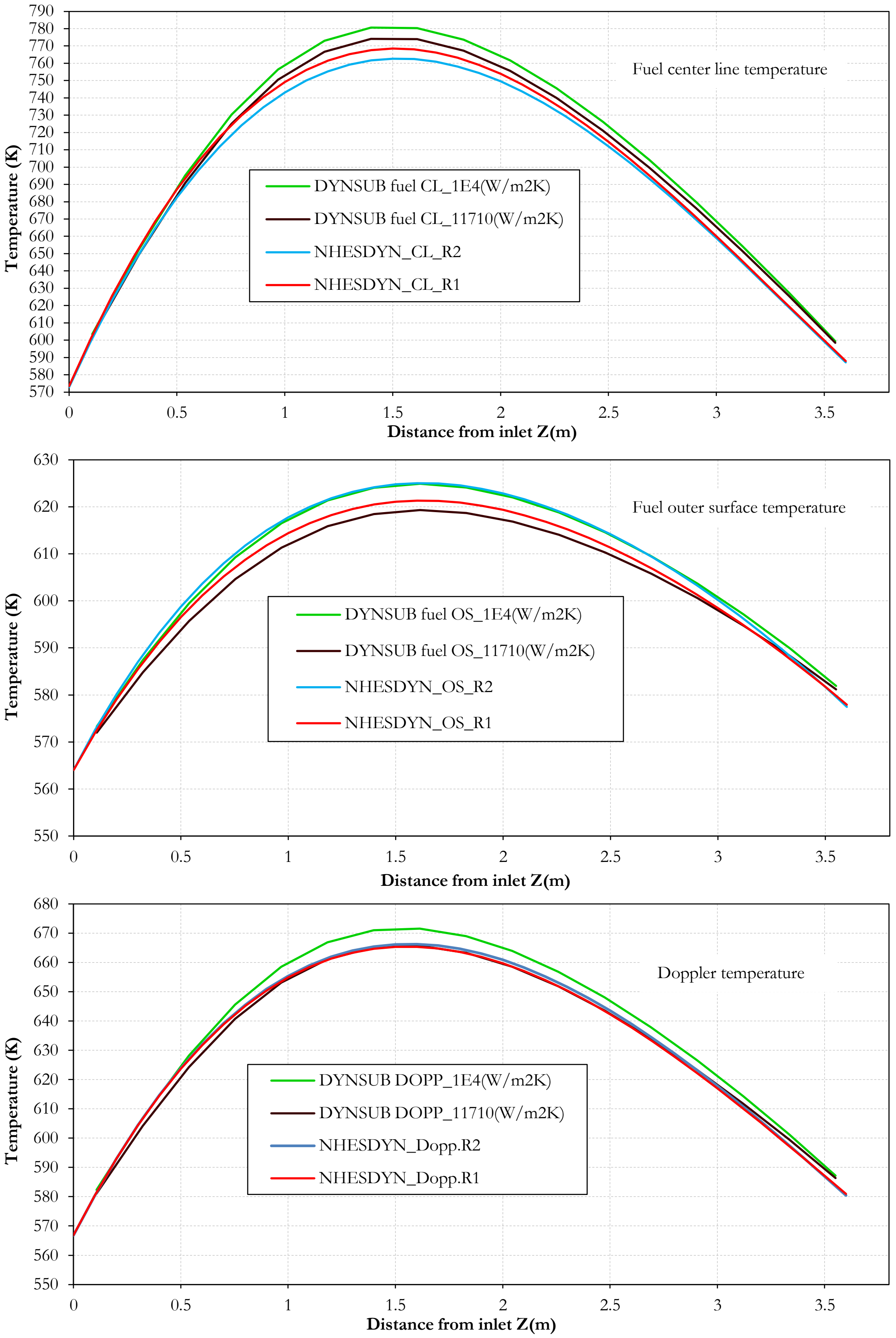

**Fig. 14-4. Axial distribution for: center line, outer fuel, and Doppler temperatures. Comparison for DYNSUB working with two HTC ($10^4$ and 11710 W/m$^2$K) and two NHESDYN resolutions (R1 and R2).**

The total averaged Doppler temperature and moderator density of the temperature step transient simulations are illustrated in Fig. 14-5 and Fig. 14-6 comparing the two different HTC for the gap modelling in DYNSUB.

The local averaged Doppler temperature of the pin (Fig. 14-5) has a better agreement with NEHSDYN cases (R1 and R2). The total averaged moderator temperature of the pin (Fig. 14-6) is not significantly affected by the change of the HTC at the gap, the since both data match. The gap modelling only affects the temperatures of the fuel domain.

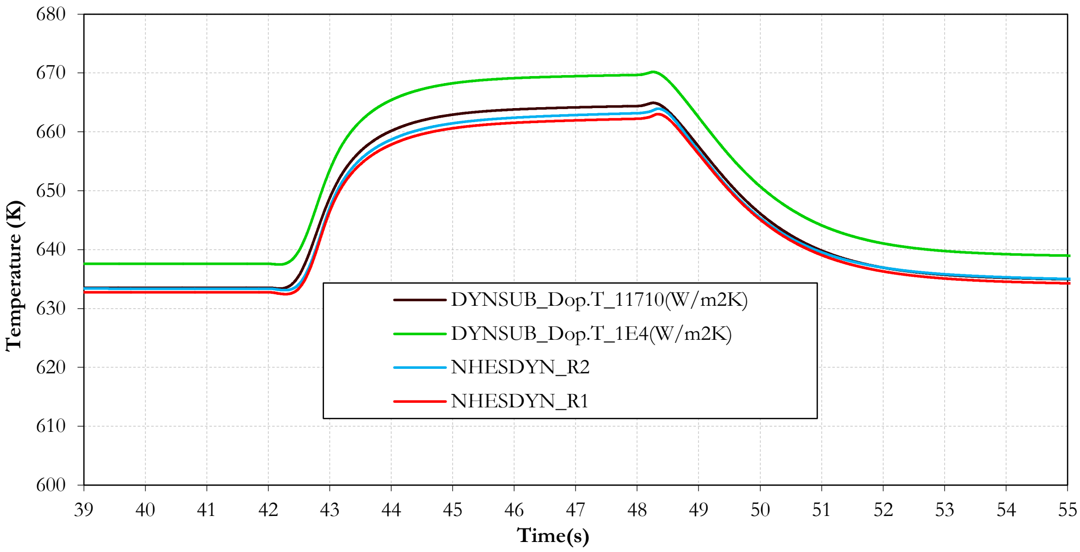

**Fig. 14-5. Total averaged Doppler temperatures: Comparison for DYNSUB working with two gap HTC ($10^4$ and 11710 W/m²K) and two NHESDYN resolutions (R1 and R2).**

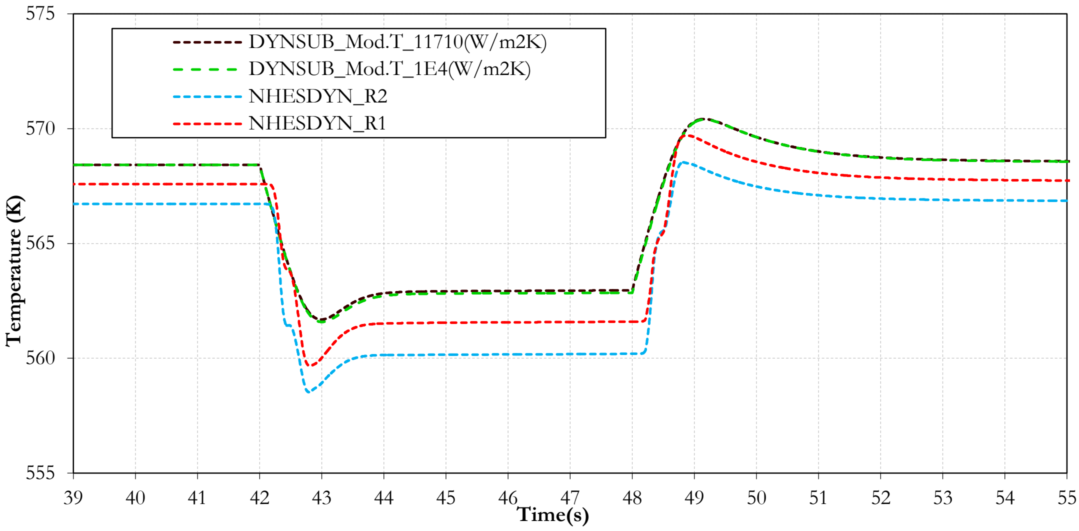

**Fig. 14-6. Total averaged moderator temperatures: Comparison for DYNSUB working with two gap HTC ($10^4$ and 11710 W/m²K) and two NHESDYN resolutions (R1 and R2).**